

In-situ studies of atmospheric-pressure dielectric barrier plasma treatment of zinc alloys and zinc oxides

Dissertation

IN FULFILMENT OF REQUIREMENTS FOR THE DEGREE OF
DOCTOR OF SCIENCE (DR. RER. NAT.)

AT THE UNIVERSITY PADERBORN

FACULTY OF SCIENCE

DEPARTMENT OF CHEMISTRY

SUBMITTED BY

MR. STEFFEN KNUST, M. SC.

BORN ON 08.04.1992 IN PADERBORN, GERMANY

Statutory Declaration

I herewith formally declare that I have written the submitted dissertation independently. I did not use any outside support except for the quoted literature and other sources mentioned in the paper.

I clearly marked and separately listed all of the literature and other sources I employed when producing this academic work, either literally or in content.

This thesis is solely submitted to the University of Paderborn.

I am aware that the violation of this regulation will lead to the failure of the thesis.

Steffen Knust

Assessment commission

<i>Chair</i>	Herr Prof. Dr. Wolfgang Bremser
<i>First examiner and the first referee</i>	Herr Prof. Dr.-Ing Guido Grundmeier
<i>Second examiner and the second referee</i>	Herr Prof. Dr. Jörg Lindner
<i>Third examiner</i>	Herr PD. Dr. Hans Egold

Submitted on

13.07.2021

Summary

In this thesis, an atmospheric-pressure dielectric barrier discharge (DBD) plasma was investigated. In so doing, its industrial relevance (in-line applicable surface treatment of a ZnMgAl alloy) was combined with fundamental research regarding plasma/surface interactions using real-time monitoring of plasma-induced changes on zinc oxide nanorods (ZnO NP) and octadecyl phosphonic acid (ODPA).

On ZnMgAl, a combination of the surface characterization techniques DPM-IRRAS and KP (in-situ), as well as XPS, TOF-SIMS, and SKPFM (ex-situ) allowed the identification of five plasma-induced surface changes after the DBD plasma treatments: (i) surface conversion of carboxylates to carbonates, (ii) etching of aliphatic carbon groups, (iii) migration of metals, (iv) increased oxide layer thickness, and (v) homogenization of the surface potential. These changes appeared in greater or lesser degree depending on the investigated gas mixture. An improvement of the adhesion properties and wettability (reduced water contact angle, increased peel-off forces of two adhesives, and high barrier properties of an octadodecyl phosphonic acid self-assembled monolayer) was observed after all plasma treatments. However, the most remarkable improvement was seen after the Ar/H₂O plasma treatment for all processes. This fact suggests that all effects contribute synergistically to the final advance in the adhesion properties. Further investigations regarding the potential use of the DBD plasma in in-line processes using Ar/H₂O showed that plasma treatments of only 5 s lead to a highly wettable surface with high natural corrosion resistance.

To gain further insights in the plasma/surface interactions, a novel backside plasma setup was developed. It enables the monitoring of surface changes (induced by the plasma effluent penetrating a coated steel mesh) in-situ and in real-time using Raman and DRIFTS. It could be shown that the backside in-situ Raman spectroscopic analysis allowed the detailed study of plasma-effluent induced changes on zinc oxide nanorods. While the plasma treatment using pure Ar led to minor interactions with the Zn sub-lattice, Ar/O₂ and Ar/H₂O plasma treatments introduced defects in the ZnO-nanorods surface near region. Ar/H₂O plasma treatments induced a steady increase in interfacial defects such as grain boundaries by roughening the surface of the nanorods. Contrary, Ar/O₂ plasma treatments rapidly increased the oxygen-related defect density (e.g., V_O) mainly during the initial phase of the plasma treatment. Thus, the presented in-situ studies demonstrated that oxygen-related reactive species must be present in the plasma effluent in order to introduce defects via interactions with the Zn sub-lattice. In another approach, the reaction of a single functional group to the plasma was monitored by coating the mesh with a self-assembled monolayer. In the resulting DRIFTS spectra, a fast decomposition of CH₂ was detected, where afterward the adsorption of excited CO₂ led to the formation of carbonates on the surface. Thereby, different reaction pathways were identified depending on the plasma gas mixture: first, the addition of oxidizing species to the plasma accelerated the decomposition of the CH₂ group and forming highly oxidized functional groups on the surface. After the decomposition, all surfaces adsorbed excited CO₂ from the gas phase forming carbonates. After the plasma treatment, the carbonates formed in the indirect Ar plasma treatment desorbed after the plasma, while carbonates formed during the indirect Ar/O₂ and Ar/H₂O plasma treatments remained on the surface.

Overall, the atmospheric-pressure plasma treatment of ZnMgAl, presenting an industrially relevant process, could be successfully understood and optimized towards increased adsorption properties by in-situ measurements and thorough ex-situ characterization. The plasma-induced changes observed on the complex alloy surface could be linked to results gained by a novel in-situ setup investigating the fundamental plasma/surface interactions, bridging the gap between fundamental and applied research.

Zusammenfassung

Diese Doktorarbeit behandelt die Anwendung von Atmosphärendruckplasmen zur Oberflächenbehandlung. Im ersten Teil wurde die industriell relevante Plasmabehandlung von ZnMgAl-Legierungen untersucht, deren Ergebnisse in einem zweiten Teil mit der grundlegenden Betrachtung der Plasma/Oberflächen-Interaktion korreliert werden konnten.

Auf ZnMgAl führte eine ausführliche Oberflächencharakterisierung mit in-situ DPM-IRRAS und KP und ex-situ XPS, TOF-SIMS und SKPFM zur Identifizierung von fünf verschiedenen plasma-induzierten Oberflächenänderungen: (i) Konversion von Carboxylaten zu Carbonaten, (ii) ätzen von aliphatischen Kohlenstoffen, (iii) Migration von Metallen, (iv) eine Erhöhung der Oxidschichtdicke und (v) eine Homogenisierung des Oberflächenpotentials. Die Stärke der Veränderungen wurde von der Zusammensetzung des Plasmagases bestimmt. Alle Plasmabehandlungen führten dabei zu einer Verbesserung der adhäsiven Eigenschaften der Oberfläche: ein reduzierter Wasserkontaktwinkel, erhöhte Abziehkräfte von zwei verschiedenen Klebstoffen und erhöhte Barriereeigenschaften einer selbstorganisierten Monolage. Die Ar/H₂O Plasmabehandlung zeigte sowohl die stärkste Verbesserung in all diesen adhäsiven Eigenschaften als auch alle plasma-induzierten Veränderungen in einem großen Umpfang, was auf eine Synergie all dieser Veränderungen bei der Verbesserung der adhäsiven Eigenschaften hindeutet. Dabei führte bereits eine Plasmabehandlung von 5 Sekunden mit Ar/H₂O zu einer hoch benetzbaren Oberfläche mit natürlicher hoher Korrosionsstabilität, was die Einsetzbarkeit in einem In-line Prozess demonstriert.

Um weitere Einblicke in die Interaktion des Plasmas mit der Oberfläche zu erlangen wurde ein neuartiger Rückseitenaufbau entwickelt, der die Oberflächenveränderungen in-situ und in Echtzeit auf der Rückseite eines Stahlnetzes mittels Raman und DRIFTS nachverfolgen kann. Die Untersuchung von ZnO Nanorods mittels Raman zeigte, dass reines Argon als Plasmagas nur geringfügige Interaktionen mit dem ZnO-Gitter zeigte, während Ar/O₂ und Ar/H₂O Defekte in der ZnO Oberfläche verursachten. Die Ar/H₂O Plasmabehandlung führte zu einer Zunahme der Rauigkeit, während die Plasmabehandlung mit Ar/O₂ einen schnellen Anstieg der Sauerstoff-Defektdichte, insbesondere am Anfang der Behandlung, verursachte. Die Ergebnisse zeigten, dass Sauerstoff in dem Plasmagas vorhanden sein muss um die ZnO Oberfläche zu verändern. In einem weiteren Ansatz wurde die Oberfläche mit einer selbst-organisierten Monolage funktionalisiert. Mittels DRIFTS wurde der Abbau von CH₂ am Beginn des Plasmas nachgewiesen, gefolgt von der Adsorption von gasphörmigen, angeregtem CO₂. Dieses führte zu der Formation von Carbonaten auf der Oberfläche, wobei die Gaszusammensetzung den Reaktionsmechanismus bestimmte: Die Präsenz von sauerstoffhaltigen Verbindungen in dem Plasmagas führte zu einem beschleunigtem Abbau der CH₂ Gruppen und zu oxidierten Funktionalitäten auf der Oberfläche. Nach diesem Abbau adsorbiert das angeregte CO₂ auf den funktionalisierten Oberflächen und bildete Carbonate. Allerdings desorbierten die so gebildeten Carbonate nach der indirekten Ar Plasmabehandlung direkt nach dem Plasma, während die Carbonate nach dem indirekten Ar/O₂ und Ar/H₂O Plasma auf der Oberfläche verblieben.

Insgesamt konnten die Einflüsse der Plasmabehandlung auf die industriell relevante ZnMgAl Legierung nachvollzogen werden und, bezogen auf die adhäsiven Eigenschaften der Oberfläche, optimiert werden. Diese plasmabezogenen Änderungen konnten mit den Ergebnissen aus einem neu entwickelten Rückseitenaufbau verknüpft werden, der die fundamentale Interaktion zwischen der Oberfläche und dem Plasma untersuchte und damit die Brücke zwischen Grundlagenforschung und angewandter Forschung schlägt.

Table of Contents

1. INTRODUCTION, MOTIVATION, AND SCIENTIFIC APPROACH	2
2. FUNDAMENTALS	6
2.1 DIELECTRIC BARRIER PLASMAS AND THEIR APPLICATIONS	6
2.1.1 <i>Basic theory</i>	6
2.1.2 <i>Plasma/surface interactions</i>	11
2.1.3 <i>Plasma treatment of metal alloys and oxides</i>	13
2.1.3.1 Influence of plasma treatments on the surface energy and adhesion of metal alloys and oxides	13
2.1.3.2 Plasma treatment of zinc oxide	13
2.1.4 <i>In-situ analysis of plasma reactions in the gas phase and at the surface</i>	16
2.1.4.1 Surface characterization subsequently after plasma treatments without contact to air	16
2.1.4.2 Real-time monitoring of surfaces in contact with a plasma	16
2.1.4.2 Real-time monitoring of gas-phase reaction in a plasma	18
2.2 ZINC ALLOYS AND OXIDES	19
2.2.1 <i>Surface chemistry of ZnMgAl alloys</i>	19
2.2.2 <i>Zinc oxide nanorods</i>	20
2.3 SELF-ASSEMBLED MONOLAYERS ON OXIDE SURFACES	22
2.3.1 <i>Binding mechanisms of phosphonic acids on metal oxides</i>	24
2.3.1 <i>Ordering and defects in SAMs</i>	25
2.4 FUNDAMENTALS OF APPLIED EXPERIMENTAL METHODS	26
2.4.1 <i>Plasma characterization</i>	26
2.4.1.1 Optical emission spectroscopy	26
2.4.1.2 Electrical characterization	27
2.4.2 <i>Spectroscopic techniques</i>	28
2.4.2.1 Infrared spectroscopy in specular and diffuse reflectance	28
2.4.2.2 Raman spectroscopy	31
2.4.2.3 X-ray photoelectron spectroscopy	31
2.4.2.4 X-ray absorption spectroscopy	33
2.4.2.5 Time-of-flight secondary ion mass spectroscopy	33
2.4.3. <i>Electrochemical techniques</i>	35
2.4.3.2 Linear sweep voltammetry for corrosion studies	36
2.4.3.4 Cyclic voltammetry	37
2.4.3.3 Electrical impedance spectroscopy	38
2.4.4 <i>Kelvin probe techniques</i>	39
2.4.4.1 Kelvin probe	40
2.4.4.2 Scanning Kelvin Probe Force Microscopy	41
2.4.5 <i>Electron microscopic techniques</i>	41
2.4.5.1 Scanning Electron Microscopy	42
2.4.5.2 Transmission Electron Microscopy	43
2.4.5 <i>Contact angle studies</i>	45
2.4.6 <i>Peel test studies</i>	46
3. EXPERIMENTAL	48
3.1 MATERIALS AND CHEMICALS	48
3.1.1 <i>Chemicals and metals</i>	48
3.1.2 <i>Adsorption of self-assembled monolayers</i>	48
3.1.3 <i>Electrochemical deposition of zinc oxide nanorods</i>	48
3.2 PLASMA TREATMENTS AND CHARACTERIZATION	49
3.2.1 <i>Plasma treatments</i>	49
3.2.2 <i>Optical emission spectroscopy</i>	49

3.2.3 Electrical characterization	49
3.3 SPECTROSCOPIC TECHNIQUES	50
3.3.1 Infrared spectroscopy	50
3.3.1.1 In-situ discrete polarization modulated IRRAS studies	50
3.3.1.2 Polarization modulated IRRAS	50
3.3.1.3 In-situ diffuse reflectance IRRAS	50
3.3.2 Raman spectroscopy	51
3.3.3 X-ray photon spectroscopy	51
3.3.4 Time-of-flight secondary ion mass spectroscopy	51
3.3.5 X-ray absorption near-edge structure spectroscopy	52
3.4 ELECTROCHEMICAL TECHNIQUES	53
3.4.3 Electrical impedance spectroscopy	53
3.4.2 Linear sweep voltammetry	53
3.4.4 Cyclic voltammetry	53
3.5 KELVIN PROBE ANALYSIS	54
3.5.2 Scanning Kelvin Probe Force Microscopy	54
3.6 ELECTRON MICROSCOPIC TECHNIQUES	55
3.6.1 Scanning Electron Microscopy and Energy-Dispersive X-ray Analysis	55
3.6.2 Transmission electron microscopy	55
3.7 CONTACT ANGLE MEASUREMENTS AND DETERMINATION OF SURFACE ENERGY	55
3.8 90°- PEEL TEST STUDIES IN HUMID ATMOSPHERE	56
3.9 ADVANCED EXPERIMENTAL SETUPS FOR IN-SITU CHARACTERIZATION	57
3.9.1 Stationary plasma chamber for in-situ DPM-IRRAS and KP studies	57
3.9.2 Backside plasma setup for DRIFTS and Raman studies	60
3.9.3 Backside plasma setup for in-situ EXAFS and XANES studies	62
4. RESULTS AND DISCUSSION	64
4.1 SURFACE MODIFICATION OF ZnMgAl-COATED STEEL BY DIELECTRIC BARRIER DISCHARGE PLASMA	65
4.1.1 Experimental approach	66
4.1.1.1 Plasma treatment	66
4.1.1.2 Time-of-flight secondary ion mass spectroscopy	66
4.1.1.3 90°- peel test under humid conditions	66
4.1.2 Results and Discussion	66
4.1.2.1 OES studies of the bulk plasma composition	68
4.1.2.2 In-situ IRRAS studies of surface chemical changes during plasma processing	69
4.1.2.4 TOF-SIMS imaging and depth profiling	75
4.1.2.5 Kelvin probe studies of average surface potentials after plasma processing	77
4.1.2.6 SKPFM imaging of surface potentials	78
4.1.2.7 Water contact angle studies	79
4.1.2.8 90°- peel test studies for the analysis of surface adhesive properties	80
4.1.3 Conclusions	81
4.2 INFLUENCE OF DIELECTRIC BARRIER PLASMA TREATMENT OF ZnMgAl ALLOY-COATED STEEL ON THE ADSORPTION OF ORGANOPHOSPHONIC ACID MONOLAYERS	82
4.2.1 Experimental approach	83
4.2.1.1 Plasma treatment	83
4.2.1.2 Octadecyl phosphonic acid adsorption	83
4.2.2 Results and Discussion	83
4.2.2.1 PM-IRRAS studies	83
4.2.2.2 XPS analysis of ODPA covered surfaces	86
4.2.2.3 Blocking properties determined by cyclic voltammetry	88
4.2.3 Conclusions	91

4.3 REACTIVITY OF AN ARGON ATMOSPHERIC-PRESSURE DBD PLASMA-ACTIVATED ZnMgAl ALLOY WITH ETOH	92
4.3.1 <i>Experimental approach</i>	93
4.3.1.1 Plasma treatment	93
4.3.1.2 Scanning Kelvin Probe	93
4.3.1.3 90°-peel test under humid conditions	93
4.3.2 <i>Results and Discussion</i>	94
4.3.2.1 Rinsing of the untreated sample with EtOH	94
4.3.2.2 Half-side Ar plasma-treated ZnMgAl	95
4.3.2.3 Rinsing of the Ar plasma-treated sample with EtOH	96
4.3.3 <i>Conclusions</i>	99
4.4 INFLUENCE OF SHORT-TIME Ar/H ₂ O ATMOSPHERIC-PRESSURE DBD PLASMA TREATMENTS ON THE ZnMgAl SURFACE	100
4.4.1 <i>Experimental approach</i>	101
4.4.1.1 Plasma treatment	101
4.4.2 <i>Results and Discussion</i>	101
4.4.2.1 Time dependence of surface modifications	101
4.4.2.2 Wettability and corrosion properties	105
4.4.3 <i>Conclusions</i>	108
4.5 IN-SITU BACKSIDE RAMAN INVESTIGATION OF ZINC OXIDE NANORODS IN AN ATMOSPHERIC-PRESSURE DIELECTRIC BARRIER DISCHARGE PLASMA	110
4.5.1 <i>Experimental approach</i>	111
4.5.1.1 Plasma treatment	111
4.5.2 <i>Results and Discussion</i>	112
4.5.2.1 Characterization of the plasma	113
4.5.2.2 Real-time in-situ backside Raman spectroscopy of ZnO coated mesh	116
4.5.2.3 XPS analysis of the plasma-treated ZnO nanorods	124
4.5.2.4 Raman spectroscopy at an expanded timescale	130
4.5.3 <i>Conclusions</i>	132
4.6 IN-SITU BACKSIDE XANES INVESTIGATION OF ZINC OXIDE NANORODS IN AN ATMOSPHERIC-PRESSURE DBD PLASMA	134
4.6.1 <i>Experimental approach</i>	135
4.6.2 <i>Results and Discussion</i>	135
4.6.3 <i>Conclusions</i>	140
4.7 IN-SITU BACKSIDE DRIFTS INVESTIGATION OF FUNCTIONAL GROUPS IN AN ATMOSPHERIC-PRESSURE DBD PLASMA	142
4.7.1 <i>Experimental approach</i>	142
4.7.1.1 Plasma treatment	142
4.7.1.2 Octadecyl phosphonic acid (ODPA) adsorption	142
4.7.2 <i>Results and Discussion</i>	143
4.7.2.1 In-situ DRIFTS evaluation of the gas phase	143
4.7.2.2 XPS characterization of the ODPA adsorption and the plasma treatments	146
4.7.2.3 In-situ DRIFTS evaluation of the surface	150
4.7.2.4 In-situ DRIFTS evaluation of the CO _x region	153
4.7.3 <i>Conclusions</i>	160
5. OVERALL CONCLUSIONS AND OUTLOOK	162
6. OUTLOOK	166
7. REFERENCES	168
GLOSSARY	181
LIST OF PUBLICATIONS	182
ACKNOWLEDGMENTS	183

1. Introduction, motivation, and scientific approach

Atmospheric-pressure plasmas present a rapidly advancing field, covering many applications, such as light source, surface treatment, thin-film deposition, and more.^{[1]-[3]} Thereby, various plasma types are available, each presenting its advantages and disadvantages.^{[2],[3]} The plasma treatments of polymers are extensively investigated and well understood, exhibiting surface cleaning, breaking of bonds, the formation of functional groups, depending on the plasma gas composition.^{[4]-[7]} Contrary, the plasma treatment of metals and their oxides have shown to be highly dependent on the respective substrate and plasma source.^{[8],[9]} This diversity hinders general predictions and makes individual investigations for material/plasma-source combinations necessary. Still, the plasma treatments of metals often lead to higher wettability and increased adhesion forces in compounds. In this regard, a plasma source able to treat large surfaces homogeneously in an in-line process is of high interest, for instance, in the steel industry. This requirement can be satisfied by dielectric barrier discharges known to treat large surfaces homogeneously and are already applied in in-line industrial processes.^{[1],[3],[10]} Therefore, DBD plasmas were chosen as plasma sources in this thesis.

Due to the complex interactions between the plasma and the substrate, even thoroughly ex-situ characterization methods are insufficient to resolve exact mechanisms at the plasma/surface interface. Therefore, in-situ and real-time methods are of high interest in the field of plasma surface modifications to deepen the understanding of its reactions and processes, thus allowing aimed improvements as well as adjustments to different applications. Thus, different in-situ and real-time setups were improved and developed in this thesis, applicable to various materials and characterization techniques. Although several in-situ setups were already developed investigating atmospheric-pressure plasmas,^{[11]-[15]} non is suitable for thoroughly studying the atmospheric-pressure plasma treatment of metals and semiconductors.

One focus of the thesis was the treatment of ZnMgAl-coated steel with a DBD plasma to enhance its surface properties such as adhesion and corrosion. Hot-dip galvanized steel is widely used nowadays due to its corrosion protection properties in the automotive and building industries. ZnMgAl alloys are of particular importance when corrosion is considered, where the ZnMgAl alloy surface showed superior corrosion resistance when compared to pure Zn,^{[16],[17]} ZnAl,^[18] and ZnMg alloys^[19]. However, other surface properties such as wettability and adhesion are of interest in addition to its corrosion properties. Although the ZnMgAl coating already exhibits reasonable adhesion forces, adhesion-increasing pretreatments are desired for critical applications. Thereby, acid etching or low-pressure plasma treatments have already been shown to increase the adhesion of a ZnMgAl alloy.^{[20]-[22]} Atmospheric-pressure plasma treatments are easier to handle than solution baths in an in-line process (no chemicals and following reduced safety issues and maintenance) and exhibit lower acquirement costs than vacuum plasma (expensive vacuum technology). Thus, the aim of the first part of the thesis was to:

1. Mimic the beneficial effects on the adhesive properties of ZnMgAl after the low-pressure plasma treatment seen before.
2. Identifying the plasma-induced changes on the ZnMgAl surface.
3. Link these changes in the surface to the surface properties.
4. Examine the plasma treatment for its in-line capability.

The respective scientific strategies and structures regarding the plasma treatment of ZnMgAl are shown in **Figure 1**.

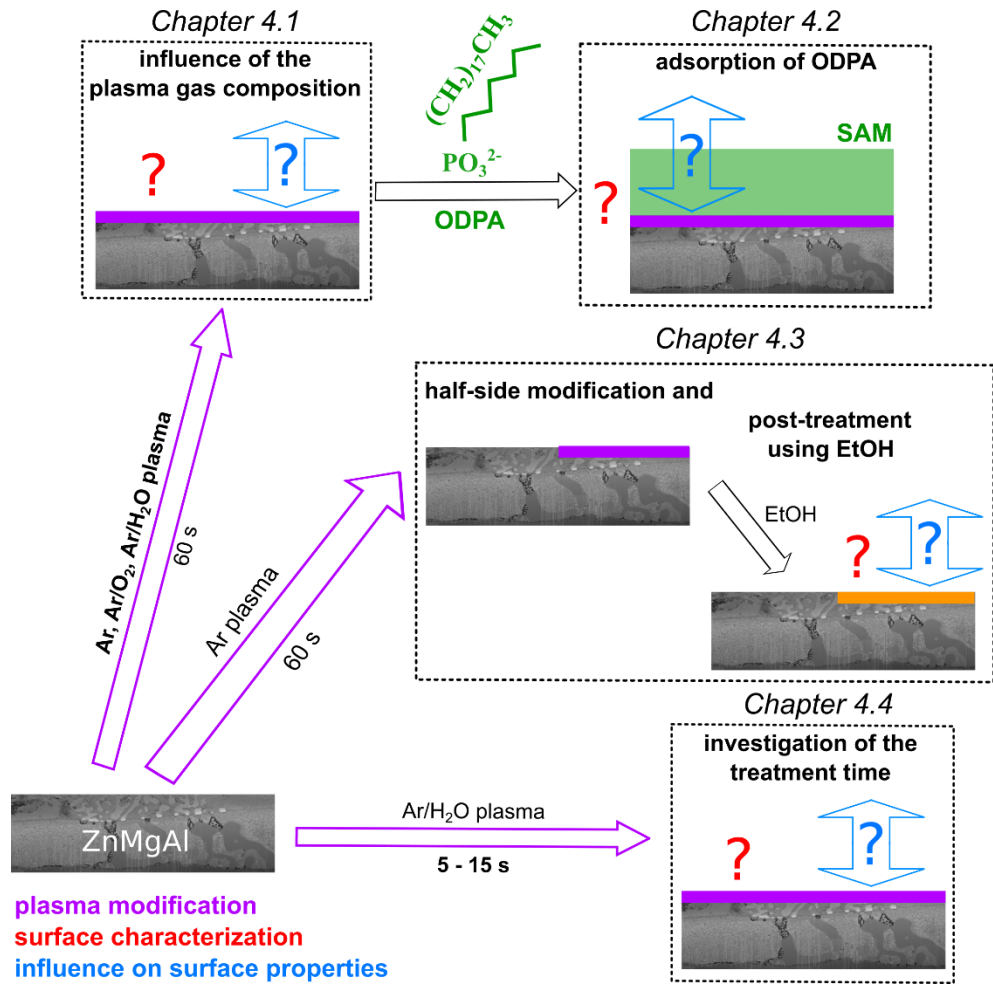


Figure 1: Overview of the scientific questions and experimental approaches regarding the technical ZnMgAl alloy.

First, the influence of the plasma gas composition on the plasma-induced changes on the ZnMgAl surface and their correlation to the adhesive and wetting behavior was investigated (see chapter 4.1). In a second step, the impact of the beforehand identified plasma-induced changes on the adsorption of a self-assembled monolayer on the surface was examined, testing the influence of the plasma treatment on a complex adsorption process (see chapter 4.2). Due to the heterogeneous structure of the ZnMgAl alloy, half-side modifications were introduced as a tool to highlight changes on the surface and applied to a post-treatment by rinsing the sample after an Ar plasma treatment using EtOH (see chapter 4.3). Last, short plasma treatment times were established for an in-line capability, using Ar/H₂O as plasma gas which showed the highest impact on the surface in the beforehand investigated chapters (see chapter 4.4).

In the second part of this thesis, novel in-situ setups were developed to satisfy the needs of monitoring the plasma-induced changes during the surface treatment of metals and semiconductors in real-time. Thereby, the necessary plasma geometry (the small gap between both electrodes of 1 or 2 mm) and disturbances by the plasma (e.g., UV radiation) hamper the monitoring of surfaces in direct contact with the plasma. Thus, the in-situ setup was designed to monitor a surface in real-time using the backside of the permeable surface in touch with the plasma. Thereby, the separation of different plasma-related effects can lead to a deeper understanding of the overall plasma process and afterward be transferred to other and more complex plasma setups, as was recently shown.^{[23],[24]} Instead of investigating the complex ZnMgAl alloy, well-defined zinc oxide nanorods were chosen. Zinc oxide and its nanostructures combine a high chemical and good mechanical resistance with exciting features such as semiconducting properties, piezo- and pyroelectric properties, biocompatibility, and more.^[25] In the field of 1D materials, nanorods have been extensively studied as they are easy to obtain and, at the same time, are suitable for revealing dependencies of electrical and thermal transport on geometric dimensions.^[26] Furthermore, nanorods are expected to increase the performance of solar cells, electroluminescent devices, photocatalytic systems, and more.^[27]

Besides the behavior of metal oxides in a plasma, the plasma treatment of organic materials is of great interest when considering the activation of polymers^{[4],[5],[28]}, sterilization^{[29],[30]} or plasma medicine^{[31],[32]}. Often, the exact mechanism of the plasma treatment is not apparent due to the presence of multiple functional groups and structures. Thus, a self-assembled monolayer was applied to investigate one defined active group interacting with the plasma.

Accordingly, the second part of the thesis aimed to:

1. Develop a plasma setup that enables the in-situ and real-time characterization of surfaces in indirect contact with the plasma.
2. Examine the setup capabilities on ZnO nanorods by revealing plasma-induced changes on the surface in-situ and in real-time.
3. Extent the material range examinable by the new setup to organic functional groups.
4. Correlate the gained results of the new in-situ setup to the results achieved on ZnMgAl.

In Figure 2, the different approaches concerning the backside setups are summarized.

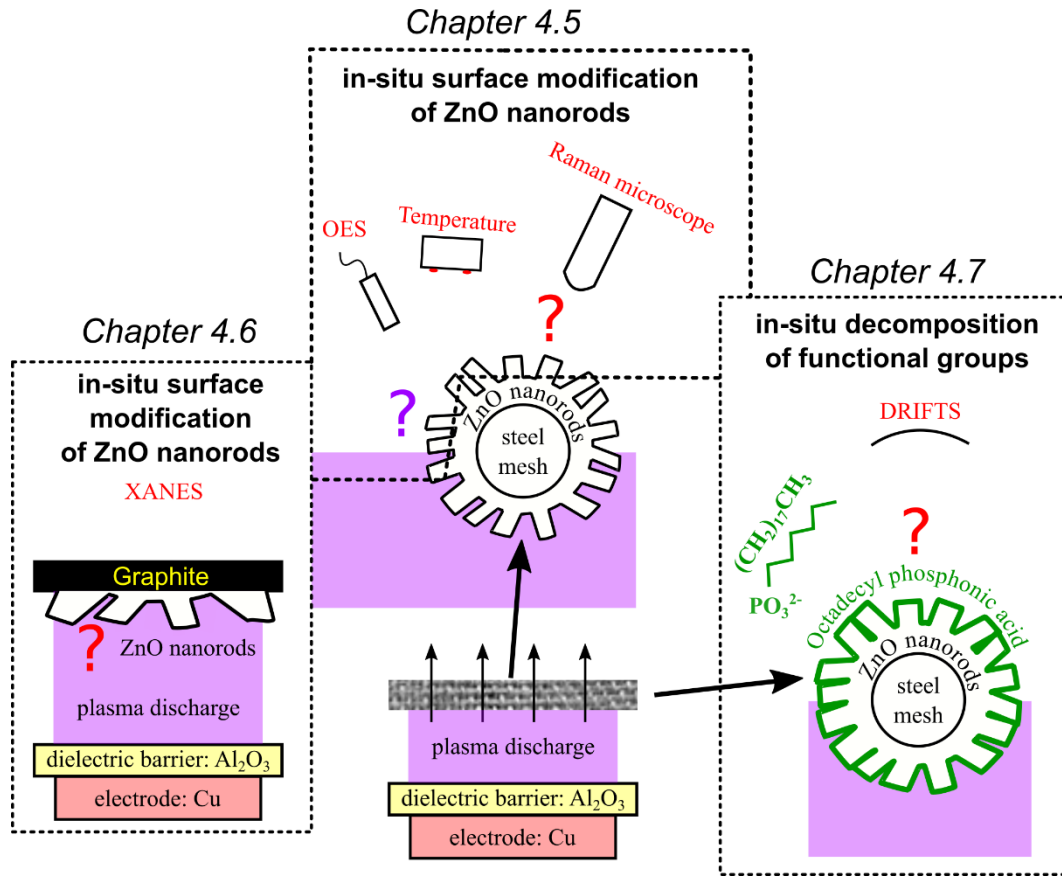


Figure 2: Overview of the scientific questions and experimental approaches investigated by novel in-situ backside setups developed by the author.

First, the backside setup was characterized (see chapter 4.5), and the modification of zinc oxide nanorods was monitored in-situ and in real-time by Raman spectroscopy (see chapter 4.5). Then, because the results did not answer all open questions, a special in-situ backside cell was developed for in-situ and real-time XANES measurements of the ZnO nanorods (see chapter 4.6). Last, the ZnO nanorods were coated with a self-assembled monolayer to investigate the interaction of specified functional groups with the plasma essential for understanding polymer modifications and plasma medicine (see chapter 4.7). Thereby, the approach of self-assembled monolayers enables the presence of defined functional groups at the plasma/surface interface.

2. Fundamentals

This thesis investigated the surface treatment of a ZnMgAl alloy, zinc oxide nanorods, and a self-assembled monolayer. This chapter aims to communicate essential knowledge of the dielectric barrier discharge, including its applications in treating substrates, the presentation of the substrate materials, and the theoretical background of each measurement method used in this thesis.

2.1 Dielectric barrier plasmas and their applications

2.1.1 Basic theory

Plasma is referred to as the 4th state of matter and is characterized by the separation of electrons from the atoms, creating charged species.^{[2],[3]} This can either be achieved by applying heat till the thermal energy is sufficient to separate atoms or electrons (equilibrium plasma discharges) or separating them by applying an external field (e.g., electric or magnetic), resulting in a non-equilibrium plasma discharge. Often, no full ionization degree is achieved, leading to neutral species being present in the plasma. Thereby, the plasma contains only charged species of different signs in the same amount and thus being overall neutrally charged (quasi-neutrality).^{[2],[3]} Equilibrium plasma discharges require a temperature of 10 000 K and more (dependent on the gas pressure), making it unsuitable for surface treatments and direct depositions.^[2] In the thermal plasma, the thermal energy is equally distributed between the electrons, ionized atoms, and neutral species, which results in similar kinetic energies for all species. Contrary, in a non-equilibrium plasma discharge, the excitation of electrons by an external field can result in different kinetic energies for the various species (electrons, charged atoms, neutral species) and thus different temperatures. Because the energy transferred by an electrical field is consumed by both the ions and electrons (where the ions have a higher mass), simply applying an electrical field results in heating the gas rather than creating a “cold” plasma. Thus, special attention must be paid to the excitation source creating alternating voltages (e.g., pulsed DC plasma or sinusoidal voltage). Thereby, the properties of a plasma depend on the gas, the setup geometry, the electrode material, the power, the type of power, and more.^[2] In a dielectric barrier discharge (DBD) plasma, the gas is excited by applying an alternating electric field to a gas, having at least one dielectric material between the electrodes. Due to the dielectric material and the alternating voltage, a non-equilibrium plasma is present where the electrons contain much higher energies than the ions.^{[2],[33]} Thus, these plasma discharges are referred to as “cold” plasmas, considering the low kinetic energy of the “heavy” gas particles (ions and neutral gas molecules).

In a fundamental consideration, the propagation of the charge within the plasma volume was modeled by Townsend, who described the initiation and sustainment of the plasma by introducing two Townsend coefficients (α, γ) resulting in the Townsend equation (**Equation 1**) valid for a simple two-electrode setup (one cathode, one anode, and an ionizable gas in between):^{[2],[34]}

$$\gamma (e^{\alpha*d} - 1) = 1 \quad (1)$$

Thereby, α embodies the ionization probability per length (d), ionizing it. Thus, the complete term $e^{\alpha*d} - 1$ responds to the total number of ions by the electron within the distance d .^{[2],[34]} When these positive ions collide with the cathode (they are attracted towards the cathode by its negative charge), secondary electrons are formed on the cathode with the probability γ . Following, the plasma enters a self-sustaining state. Thereby, α depends on the gas type (ionization energy) and pressure (free mean path, collision frequency), while γ depends on the material of the electrodes, the gas, the

2.1 Dielectric barrier plasmas and their applications

temperature and additional effects such as UV radiation.^[2] Interestingly, ceramic materials often show a higher γ than metal electrodes, allowing the fast removal of charges accumulating on the dielectric material in contact with the plasma discharge during one plasma discharge in a DBD plasma.^[2] Additional mechanisms can be present not described by the Townsend equation, for instance, additional ionization due to the Penning effect when collisions between excited metastable particles achieve ionization.

The dependence of the breakdown voltage (V_B , the lowest voltage needed to ignite a plasma discharge) on the pressure (p) and the electrode distance (d) is described by the Paschen curve, which exhibits a concave up form based on following **Equation 2**:^[2]

$$V_B = f(pd) \quad (2)$$

The experimental factor f depends on the gas. The equation demonstrates that a minimum breakdown voltage can be found by adjusting the electrode distance to the pressure for a given gas. Thereby, for high pressures such as atmospheric-pressure plasmas, only small distances lead to low ignition voltages. At higher distances, significantly higher voltages have to be applied.

In an atmospheric-pressure discharge, four basic types of discharges are observed, which are displayed in **Figure 3**.

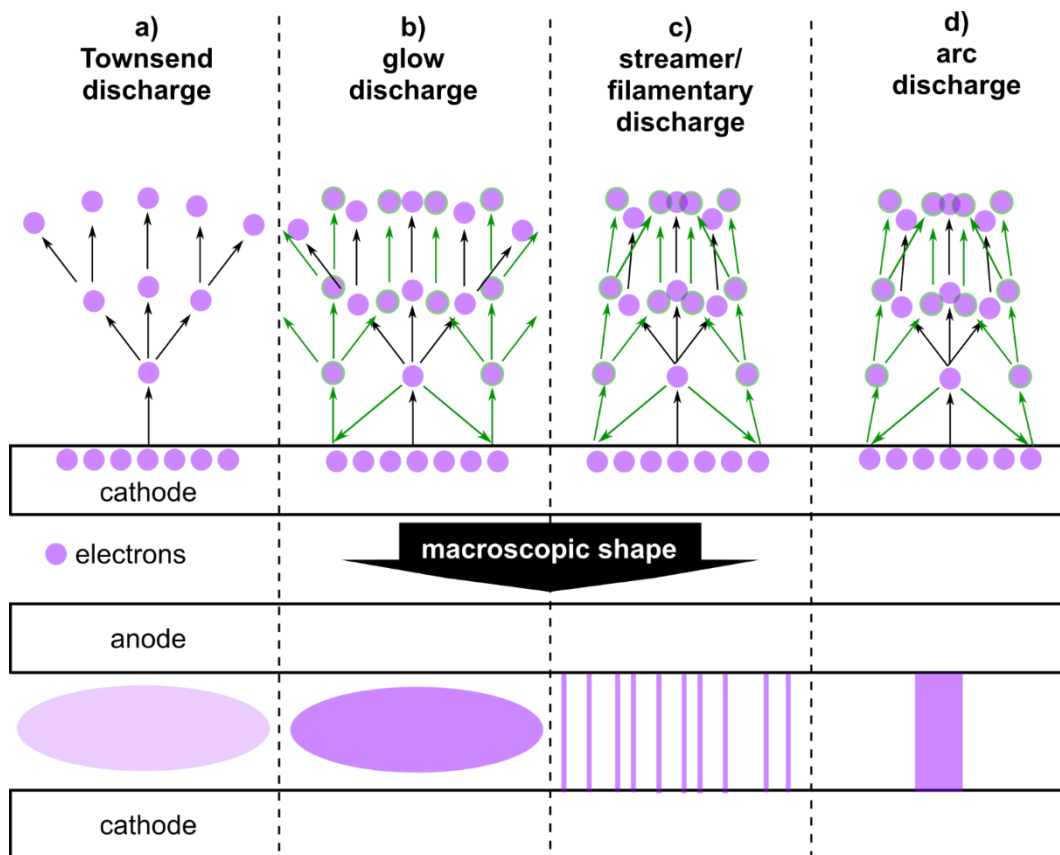


Figure 3: Principle discharge types observed in an atmospheric-pressure plasma. On top, the schematic paths of electrons for the respective discharge are shown, where the black arrows indicate the ionization path of the primary emitted electrons and the green arrows symbolize secondary electron emissions. Below, the macroscopic shape of the respective plasma is displayed.

2.1 Dielectric barrier plasmas and their applications

In **Figure 3a**, the Townsend discharge follows the propagation described by Townsend, where the propagation of the charge through the gas dominates (low γ).^{[33],[34]} Thus, a homogenous discharge evolves between the cathode and anode. However, due to its weak ionization fraction, it does not play an important role in technical applications. Contrary, the glow discharge in **Figure 3b** presents a higher electron density due to the additional secondary electron emissions (high γ). However, it is in direct competition to the (more often observed) streamer or filamentary mode (**Figure 3c**) and the arc discharge (**Figure 3d**).^{[1],[33]} In these three discharge modes, the secondary emitted electrons are always created locally around the first emission spot.^{[1],[33]} However, caused by a rapid electrical breakdown of the gas, electrical field gradients are present around the excitation spot, leading to a compression of the electrons and forms localized streamers. Thereby, the ionization of the gas leads to higher conductivity of the streamers compared to the residual gas, making the streamer the preferred current dissipation pathway. Thus, if the lifetime of the streamer is not limited, stable and localized arcs are forming and leading to a significant local power formation (heat, current density). Contrary, if the rapid breakdown is considerably slowed down, a homogenous distribution of the electrons can be obtained.^{[1],[2],[33]}

While the lifetime of the streamers can be sufficiently shortened by a dielectric (= insulating) material between the two electrodes (dielectric barrier discharge), the breakdown velocity is mainly determined by the gas. Here, often glow discharges are achieved in He due to its relatively high gas ionization, low electrical breakdown, and additional Penning ionization.^{[1],[2],[33]} Following, the most observed discharge mode in DBD plasmas for different gases is the streamer mode (arc formation is suppressed by the short streamer life times). Thereby, the streamer spread on the dielectric barrier surface, covering a larger area than the initial streamer. The charges accumulate on the surface, damping the effect of the applied electric field and thereby limiting the lifetime of the streamer.^{[1],[33]} Because the accumulated charge prevents the direct formation of a new streamer at the same position, a random (and thus assumed homogeneous) distribution of the streamers is achieved. Because of the accumulation of charges, an alternating voltage must be applied to constantly remove the charge from the dielectric barrier. Often, this frequency is in the kHz range, but also pulsed DC voltages and radiofrequency are possible.^[2] The lifetime and dimension of the streamers depend on the gas and the plasma geometries (most notably the gap (in the range around 0.1 – 10 mm)), but typical properties of the streamers are lifetimes of several tens of nanoseconds, exhibiting a radius of around 100 μm , and showing current densities up to 1000 A/cm^2 .^{[1],[33]}

2.1 Dielectric barrier plasmas and their applications

Overall, DBD discharges offer a great range of possible geometries, containing a high voltage electrode, a grounded electrode, and at least one dielectric barrier of various shapes. Some typical DBD plasma setups are presented in **Figure 4**.

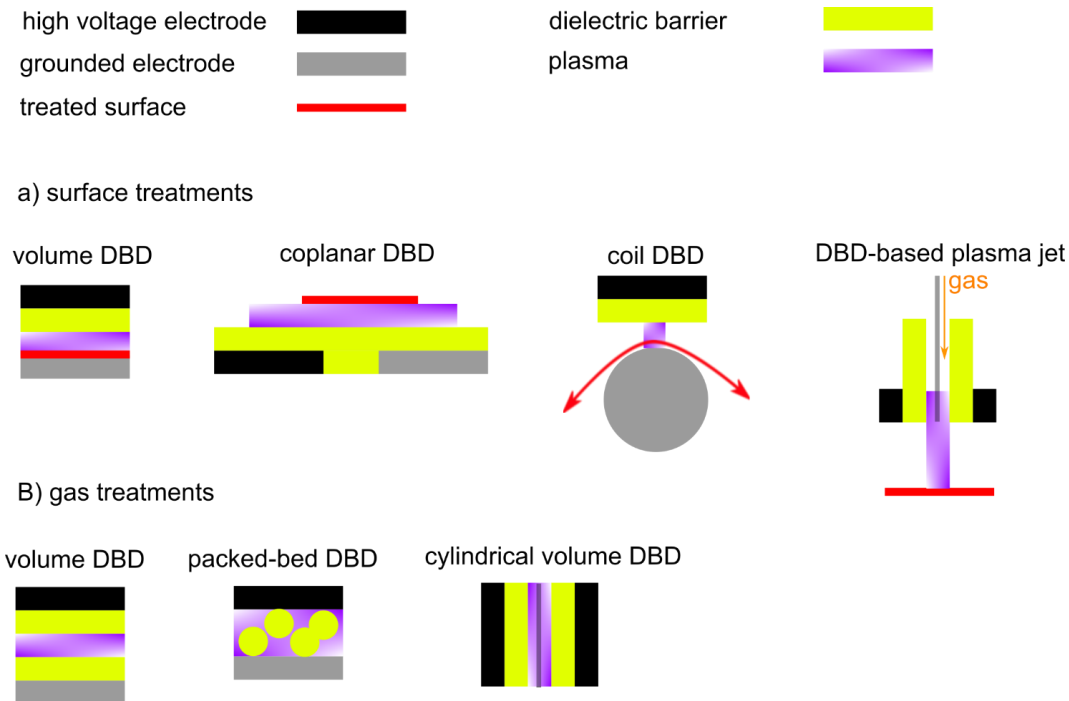


Figure 4: Different DBD plasma reactor geometries for a) surface treatments and b) gas treatments (based on [1]).

Each approach shown in **Figure 4** for treating surfaces and/or gases has its requirements, benefits, and disadvantages. For a detailed view, the reader is referred to references [1] and [33]. For instance, a volume DBD for surface treatments requires either a conductive substrate or a substrate applied on a conductive material. Thus, its disadvantage is its limitation to certain substrates. However, it offers a simple setup with a homogeneously distributed high impact on the sample and also including synergetic effects. Contrary, the surface treatments using plasma jets are applicable to each substrate type but lack the high impact and are very limited in the size of the directly treated area. Thus, to treat large samples, a movement of the substrate or the plasma source is required.

In all plasma setups, mainly the dielectric barrier determines the stability and discharge parameter of the plasma by its dielectric constant, chemical and mechanical stability, surface chemistry, and more. [1],[33] Thereby, it serves as a protection of the metal electrode from the plasma and increases the electrical field strength E , where the field strength depends on the applied voltage V , the thickness l of the dielectric barrier (1) and the gas (2), and the respective dielectric constant ϵ . [33]

$$E_2 = \frac{V\epsilon_1}{2l_2\epsilon_1 + l_1\epsilon_2} \quad (3)$$

Thus, the electrical field strength is increased in the gas gap, leading to electrical breakdowns at lower voltages compared to a setup where a gas replaces the dielectric barrier. If only the discharge gap is compared, a higher voltage must be applied in a DBD setup due to the increased distance between the electrodes. Typically, the discharge gap is between 0.1 – 10 mm, requiring voltages between 1-100 kV (peak to peak). [1]

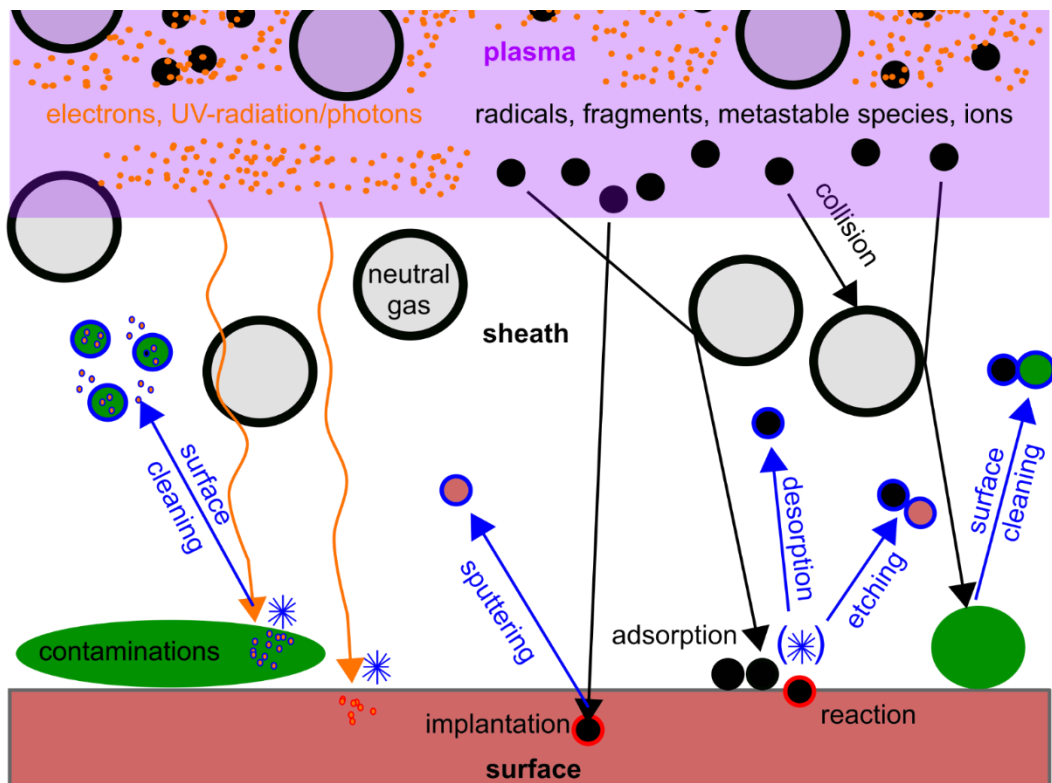
2.1 Dielectric barrier plasmas and their applications

The application of DBD plasma setups are quite diverse due to its high adaptability: By adjusting the geometry, changing the carrier gas, adding reactive species to the plasma gas, and varying plasma parameters (such as the gas flow, the voltage, the frequency, and more), the plasma treatment can be adopted to various treatments. Thereby, plasmas are seen as an environmentally friendly process due to its (in most cases) unhazardous gases, the prevention of waste (in comparison to chemical treatments), its high efficiency (leading in the case of surface and gas treatments to short treatment times (seconds to minutes)), and its applicability in in-line processes treating large surfaces or amounts of gases (e.g., coil DBD).

Thus, DBD plasmas are frequently used in gas sensors, actuators, thin film deposition, waste treatment in gases and liquids, catalysis in gas phase reaction, plasma medicine, and treatment of surfaces for cleaning, activation, or passivation.^{[1],[2],[33]} In most of these applications, the plasma/surface interaction is of great interest, either in their direct form (e.g., surface treatments, film deposition) or as an intermediate step (e.g., plasma catalysis, plasma medicine).^{[35],[36]} Thus, the plasma/surface interactions will be presented in more detail in the following section.

2.1.2 Plasma/surface interactions

In a plasma, the density of electrons and positive ions is equal (quasi-neutrality), and relatively unconstrained collisions of electrons and particles take place. Contrary, a surface (e.g., the electrode) exhibits a different potential than the plasma, leading to a sheath region between the plasma bulk and the surface, separating them.^[37] If the sample is grounded or biased, the potential gradient is constantly present. At the same time, a floating surface can lead to a converging of the plasma and surface potentials with increasing time. When the potential gradient is present, the only interactions between the surface and plasma consist of species (such as radiation, electrons, ions, radicals, and more) escaping the plasma bulk due to their kinetic energy and hitting the surface.^[37] Because the plasma/surface interactions strongly depend on the voltage applied to a surface, a grounded surface will be considered in the following paragraph. Some interactions of these species with a grounded surface are presented in **Figure 5**.



✿ excited state by e.g. excitation of vibrations/rotations, ionization, build up of radicals, forming of electron-hole pair (semiconductors), charging, heating

Figure 5: Schematic interactions between a plasma and a surface separated by a sheath region. The primary impact of the plasma species is indicated by a black arrow, while blue arrows and blue frames indicate the following processes. (based on^[35])

In the plasma, reactive species (such as ions, radicals, photons, and more) are formed due to the electron ionization presented before (**Figure 5** upper purple part). Thereby, the kind and number of the species depend on the plasma gas, the plasma discharge mode, the applied voltage, and more. In the sheath region, the propagation is stopped due to the drop in the potential towards the surface. Although no reactive species are created in the sheet region, reactive species in the plasma bulk move toward the surface due to their initial kinetic energy. However, not reacted, neutral gas is naturally present in the sheath region, leading to collisions with the reactive species emitted from the plasma (**Figure 5** black arrows). The neutral gas density depends on the pressure: At low pressures,

2.1 Dielectric barrier plasmas and their applications

only a few neutral gas molecules are present in the sheath region, whereas, at high pressures (including atmospheric pressure), a high density of the neutral gas molecules is present. Thereby, the collisions can either retract the reactive species back into the plasma, neglect the reactive species by reacting with it, or redirect the reactive species (**Figure 5** black arrows). Thereby, each collision is associated with a loss in energy, dampening the power of the incoming species when reaching the surface. Electrons and photons emitted from the plasma only experience a few collisions due to their small sizes and high energies, leading to impact powers similar to their energy in the plasma. On the surface, they can interact with surface adsorbates and the surface, exciting the target and sometimes even decompose certain bindings in organic components. In addition to the breaking of chemical bindings, the plasma can lead to excitation of vibration or rotation modes, ionization or radical formation on the target, creating electron-hole pairs in a semi-conductor, and, consequently, of all processes, induce heat.^[37] Thereby, this thermal energy is delivered only locally, leading to temperatures exceeding the low temperatures of the plasma.^[37] Thus, electrons and photons can support other processes at the surface by delivering additional energy to overcome activation energies.

For larger reactive species of the plasma (e.g., radicals, ions), collisions in the gas phase are much more likely, leading to a significant decrease in their energy, especially at atmospheric pressure.^{[36],[37]} When these particles hit the surface, different processes can be initiated depending on the reactive species, its energy, and the target properties.^[35]

1. If an incoming particle possesses high energy, it can penetrate the surface and implant itself into the material. As a consequence, a surface particle can be removed from the surface (sputtering). The energy required to induce a sputtering process depends on the surface composition and properties. Thereby, the implanted particle remains in the surface, causing a change in the local structure of the surface.
2. Suppose the energy is not high enough to penetrate the surface. In that case, a particle might simply hit the surface, transfer its energy to the surface, and be reflected (reaction not displayed in **Figure 5**).
3. Instead of being reflected, the particle might also adsorb on the surface. The probability of the atom being reflected or adsorbed depends on the substrate composition and morphology, the kind of particle, and its energy. If the adsorption is only weak, the particle can simply desorb after a certain time. In the meantime, the adsorbed particle can participate in further reactions, either with other adsorbed particles (plasma catalysis) or with the surface.
4. The reaction of a particle and the surface can also take place directly without an intermediate adsorption step. When the reaction product is volatile, an etching process is present. Otherwise, the reaction alters the surface composition, for instance introducing functional groups (e.g., oxides, hydroxides).

Suppose one of these processes leads to the removal of organic contaminations. In that case, the process is called surface cleaning and is one of the most common observed processes in plasma treatments due to the relatively low stability of organic components.^[1] Due to the high energy loss in the sheath region for atmospheric pressures, the implantation of particles in the surface and a following induced sputter process is nearly impossible.^{[2],[38]} Thus, the plasma-induced surface modifications at atmospheric pressures are dominated by processes three and four supported by the electron and photon bombardment.

2.1.3 *Plasma treatment of metal alloys and oxides*

As organic bounds are easy to modify by plasma treatments, the cleaning of surfaces and the modification of polymers became very popular.^{[4]–[6],[28]} The treatment often introduces polar groups into a prior non-polar polymer, increasing the water-wettability of the polymer. However, the plasma treatment of metals can lead to beneficial effects besides surface cleaning as well.

2.1.3.1 *Influence of plasma treatments on the surface energy and adhesion of metal alloys and oxides*

Giner et al. found that a low-pressure water plasma treatment aluminum increased the hydroxide density on the surface, while a low-pressure Ar treatment formed oxides on the surface.^[39] These changes directly influenced the adsorption of water molecules on the treated surface, as was proven in-situ by quartz crystal microbalance and polarization modulated infrared reflection absorption spectroscopy.

When applying atmospheric-pressure plasmas, a positive effect of a He/O₂ plasma treatment on the adhesive properties of an AA6062-T6 aluminum alloy was found by Saleema et al.^[40] The increased adhesion strength of an adhesive was assigned to changes in the surface chemistry, including increased polar functions such as AlOOH and Al₂O₃.

Similarly, Acero et al. improved the mechanical strength of a composite structure based on aluminum by an atmospheric-pressure treatment. The plasma treatment of the Al showed a superior enhancement of the adhesion compared to chemical cleaning and acid pre-treatments.^[41]

That this effect is not limited to Al was shown by Panousis et al., who treated a titanium alloy with an atmospheric-pressure jet and found a cleaning effect accompanied by a change in the oxide layer composition, including the appearance of NO_x functionalities.^[9] These changes increased the free surface energy of the titanium alloy.

Atmospheric-pressure plasma treatments of steel have been shown to produce a similar effect, including cleaning the surface and increasing the polar component of the surface energy by adding polar functional groups.^[42]

2.1.3.2 *Plasma treatment of zinc oxide*

Plasma treatments of ZnO have been shown to be able to improve the electrical properties of ZnO thin films^[43], the adhesive properties of ZnO nanowires^[44], and even the corrosion properties of ZnO nanorods^[45]. It is understood that defects are introduced by the plasma, which in turn changes the semiconducting properties of the film.^{[43],[46]}

Lee et al. investigated the impact of a low-pressure oxygen plasma treatment on atomic-layer deposited ZnO thin films.^[43] They found that the oxygen plasma reduced the amount of surface-near oxygen vacancies in the ZnO film and the formation of adsorbed oxygen on the surface. Thus, only the surface was affected, making it a suitable treatment technique to control the electrical properties required in thin-film transistors.

These observations are supported by Meena et al., who found the same results on flexible, free-standing ZnO thin films.^[46] However, only for plasma treatments having low power and treatment times lower than 2 minutes, an improvement of the thin-film transistors was found, while for treatment times higher than 5 minutes, a worsened performance was found. This behavior was explained by the affected depth: For lower treatment times and power, only the surface was affected as before. At larger treatment times, however, the backchannel of the transistor was affected as well due to an increased penetration depth. This reduced either the free charge carriers or increased the surface trap density, worsening the thin-film transistor's performance.

2.1 Dielectric barrier plasmas and their applications

In a similar study, the effect of a low-pressure oxygen plasma treatment of nanorod arrays by Jiang et al. demonstrated a plasma-induced change in photoluminescence dependent on the diameter of the nanorods.^[47] It was found that for ZnO nanorods with a diameter below 100 nm the photoluminescence could be enhanced mainly by the oxygen plasma treatment due to changes in the depletion region, inducing band bending. The restriction to low ZnO diameters was explained by the low penetration depth of the reactive oxygen species and the effect of the depletion region being most dominant at low ZnO nanorod diameters.

The loss of free charge carriers after a low-pressure oxygen plasma-treated was observed by Ozcan et al. for ZnO nanorods, too.^[45] This shows that ZnO reacts similarly to low-pressure oxygen plasma treatments despite its shape and substrate. Interestingly, an increase in the free charge carriers discharge was found after a low-pressure hydrogen plasma. Thereby, both plasma treatments affected the current density investigated by linear sweep voltammetry of the ZnO nanorods, showing, on the one hand, the suppression of the cathodic current density for the oxygen plasma treatment and, on the other hand, the suppression of the anodic current density after the hydrogen plasma treatment. The current density allows the estimation of the corrosion properties of the material. Thus, the ZnO can be expected to exhibit an enhanced corrosion resistance of the pure surface after the hydrogen plasma treatment. In contrast, the oxygen plasma treatment could increase the interfacial corrosion resistance after being coated with a polymer.

The increased charge carriers density after the low-pressure hydrogen plasma was explained by Windisch et al., who showed by Raman spectroscopy that hydrogen from low-pressure hydrogen plasmas could occupy oxygen vacancies and interstitial sites. These increased the charge carrier density and creating disorder in the material.^[48]

In addition to the implantation of hydrogen, an increased roughness was found on low-pressure hydrogen plasma treated ZnO films by Bang et al., which was assigned to etching of the surface by reactive hydrogen species.^[49] Still, the hydrogen plasma treated ZnO films showed a superior optical appearance and overall improved characteristics. In all before mentioned studies, the semiconducting properties of the ZnO were of interest and altered by the respective plasma treatments.

In comparison, Meng et al. investigated the influence of a low-pressure oxygen plasma treatment on the water wettability of ZnO nanowires. They found that the plasma treatment led to a hydrophilic surface. Furthermore, post-annealing of the ZnO nanowires in oxygen led to a hydrophobic surface, showing the tunability of the wetting behavior. Thereby, the change in the wettability was based on changes in the surface states of the ZnO rather than its semiconducting properties.

In one of the rare atmospheric-pressure plasma treatments, Daria et al. compared the effect of nitrogen and air as plasma gas on ZnO tetrapods.^[50] They found a decisive change in the surface morphology accompanied by an increase in oxygen vacancies. Following this, the water contact angle was reduced.

Changes in semiconducting properties were also found on MgZn₂ after reductive and oxidative low-pressure plasma treatments by Giza et al.^[51] Thereby, a low-pressure hydrogen plasma treatment led to a negative shift of the Volta potential as measured by the Kelvin probe. The resulting surface potential was lower than the respective free corrosion potential, resulting in an inhibition of any oxygen reduction on the surface and thus providing excellent protection against cathodic deadhesion of polymers at the interface. The plasma-induced change in the surface potential was accompanied by an accumulation of Mg on the surface, while the surface's hydroxide density was decreased. On the contrary, the low-pressure oxygen plasma treatment led to an increased oxide layer thickness with increased Mg content. Due to the oxide layer, an increased surface potential was found, leading

2.1 Dielectric barrier plasmas and their applications

to accelerated delamination and thus corrosion of the metal under a polymer film after the oxygen plasma treatment.

Using the same experimental conditions, Pohl et al. investigated the adsorption of a self-assembled monolayer on plasma-treated ZnMgAl surfaces.^[21] They found similar dependencies of the surface composition on the plasma gas, namely and enrichment of Mg and Al on the surface after the hydrogen plasma treatment and an increase in the oxide layer thickness after the oxygen plasma treatment. Both plasma treatments reduced the dissolution of Zn from the surface, as was shown by cyclic voltammetry, and increased the order of an adsorbed self-assembled monolayer and its stability in water.

The effect of different plasma gas compositions (air, water, nitrogen, humid air, humid nitrogen) on the ZnMgAl surface was investigated by Duchoslav et al. using an atmospheric-pressure plasma spark-jet system.^[52] They found that the changes in ZnMgAl largely depended on the plasma gas composition, where all treatments led to significant but distinct changes in the surface chemistry and morphology. Thereby, the changes could be explained as a result of an acid attack by the plasma: the reactive species interact with the naturally adsorbed water layer on top of the ZnMgAl surface, lowering its pH value. Thus, the plasma initiated a corrosive attack on the surface, leading to changes in the oxide layer's chemical compositions and morphology. The observed changes strongly depended on the pH value rather than on other interactions with reactive species present in the plasma.

2.1 Dielectric barrier plasmas and their applications

2.1.4 *In-situ analysis of plasma reactions in the gas phase and at the surface*

In-situ and real-time monitoring of plasma treatments deepen the understanding of its reactions and processes. In-situ experiments regarding plasma applications can be roughly distinguished into three categories. In the first category, the plasma is performed, and subsequently, the sample is measured without being in contact with air (e.g., in vacuum or inert gas). This can include that the plasma treatment and measurement techniques are in different locations, and the sample is transferred in between.

2.1.4.1 *Surface characterization subsequently after plasma treatments without contact to air*

Some in-situ studies measured subsequently after the plasma (category 1) were already reported in section 2.1.3 (Giza et al.^[51] and Pohl et al.^[21]). Here, discrete polarized infrared spectroscopy combined with Kelvin Probe measurements was performed in-situ after the plasma treatment, investigating the surface's chemical composition and semiconducting properties. In a similar study, Grundmeier et al. investigated the low-pressure plasma treatment of iron oxides by combining infrared spectroscopy and quartz crystal microbalance, allowing to correlate changes in the weight to the surface composition.^[53] They related the observed changes after an oxygen plasma treatment to the removed contaminations and formed oxide layer, where they ruled out sputtering effects after a subsequent Ar plasma treatment. The same approach on Zn substrates led to similar results (cleaning, oxide layer growth).^[54] Although the in-situ measurement was performed after the plasma treatment, adsorbed CO₂ was found on the surface as a stable intermediate of the cleaning process. Despite metals, this approach can also be applied to other substrates such as Si, as was shown by Anthony, who investigated the cleaning capability of low-pressure hydrogen plasmas.^[55]

This approach was also chosen in this thesis for studies on ZnMgAl alloys because it can be applied without restrictions for short treatment times. However, this approach cannot detect intermediate products, limiting its insight into the macroscopic mechanism of the plasma treatment.

2.1.4.2 *Real-time monitoring of surfaces in contact with a plasma*

Instead of measuring the sample after the plasma treatment, efforts have been made to measure the plasma-induced changes in real-time during the plasma treatments. This approach enables the detection of intermediate products, thus increasing the insight into the respective mechanism. However, this approach is problematic due to the necessary plasma geometry (the small gap between both electrodes of 1 or 2 mm at atmospheric conditions), disturbances by the plasma (e.g., reactive species, radiation), and long treatment times (treatment time has to exceed the measurement time). The restrictions of the small gap geometry can be softened either by using a plasma jet, where only the plasma effluent is used, or vacuum conditions (compare Paschen curve (2.1.1)).

In this regard, Budde et al. followed the decomposition of poly(propylene) at low pressures using real-time FTIR regarding the synergistic effects of Ar-ions and UV radiation.^[23] They found that UV radiation and Ar-ions combined led to a higher graphitization probability than each effect alone and proposed a decomposition model. Recently, this model was validated in a low-pressure inductively coupled plasma setup by in-situ ellipsometry by Corbella et al.^[24] Because of the low pressures and, in the first case, the limited amount of reactive species (ions + UV-radiation), large distances between the plasma source and the sample, as well as low interferences from the plasma were obtained enabling the real-time study.

2.1 Dielectric barrier plasmas and their applications

Although atmospheric-pressure plasmas are more challenging, quite a number of in-situ setups were recently developed.^{[11]-[15]} Some in-situ plasma cells used in the literature to monitor the plasma/surface interactions in real-time at atmospheric pressure are displayed in **Figure 6**.

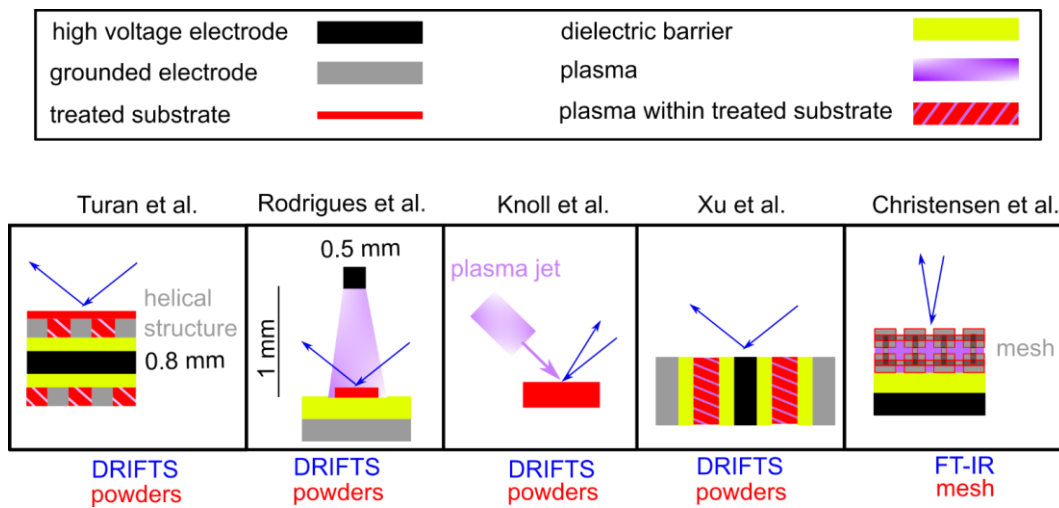


Figure 6: Schematics of in-situ plasma cells used in the literature to monitor surfaces in contact with plasmas in real-time. Above each setup, the respective first author of the publication is displayed, based on the following references: Turan et al.^[14], Rodrigues et al.^[13], Knoll et al.^[12], Xu et al.^[15], and Christensen et al.^[11] Below each setup, the respective measurement method and the substrate type is given.

Although all setups exhibit different electrode geometries (e.g., sample on top of dielectric, grounded electrode as helical, plasma jet), all setups enable the monitoring of the changes by IR (infrared) spectroscopy to monitor the surface reactions. Most setups use DRIFTS (diffuse reflectance infrared Fourier transformed spectroscopy, chapter 2.4.2.1) to adapt to the rough surface structure of the samples. IR has the advantage of being very fast and sensitive to organic components, making it an ideal candidate for in-situ measurements of organic materials. These processes are essential in polymer modifications, plasma catalysis for volatile organic component (VOC) removal, or gas phase conversion processes.^[56]

Turan et al. developed an in-situ setup based on a helical electrode configuration. The sample powder (in their case, KBr crystals for presenting their setup) is filled between the helical windings interacting with the plasma (**Figure 6**).^[14] They found that the discharge behavior heavily depended on the plasma gas composition (especially the humidity), observing changes between filamentary and glow discharges. These changes became critical when naturally adsorbed humidity was desorbed during the plasma treatment, changing the discharge mode during the treatment.

Rodrigues et al. (**Figure 6**) investigated the decomposition of isopropanol and toluene dependent on the catalyst powder (γ -Al₂O₃, TiO₂, and CeO₂).^[13] The organic component was adsorbed on the catalyst prior to the plasma treatment, and the IR spectra were collected during the plasma treatment. They were able to follow the decomposition with a measurement interval below one minute, thereby revealing the secondary decomposition products. Based on the products, they proposed the respective decomposition mechanism: toluene undergoes an opening of the aromatic ring followed by complete oxidation, leading to various carboxylic acids adsorbed on the surface, while isopropanol was decomposed in the plasma to adsorbed acetone, propene, acetic acid and/or formic acid.

Instead of investigating pre-adsorbed organic components, Knoll et al. investigated methane gas/surface interaction on a nickel catalyst using a plasma jet and both gas-phase IR and surface DRIFTS spectroscopy to monitor the surface (**Figure 6**).^[12] Both measurements were conducted in

2.1 Dielectric barrier plasmas and their applications

real-time, leading to a correlation between the catalysis state and the gas phase product, showing that methane was decomposed into CO, CO₂, and H₂O. The mechanism and kinetics depended on the Ni temperature and the plasma power. No CO is formed in the gas phase at low catalyst temperatures and plasma powers (<2.5 W). At higher plasma powers, CO formed, likely being a product of interactions between the plasma and the catalyst. Contrary, the amount of CO₂ in the gas phase depended mainly on the temperature of the catalyst, showing a change in the decomposition mechanism. This was related to carboxylic acids forming on the catalyst surface at lower temperatures, getting unstable at higher temperatures giving rise to the CO₂ amount. Additionally, the surface state of the Ni changed during the plasma treatment forming NiO.

Xu et al. investigated the water-gas shift reaction on different metal-organic frameworks in-situ by DRIFTS (**Figure 6**).^[15] They followed the Cu(I)/Cu(II) transition states related to the CO adsorption and plasma treatment, confirming the catalytic role of Cu sites. Additionally, adsorbed carbonates were found on the surface during the plasma treatment, likely an intermediate product giving rise to the plasma catalysis efficiency.

Instead of investigating powders, Christensen et al. used a metal Ni mesh to investigate the plasma/surface interaction in-situ during the plasma-driven conversion of CO₂ to CO (**Figure 6**) based on results generated by the same plasma-supported reaction in an in-situ transmission cell.^[11] They found no CO conversion in the reflectance cell when applying the same parameters as in the transmission cell where CO conversion was found. This shows that not all processes can be transferred to new setups without difficulties. Additionally, they could show that the plasma initiates the conversion rather than the temperature. Their transmission plasma cell exhibited a CO conversion during plasma treatment, while a comparative experiment using heat (up to 600 °C) showed no such behavior, demonstrating the beneficial effect of the plasma treatment.

Based on these results, an in-situ cell was developed in this thesis, enabling the real-time measurement using DRIFT and Raman of a mesh in indirect contact with the plasma.

2.1.4.2 Real-time monitoring of gas-phase reaction in a plasma

Transmission measurements thereby build the third category of in-situ and real-time measurements possible for plasma treatments to monitor the gas phase only. In addition to the already mentioned results from Knoll^[12] and Christensen^[11], Stewig et al. investigated the excitation of CO and CO₂ in argon and helium discharges at atmospheric pressure by IR spectroscopy.^[57] They found that Ar provided higher vibrational temperatures to the CO and CO₂ molecules, leading to higher conversion efficiencies. This was related to the collision rate and quenching of vibrational states by ground state noble gas species, thus exhibiting a strong dependence on the plasma gas.

To sum up, there are many different in-situ plasma setups available, but most are limited to organic materials and powders. Additionally, as was seen by Christensen et al.^[11] not all results are transferable to each plasma setup, requiring adjustments to the respective applications. Moreover, when the surface is of interest, additional methods monitoring the surface sufficiently are of interest, for instance, Raman spectroscopy (a respective experimental setup is presented in this thesis).

2.2 Zinc alloys and oxides

2.2.1 Surface chemistry of ZnMgAl alloys

Hot-dip galvanized steel is widely used nowadays due to its corrosion protection properties in the automotive and building industries. The protective Zn coating formed at the surface can be modified into a ZnMgAl alloy by adding low amounts of magnesium and aluminum to the zinc bath.^{[19],[58]} Thereby, a complex and heterogeneous structure is formed, displayed in **Figure 7**.

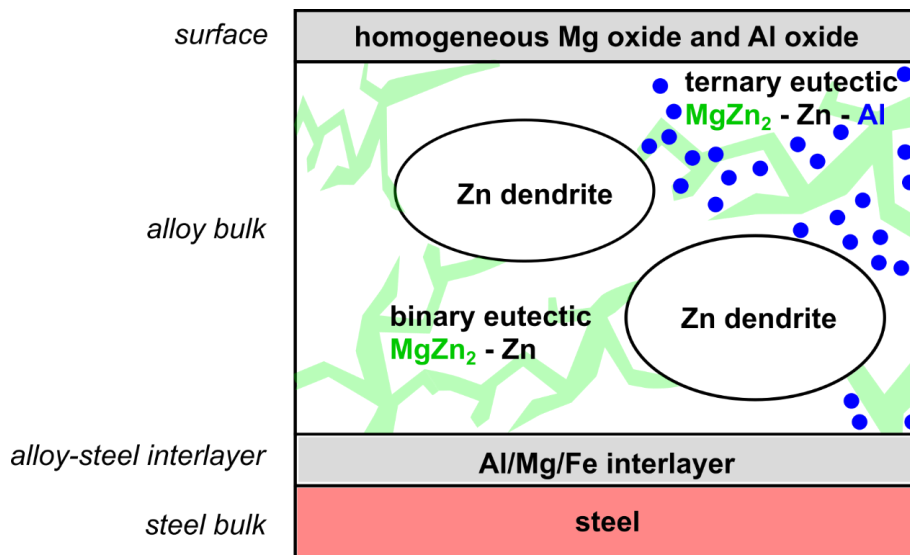


Figure 7: Schematic structure of a ZnMgAl alloy on steel showing the different interfaces and the different phases within the ZnMgAl (based on ^[59]).

ZnMgAl bulk consists of three different phases: Zn dendrites, binary eutectic MgZn₂-Zn, and ternary eutectic MgZn₂ – Zn - Al which are randomly distributed throughout the material.^{[22],[58],[59]} Thereby, their appearance and volume fraction strongly depends on the Al and Mg content in the galvanic bath.^[58] Despite its bulk inhomogeneity and Zn-rich bulk, the top surface layer (4-5 nm) consist of homogeneously distributed Mg oxides and Al oxides.^[59] This distribution is explained by an early oxide formation where the oxide layer is formed while the underlying Zn layer is still liquid and solidifies later. Thus, the oxide layer is dominated by Mg and Al despite their low weight amount in the bath and independent of the alloy bulk structure.^[59]

ZnMgAl alloys are of particular importance when corrosion protection is considered: The ZnMgAl alloy surface showed superior corrosion resistance when compared to pure Zn,^{[16],[17]} ZnAl,^[18] and ZnMg alloys^[19]. The resulting increased corrosion mechanism is still not fully understood due to the complex corrosion conditions, including different corrosive species (Cl⁻, SO₄²⁻, CO₂) and electrolyte applications (spraying, immersion). Furthermore, the complex dependence of the microstructure of the ZnMgAl alloy on the galvanic process complicates the comparison between different ZnMgAl alloys. However, some common mechanisms are proposed in the literature explaining the increased corrosion behavior:^{[16],[17],[60],[61]} During the initial corrosion attack, Zn and Mg are preferential dissolved from the surface. Thereby, Zn²⁺ forms corrosion products on the surface, inhibiting further corrosion attacks. Under certain circumstances, Mg corrosion products were found as well. Furthermore, the Mg²⁺ leads to the complexation of corrosive species, increasing the stability of the Zn corrosion products. When a high amount of Mg has dissolved and either the pH or the electrochemical potential increases, Al dissolved from the surface and either participate in the Zn

2.2 Zinc alloys and oxides

corrosion products, increasing their stability further or creating layer double hydroxides with Zn^{2+} and Mg^{2+} . In either way, a highly protective surface is formed, inhibiting or slowing down the further corrosion. Thus, overall a synergistic effect of the Mg and Al is assumed, which highly depends on the Mg:Al ratio.

In addition to its corrosion properties, other surface properties such as wettability and adhesion are of interest. Although the ZnMgAl coating already exhibits reasonable adhesion forces, for critical applications, several pretreatments are desired. Thereby, acid etching or low-pressure plasma treatments have been shown to increase the adhesion of a ZnMgAl alloy.^{[20]–[22]} Here, the presented thesis will show the influence of DBD plasma treatments on the ZnMgAl alloys.

2.2.2 Zinc oxide nanorods

Zinc oxide (ZnO) is a material with tunable surface activities during its crystal growth, allowing it to form multiple nanostructures, going from 1D materials (e.g., nanorods, wires) to 2D (e.g., nanoplates, nanopellets) and even 3D (e.g., flowers, dandelions) configurations.^{[25],[62]} It thereby combines a high chemical and good mechanical resistance with special features such as semiconducting properties, piezo- and pyroelectric properties, biocompatibility, and more.^[25] In the field of 1D materials, nanorods have been extensively studied because nanorods are easy to obtain and, at the same time, are suitable for revealing dependencies of electrical and thermal transport on dimensions.^[26] Furthermore, ordered nanorods are expected to improve the performance of solar cells, electroluminescent devices, photocatalytic systems, and more.^[27]

ZnO nanorods exhibit a hexagonal wurtzite crystal structure displayed in **Figure 8**.^{[26],[27]}

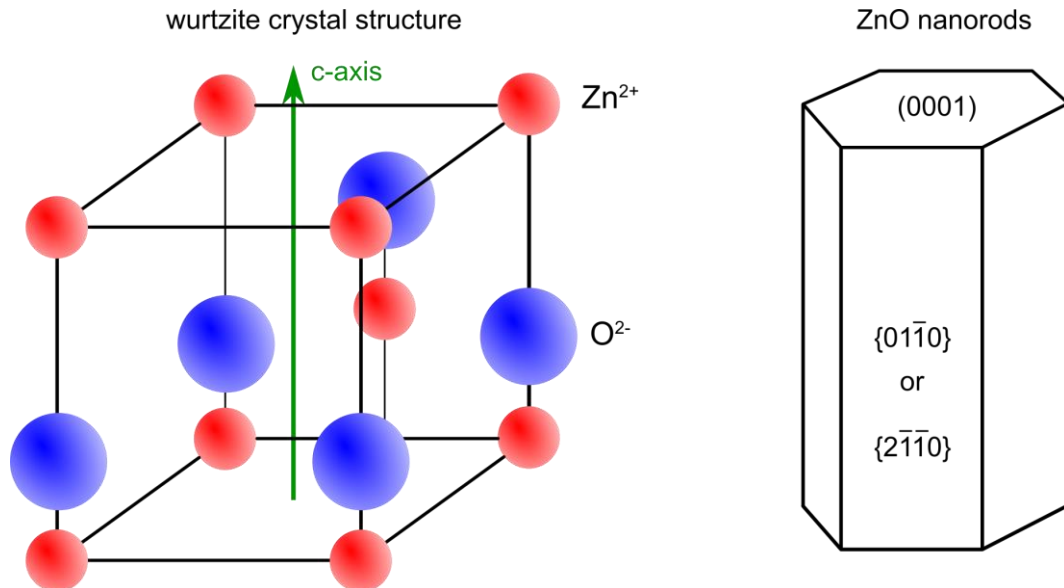


Figure 8: Schematic representation of the wurtzite crystal structure of ZnO and a representation of a ZnO nanorod including facets of the respective surface plane (based on^[62]).

It can be described as alternating planes of tetrahedral coordinated Zn cations along the c-axis.^[27] Based on the crystal structure, polar and nonpolar planes exist within the ZnO nanorods, where the polar surfaces exhibit high surface energies, making it the plane showing the highest growth rate.^[27] Thereby, the polar surfaces can be terminated either with Zn (0001; positive surface charge) or O (0001; negative surface charge).^[27] Contrary, many nonpolar planes can be distinguished, but all show smaller surface energies.^[27] Due to this difference in surface energies, the nanorods are

2.2 Zinc alloys and oxides

growing preferentially in the (0001) direction, showing polar surfaces on top and nonpolar surfaces at the sides (**Figure 8**).^{[26],[27]} However, the exact kinetic ratio is determined by many factors, such as growth techniques, Zn precursors, Zn²⁺ concentration, pH, additives (e.g., ligands), and many more.^{[26],[27]} There are multiple techniques to grow ZnO nanorods, including thermal evaporation, metal-organic chemical vapor deposition, hydrothermal synthesis, sol-gel, electrochemical growth, and more.^{[26],[27]} Each experimental technique depends on different parameter sets discussed in detail in ^[26]. When using electrochemistry (as was done in this thesis), the shape and orientation of the resulting nanostructures depend on the pre-treatment of the substrate, type and concentration of the ZnO precursor, the temperature, the electrical parameter, and organic and inorganic additives.^[27]

The fundamental reaction for the continuous deposition of ZnO is the deposition of zinc hydroxide which dissipates in the presence of heat into ZnO and water (**Equation 4**):^[27]



This equation thereby strongly depends on the pH (ZnO and Zn(OH)₂ are not stable at acidic pH values) and the temperature (increase in temperature shifts the pH stability of ZnO and Zn(OH)₂ to more acidic values).^[27] However, before a continuous deposition of ZnO can be present, nucleation on the substrate has to occur. Nucleation is either achieved when the solution achieves supersaturation, caused by the supply of electrons, or by pre-treating the material to create seeds on the surface (e.g., pre-coating with ZnO).^[27] Additionally, during the electrochemical deposition of ZnO, the electroreduction of oxygen and nitrate can supply additional hydroxide ions, supporting the formation of Zn(OH)₂ on the ZnO nanorods further.

2.3 Self-assembled monolayers on oxide surfaces

When molecules adsorb on a surface and show a spontaneous orientation, a self-assembled monolayer (SAM) is formed.^{[63],[64]} Typical examples are alkanethiols on gold, alkylsilanes on silica, or alkyl phosphonic acids on metal oxides.^{[63],[65]} Thereby, the resulting surface properties can be tuned in a broad range by the chosen molecule allowing a molecular design.^[64] Combined with its easy application, SAMs are an inexpensive and versatile surface coating for applications such as chemical resistance, corrosion resistance, biocompatibility, control of wettability and adhesion, and more.^[64] However, SAMs lack mechanical robustness limiting their application possibilities.^[65]

Thereby, the molecules of a SAM are amphiphilic, having at least one hydrophobic head group (e.g., phosphonic acids, thiols) and a hydrophilic group (e.g., alkane chains, aromatic groups).^{[64],[65]} The head group has to be adjusted to the substrate forming a favorable and specific interaction with the substrate resulting in a stable monolayer even when the solvent is removed.^[64] The hydrophilic group determines the orientation of the SAM, where long alkyl chains have shown to exhibit higher order than short alkyl chains due to their stronger intermolecular interactions.^{[63],[66]} By adding a second functional group on the molecule, which has no favorable interaction with the surface, the surface properties of the SAM can be determined.

During the adsorption of the SAM, multiple steps are involved.^[64] In **Figure 9**, three fundamental steps are shown.

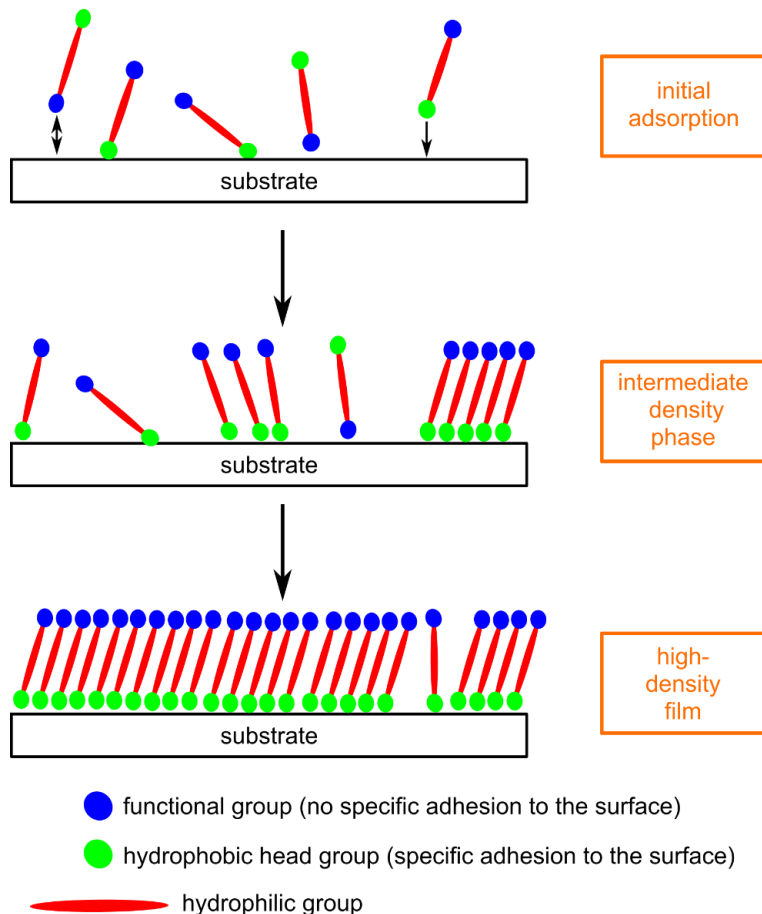


Figure 9: Fundamental steps during the deposition of a SAM on a surface (based on^[64])

2.3 Self-assembled monolayers on oxide surfaces

First, during the initial adsorption, the SAM molecules adsorb randomly on the surface. When the head group comes in contact with the surface, specific bonds are created and preventing its desorption. Contrary, molecules adsorbing with the second functional groups simply desorb over time, leading to a continuous coverage of the surface adsorbed with the head group. The head group's interaction with the substrate must be optimized to obtain stable and highly-ordered SAMs (e.g., thiol on gold) where different interactions (chemical bonding, hydrogen bridges, etc.) can be present. This is discussed further in the following chapter 2.3.1.

After the initial adsorption, an intermediate density phase is present on the surface, consisting of islands of the SAM molecule. Due to the favorable interaction of the hydrophilic groups, adsorption near an already existing island is more favorable than random adsorption. Thus, islands are growing together over time, forming, in the end, a high-density film on the surface. However, these steps are only the fundamental steps and can be accompanied by multiple other processes (e.g., etching) leading to a complex SAM formation.^[64]

2.3.1 Binding mechanisms of phosphonic acids on metal oxides

The binding mechanisms of the respective head group mainly determine the selectivity and stability of the SAM and thus are of great interest. For detailed descriptions of the interactions of different head groups and substrates, the reader is referred to reference [67]. For example, for phosphonic acids ($O=PR-(OH)_2$) two different coordination pathways are present, depending on the Lewis acidity of the metal oxide:[67] If the metal is Lewis acid, the phosphoryl oxygen atom ($O=P$) coordinates to the Lewis acid site. Following, a heterocondensation is induced by the highly electrophilic phosphor with the neighboring surface hydroxide group. Thereby, a robust P-O-M binding is achieved, anchoring the molecule on the surface. On the other hand, if the metal oxide only shows low Lewis acidity, the heterocondensation is induced by a hydrogen bonding between one P-OH group and a surface hydroxide group. In further steps, additional heterocondensations can lead to further bindings. Thus, the hydroxide density of the surface determines the adsorption kinetics and binding mode. Overall, mono-, bi, and tri-dentate binding modes can be present, depending on the metal oxide, the reaction conditions (e.g., temperature, solvent), and the hydrophilic group attached to the phosphonic head group (**Figure 10**).

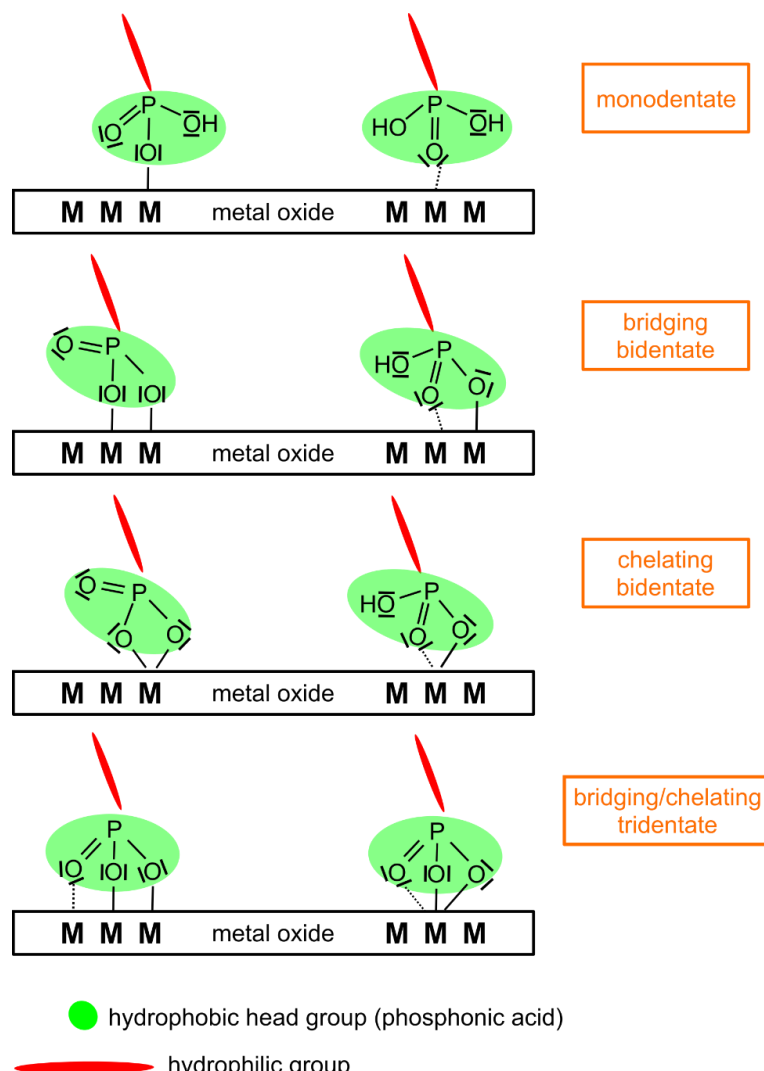


Figure 10: Different binding modes of phosphonic acids on metal oxides (based on [67]).

2.3.1 Ordering and defects in SAMs

Different defects can emerge in the SAM film during the assembly on the surface, reducing the molecules' ordering.^[68] These defects can be caused by different steps in the SAM formation displayed in **Figure 9**. For instance, when two islands of different orientations grow together (step from intermediate density phase to high-density phase), a line defect is formed between the two islands being in the nanometer scale.^[68] The defects between two islands can include dislocations, vacancies, and even missing rows. Thereby, the ordering of the islands is mainly determined by the hydrophilic group, where a longer alkyl chain length led to a higher ordering of the islands and following a higher ordering in the high-density phase.^[64] Similarly, pinholes can be created by single misaligned molecules blocking adjusted adsorption sites. This can be caused, for instance, by the adsorbed and agglomerated SAM molecules from the solvent. Another type of defect emerges in the high-density phase, where single SAM molecules and agglomerations can adsorb on the high-density SAM, forming a weakly adsorbed multilayer.

Thereby, the ordering and defects of a SAM film can be investigated in many ways. For instance, ellipsometry^[69] and contact angle hysteresis^[63] can be used to determine the macroscopical denseness of the films. Cyclic voltammetry can investigate large areas as well but is more sensitive to smaller defects.^[21] Thereby, HR-XPS provides the composition of the surface, confirming the deposition of the SAMs, especially when the SAM introduces a not-foreign atom species.^{[63],[66]} To reveal the binding modes and ordering of aliphatic carbon chains, IR spectroscopy has proven useful. Here, the absence and presence of the head group give rise to the respective binding modes, and the position of the CH₂ vibration depends on the ordering.^{[66],[70]} Going even further, NEXAFS studies can access the molecular order and determine the tilt angle of the SAM film.^[71] To monitor the defects on even lower scales, scanning tunnel microscopy can be used on highly defined surfaces (for instance, flame-stripped gold), detecting defects directly at their position.^[72]

2.4 Fundamentals of applied experimental methods

In this section, the theory of the experimental methods used during this thesis will be presented. It is divided into methods used to characterize the plasma, spectroscopic techniques, electrochemical techniques, the Kelvin probe, microscopic techniques, contact angle measurements, peel-off force, and presenting the improved and developed experimental in-situ setups.

2.4.1 Plasma characterization

Optical emission spectroscopy and electrical characterization of the plasma were performed to characterize the plasma regarding its excited species and dissipated power.

2.4.1.1 Optical emission spectroscopy

Optical emission spectroscopy (OES) is a non-destructive tool to monitor the plasma in-situ by measuring the emission of the plasma in the optical range.^{[73],[74]} In a plasma, species are excited by various processes (compare chapter 2.1). When the excited processes relax, radiation is emitted (**Figure 11**).

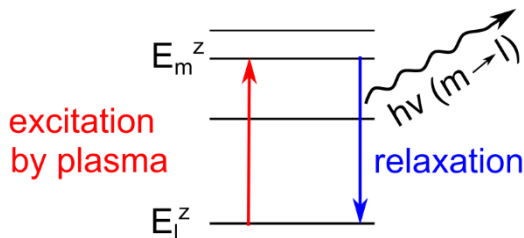


Figure 11: Fundamental quantum process emitting radiation for quantum transitions (based on ^[74]).

The characteristic line radiation is emitted during transitions from an upper quantum state to a lower quantum state following the usual selection rules.^[73] In this case, the observed wavelength can be attributed to specific species being present in the plasma allowing the identification of excited (and therefore potentially reactive) species in the plasma.^[74] Additionally, radiation emitted by recombination of a free electron with the ion (free-bound radiation) and bremsstrahlung (free-free radiation created during acceleration of charged particles) contributes to the emission contribute to the emitted radiation.^[73] However, due to their continuous nature (caused by at least one not-constrained collision partner), they mainly contribute to the background noise. For OES, this radiation is detected in the optical wavelength (~200 nm – 1100 nm) by a respective broadband spectrometer.

2.4.1.2 Electrical characterization

In this thesis, the plasma was created by a sinusoidal voltage, introducing the current into the system. Thereby, the plasma electrode forms a capacitor (metal, dielectric barrier + gas, metal), resulting in a time shift of the current response. The simple equivalent electric circuit, including measurement options for the system's voltage and current, is displayed in **Figure 12**. For a more complex representation and modeling approach of the electrical circuit, the reader is referred to reference [75].

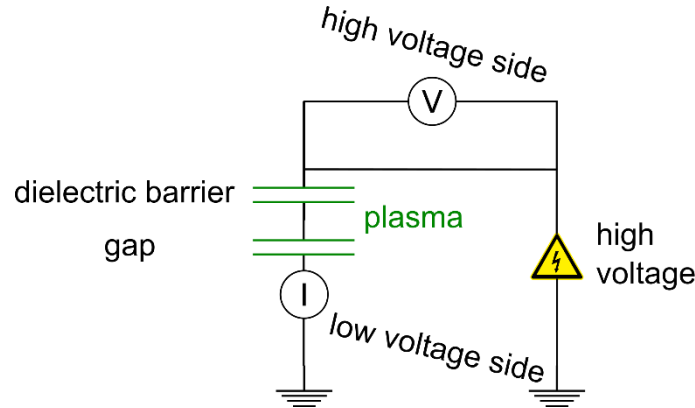


Figure 12: Equivalent electric circuit of a plasma (based on reference [76]).

When the breakdown voltage is exceeded, filaments are formed, allowing the current to penetrate the capacitor leading to current pulses above the breakdown voltage.^[76] Thus, by monitoring the current of the system, the successful ignition of the plasma can be confirmed without a direct line of sight.

The power dissipated in the plasma can be calculated using the charge, which can be obtained by integrating the current over time. The obtained charge-voltage (Q-V) diagram results in a straight line for voltage below the plasma ignition voltage. A parallelogram is obtained for voltages higher than the breakdown voltage due to charges on the dielectric surface during the plasma phase.^[76] The area enclosed is the time-averaged power dissipated in a complete discharge cycle \bar{P} when multiplied with the frequency as is derived in **Equation 5**:^[76]

$$\bar{P} = \frac{1}{T} \int_0^T V(t) \cdot i(t) dt = \frac{1}{T} \oint V(t) dQ(t) \quad (5)$$

where T is the discharge time, t the time, V the Voltage, i the current, and Q the charge. This evaluation thereby does not rely on a “perfectly” shaped Q-V diagram (parallelogram). A distortion of the Q-V diagram can be caused by a partial discharge of the available area, gradual expansion of the plasma during one cycle, a significant residual electron density in the plasma off phase, or a low number of individual streamers.^[76] .

2.4.2 Spectroscopic techniques

The spectroscopic techniques presented here are used to determine the composition and chemical oxidation states of substrates, either by investigating their interactions with photons or analyzing fragments sputtered from the substrate.

2.4.2.1 Infrared spectroscopy in specular and diffuse reflectance

In infrared (IR) spectroscopy, the spectrum is created by detecting light in the infrared wavelength range after interacting with the substrate. Thereby, the infrared beam excites rotation and vibration modes on the substrate leading to losses in the infrared intensity at the detector.^{[77],[78]} Due to the quantum quantization of rotation and vibration in molecules and atoms, the energy of changes in the quantum states (ϵ) are restricted and thereby determine the wavelength (ν) of the light as seen in **Equation 6** taking into account the Planck constant (h):^{[77],[79]}

$$\epsilon = h \cdot \nu \quad (6)$$

Thus, the absorption wavelength is determined by the excited mode, leading to the identification of molecules and functional groups using characteristic adsorption wavelengths and patterns. The selection rules thereby limit the excitation.^{[77]-[79]} These contain that the vibration must have a dipole momentum which changes during the vibration, and only quantum transitions ± 1 are allowed. To obtain a set of distinct wavelengths, a Michelson interferometer combined with an IR source is used to adjust the wavelength by regulating the distance between its mirrors, creating interferences.^[80] By Fourier transformation, the measured interferogram is converted into a single spectrum (I_1). By dividing the substrate by a reference (I_0 ; e.g., gold mirror or sample before the treatment), a transmission or reflectance spectra is obtained. When the logarithmic intensity ratio is multiplied by -1, the respective absorbance spectra (A) is gained (**Equation 7**).

$$A = -\log_{10} \left(\frac{I_1}{I_0} \right) \quad (7)$$

2.4 Fundamentals of applied experimental methods

In IR spectroscopy, different measurement setups are available for satisfying special needs and requirements (e.g., diffuse reflectances in the case of powders). Some measurement methods are schematically presented in **Figure 13**.

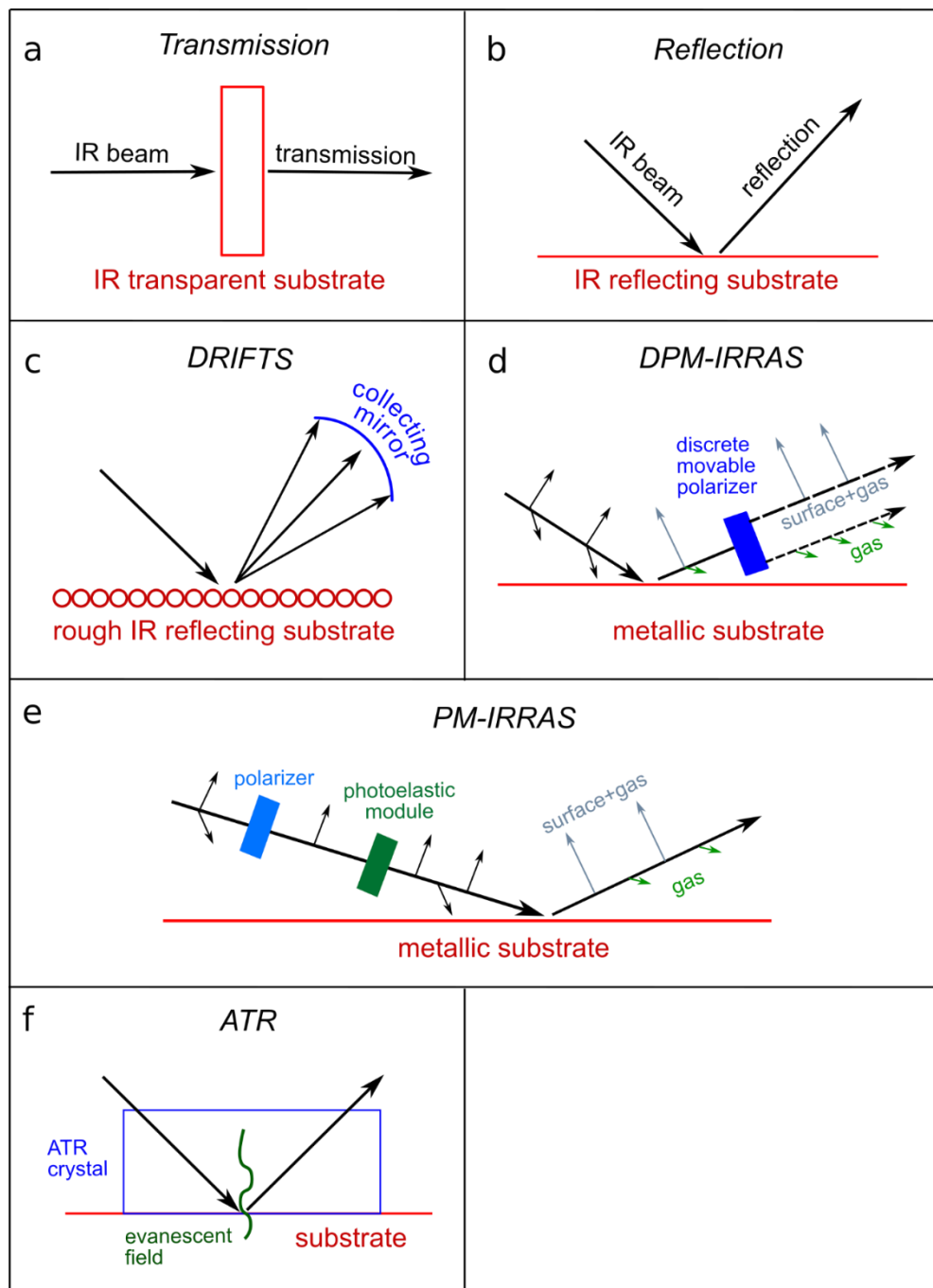


Figure 13: Schematics of different IR techniques: a) Transmission, b) Reflection, c) DRIFTS, d) DPM-IRRAS, e) PM-IRRAS, and f) ATR spectroscopy (based on [81]).

In **Figure 13a**, the sample is measured in transmission where most of the substrate is transparent in the IR region (e.g., silicon wafer), leading to an interaction of the IR beam with the sample of interest inside or on top of the substrate. Complementary, in **Figure 13b**, the reflection mode is presented. Here, the IR beam and substrate interaction are limited to the IR reflective surface (e.g., metals) and thin coatings applied thereon (IRRAS). A special form of reflection infrared measurements is the diffuse reflectance infrared Fourier transformed spectroscopy (DRIFTS, **Figure**

2.4 Fundamentals of applied experimental methods

13c). A large elliptical mirror allows the collection of stray light from the sample, making it suitable for measuring rough surfaces such as powders. In **Figure 13d and e**, the dependence of the interaction between the IR beam and a metallic surface on the direction of the electrical waves of the IR beam (polarization) is used. This dependence is due to the large dielectric function of the metal.^{[81],[82]} When the polarization is parallel to the surface normal (p-polarized), the signal coming from the metal and thereon adsorbed species is enhanced. In contrast, polarized light perpendicular to the surface normal (s-polarized) is canceled.^{[81],[82]} The enhanced response of the parallel configuration is dependent on the angle of incidence being maximal for grazing incidents.^{[81],[82]} Because the orientation of the gas phase molecules is randomly distributed, it interacts with all polarization directions of the beam, contributing to all of them in the same way. Thus, in the end, an enhanced signal is recorded for the p-polarized light (containing contributions of the surface and the gas phase) and a weaker signal for the s-polarized light (containing only information from the gas phase).^{[79],[81],[82]}

Although both discrete polarization modulated IRRAS (DPM-IRRAS) and polarization modulated IRRAS (PM-IRRAS) are based on this effect, the implementation is quite different. For DPM-IRRAS, unpolarized light is directed to the surface in the same way as standard reflection measurements. However, after the interaction with the surface, the light is directed through a discrete movable polarizer filtering the beforehand unpolarized light (**Figure 13d**). Thereby, at least two separate spectra have to be measured per sample, one for the p-polarized light and one for the s-polarized light. Then, the absorbance spectrum has to be obtained individually for each polarization direction by using respective reference spectra (**Equation 8 and 9**) and subtracted to obtain only the signal from the surface (p – s = (gas + surface) – gas = surface)(**Equation 14**).

$$A_p = -\log_{10} \left(\frac{I_{1p}}{I_{0p}} \right) \quad (8)$$

$$A_s = -\log_{10} \left(\frac{I_{1s}}{I_{0s}} \right) \quad (9)$$

$$A = A_p - kA_s \quad (10)$$

Thereby, a factor k is introduced. In theory, k should be equal to one because the gas phase contributes equally to both polarizations. However, as both spectra are not obtained simultaneously but consecutively, the gas phase can change between the measurements. Therefore, k has to be adjusted individually for each measurement.

Contrary, in PM-IRRAS, the IR beam is polarized before hitting the sample. A photoelastic modulator modulates the polarization of the IR beam by mechanically changing the birefringence of a crystal (often ZnSe).^[83] This modulation results in a sinusoidal modulation of the polarization at high frequencies.^{[81],[83]} This modulation adds a high-frequency signal to the usual interferogram. By separating both signals electrically by applying respective frequency filters, the differential reflectance spectrum (ΔR) can be calculated by **Equation 11**:^[81]

$$\Delta R = R \cdot \frac{I_p - I_s}{I_p + I_s} \cdot J_2(\phi_0) \quad (11)$$

where R is the average reflectance spectrum obtained by the interferogram, I_p and I_s are the intensities of the p- and s-polarized light, ϕ_0 a constant that depends linearly on the amplitude of the mechanical modulation of the photoelastic module, and J_2 the second-order Bessel function.

2.4 Fundamentals of applied experimental methods

Although the PM-IRRAS setup requires an additional photoelastic modulator compared to DPM-IRRAS, its benefit is the exclusion of a reference spectrum, making it a robust measurement technique to analyze surfaces and thin surface coatings.

Last, attenuated total reflectance spectroscopy (ATR, **Figure 13f**) is based on an evanescent field created during a total internal reflectance.^{[79],[81]} The IR beam is directed at a certain angle through an infrared-transparent crystal leading to a total reflection at the crystal/substrate interface. Due to the superimposition of the electric field of the incident and reflected IR beam, an evanescent field decays exponentially into the rarer medium, giving information about the surface.^[81] Thereby, the penetration depth of the evanescent field depends on the wavelength of the beam, the angle of incidence, and the refractive indices of both the crystal and the substrate.^[81]

2.4.2.2 Raman spectroscopy

In Raman spectroscopy, similar to infrared spectroscopy, vibration quantum modes are excited. However, instead of exciting the quantum transition into an adjusted quantum state, the vibration is excited into a much higher quantum state. The subsequent relaxation results in the emission of radiation. As the energy difference between the initial and last quantum states is the same for IR and Raman, the absorption wavelength is identical. The transition from the ground state to a higher quantum state is called Stokes Raman spectrum, while the transition from an excited state to the ground state is called anti-Stokes Raman spectrum (**Figure 14**).^{[84],[85]}

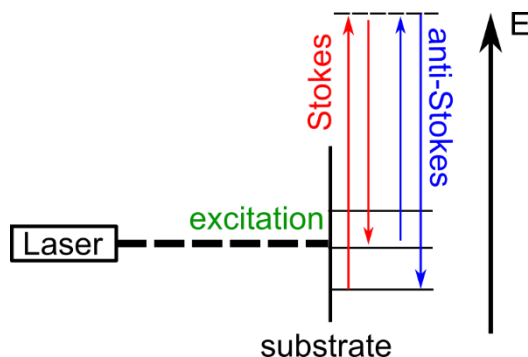


Figure 14: Schematic of the fundamental processes in Raman spectroscopy (based on ^[84]).

Because the number of excited states at standard conditions is very low, the Stokes Raman spectrum has a much higher intensity.^[84] Contrary to IR spectroscopy, a change in the polarization is required for a vibration to be measured using Raman spectroscopy.^{[78],[79]} This makes Raman and IR complementary vibrational spectroscopic methods.^{[79],[85]}

2.4.2.3 X-ray photoelectron spectroscopy

In contrast to the spectroscopic techniques before, X-ray photoelectron spectroscopy (XPS) electrons are excited in the substrate instead of vibration and rotation quantum states. For the excitation, higher energies are required and introduced as soft X-rays.^{[86],[87]} Thereby, the electron is removed from its respective orbital containing a specific kinetic energy (E_{kin}^ϕ). In a simplified model, this can be described by three steps^[88]: First, the excitation photon ($h\nu$) is absorbed, leading to the photoexcitation of the electron. In the second step, the electron is transported to the surface, escaping the surface into a vacuum state in the third step. The second step limits the escape depth of the electrons to only a few nanometers, making XPS a surface-sensitive method.

2.4 Fundamentals of applied experimental methods

For the first process, the kinetic energy is simply determined by the energy of the X-ray radiation, the binding energy of the electron before excitation (E_{BE}^ϕ) and the work function of the spectrometer (ϕ_{sp}):^[87]

$$E_{kin}^\phi = h\nu - E_{BE}^\phi - \phi_{sp} \quad (12)$$

By rearranging **Equation 12**, the binding energy of the emitted photoelectron can be determined by measuring its kinetic energy. However, the second and third steps give rise to inelastic scattering, leading to an inelastic tail contributing to the background.^{[79],[88]} Due to the structures of the atoms, each element has its unique set of binding energies making XPS an excellent tool for identifying elements on a surface. Additionally, the spin-orbit coupling can be resolved.^{[79],[87]}

The ratio of the peak splitting is determined by the total angular momentum (j) consisting of the orbital angular momentum (l) and spin quantum number (s) (**Equation 13**):^{[86],[87]}

$$j = l + s \quad (13)$$

In addition to its orbital structure, the exact binding energy (representing the strength of the interaction between the electron and the atomic nucleus) is determined by its chemical surroundings.^{[79],[86],[87]} Therefore, information on the chemical environment of the element can be deduced from XPS data using reference data. Wagner plots can be used to analyze the composition further when the chemical shift is not resolved in the core-level spectra and Auger peaks are present for the respective element. Auger peaks are present due to a secondary process after removing one electron from the orbital: the hole left by the electron can be refilled by an electron of an orbital having higher energy by emitting a third electron. This electron also appears in the XPS spectrum, containing a different energy set than the prominent peak.^{[86],[87]} Thereby, the Auger peak is more sensitive to the chemical environment. The modified Auger parameter (α') is used to obtain reproducible data and neglect the charging of the surface. It is calculated in **Equation 14** by the binding energy of the prominent peak (E_{BE}^ϕ) and the respective kinetic energy of the Auger transition ($E_{KE}^\phi(A)$), increasing the sensitivity to chemical shifts and the overall comparability with reference data:^{[79],[87]}

$$\alpha' = E_{BE}^\phi + E_{KE}^\phi(A) \quad (14)$$

These chemical shifts can be used for further statements about the surface state, especially when reference data are available.

Furthermore, when an oxide layer is present on top of its respective metal, its thickness can be calculated following Strohmeier (**Equation 15**):^[89]

$$d = \lambda_o \sin(\theta) \ln \left[\frac{N_m}{N_o} \frac{\lambda_m}{\lambda_o} \frac{I_o}{I_m} + 1 \right] \quad (15)$$

where d is the oxide layer thickness, λ_m and λ_o are the inelastic mean free paths of the emitted photoelectrons within the metal and oxide layers, θ is the take-off angle with respect to the surface,

2.4 Fundamentals of applied experimental methods

N_m and N_o are the volume densities of the metal and oxide phases and I_m and I_o are the fitted intensities of the respective metal and oxide photoelectron peaks.

2.4.2.4 X-ray absorption spectroscopy

While in XPS only one specified X-ray wavelength (and therefore energy) is used for excitation, in X-ray absorption spectroscopy (XAS) the absorption of photons is determined as a function of the wavelength (and therefore energy).^{[79],[90]} This tunability is achieved, for instance, by using synchrotron radiation.^{[79],[90]} Here, two different regimes of XAS are differentiated: X-ray absorption near-edge structure (XANES) and extended X-ray absorption fine structure spectroscopy (EXAFS). XANES is sensitive to the oxidation state and coordination geometry, while EXAFS allows the determination of distances, coordination numbers, and species of the neighbors of the absorbing atom.^[79]

The absorption coefficient for photons depends mainly on the atomic number of the probed atom allowing a good separation of different element species in one material by adjusting the incident beam energy.^[79] This allows a thorough investigation of a distinct element even in a heterogeneous matrix by its absorption edge. Unlike XPS, instead of removing an electron into the vacuum, in XANES, the electrons are excited from the atomic core state to different excited bound states, resulting in an absorption edge rather than a peak.^{[79],[90]} For energies higher than the absorption edge, the electrons are excited into the continuum (EXAFS). The shape of features at higher energies than the edge is created by interferences of scattered electrons and can be described by the “multiple scattering theory”.^[79] When applying “ab-initio molecular orbital theory” or “multiple scattering theory”, the spectra can be fitted to determine the coordination number, inter atomic distance, and more.^{[79],[91]} Instead of measuring the electrons not absorbed in transmission mode, fluorescence can be used, too. Fluorescence is created during the decay of the excited states, being characteristic of the atoms as well.^[79]

2.4.2.5 Time-of-flight secondary ion mass spectroscopy

In time-of-flight secondary ion mass spectroscopy (TOF-SIMS), the surface of interest is bombarded with a primary particle (often positive ions), inducing a sputtering process on the surface.^{[92],[93]} Thereby, the energy is transferred by inelastic collisions from the primary particle to the substrate creating secondary particles (**Figure 15**). Dependent on the inelastic collision cascade, a set of secondary particles are created that have different sizes and charges.

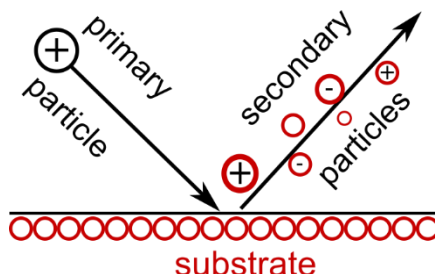


Figure 15: Schematic of the sputtering process induced by one primary particle in TOF-SIMS.

The detection of secondary particles depends on the primary ion current, the sputter yield, the degree of ionization, the relative volume concentration of an element, and the transmission.^[93] Thus, the amount and mass/size distribution strongly depends on the sputtered substrate and its surrounding matrix.^{[94],[95]} For example, an element in its oxide form exhibits a significantly enhanced signal compared to its pure state.^{[96],[97]} Using a time-of-flight detector, differences in the kinetic energies of

2.4 Fundamentals of applied experimental methods

the secondary particles leading to different times they arrive at the detector after the pulsed bombardment.^[92] Due to the acceleration of the secondary particles, the mass to charge (m/z) ratio determines the arrival of the secondary particles. Thus, the detection times cannot be assigned to one specific species in general. However, using complementary methods such as XPS or evaluating the distribution of secondary particles allows assigning the peaks to distinct fragments. By knowing the fragments, conclusions of the initial surface state can be drawn. By focusing the primary ion beam on the substrate, a spatial resolution can be achieved.^{[92],[93]} Combined with repeated sputtering, a spatially resolved sputter profile is achieved.

2.4.3. Electrochemical techniques

The here presented electrochemical techniques are all based on a three-electrode setup presented in **Figure 16**.

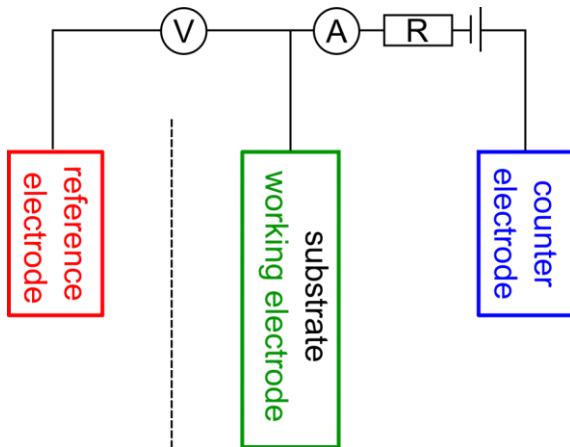


Figure 16: Three-electrode setup consisting of a working electrode, a reference electrode, and a counter electrode connected to a potentiostat to control and monitor the voltage and current of the setup (based on [98]).

For all electrochemical techniques, either the voltage or the current is monitored, often as a response to its counterpart.^[77] The voltage is determined between the substrate and the reference electrode, while the current is measured between the counter electrode and the substrate. In this way, the current does not interfere with the voltage measurement at the reference electrode.^[99] For all techniques presented here, the current is measured as a response to the applied potential. The three-electrode setup contains an electrolyte either to conduct charges or to participate in the reaction.^[99]

In solution and at solid/solution interfaces, an equilibrium of reduced (*Red*) and oxidized (*Ox*) species is formed, supplying electrons for further reactions:^[99]



In this equilibrium, the currents caused by the oxidation and reduction processes are equal, resulting in an overall zero current. Thereby, the potential that forms in the solution (open-circuit potential) is described by the Nernst equation. The Nernst equation (**Equation 17**) correlates the potential (*E*) to the activity coefficients (*a*) of the reactive participants (in equilibrium):^[98]

$$E = E^0 - \frac{RT}{nF} \sum_i \ln(a_i^{\gamma_i}) \quad (17)$$

where E^0 is the standard electrode potential, R the universal gas constant, T the temperature, n the number of electrons transferred during the reaction, and F the Faraday constant.

However, in the electrochemical techniques presented here, the reaction rate is much faster than the time needed to achieve equilibrium. Therefore, the kinetics of the reactions have to be considered. Four different steps can govern the reaction rate:^[100] (i) mass transfer to the electrode, (ii) kinetics of electron transfer, (iii) preceding and ensuing reactions, and (iv) possible surface reactions such as adsorption. The slowest process determines the overall reaction kinetics. If the electron transfer is the rate-determining step (thus not applicable for large overpotentials, where the

2.4 Fundamentals of applied experimental methods

mass transport becomes the rate-determining step), the Butler-Volmer equation (**Equation 18**) describes the resulting current density (i) dependent on the overpotential (η), where the overpotential describes the difference of the applied voltage to the equilibrium potential:^[100]

$$i = i_0 \left(e^{\frac{\beta nF\eta}{RT}} - e^{-\frac{(1-\beta)nF\eta}{RT}} \right) \quad (18)$$

where β is a symmetry factor and i_0 the exchange current density. Contrary, based on Fick's law of diffusion, the mass-transfer limited current density can be described by **Equation 19**:^[100]

$$i = \frac{nFDc}{\delta_N} \quad (19)$$

where D is the diffusion coefficient, c the concentration of the reactive species in bulk, and δ_N the Nernst diffusion layer thickness. It has to be noted that the overpotential is missing in this equation as the electron transfer is not the rate-determining step.

2.4.3.2 Linear sweep voltammetry for corrosion studies

In linear sweep voltammetry (LSV), the potential is changed linearly with time between two chosen potentials.^{[101],[102]} For corrosion studies, a quasi-steady-state is desired, and thus, slow sweep rates are applied. The range of the applied potential is chosen to position the open circuit potential of interest (in the case of corrosion studies called corrosion potential) near the center. The response of the current density to the applied (over-)potential is described by the Butler-Volmer equation (**Equation 18**). When sufficient high (over-)potentials are applied (but not as high as entering the mass transfer limited reaction), the reverse reaction can be neglected, allowing splitting **Equation 18** into two separate parts. One equation completely describing the anodic branch (**Equation 20**) while the other represents the cathodic branch (**Equation 21**):^[102]

$$\text{anodic: } i = i_0 \cdot e^{\frac{\beta nF\eta}{RT}} \quad (20)$$

$$\text{cathodic: } i = i_0 \cdot e^{-\frac{(1-\beta)nF\eta}{RT}} \quad (21)$$

When the logarithmic Butler-Volmer equation (linearization) is rearranged to simplify the evaluation of the exponential relation between the overpotential and current density, the resulting equations are called the Tafel equation (**Equation 22 and 23**):^[98]

$$\text{anodic: } \lg(|i|) = \lg(i_0) + \frac{\beta nF}{2.3 RT} \cdot |\eta| \quad (22)$$

$$\text{cathodic: } \lg(|i|) = \lg(i_0) - \frac{(1-\beta)nF}{2.3 RT} \cdot |\eta| \quad (23)$$

As long as the electron transfer remains the rate-determining step, the plot of the logarithmic current density over the overpotential results in a linear slope. Because the reverse reaction of the Butler-Volmer equation cannot be neglected near the corrosion potential, the exchange current density has to be obtained by extrapolation of the anodic and cathodic current density to the corrosion potential.^{[100],[102]} Therefore, the exchange current can be described as the intersection of the anodic and the cathodic branch, where both processes result in an equal current density and thus an overall current density of zero.^[103]

2.4.3.4 Cyclic voltammetry

Cyclic voltammetry (CV) is a linear sweep voltammetry performed forth and back at least one time, resulting in a sawtooth-shaped applied potential^[99]. Unlike LSV for corrosion studies, typically, fast sweep rates and potential ranges around the reaction of interest are chosen. A typical cyclic voltammogram is shown in **Figure 17**.

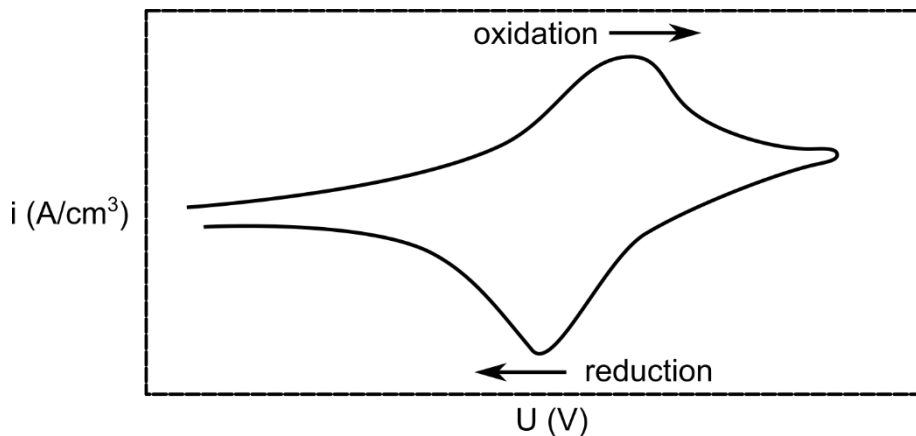


Figure 17: Schematic cyclic voltammogram for one sweep back and forth.^[77]

When the applied potentials are more positive than the standard electrode potential of the reaction of interest, the oxidation is monitored. When the range of the overpotential is large enough, a change in the rate-determining step can be observed (**Figure 17**)^[101]. First, at potentials near the standard electrode potential, the process is governed by the electron transfer and thus the current density increases exponentially as described by the Butler-Volmer equation (**Equation 18**). With steadily increasing potentials, a transition region is entered where both the electron transfer and the mass transfer influence the current density. Therein, at a certain point, the reactive species are depleted at the surface, leading to a decrease in the current density. Finally, at even more positive potentials, the current density is determined by the mass transfer and thus independent of the potential as described by Fick's law (**Equation 19**). The reduction is observed on the linear sweep back to more negative potentials, exhibiting the same behavior as the oxidation if a reversible reaction is present. If the reaction is not reversible, the peaks can differ in shape, size and position.^[101]

2.4 Fundamentals of applied experimental methods

2.4.3.3 Electrical impedance spectroscopy

While LSV and CV induce changes in the sample caused by their applied overpotentials, electrical impedance spectroscopy (EIS) aims to not alter the surface processes (steady-state) by applying only small overpotentials using a sinus function.^[104] Following the voltage, a sinusoidally current is obtained as a response. Correlating the magnitude and phase (ϕ) of both the overpotential and current, the impedance is determined. Thereby, the impedance (Z), as function of the applied angular frequency (ω), can be written either as^[104]

$$Z(j\omega) = Z' - jZ'' \quad (24)$$

where $j = \sqrt{-1}$ and $Z' - Z''$ are frequency-dependent real numbers related to the magnitude and phase^[104], or as

$$Z(j\omega) = |Z|e^{j\phi} \quad (25)$$

Because both equations are valid at the same time, two different plots express and evaluate EIS, either the Nyquist plot (Z' vs $-Z''$) or the Bode plot ($|Z|$ and ϕ vs ω).

Thereby, the impedance as function of the angular frequency is determined at least by the polarization resistance, the charge-transfer resistance, a solution resistance, the mass transfer resistance, and the double-layer capacity.^{[101],[105]} All these influences can be modeled in different electrical equivalent circuits, allowing the EIS data to be fitted, gaining further insight into the reactions and structures on the surface.^{[104],[105]}

2.4.4 Kelvin probe techniques

The Kelvin Probe is a method to measure the Galvani potential (potential necessary to remove a Fermi-level electron from the surface). Thereby, a plate is approached to a metallic surface to a distance d_0 , forming a capacitor. When both the tip and substrate are connected (either directly or via the ground), their Fermi levels become equivalent, forming a potential in the capacitor (V_{cpd}).^{[106],[107]} Now, a vibration (ω) is applied to the tip, leading to a change in d and therefore in the capacity (C) and finally inducing a current (i) as gets obvious from **Equations 26-30**.^{[106],[107]}

$$C(\omega) = \frac{\epsilon A}{d(\omega)} \quad (26)$$

$$Q(\omega) = C(\omega) \cdot V \quad (27)$$

$$V = V_{cpd} - V_b \quad (28)$$

$$i(\omega) = \frac{dQ(\omega)}{dt} \quad (29)$$

$$\rightarrow i(\omega) = -(V_{cpd} - V_b) \frac{\epsilon A L_0 \omega \cos(\omega t)}{d_0 + L_0 \sin(\omega t)^2} \quad (30)$$

where **Equations 26 and 27** describe the basic properties of a plate capacitor. Here, ϵ is the dielectric constant of the capacity, A the area of the plates, d the capacitor gap, Q the charge and V the voltage. Thereby, the voltage is a combination of the spontaneous voltage (V_{cpd}) and a backing voltage (V_b) applied to the system (**Equation 28**). When a sinusoidal vibration is applied, the derivation (**Equation 29**) results in **Equation 30**.^[106] Although in **Equation 30** the influence of the frequency is quite complicated (for instance, including the amplitude of the vibration (L_0)), the most important aspect is the influence of the voltage (which is independent of the frequency): The current depends linear on the voltage, and if the overall voltage is zero, the current becomes zero.

2.4 Fundamentals of applied experimental methods

2.4.4.1 Kelvin probe

In the Kelvin probe (KP), a tip with microscopic dimensions (few mm to hundreds of μm) is brought at a close distance to the surface. This distance depends on the tip diameter but is in the range of μm . Then, other interactions between the surface and the tip can be neglected (e.g., attractive forces). Then, the applied backing voltage can determine the Galvani potential when the measured current is zero. In **Figure 18a**, the schematic electrical circuit of the Kelvin Probe is displayed. In **Figure 18b**, the applied sinusoidal vibration with the resulting current is displayed, while in **Figure 18c**, the linear dependency of the current on the voltage is demonstrated.

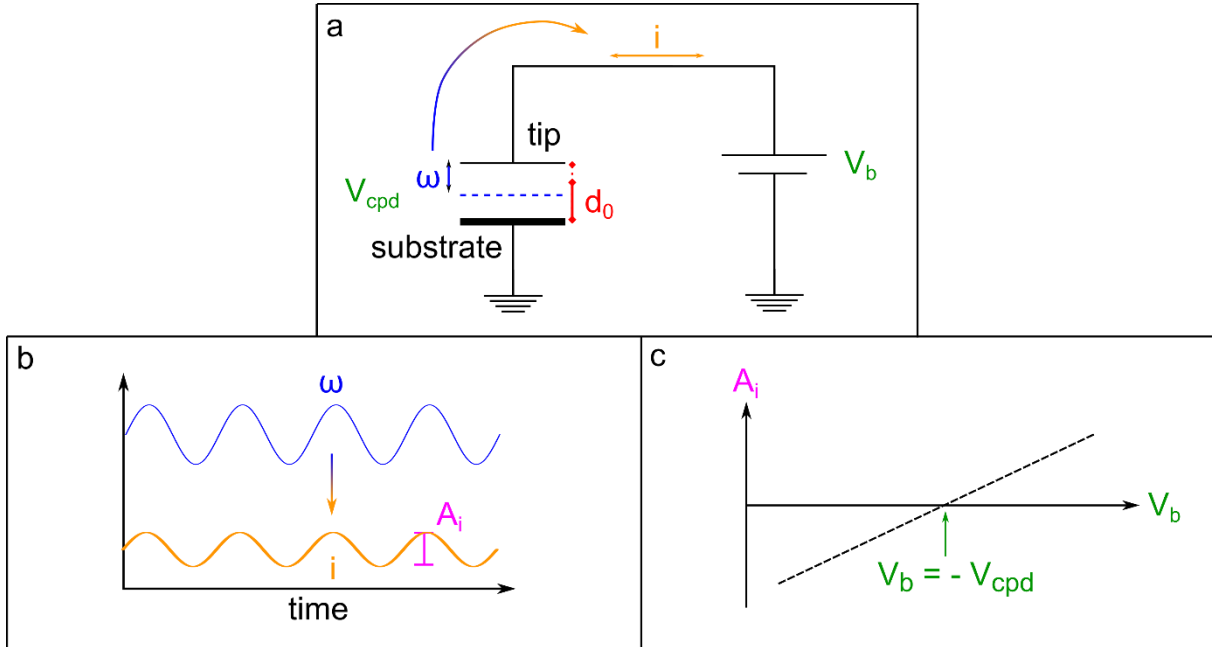


Figure 18: a) Schematic electrical circuit of the Kelvin probe, where a capacitor is brought into vibration (ω), leading to a current response (i). b) A sinusoidal vibration of the capacitance leads to a respective sinusoidal current response with an amplitude (A_i), which c) linear depend on the backing voltage applied to the electrical circuit.

Thereby, the Galvani potential difference ($\Delta\phi_{Ref}^{Me}$) measured by the KP between the substrate and the tip is determined by the sum of all potential differences at all interfaces according to **Equation 31**:^{[108],[109]}

$$\Delta\phi_{Ref}^{Me} = \Delta\phi_{Ox}^{Me} + \Delta\phi_{ox} + \chi_{ox} + \Delta\Psi_{Ref}^{ox} - \chi_{Ref} \quad (31)$$

where $\Delta\phi_{Ox}^{Me}$ is the potential difference between the oxide and the metal. $\Delta\phi_{ox}$ describes the potential drop across the oxide layer and is determined by such factors as the oxide layer's chemical composition, thickness, and conductivity.^{[108],[110],[111]} χ_{ox} is the surface potential of the oxide and is determined by the adsorbed layer on the oxide. Thereby, dipoles formed on the oxide surface play a great role as well as the intrinsic dipole moment of the adsorbed layer.^{[111],[112]} $\Delta\Psi_{Ref}^{ox}$ and χ_{Ref} are the Volta potential and the surface potential of the probe, respectively, and are constant values. Thus, KP measurements have only direct applications on one dimensional processes (e.g. delamination) or have to be accompanied by complimentary methods to distinguish the effects at the interfaces.^[109] When the tip or substrate is movable in x- and y-direction, the process is called Scanning Kelvin Probe (SKP) and is able to monitor the topography as well.

2.4.4.2 Scanning Kelvin Probe Force Microscopy

The Scanning Kelvin Probe Force Microscopy (SKPFM) combines the measurement principle presented for the KP (2.4.4.1) with an atomic force microscopy (AFM) setup, allowing broad applicability and high resolutions.^{[113],[114]} Thereby, the measurement principle is quite similar. Still, instead of a current, the force of the oscillation caused by the electrostatic forces is minimized by applying an external voltage to the tip.^{[113],[114]} Due to the close distance (in the nm range), other forces cannot be neglected, leading to a superimposition of attractive and repulsive forces. Using different feedback loops dependent on the frequency, either the applied backing voltage minimizes the force, or the electrical influence is separated by a lock-in amplifier leading to a similar measurement method than for the KP.^{[113],[114]} Alternatively, the “lift-mode” can be applied: First, the topography is measured. This topography is retraced at a certain distance to the surface in a second run while a constant voltage is applied (**Figure 19**).^[113]

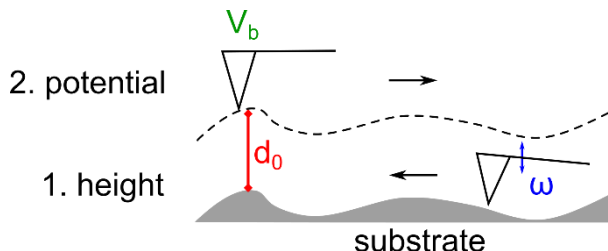


Figure 19: Schematic of a SKPFM measurement conducted in lift mode (based on ^[113]).

By this method, other influences from the surface are minimized. Due to the applied voltage, the tip has to be conductive. Thereby, a sub-nanometer resolution and an energy resolution up to 10 meV can be achieved.^[114]

2.4.5 Electron microscopic techniques

In microscopy, the resolution (R) is limited by Abbe's equation:^[115]

$$R = 0.612 \frac{\lambda}{n} \sin(\alpha) \quad (32)$$

where λ is the wavelength of the imaging radiation, n the refractive index of the medium between lens and condenser, and α the numerical aperture. Therefore, the magnification accessible by optical microscopy is limited to $\sim 1000\times$.^[116] For electrons, the energy of the electrons determines the wavelength (shown by de Broglie), leading to very small wavelengths for high energies (keV) and, in the following, to a high resolution (theoretically for 100 keV at 0.004 nm).^[116] If these electrons penetrate a sample, Transmission Electron Microscopy (TEM) is applied. If electrons are monitored that are directed back from the surface, Scanning Electron Microscopy (SEM) is present.^[116] Thereby, in both techniques, the electron beam created in an electron source is shaped and directed on the sample surface in a series of electromagnetic and electrostatic lenses in a strong vacuum.^{[115],[116]} By applying spherical- and chromatic-aberration corrections, the resolution of the TEM can be significantly increased and even enabling the observation of single atoms (high-resolution TEM (HRTEM)).^[117]

2.4.5.1 Scanning Electron Microscopy

In Scanning Electron Microscopy (SEM), electrons are emitted from the surface after radiation by an electron beam. These electrons can either arise from the backscattering of the electron beam, by the emission of electrons by ionization (secondary electrons), or by the Auger effect (Auger electrons).^{[115],[116]} The emission of electrons is accompanied by characteristic x-rays, which can be used for Energy-Dispersive X-ray Spectroscopy.^[115] The characteristic information depth of each process is displayed in **Figure 20**. The absolute penetration depth depends on the energy of the electron beam, the atomic mass of the elements, and the angle between the electron beam and substrate.^[116]

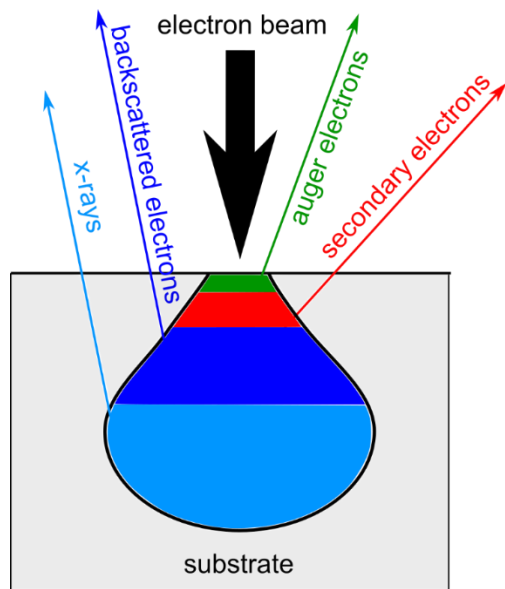


Figure 20: Schematic representation of the information depth from a teardrop-shaped volume of detectable electrons after excitation with an electron beam (based on ^[115]).

Thereby, separate detectors are used to detect the different emitted species. An 2D-image is obtained by scanning the substrate with the electron beam. Thereby, secondary electrons are mainly used to obtain surface near signals with high signal intensity and high spatial resolution, while backscattered electrons enables the differentiation between different materials and structures.^{[115],[116]} In total, the SEM can provide information on the surface topography (calculated 3D surface structures), crystalline structures, chemical compositions, and electrical behavior.^[116]

2.4.5.2 Transmission Electron Microscopy

In comparison to SEM, Transmission Electron Microscopy (TEM) images are based on the transmission of electrons. Thereby, the microscopy setup of the TEM is very similar to the visible-light microscopy and is schematically shown in **Figure 21a**.^[118] The electron beam is directed on the sample by an electro-magnetic condenser lens system. The electron beam penetrates the thin sample, leading to various interactions in the substrate presented in **Figure 21b**.^[117]

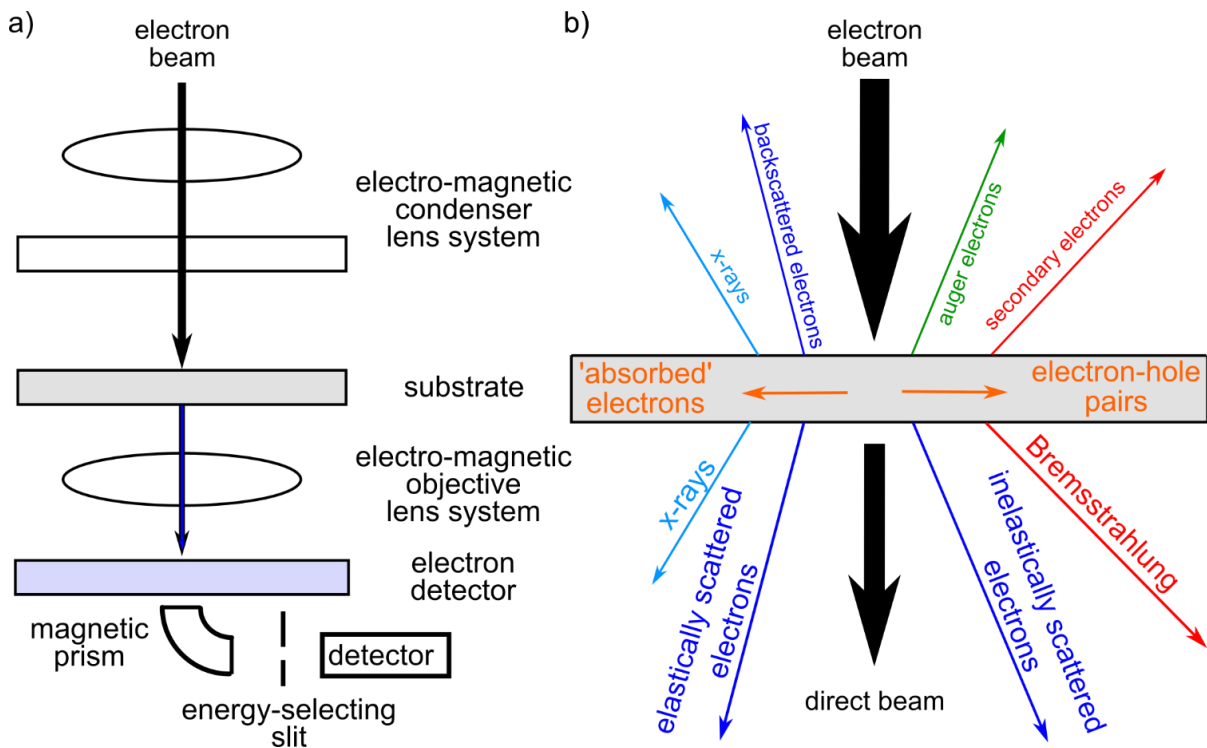


Figure 21: a) Schematic setup of a Transmission Electron Microscope (based on^[118]). b) Signals generated in TEM when a high-energy beam of electrons hits the substrate (based on^[117]).

First, the same signals as in SEM are generated (compare **Figure 20**). As the sample has to be very thin to enable transmission of the electrons, these signals are very small and are not used for further evaluations of the sample in TEM. As the electrons travel through the substrate, a part of the electron beam gets scattered in the substrate, leading to elastically and inelastically scattered electrons leaving the substrate in different angles than the original beam. Still, a part of the original electron passes the substrate unchanged.^[117] By adjusting the method for the created electron beam, two different operating modes can be differentiated:^[119] In TEM, the sample is illuminated by parallel beams, while in scanning TEM (STEM), the electron beam is focused on the sample and scans the substrate pixel by pixel.

2.4 Fundamentals of applied experimental methods

Dependent on the detection method of the electrons, different operating modes can be chosen in TEM. Some operating modes are presented in **Table 1**.

Table 1: Selection of different operating modes in TEM (based on ^[119])

Operating mode	Sample property influencing the electron beam:	Comment
Bright-field TEM (BFTEM)	Atomic potentials/Mass thickness	Detection of the direct electron beam
Bright field scanning TEM (BFSTEM)	Atomic potentials/Mass thickness	Detection of the direct electron beam by scanning the sample pixelwise
Annular dark-field STEM (ADF STEM)	Atomic potentials/Mass thickness	Detection of the scattered electron beam
Energy filtering TEM (EFTEM)	Element, edge selection, specimen thickness, and electronic structure	Adjustment of single energy window allows contrast tuning to particular sample properties

While the direct electron beam is used in bright-field TEM (BFTEM) to image the mass thickness of the substrate, annular dark-field TEM (ADF TEM) uses the scattered electron beams instead. The electron beam can be filtered regarding its energy to enhance the contrast of the images. In modern TEMs, typically, post-column energy filters are used. These filters are attached to the microscope below the projection lens system and consist out of a magnetic prism, which splits up the electron beam regarding its energy, a slit for filtering a specific energy window, and a subsequent lens system projecting either a spectrum (electron energy loss spectroscopy - EELS) or an image (EFTEM) onto a camera.^[120] Thus, in EFTEM, images with defined energy windows can be captured by setting the slit leading to a tunable contrast in the images. Utilizing these images, elementary maps can be obtained by applying the three-window method.^[121] In the three-window method, the intensity of a characteristic signal, e.g., carbon K edge, is determined by calculating the background with two pre-edge images and subtracting the background from the image displaying the intensity at the edge. Thus, the signal arising from the specific interaction with the element can be calculated, and its distribution is mapped within the sample. The intensity of the signal thereby depends on the element, the edge selection, the specimen thickness, and the material's electronic structure.^[118] In addition to the elemental mapping, the local specimen thickness (in values of the mean free path) can be estimated by comparing the complete intensity of the electron beam with the elastically scattered intensity. The local specimen thickness in values of the mean free path can be converted into nanometers by utilizing the model of Iakoubovski.^[122] This model describes a strong dependency of the mean free path to the local density. Furthermore, when investigating the diffraction of the electrons, the crystalline structure as well as grain boundaries, defects in the atomic structure, and well-aligned area with an atomic arrangement of nanostructures can be investigated and correlated to a TEM image by the fast Fourier transform technique.^[117] ^[123] Additionally, EDX can be performed in TEM similarly to SEM based on characteristic emitted x-ray radiation.

2.4.5 Contact angle studies

The contact angle (CA) of a liquid on a solid substrate allows a qualitative analysis of the wetting behavior of the substrate. When a drop of a liquid (l) is put on a solid substrate (s) in a gas environment (g), the drop will obtain a shape dependent on the surface forces of each phase, forming an angle (θ) between the liquid and the substrate determined by the surface tensions of each element. The Young equation describes the balance of the surface tensions (γ)^{[124],[125]}

$$\gamma_{s,a} = \gamma_{s,l} + \gamma_{l,a} \cos(\theta) \quad (33)$$

The Young equation is only applicable to ideal surfaces when the surface is smooth, flat, homogenous, and inert (insoluble, non-reactive, and non-deformable). Nonetheless, the contact angle offers an easy-to-use approach to access the wetting behavior of real substrates. For instance, the wetting behavior is of great relevance when applying paints, where the surface has to exhibit a high wettability for the respective paint. A perfect wetting is achieved for angles towards 0°, while angles above 90° indicate a repelling of the liquid.^{[124],[126]} If the liquid is water, a contact angle below 90° indicates a hydrophilic surface, angles between 90° and 150° a hydrophobic surface, and angles above 150° a superhydrophobic surface.

In the Young equation, the gas, surface, and liquid surface tensions are averaged values over the complete medium. However, different adhesion forces are present on two surfaces in contact, such as Van-der-Waals forces, electrostatic forces, acid-base interactions, and hydrogen bindings.^[124] The sum of these interactions results in the total free energy of the surface.^[127] For liquids, the surface tension is equal to its surface energy, allowing the determination of the substrate's surface energy (which is not equal to the surface tension of the substrate but a combination of surface tension and tensile stress).^[124] So, if the distribution of the interactions is known for different liquids, the distribution of the surface can be accessed. Thereby, the number of liquids necessary is equal to the number of contributions.^[126]

For instance, in the Owens-Wendt-Rabel-Kaelble model, the contributions are summed up in a dispersive part (γ^d) and a polar part (γ^p) leading to **Equation 34**:^[127]

$$1 + \cos(\theta) = 2\sqrt{\gamma_s^d} \left(\frac{\sqrt{\gamma_l^d}}{\gamma_{l,s}} \right) + 2\sqrt{\gamma_s^p} \left(\frac{\sqrt{\gamma_l^p}}{\gamma_{l,s}} \right) \quad (34)$$

These polar and dispersive contributions for different liquids are listed in the literature, allowing, by using two known liquids, to determine the substrate's surface energy and differentiating between its dispersive and polar part.

2.4.6 Peel test studies

There are two essentially different types of engineering tests to investigate the macroscopic adhesion of thin films:^[128] tensile tests (e.g., direct tensile, shock wave) and shear tests (direct shear, direct peel). Thereby, the peel test belongs to the shear tests. In this manner, a coating or adhesive is applied to the surface of interest and afterward removed from the surface by applying a force at a defined angle with respect to the surface (**Figure 22a**). Thereby, the adhesion of the adhesive to the surface has to be weaker than the stability within the adhesive film. Else, the adhesive film breaks first.^[128] The substrate is moved to maintain the angle during the measurement at a constant speed adjusted to the pull-off force.

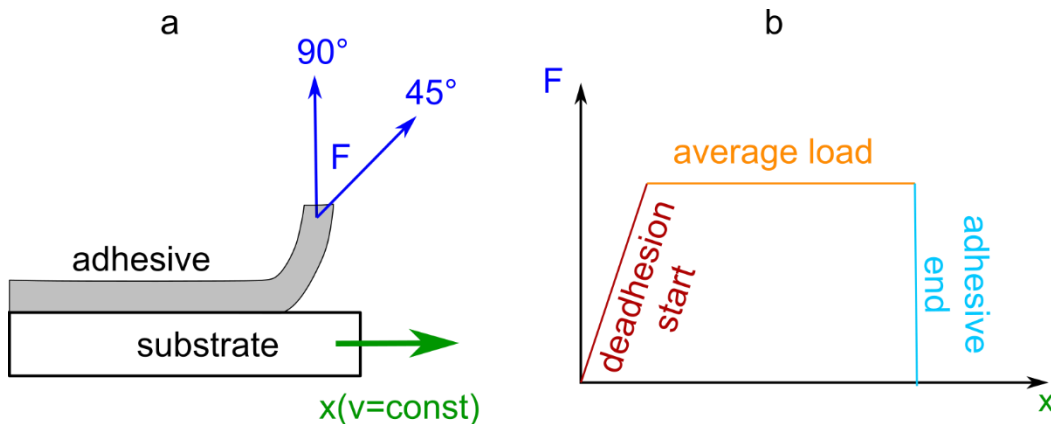


Figure 22: a) Schematic setup of a 45° and 90° peel test where an adhesive is removed from the surface by applying a force F at a defined angle with respect to the surface. b) Schematic force-distance curve recorded during the deadhesion.

Thereby, the overall measured force accumulates the adhesion to the surface and the bending and stretching of the adhesive.^{[128],[129]} This results in a force gradient at the beginning where the adhesive is stretched parallel to the deadhesion of the adhesive from the surface (**Figure 22b**). When the adhesive is fully extended, a constant force is observed (averaged load). Here, the deadhesion of the proceeding delamination and the stretching of the newly freed adhesive film are recorded. At some point, the adhesive film ends, leading to an abrupt and complete loss in the force. A break in the adhesive film results in a similar abrupt decrease. Thus, from the peel test, the interfacial bond strength is not easily accessible, but qualitative comparisons using the same adhesives preparation method (e.g., the chemical composition of adhesive, its application) and measurement parameters (peeling angle, peeling speed) are straightforward.^[128]

2.4 Fundamentals of applied experimental methods

3. Experimental

This section introduces the experimental details for all materials, modifications, and analytic techniques utilized in chapter 4. If necessary, details are specified in the respective experimental section. Some sections are adopted from reference ^[109] with permission of the Royal Society of Chemistry, from reference ^[130] with permission of the Journal of Surface and Interface Analysis, and reference ^[131] with permission of the Journal of Raman Spectroscopy.

3.1 Materials and chemicals

3.1.1 Chemicals and metals

All solvents were analytical reagent grade and were used without further purification. ZnMgAl alloy coated mild steel sheets with a sheet thickness of 1 mm and a coating thickness of about 5 μm were supplied by ThyssenKrupp Steel. The alloy had a composition in the melt of 98 w% Zn, 1 w% Al, and 1 w% Mg. The ZnMgAl alloy was cleaned consecutively in tetrahydrofuran (THF), isopropanol, and ethanol (EtOH), each 10 minutes in an ultrasonic bath. Afterward, the samples were dried in an air stream.

3.1.2 Adsorption of self-assembled monolayers

A 1 mM solution of octadecyl phosphonic acid (ODPA) in EtOH or THF was used in order to form a SAM on the surface. The concentration of 1 mM has been established as a typical concentration for obtaining self-assembling monolayers on various substrates. The samples were immersed in the ODPA-solution for 2 h or 24 h, subsequently rinsed with ethanol, and dried with a stream of dry air.

3.1.3 Electrochemical deposition of zinc oxide nanorods

Zinc oxide nanorods (ZnO-NR) were grown on stainless steel mesh or graphite foils by cathodic electrodeposition in a three-electrode setup as already described elsewhere.^[132] While the mesh was cleaned in an ultrasound bath of (sequentially) tetrahydrofuran, isopropanol, and ethanol, the graphite foils were rubbed with a wet paper towel (cleaning the graphite with EtOH led to a decreased coverage of the ZnO nanorods). Afterward, the ZnO deposition was carried out in an aqueous solution of 10 mM hexamethylenetetramine and 10 mM $\text{Zn}(\text{NO}_3)_2 \cdot 6 \text{ H}_2\text{O}$. The substrate was clamped into the preheated electrolyte solution ($T = 80 \pm 2 \text{ }^\circ\text{C}$), and a constant current density of -1 mA/cm² was applied for 900 s (the current density refers to the substrate size immersed into the solution). Electrochemistry was performed using a Reference 600 potentiostat (Gamry Instruments). A cylindrical tube (stainless steel) was used as a counter electrode to provide a homogenous electric field over the complete mesh. The reference electrode was a KCl-saturated Ag/AgCl electrode connected to the solution using a salt bridge (0.1 M NaNO_3 aqueous solution) to inhibit the heating of the reference electrode. After the deposition was finished, the samples were immediately taken out of the electrolyte, rinsed with ultrapure water (ultra-clear TWF, SG water, Hamburg, Germany), and dried with clean compressed air.

3.2 Plasma treatments and characterization

3.2.1 Plasma treatments

The plasma treatments were carried out either in a homemade plasma chamber (chapter 3.9.1), the backside setup (chapter 3.9.2), or the in-situ cell for EXAFS and XANES (chapter 3.9.3).

The used gases had a purity of 99.999 % and were purchased from Linde. Three different gas mixtures were often compared in this work: Pure argon, argon with 5 % oxygen (Ar/O₂), and argon with 5 % water (Ar/H₂O). The flows were controlled using mass flow controllers (red-y-compact, Vögtlin instruments, Swiss) calibrated to the corresponding gas. To determine the flow ratio, the oxygen content was measured before the experiments with a lambda probe (BA 4510, Bühler, Germany) and the water content with a humidity sensor (UTF75, Sensor-Tec, Germany). The gas flow ratios were adjusted so that the total flow was always 2 l min⁻¹. All measurements were performed at atmospheric pressure.

A G2000 high voltage generator (Redline, Germany) was used to power the discharge. The voltage was monitored using a high voltage probe (PHV 4002-3, PMK, Germany) and an oscilloscope (HMO 1002, Rohde & Schwarz, Germany). The discharge frequency was around 35 kHz, leading to a sinus-like voltage signal.

Before each plasma treatment, reference measurements (varying on the plasma setup used) were recorded for each sample. During the reference measurements, the chamber was flushed with pure argon (2 l/min) for at least 15 minutes. When a gas mixture was used, the second gas was added continuously 5 minutes before the plasma was ignited. When adding the reactive gas, the flow of pure argon was correspondingly reduced so that a total gas flow of 2 l min⁻¹ was maintained. For in-situ and real-time measurements (DRIFTS, Raman, XANES), the measurement series was started a certain amount of time before the plasma ignition. After a certain amount of spectra, the plasma was started during the measurement series. After the treatment time of interest (most time 10 min), the plasma was turned off while the measurement was still running. The measurement ended a certain amount of time after the plasma, allowing to allocate direct effects of the plasma and at the same time access the stability of the plasma modifications.

3.2.2 Optical emission spectroscopy

The plasma discharge was monitored by optical emission spectroscopy (OES) to investigate the plasma composition and reproducibility. The spectrometer was a USB2G (Plasus GmbH, Germany) with a resolution of 0.4 nm. The light passed through a glass window (cut-off at about 290 nm), was collected by a quartz lens, and transmitted to the spectrometer by a glass fiber. The distance to the discharge in the stationary plasma setup was approximately 60 mm, in the backside setup around 10 mm.

3.2.3 Electrical characterization

The voltage at the high voltage side of the plasma and the current on the low voltage side were measured to determine the plasma discharge power. The high voltage (measured by a high voltage probe (PHV 4002-3, PMK, Germany)) and the current (determined by using a homemade resistor with a resistance of 10 Ω) were monitored using an oscilloscope (HMO 1002, Rohde & Schwarz, Germany). The recorded voltage and current were processed using OriginLab 2019b by integrating

3.3 Spectroscopic techniques

the current over time, plotting the voltage against the obtained charge, and determining the enclosed area using the origin app “Hysteresis”.

3.3 Spectroscopic techniques

3.3.1 Infrared spectroscopy

3.3.1.1 In-situ discrete polarization modulated IRRAS studies

The plasma-treated ZnMgAl surfaces were characterized in-situ by means of discrete polarization modulated IRRAS (DPM-IRRAS) in the stationary plasma chamber (chapter 3.9.1).^[133] The spectrometer used was a Bruker Vertex 70 (Bruker Optik GmbH, Germany). The IR beam was focused on the sample with a gold-coated parabolic mirror through a ZnSe-window. The beam reflected from the sample exited the chamber through a second ZnSe window and was guided with gold-coated mirrors through a rotatable KRS-5 polariser. The polariser was moved between two settings, one horizontal (p-polarized) and one perpendicular to the plane of incidence (s-polarized). The beam was then focused on a liquid-nitrogen-cooled mercury-cadmium-telluride detector (MCT). The sample was investigated under an incidence angle of 75°. The final absorbance spectrum (A) was calculated by subtracting the averaged absorbance spectrum of s-polarized infrared light (A_s) from the averaged absorbance spectrum of p-polarized infrared light (A_p) according to the following equations:

$$A_p = -\log_{10} \left(\frac{I_{1p}}{I_{0p}} \right) \quad (35)$$

$$A_s = -\log_{10} \left(\frac{I_{1s}}{I_{0s}} \right) \quad (36)$$

$$A = A_p - A_s \quad (37)$$

where I_{1p} and I_{0p} are the intensities after and before plasma treatment for the p-polarized light, while I_{1s} and I_{0s} are the intensities after and before plasma treatment for the s-polarized light. The I_0 and I_1 measurements were performed at the same spot for each sample. Four spectra of 64 scans each were averaged per polarisation direction, with s- and p-polarized light measurements performed alternatively to minimize the effect of changes in the overall atmosphere. The spectral resolution was 4 cm⁻¹.

3.3.1.2 Polarization modulated IRRAS

Polarization modulated IRRAS (PM-IRRAS) was performed to study the surface chemistry before and after the respective treatments on ZnMgAl.^[81] A ZnSe photo-elastic modulator (PMA50, Bruker Optik GmbH, Germany) modulates an aluminum wire grid at 50 kHz to polarize the light, which is attached to a Vertex 70 spectrometer (Bruker Optik GmbH, Germany). The sample was investigated under an incident angle of 80°. The reflected light was collected using a ZnSe lens onto a liquid-nitrogen-cooled MCT detector. 512 single scans were measured with a resolution of 4 cm⁻¹.

3.3.1.3 In-situ diffuse reflectance IRRAS

Diffuse reflectance IRRAS (DRIFTS) was used to investigate the plasma-induced changes on a mesh in-situ using the backside setup (chapter 3.9.2). The backside setup was introduced into a homemade DRIFTS cell in a Vertex V70 spectrometer (Bruker Optik GmbH, Germany). The beam was collected by a liquid-nitrogen-cooled mercury-cadmium-telluride detector (MCT). To increase

3.3 Spectroscopic techniques

the time resolution of the in-situ measurements, the mesh before the plasma treatment (reference) was measured using 2048 single scans with a resolution of 8 cm^{-1} . Thus, the in-situ measurements could be performed using 64 single scans, resulting in a measurement time of approximately 35 s.

3.3.2 Raman spectroscopy

To characterize the zinc oxide nanostructures, Raman measurements were performed in-situ and ex-situ, combining the backside setup (chapter 3.9.2) with an "InVia Renishaw Raman microscope" (Renishaw, Gloucestershire, UK) using a 532 nm YAG-Laser, a 50x objective, an 1800 l/mm grating, and a CCD detector. The laser power used for all measurements was determined at the end of the objective by a calibrated USB photodiode (DIN EN ISO 9001, THORLABS, Germany) to be 1.24 mW (10 % of the total laser power was set in software). The Raman spectrometer was calibrated using the peak position of 520.0 cm^{-1} ($\pm 0.5\text{ cm}^{-1}$) of a reference silicon wafer. The recording time was set for the ex-situ measurements to 10 s with 15 accumulations and the in-situ measurements to 5 s with 6 accumulations, resulting in an in-situ recording time of 30 s. Thereby, 20 measurements were recorded before, 20 measurements during, and 20 measurements after the plasma, leading to 30 minutes recording time in total. A focus tracker between each accumulation automatically adjusted the focus. To compare the in-situ and ex-situ measurements, the resulting Raman spectra were normalized to the E_2^{high} at 437 cm^{-1} without further corrections.

3.3.3 X-ray photon spectroscopy

Surface chemical characterization was performed by means of X-ray photoelectron spectroscopy (XPS) implemented in an ESCA+ facility (Oxford Instruments, Taunusstein, Germany) at a base pressure $<3.0 \times 10^{-10}$ mbar using monochromatic Al K α radiation (1486.7 eV). No neutralization was used. The calibration was performed using the C 1s signal (at 284.6 eV) of adventitious carbon as an internal reference. The samples were measured using a take-off angle of 30° with respect to the surface. Surveys were recorded at a pass energy of 100 eV and a step size of 0.2 eV, while core level peaks were recorded at a pass energy of 20 eV and a step size of at least 0.1 eV (0.05 eV in some cases).

3.3.4 Time-of-flight secondary ion mass spectroscopy

Time-of-Flight secondary ion mass spectroscopy (TOF-SIMS) measurements were performed using a TOF-SIMS 5-100 from IONTOF at the Interdisciplinary Centre for Analytics on the Nanoscale (ICAN) of the University of Duisburg-Essen. A 30 kV Bi $^{+}$ ion gun operated in spectrometry mode at a nominal lateral resolution of 3-10 μm was used as the primary ion source. Secondary metal ions were recorded in positive polarity. Interlaced sputtering was carried out using a 2 kV Xe $^{+}$ ion gun as a secondary ion source. A Xe $^{+}$ ion gun rather than an O $_{2}^{+}$ ion gun was chosen in order to avoid material oxidation throughout depth profiling.

3.3 Spectroscopic techniques

3.3.5 X-ray absorption near-edge structure spectroscopy

All experimental details are identical for both XANES and EXAFS except for their measurement range and measurement time. The measurements were performed at the P65 beamline at PETRA III at the DESY in Hamburg in cooperation with Steffen Schlücker, Yannik Vukadinovic, and Michal Nowakowski in total fluorescence mode. Because the samples were measured in-situ in a closed plasma reactor (described in detail in chapter 3.9.3), only fluorescence could be measured by placing the plasma reactor at 45° with respect to the incoming beam and the PIPS detector (**Figure 23**). To suppress any signal emitted by the plasma itself, a Z-1 filter (Cu, 3 μm) was placed in front of the PIPS detector.

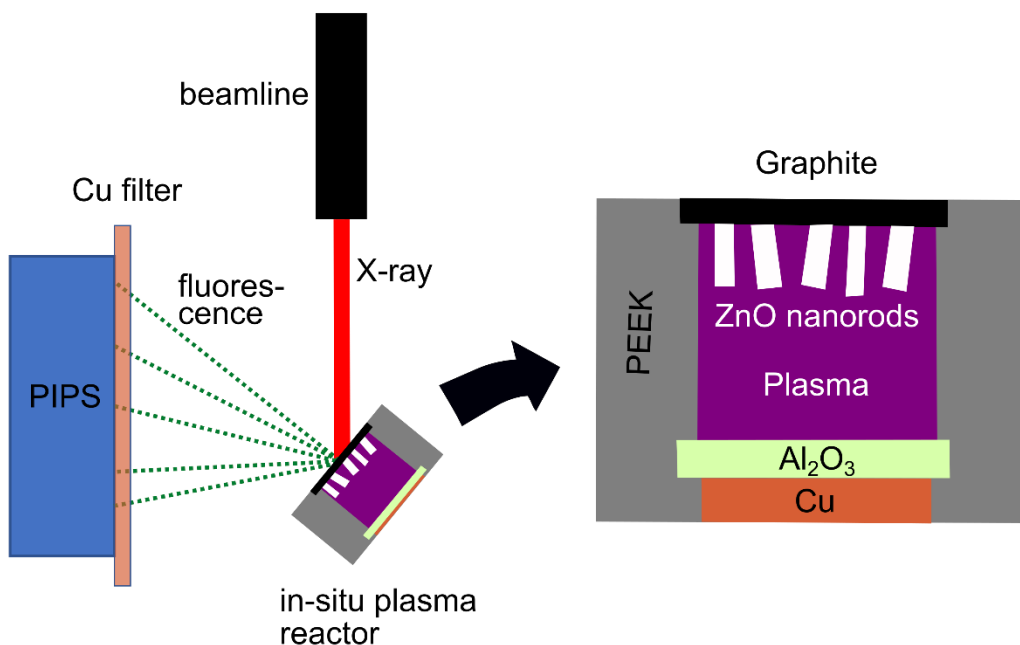


Figure 23: Schematic of the *in-situ* backside setup at beamline P65 at the DESY and the plasma reactor used in the experiments.

The spectra were calibrated to the first inflection point measured on a reference Zn foil (9659 eV). The beam was monochromized by a Si(111) double crystal monochromator (DCM) and focused by Si coated Kirkpatrick-Baez mirrors resulting in a beam spot size of 0.3x2 mm. The *in-situ* XANES measurements were performed in an energy range of -30 - 150 eV from the Zn K edge with 30 s acquisition time per spectrum. However, since the DCM moves back to its starting point between each scan, a total time of around 60 s was needed per spectra. In comparison, the *ex-situ* EXAFS scans were performed in an energy range of -150 - 1000 eV from the Zn K edge, having 180 s acquisition time per spectrum.

3.4 Electrochemical techniques

3.4.3 Electrical impedance spectroscopy

Electrical impedance spectroscopy (EIS) was performed in a borate buffer solution (0.2M H_3BO_3 + 0.05 M Na_2SO_4 + 0.05M Na_2BO_4 , pH 8.4) to investigate the corrosion behaviour of ZnMgAl. A three-electrode setup equipped with a saturated Ag/AgCl reference electrode (DriRef, WPI) and a platinum wire as the counter electrode was used. The sample served as the working electrode. In the following, the potential is quoted against the standard hydrogen electrode (SHE). Polarisation was done using a Reference 3000 potentiostat (Gamry Instruments, USA) in a frequency range from 10000 Hz to 0.1 Hz with 10 points/decade against OCP after 60 s.

3.4.2 Linear sweep voltammetry

Linear sweep voltammetry (LSV) was performed directly after the EIS measurements in the same measurement setup (borate buffer solution (0.2 M H_3BO_3 + 0.05 M Na_2SO_4 + 0.05 M Na_2BO_4 , pH 8.4), (three-electrode setup equipped with a saturated Ag/AgCl reference electrode (DriRef, WPI) and a platinum wire as the counter electrode, sample served as the working electrode) to investigate the corrosion properties. Here as well, the potential is quoted against SHE. Polarisation was done using a Reference 3000 potentiostat (Gamry Instruments, USA) in a potential range from -0.8 V to -1.1 V (vs. SHE). The sweep rate was set to 0.5 mV s⁻¹.

3.4.4 Cyclic voltammetry

Cyclic voltammetry (CV) was performed in a borate buffer solution (0.2 M H_3BO_3 + 0.05 M Na_2SO_4 + 0.05 M Na_2BO_4 , pH 8.4) to investigate the blocking properties and the defect density of the adsorbed ODPA layer on ZnMgAl. A three-electrode setup equipped with a saturated Ag/AgCl reference electrode (DriRef, WPI) and a platinum wire as the counter electrode was used. The sample served as the working electrode. Here as well, the potential is quoted against SHE. Polarisation was done using a Reference 3000 potentiostat (Gamry Instruments, USA) in a potential range from -0.6 V to -1.1 V (vs. SHE). The sweep rate was set to 100 mV s⁻¹, and 5 cycles were recorded.

3.5 Kelvin probe analysis

3.5 Kelvin probe analysis

In the stationary plasma chamber (described in the following chapter 3.9.1), the plasma-induced changes in the chemistry and semi-conduction properties of the sample were measured in-situ using a Kelvin Probe (KP). The tip was made of CrNi and had a diameter of 2 mm. Potentials were measured as a function of bias voltages at three different distances from the surface using a M-230 Linear Actuator (PI, Germany), following the measurement principle used by Tahara et al.^[106] At each distance, the potential was recorded at 40 different bias voltages. Since the measured peak-to-peak distance depends linearly on the bias and is quadratically proportional to the tip-sample distance (d)^[107], the three measurements produced three linear plots with different slopes dependent on the tip-sample distance (**Figure 24**).

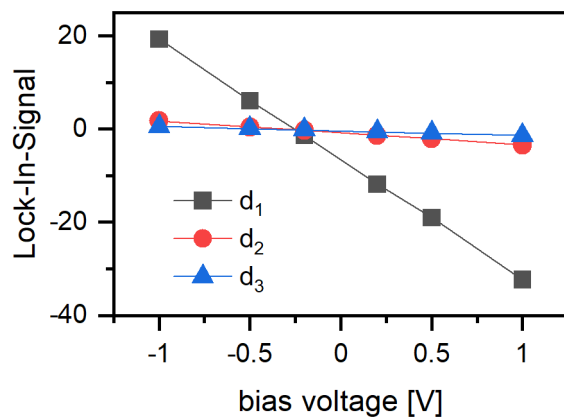


Figure 24: KP measurement showing the dependence of the Lock-In signal (potential) and the bias voltage on the sample-tip distance d .

The potential at the intersection of the linear plots gives the surface potential. With this method, the error in determining the surface potential was between $\pm 10 - 80$ mV.

3.5.2 Scanning Kelvin Probe Force Microscopy

Scanning Kelvin Probe Force Microscopy (SKPFM) was performed using a MF3PD-AFM setup (Asylum Research, England). A platinum-coated tip with a force constant of 40 N/m and a resonance frequency of 350 kHz was used. The scan rate was 0.1 Hz, and the resulting images were 70 x 70 μm^2 in size. For each measurement, the P and I gain were adjusted to the sample being different than zero.

3.6 Electron microscopic techniques

3.6.1 Scanning Electron Microscopy and Energy-Dispersive X-ray Analysis

Field emission Scanning Electron Microscopy (FE-SEM) and Energy-Dispersive X-ray (EDX) analysis were performed by means of a “NEON 40” FE-SEM (Carl Zeiss SMT AG, Oberkochen, Germany) by Nadine Buitkamp (Paderborn University, CMP).

3.6.2 Transmission electron microscopy

To analyze the crystallographic structure and surface roughness of untreated and Ar/H₂O plasma-treated zinc oxide nanorods (ZnO-NR), transmission electron microscopy (TEM) was performed by Julius Bürger (work group of Prof. Dr. Lindner, University of Paderborn). Therefore, high-resolution transmission electron microscopy (HRTEM) and energy-filtered transmission electron microscopy (EFTEM) were conducted using a JEM-ARM200F (JEOL Ltd., Tokyo, Japan) equipped with a GIF-Quantum ER energy filter (GATAN Inc., Pleasanton, US) at an acceleration voltage of 200 kV. The local specimen thickness was mapped by utilizing the t/λ-method within EFTEM^[134], and a mean free path of 119.9 nm in ZnO was calculated by the model of Iakoubovskii for the mean free path to thickness conversion [Iakoubovskii].^[122] TEM specimens were prepared by placing the ZnO-NR containing steel mesh on a lacey-grid (S166-3, Plano GmbH, Germany) and subsequently scraping off ZnO-NRs with a razor blade. To prevent radiolysis of ZnO-NR under a 200 kV electron beam, only ZnO-NRs with adequate connection to the underlying carbon films were analyzed.

3.7 Contact angle measurements and determination of surface energy

Static water contact angle measurements were carried out with an OCA 15 plus (Dataphysics, Germany), using 5 μL ultrapure water and, when determining the surface energy, 5 μL dimethylsulfoxide (DMSO) droplets. The contact angles were determined by the Laurentian method and the surface energy (γ) with its dispersive (γ_l^d) and polar (γ_l^p) part was determined by the Owens, Wendt, Rabel, and Kaelble (OWRK) method using the library of the OCA 15 providing the data of the liquids. The respective values of water and DMSO are shown in **Table 2**.

Table 2: Surface energy for water and DMSO including the respective dispersive and polar parts, taken from the OCA 15 library.

	water	DMSO
γ	72.1	44
γ_l^d	19.9	36
γ_l^p	52.2	8

3.8 90°- peel test studies in humid atmosphere

Peel forces were determined under humid conditions by 90°-peel test measurement for two different adhesives: **(a)** acrylate adhesive tape (Scotch® Magic Tape (3M, Germany)); **(b)** 2-component epoxy amine adhesive consisting of Epoxy resin D.E.R 331 (DOW Chemicals, USA) and Amine poly(propylene glycol)bis(2-aminopropylether) (Sigma Aldrich, Germany).

For the two-component epoxy amine adhesive, 3.73 g of D.E.R. 331 and 2.26 g poly(propylene glycol)bis(2-aminopropylether) were mixed and then degassed in a vacuum ($<1 \times 10^{-2}$ mbar) for 2 h. To create a well-defined film thickness of 150 μm , spacers consisting of three layers of commercial adhesive tape were applied to the samples. The adhesive was applied in a dry atmosphere ($<6\%$ r.h.) at room temperature. The coated samples were put on PTFE blocks wrapped with aluminum foil, fixed with clamps, and hardened at 120 °C for 75 minutes in an oven (“sandwich configuration”). After the hardening, the PTFE block with the aluminum foil and the spacers were removed from the samples.

Scotch® Magic Tape was applied in a dry atmosphere ($<6\%$ r.h.) by moving a 2 kg rubber roller 8 times over the Scotch® Magic Tape on the sample.

All samples were exposed after applying the adhesive for 18 h at 40°C to humid air ($>95\%$ r.h.). Subsequently, the 90° peel test was performed in a MV-220 Motorized Test Stand (Imada, Japan) at about 85 % r.h at RT. The pull-off force was measured with a gauge of type Model ZP-5 (Imada, Japan). The peel-off speed was set to 1 mm s^{-1} .

3.9 Advanced experimental setups for in-situ characterization

The main point of this thesis were in-situ studies of atmospheric-pressure dielectric barrier discharge plasmas for surface treatments of zinc oxide and its alloys. Therefore, three different in-situ setups were improved and developed. To increase the comparability between these setups, the main construction was kept similar: The DBD plasma electrode consisted of a copper disk due to its high conductivity. The metal disk was capped with an Al_2O_3 ceramic disk (Frialit-Degussit, FRIATEC), which acted as a highly inert dielectric barrier. Thereby, the diameter of the ceramic disk was chosen to be greater than the copper disk to ensure protection against electrical breakthroughs. The whole electrode was enclosed in a polyether ether ketone (PEEK) container due to its high chemical resistance and dielectric strength. The sample acted as the grounded counter electrode. The high voltage connection was achieved using a high voltage coaxial jack by Redline Technologies, where a copper adapter (homemade) was screwed to the jack. If necessary, copper cables were soldered to the adapter and the copper electrode. Before the measurements, it was essential to ensure that a closed circuit was present by connecting the sample to the ground. First, the stationary plasma chamber will be presented, which was modified to enable atmospheric-pressure plasma treatments and increase the quality of the DPM-IRRAS and KP studies.

3.9.1 Stationary plasma chamber for in-situ DPM-IRRAS and KP studies

The plasma treatments of ZnMgAl were carried out in an improved homemade plasma chamber (shown in **Figure 25**). The chamber was used before for vacuum plasma treatments of similar materials (additional information can be found in reference ^[51]).

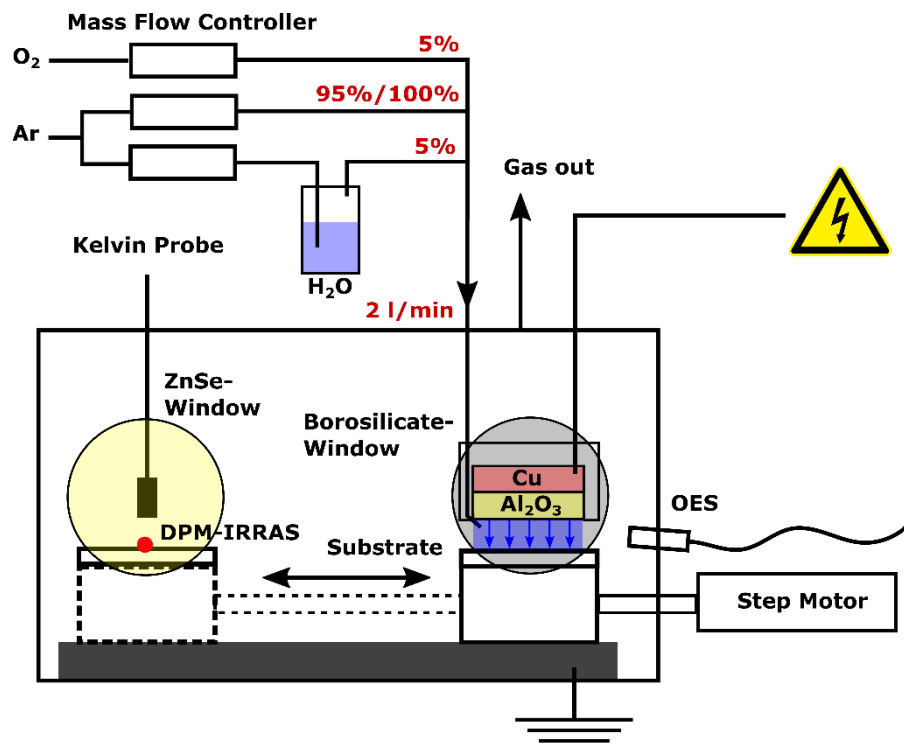


Figure 25: Stationary plasma chamber used to treat the ZnMgAl surface. investigating the plasma-induced changes in-situ with discrete polarized modulated FT-IRRAS and Kelvin Probe.^[109]

One advantage of this setup is that the sample can be moved between the plasma treatment position and an analytic position without opening the chamber to air (therefore called in-situ).

3.9 Advanced experimental setups for in-situ characterization

Further parameters of the setup are presented in **Table 3**.

Table 3: Characteristics of the stationary plasma chamber.

Diameter copper (cm)	18
Diameter Al_2O_3 (cm)	20
Thickness Al_2O_3 (cm)	2
Discharge gap (mm)	1
In-situ analytic methods	DPM-IRRAS, KP, OES
Ground electrode used in this work	ZnMgAl

At the analytic position, discrete polarisation modulated IRRAS (DPM-IRRAS) and Kelvin probe (KP) measurements were performed before and after the plasma treatments. For the DPM-IRRAS measurements, the chamber is attached to a Vertex 70 spectrometer, using its right beam exit and directing the beam to the sample using Al and Au coated mirrors. The beam is then directed through a movable KRS polarizer and collected in a MCT detector. The path of the IR beam in the complete setup is presented in **Figure 26**.

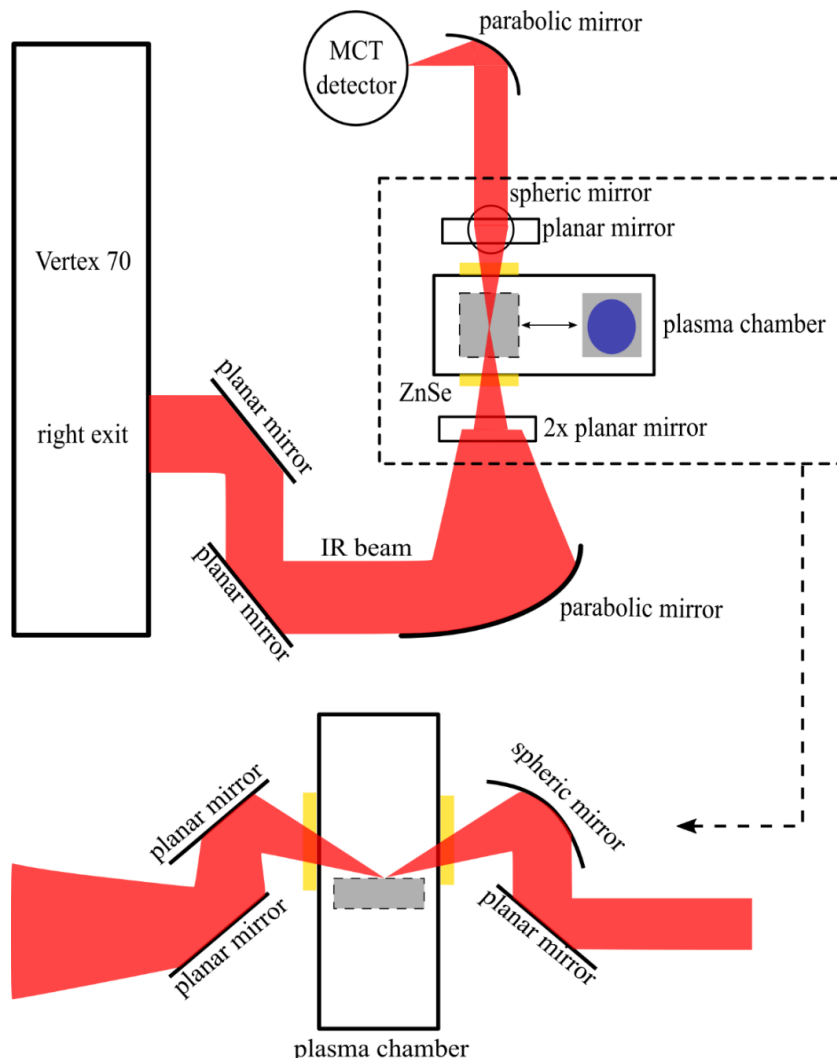


Figure 26: Schematic path of the IR beam in the in-situ plasma chamber attached to the Vertex 70. The image above shows the complete IR path from the Vertex 70 to the detector, while the image below focuses on the entrance and exit of the IR beam in the plasma chamber.

3.9 Advanced experimental setups for in-situ characterization

Two planar mirrors direct the IR beam leaving the Vertex 70 spectrometer on a parabolic mirror. The parabolic mirror focuses the beam on the sample, having the distance between the mirror and the plasma chamber adjusted to the focal point of the parabolic mirror (so that the focus point is as near to the sample as possible). Thereby, the IR beam passes two planar mirrors, present to determine the angle of incidence. When leaving the plasma chamber, the IR beam is collected by a spheric mirror where the focus point is on the sample as well, leading to an exiting parallel beam. This beam is then directed to the MCT detector, where a parabolic mirror focuses the IR beam directly into the detector. Due to the confinements by the mirrors' focus points, the mirrors' position and angles are quite restrained.

The electrode was introduced into the chamber on a one-way movable KF 40 flange. To ensure a defined electrode-sample distance of 1 mm, spacers were included in the latest electrode design. The gas was directed through the flange connection by a tube and then introduced in the plasma gap from the side.

The sample holder was designed to offer flexibility in sample height and size while ensuring a tight fit and a not-tilted surface for the DPM-IRRAS measurements. When the sample was not fixed correctly, the measurement of both the s- and p- polarized light was distorted precisely the same way. However, when a correction factor different of 1 had to be used for the atmospheric correction, this distortion ruins the measurements. The fixation of the sample was checked by moving the sample between two fast DPM-IRRAS reference measurements. If the sample was not fixed properly, a distorted baseline was visible without any treatment. The tilt of the sample is essential as well: If the path was not perfectly aligned, a much lower or no signal was obtained. Additionally, the angle of the sample is vital due to the dependence of the p- and s-polarized light on the angle of incident. The angle was adjusted to be around 75°, making even small tilts in the sample noticeable. Additionally, the sample holder ensured the grounding of the sample through the complete chamber (all parts of the chamber consisting of conductive material).

3.9.2 Backside plasma setup for DRIFTS and Raman studies

A backside plasma reactor was designed to investigate the effect of the plasma in real-time. Thereby, the necessary plasma geometry (the small gap between both electrodes of 1 or 2 mm) and disturbances by the plasma (e.g., UV radiation) hamper the monitoring of surfaces in direct contact with the plasma (as present in the stationary plasma chamber). Thus, the in-situ plasma setup was designed to enable the monitoring in real-time (compared to the stationary plasma chamber) of a surface on the backside of the plasma. Thereby, the separation of different plasma-related effects can lead to a deeper understanding of the overall plasma process and afterward be transferred to different and more complex plasma setups, as was recently shown for different setups. [23],[24]

The idea of the backside setup is the following: The plasma is ignited between the conventional high voltage side and a porous substrate as the ground electrode (Figure 27).

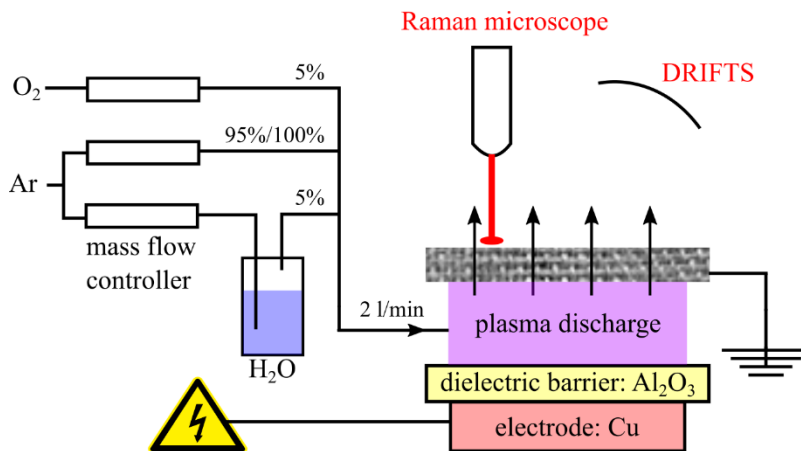


Figure 27: Schematic of the backside setup developed to monitor the indirect plasma-modified surface in real-time using Raman spectroscopy and DRIFTS.

The porous electrode allows the plasma effluent to penetrate, and on its way, modify the porous surface. Of course, this approach is only a simplification for surfaces in direct contact with the plasma due to the neglected radiation effects, including synergistic effects. However, the interaction of long-living reactive species with the surface can play a significant role in the overall plasma-induced surface modification. Furthermore, the results gained by the backside setup are of great interest for plasma jets and similar devices, which are based on the plasma effluent rather than the direct contact with the plasma. On top of that, a considerable advantage of this setup is its excellent combination potential with different characterization methods. Raman spectroscopy and DRIFTS measurements were used in this work, but the setup is not limited to them.

Because the setup was meant to be implemented into the DRIFTS cell, the backside setup geometry adapted the DRIFTS cell dimensions (penetration depth, sample position, and DRIFTS cell opening), making the backside setup quite long.

3.9 Advanced experimental setups for in-situ characterization

Further parameters are summarized in **Table 4**.

Table 4: Characteristics of the backside plasma setup.

Diameter copper (cm)	18
Diameter Al ₂ O ₃ (cm)	20
Thickness Al ₂ O ₃ (cm)	3
Discharge gap (mm)	1
In-situ analytic methods	DRIFTS, Raman, OES, electrical characterization, temperature
Ground electrode used in this work	ZnO/ODPA coated steel mesh

The defined discharge gap was achieved by an interlayer of Al of 1 mm thickness and a hole with a diameter relatively larger than the diameter of the DB to prevent discharges to the side walls. The sample then was fixed by pressing a second Al plate on top, including a way for the (plasma-activated) gas to escape and provide an opening for the DRIFTS beam. The gas was introduced from two sides meeting below the sample, directing the gas through the porous electrode. However, the gas was not hindered from diffusing into the measurement chamber, which was only lately achieved by an ATR coated Ge-window (3-12 µm). Screws then fixed the plates to ensure a tight fit of the sample and a good gas imperviousness. However, to ensure complete gas imperviousness, the contact areas of the parts have to be sealed by adhesive tape.

3.9.3 Backside plasma setup for in-situ EXAFS and XANES studies

To analyze the plasma-induced changes in the atomic structure of zinc oxide further, a plasma reactor was developed for in-situ studies using EXAFS and XANES. Like before, a backside approach was chosen. However, since the X-ray beams at high energies are insensitive to carbon, a graphite sample was coated with the ZnO nanorods instead of a mesh. In addition, because the space at the beamtime was limited, a new cell was developed to fit inside the given space. The schematics and a photograph of the cell are shown in **Figure 28**.



Figure 28: Schematic and photograph of the second backside plasma setup for in-situ investigation using XANES and EXAFS of the plasma-induced changes on ZnO nanorods.

Because of the limited space, adjustments had to be made, leading to a smaller plasma diameter and larger plasma gap shown in **Table 5**.

Table 5: Characteristics for the second backside plasma setup.

Diameter copper (cm)	6
Diameter Al ₂ O ₃ (cm)	8
Thickness Al ₂ O ₃ (cm)	2
Discharge gap (mm)	2
In-situ analytic methods	electrical characterization, XANES, EXAFS
Ground electrode used in this work	ZnO coated graphite

The smaller dimensions led to a direct connection between the high voltage electrode and the high voltage coaxial jack by directly screwing the jack in the copper electrode. An additional enclosure was made of Teflon to cover this connection. To ensure the safety of the connected enclosures, the alignment was given by the chosen geometry and was fixed by two screws. A cap was included to fix the sample, which was connected to the enclosure by screws. It was made from aluminum to connect the sample via a banana connector to close the circuit. Alternatively, a PEEK cap was used, where the electrical connection was made via an adhesive copper band. A 5M thread was placed on the side of the Teflon cap to mount the sample on an optical table using ThorLabs equipment. To ignite the plasma, the coaxial jack must be put in the Teflon enclosure and be screwed in the copper. Afterward, fix the Teflon enclosure to the PEEK enclosure and connect the high voltage cable. If your sample is only on the plasma side conductive, you must apply a copper band to the sample compartment. If your sample is overall conductive, the connection can be accomplished by the aluminum cap. Insert the sample and fix the cap with all screws and close the circuit.

3.9 Advanced experimental setups for in-situ characterization

4. Results and Discussion

The scientific questions phrased in the introduction were addressed by investigating the influence of a DBD plasma treatment on a technical ZnMgAl alloy and ZnO nanorods using different plasma gases (Ar, Ar + 5 % O₂ (Ar/O₂) and Ar + 5 % H₂O (Ar/H₂O)). Based on the used in-situ setup, the results and discussion chapter is divided into two major parts. First, in chapter 4.1 till chapter 4.4, the plasma treatment of ZnMgAl was investigated regarding the plasma-induced changes on this heterogeneous alloy and its influence on the adhesive and corrosion properties (**Figure 1**):

1. Identification of plasma-induced changes after 60 s atmospheric-pressure plasma treatment on ZnMgAl and its influence on the wettability and adhesion properties. (*chapter 4.1*)
2. Influence of the 60 s atmospheric-pressure plasma treatment of ZnMgAl on the adsorption of octadecyl phosphonic acid. (*chapter 4.2*)
3. Half-side Ar plasma modification of ZnMgAl is used as a tool to identify plasma-induced changes and its application to an EtOH post-treatment. (*chapter 4.3*)
4. Time dependence of an Ar/H₂O plasma treatment on ZnMgAl and its influence on the wettability and corrosion properties. (*chapter 4.4*)

From chapter 4.5 till chapter 4.7, novel backside setups will be presented for in-situ studies (**Figure 2**). Two different systems were investigated: First, zinc oxide nanorods were investigated in-situ regarding their defect structure monitored in-situ by Raman spectroscopy and XANES/EXAFS. Second, the zinc oxide nanorods were coated by a self-assembled monolayer to determine the interaction between a specific functional group and the plasma by DRIFTS measurements:

5. In-situ backside investigation of zinc oxide nanorods in an atmospheric-pressure dielectric barrier discharge plasma by Raman spectroscopy. (*chapter 4.5*)
6. In-situ backside investigation of zinc oxide nanorods in an atmospheric-pressure dielectric barrier discharge plasma by EXAFS/XANES. (*chapter 4.6*)
7. In-situ backside investigation of octadecyl phosphonic acid in an atmospheric-pressure dielectric barrier discharge plasma by DRIFTS. (*chapter 4.7*)

4.1 Surface modification of ZnMgAl-coated steel by dielectric barrier discharge plasma

The plasma treatment of polished ZnMgAl alloys using vacuum plasma (as discussed in chapter 2.1.3) performed by Pohl et al. showed increased corrosion protection of the pure surface and improved barrier properties of ODPA adsorbed on the plasma-treated surface.^[21] This behavior was explained by cleaning effects and the formation of an Mg-Al-rich surface layer.^[21] This chapter aims to mimic the former results achieved in vacuum plasma in an atmospheric-pressure plasma process suitable for integration into in-line production lines.



Figure 29: Chapter 4.1 aimed to identify the plasma-induced changes in the ZnMgAl surface and correlate these to different adhesive properties of the surface.

The main focus of this chapter was the characterization of the plasma-induced surface changes depending on the plasma gas composition and their correlation to adhesive properties of the surface (Figure 29). Thereby, the addition of different oxidizing species to Ar as (carrier gas) was investigated, giving three different gas mixtures (Ar, Ar + 5 % O₂ and Ar + 5 % H₂O). Because the plasma gas composition determines the properties of the plasma discharge (reactive species, emission, power, etc.), it is a versatile parameter to determine the resulting surface properties.

The following chapter is adapted from reference ^[109] with permission of the Royal Society of Chemistry and can be found at <https://pubs.rsc.org/en/content/articlelanding/2019/RA/C9RA07378G#!divAbstract>.

4.1 Surface modification of ZnMgAl-coated steel by dielectric barrier discharge plasma

4.1.1 Experimental approach

4.1.1.1 Plasma treatment

Before the measurement, the ignition voltage for the given electrode-sample distance was determined for each gas mixture. Then, the voltage was set 165 V higher than the ignition voltage for each gas mixture, leading to an applied voltage of 2.9 kV for pure Ar, 3.6 kV for Ar/O₂, and 2.6 kV for Ar/H₂O. The duration of the plasma treatment in all cases was 60 s.

4.1.1.2 Time-of-flight secondary ion mass spectroscopy

Two different field size settings were used at otherwise identical instrument parameters. Firstly, an analysis field size of 100 x 100 μm^2 at a sputter field size of 300 x 300 μm^2 was used for fast small area depth profiling through the complete ZnMgAl-coatings. The end of the coating was identified by the appearance and stabilization to a constant value of the Fe⁺ signal (corresponding to the steel substrate). Secondly, an analysis field size of 400 x 400 μm^2 at a sputter field size of 1000 x 1000 μm^2 was used for large area depth profiling of the surface-near region of the ZnMgAl-films at lower sputtering rates.

4.1.1.3 90°- peel test under humid conditions

Peel forces were determined under humid conditions by 90°-peel test measurement for two different adhesives: **(a)** acrylate adhesive tape (Scotch Magic Tape (3M, Germany)); **(b)** 2-component epoxy amine adhesive consisting of Epoxy resin D.E.R 331 (DOW Chemicals, USA) and Amine poly(propylene glycol)bis(2-aminopropylether) (Sigma Aldrich, Germany). The application of the adhesive was performed immediately after the plasma treatment.

All other modifications and measurements were carried out as described in chapter 3.

4.1.2 Results and Discussion

The samples were characterized previously to the plasma treatments with scanning electron microscopy (SEM), energy-dispersive X-ray spectroscopy (EDX), and X-ray photoelectron spectroscopy (XPS).

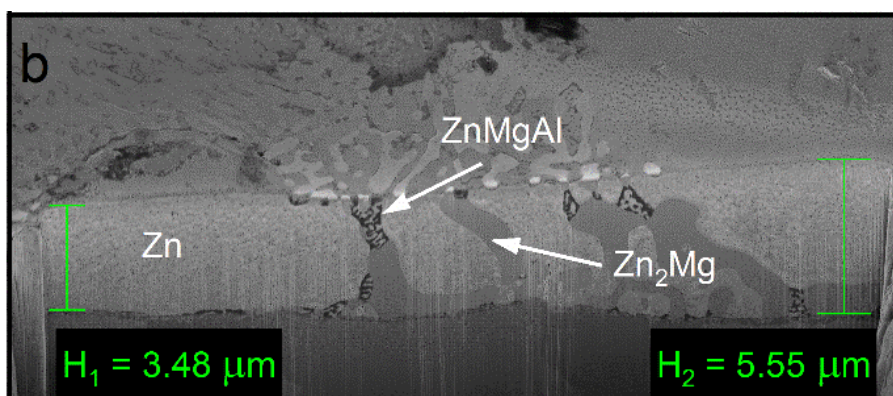


Figure 30: SEM cross-section of the ZnMgAl alloy on steel. The respective phases and coating thicknesses are marked.^[109]

Cross-sectional SEM images show ZnMgAl-coating thickness between 3.5 and 5 μm (Figure 30). The internal structure of ZnMgAl coatings is not homogeneous, but it consists of separated regions of Zn, binary Zn₂Mg, and ternary ZnMgAl,^{[135],[136]} forming dendrites that can reach sizes between 5-10 μm in diameter.^{[18],[135],[136]}

4.1 Surface modification of ZnMgAl-coated steel by dielectric barrier discharge plasma

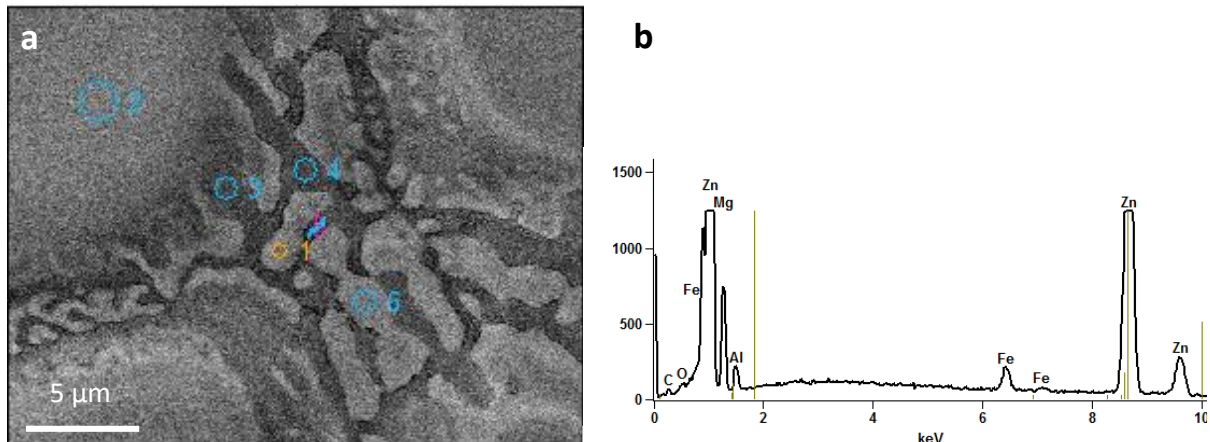


Figure 31: a) SEM image of an untreated ZnMgAl sample. The circles (spots 1 to 6) mark the positions where EDX measurements were performed. b) Typical EDX measurement showing Zn, Mg, Al, Fe, O, and C on the surface.^[109]

Figure 31a shows a SEM image of an untreated ZnMgAl showing the positions where EDX-measurements were performed. A characteristic EDX-spectrum is shown in **Figure 31b**. Iron, zinc, magnesium, aluminum, oxygen, and carbon were present on the surface. The results of the quantifications are presented in **Table 6**.

Table 6: Quantification of the EDX spectra measured at the spots shown in Figure 31.^[109]

Atom-%	C-K	O-K	Mg-K	Al-K	Fe-K	Zn-K
Spot 1	5.72	3.11	3.58	2.55	2.57	82.47
Spot 2	5.49	2.53	1.23	2.57	2.93	85.26
Spot 3	3.66	1.99	18.07	2.90	2.26	71.11
Spot 4	3.90	2.01	21.62	5.51	1.83	65.12
Spot 5	3.15	2.94	1.98	19.38	2.15	70.40
Spot 6	4.62	3.60	2.80	3.31	2.51	83.16

The composition as determined by EDX is similar to that of other ZnMgAl alloys in literature,^{[16],[136]} showing a high amount of Zn of about 80-90 at% in the bulk material and a spatial-dependent amount of Mg and Al between zero and 20 at% at different Mg/Al ratios.

XPS measurements show that the uppermost oxide layer is dominated by aluminum oxide. Mg is also present at the surface but in lower concentrations, while Zn is almost not existent. The enrichment of Al and Mg at the surface is a known aspect of ZnMgAl alloys; however, the enrichment is typically seen to be dominated by Mg, while in our work, Al dominates at the surface-near region.^{[59],[136]}

4.1 Surface modification of ZnMgAl-coated steel by dielectric barrier discharge plasma

4.1.2.1 OES studies of the bulk plasma composition

Optical emission spectroscopy (OES) was performed on the Ar and Ar/H₂O plasmas in order to identify active species in the plasma and to monitor the stability and reproducibility of the plasma discharge (the Ar/O₂ plasma could not be measured due to low emission in the visible range). Characteristic OES spectra of the Ar and Ar/H₂O discharges are shown in **Figure 32**.

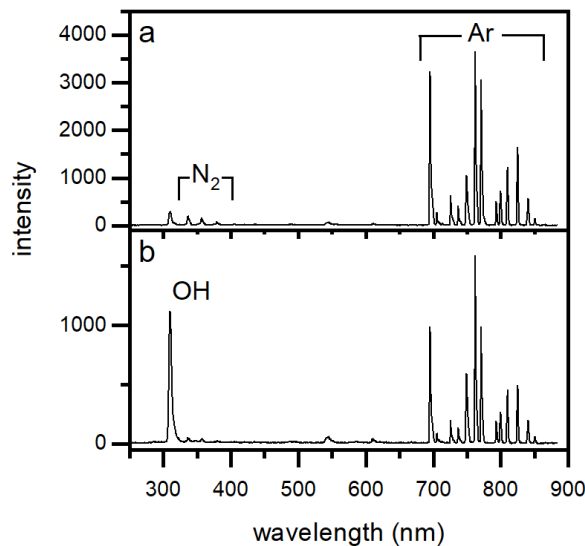


Figure 32: OES spectra of a) pure Ar plasma and b) Ar/H₂O plasma.^[109]

In general, argon plasmas exhibit emission peaks in the region between 690 and 850 nm.^[137] These lines were consistently observed in all experiments, with relative intensity ratios characteristic of each gas mixture. Additional emission lines were observed around 300 and 400 nm. These are assigned to hydroxyl OH radicals (310 nm) and N₂-species (340, 360, 380 nm).^[137] We attribute the appearance of these peaks to residual air in the system. Comparing the OES of pure Ar and Ar/H₂O plasmas, the peak at 310 nm increased by a factor of 4 for the Ar/H₂O mixture, while the Ar lines decreased by a similar factor. The decrease of intensity for the Ar lines in the presence of oxygen and water is attributed to the quenching of the emission of Ar by water and oxygen molecules.

4.1 Surface modification of ZnMgAl-coated steel by dielectric barrier discharge plasma

4.1.2.2 *In-situ* IRRAS studies of surface chemical changes during plasma processing

Due to its high surface sensitivity^[81], PM-IRRAS (ex-situ) was performed to investigate the IR-active species on the untreated samples. DPM-IRRAS (in-situ) was used to identify the plasma-induced changes in the surface by performing a direct comparison between the samples before and after the plasma exposure. In this case, the reference was a measurement done on the same spot of each sample immediately before the plasma treatment.

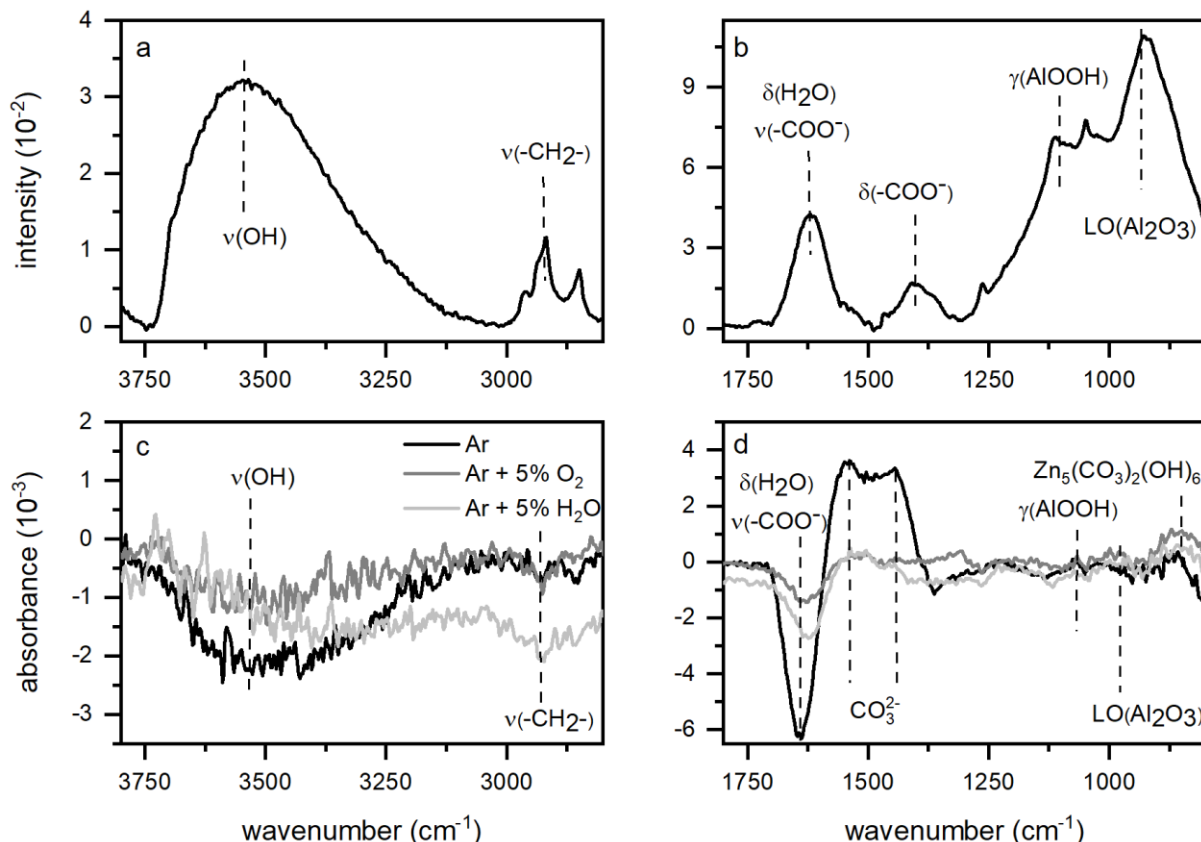


Figure 33: a, b) PM-IRRAS of untreated ZnMgAl in two spectra regions. c, d) *In-situ* DPM-IRRAS of ZnMgAl after 60 s plasma treatment with different gas mixtures with respect to the initial state.^[109]

The PM-IRRAS spectra of the untreated, cleaned surfaces (**Figure 33a and b**) showed signals corresponding to adsorbed water (3200 cm^{-1}), aliphatic carbon groups ($2850\text{-}2960\text{ cm}^{-1}$), carboxylates (1620 cm^{-1}), Al-oxide (920 cm^{-1}), and Al-hydroxide (1090 cm^{-1}).

4.1 Surface modification of ZnMgAl-coated steel by dielectric barrier discharge plasma

The peak assignments are summarised in **Table 7**.

Table 7: Summary of the peaks observed by means of PM-IRRAS and DPM-IRRAS before and after the plasma treatments.^[109]

Solvent cleaned	peak position (cm ⁻¹)			peak assignment
	Ar plasma	Ar/O ₂ Plasma	Ar/H ₂ O plasma	
	860	855	860	Zn ₅ (CO ₃) ₂ (OH) ₆ ^{[16],[138]}
920	--	940	940	LO(Al ₂ O ₃) ^[39]
1020	1020	1020	1020	δ(OCH) ^[139]
1090	1070	1070	1070	γ(AlOOH) ^[140] [39]
	1150-1320	1150-1320	1150-1320	absorbed CO ₃ ²⁻
				δ(CO ₂ ⁻) from both carbonates and carboxylates ^{[140]-[142]}
1440	1440	1450	1450	δ(CH ₂) ^[140]
1465				
1540	1535	1520	1510	absorbed CO ₃ ²⁻
				ν(CO ₂ ⁻) from carboxylates ^{[142],[143]} , δ(H ₂ O) ^[39]
1620	1630	1630	1625	
2850-2960	2850-2960	2850-2960	2850-2960	ν _s (CH ₂), ν _s (CH ₃), ν _a (CH ₂), ν _a (CH ₃) ^[142]
3500-3200	3500-3200	3500-3200	3500-3200	ν(OH) ^[39]

The presence of carbon groups is associated with the existence of so-called adventitious carbon on the sample surface. Since carboxylates are known to contain aliphatic carbon chains and adsorb on oxide-covered metal surfaces, we infer from the IRRAS measurements that the metal surface is covered by carboxylates containing aliphatic carbon chains.^{[66],[111],[112],[144]} (This assumption is also confirmed by XPS.)

All plasma treatments (**Figure 33c and d**) induced the removal of adsorbed aliphatic species, water, and carboxylates, identified by the appearance of negative bands at the corresponding band positions. Further, all plasma treatments build up carbonates. Two different (positive) bands were associated with carbonates: a peak at 860 cm⁻¹, corresponding to zinc carbonate in form of hydrozincite,^{[16],[138]}, and a broadband centered around 1500 cm⁻¹, due to un-specified carbonates. Carbonate bands appear typically in a broad spectral region between 1540-1150 cm⁻¹ and the precise band position depends both on the type of substrate^{[16],[138],[141],[142]} and on the binding mechanism^{[139],[141],[142]}. The two observed carbonate signals appear after all plasma treatments, independently of the gas mixture used. Additionally, the increase of the carbonate peaks was correlated to the decrease in the carboxylate band, suggesting that the plasma treatments converted carboxylates to carbonates. Therefore, contact with the plasma seemed to induce a carbonate conversion that affected both the adsorbed “adventitious” carbonates and the metal carbonates incorporated into the oxide layer. Additional modifications to the oxide layer, dependent on the specific gas mixture, can be seen in the changes in the AlOOH and Al₂O₃ bands.

By evaluating at least eight samples per plasma gas mixture, specific changes in surface chemistry after the plasma treatment could be associated unequivocally with the respective plasma-gas mixture. The gas mixture mainly determined the conversion of carboxylates and carbonates in terms of the peak intensities as well as the peak positions associated with carbonates in the region between 1540 and 1150 cm⁻¹. The highest carbonate build-up was observed for the case of pure Ar plasma.

4.1 Surface modification of ZnMgAl-coated steel by dielectric barrier discharge plasma

To sum up, DPM-IRRAS measurements showed a decrease in aliphatic carbon and absorbed water and the conversion of carboxylates to carbonates as a result of the plasma treatment. The conversion degree was seen to depend on the plasma gas mixture.

4.1.2.3 Ex-situ XPS analysis of surface chemical changes after plasma processing

XPS was used for additional ex-situ chemical characterization of the sample surface before and after the plasma treatments. The average stoichiometry (several samples were characterized for each treatment) is presented in **Table 8**. The ratio between the metals was calculated by dividing the metal concentration by the Zn concentration.

Table 8: Quantitative XPS analysis of ZnMgAl before and after the respective plasma treatments.^[109]

Substrate treatment	Zn 2p 3/2 [at %]	Mg 1s [at %]	Al 2p [at %]	O 1s [at %]	C 1s [at %]	Zn:Mg:Al
Reference (solvent cleaned)	0.9 ± 0.3	2.2 ± 0.4	12.3 ± 1.8	41.3 ± 2.8	43.3 ± 2.7	1:2.7:16.3
Ar	1.6 ± 0.4	5.3 ± 0.2	15.7 ± 0.7	58.1 ± 1.0	19.3 ± 3.5	1:3.5: 10.6
Ar + 5% O₂	2.0 ± 0.6	4.1 ± 0.2	15.6 ± 2.3	54.2 ± 2.3	24.3 ± 2.2	1:2.2:8
Ar + 5% H₂O	3.5 ± 0.3	4.6 ± 0.6	10.6 ± 0.7	54.7 ± 1.1	26.8 ± 1.3	1:1.3:3

All investigated samples showed only the presence of Al, Mg, and Zn plus oxygen and carbon. From the stoichiometric data shown in **Table 8**, it can be seen that the metal component of the untreated surface is dominated by Al. The high C concentration is due to adventitious carbon, as already reported for similar samples.^{[135],[136]}

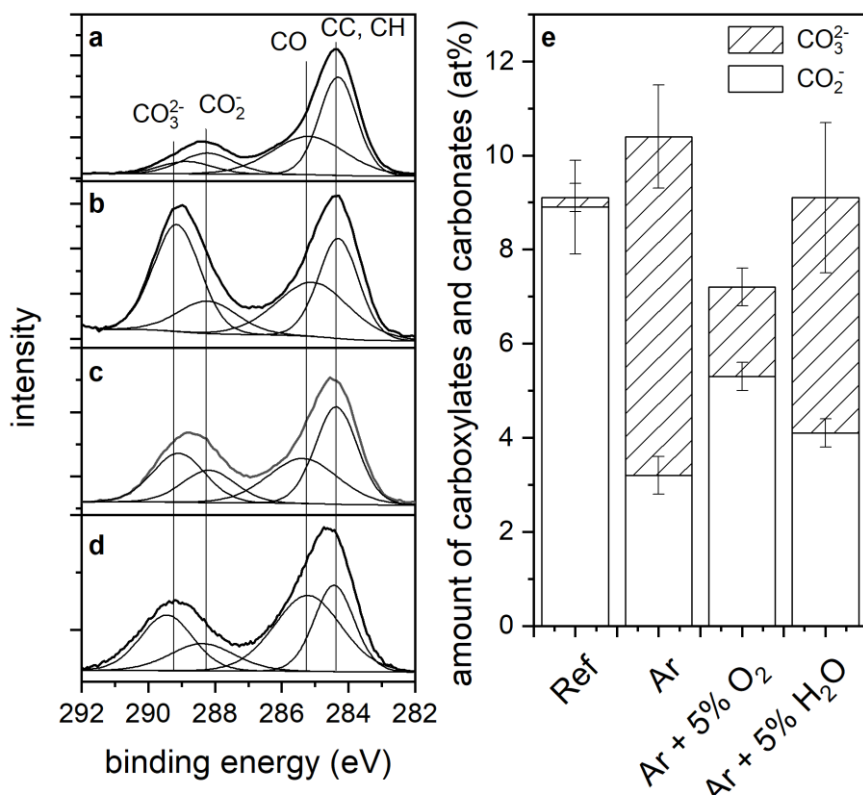


Figure 34: Element spectra of C 1s before (a) and after the plasma treatment with Ar (b), Ar/O₂ (c), and Ar/H₂O (d). Quantification of carboxylates and carbonates determined by XPS before and after the plasma treatments (e).^[109]

4.1 Surface modification of ZnMgAl-coated steel by dielectric barrier discharge plasma

As already observed in the IR analysis, XPS characterization showed the removal of surface carbon after all plasma treatments. The C1s core level peaks were fitted into four components (**Figure 34**). The component at 284.6 eV is associated with aliphatic carbon species, the component at 285.1 eV to ethers, the component at 288.2 eV to carboxylates, and the component at 289.2 eV to carbonates.^{[142],[145]} As can be seen in **Figure 34a-d**, the plasma treatments led to a distinct increase in carbonate species, while all other components decreased in intensity.

In order to compare the absolute amounts of carboxylate and carbonates, the peak percentage corresponding to each peak component was normalized to the total at% of carbon as determined by XPS (**Figure 34e**). Interestingly, the sum of carboxylates and carbonates remained nearly constant during the plasma process, and only the ratio of carbonates to carboxylates changed. Thus, the conversion from carboxylates to carbonates implied by the IR analysis was confirmed by XPS. As already seen in the IR spectra, XPS also confirmed that plasma treatments with pure Ar resulted in the highest carbonate formation and Ar/O₂ the smallest.

Interestingly, the different plasma treatments influenced the metal ratios as well at the near-surface region. In all cases, the Al concentration decreased. Pure Ar plasma led to a strong increase in Mg, while Ar/H₂O plasma mainly caused a surface enrichment of Zn. Changes in surface composition after exposure to low-pressure plasmas have already been reported before,^{[21],[51]} and the compositional changes were assigned to a field-induced oxide growth followed by migration. Note that changes in surface composition due to preferential sputtering of the substrate can be excluded due to the small fraction of energetic ions expected to reach the sample surface owing to the high collision rate in the gas phase in an atmospheric-pressure plasma.^{[2],[38]}

4.1 Surface modification of ZnMgAl-coated steel by dielectric barrier discharge plasma

In the untreated samples, the core level peaks of Mg1s showed a fully oxidized Mg component, while in the case of the Al2p and Zn2p peaks, weak components associated with metallic Zn and Al were seen (**Figure 35**). Therefore, for each peak, two components were fitted, representing the oxidized and reduced species respectively (Zn2+ (1021.8 eV) and Zn0 (1019.6 eV) or Al3+ (73.6 eV) and Al0 (70.6 eV)). The fitted peaks are displayed as dashed lines.

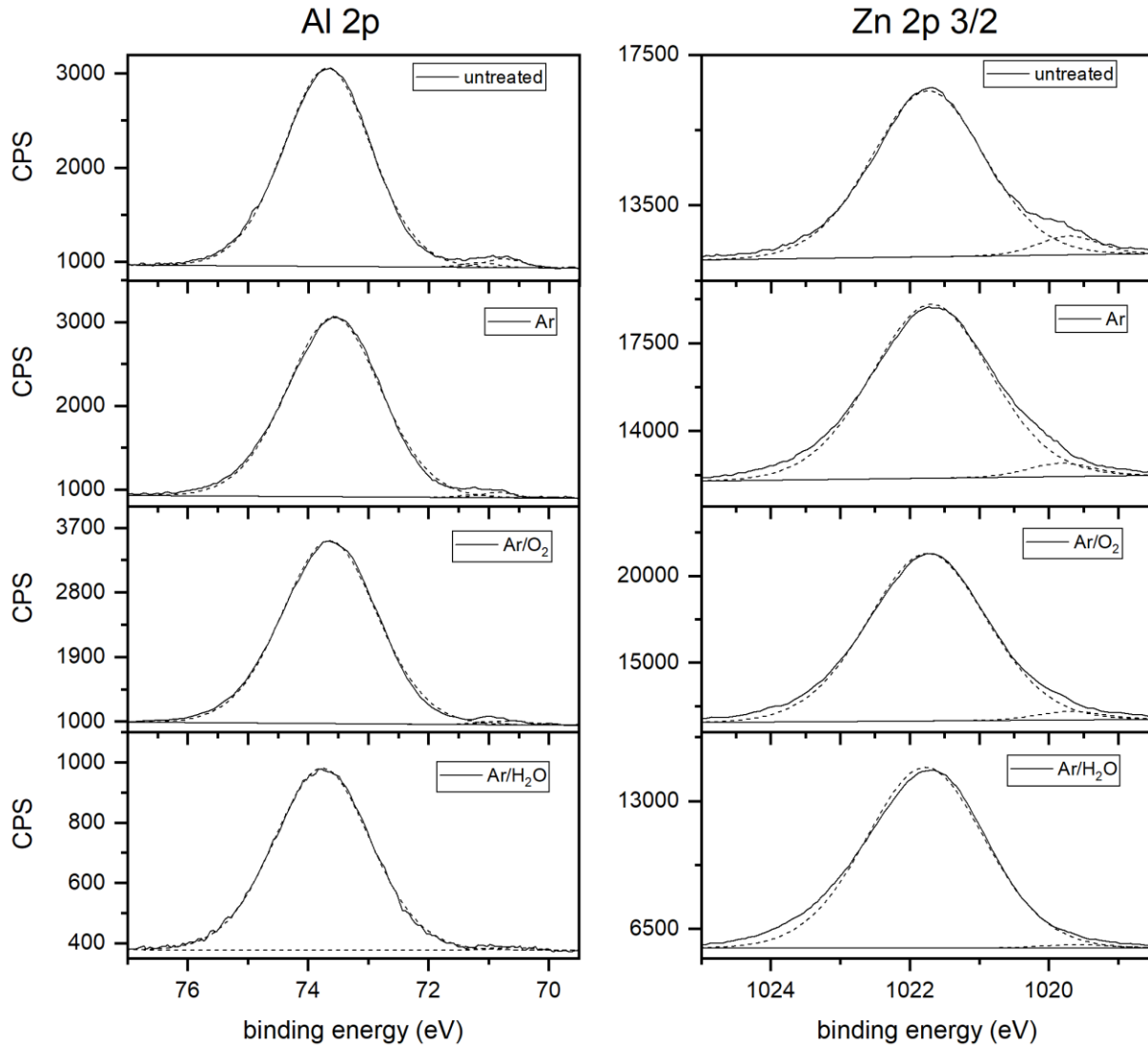


Figure 35: Al 2p and Zn 2p 3/2 XPS core level peak of an untreated ZnMgAl sample and samples after the plasma treatments. The fits are displayed as dashed lines.^[109]

The oxidation and hydroxylation of aluminum due to the plasma treatment could be seen by DPM-IRRAS. This effect is consistent with the XPS characterization since the metallic component of the Al2p peak was seen to decrease (the same effect was observed in the Zn2p core level peak). However, it was not possible to distinguish between metal oxides, hydroxides, and carbonates, neither in the core level peaks nor by evaluating the Auger parameters.^{[146],[147]}

4.1 Surface modification of ZnMgAl-coated steel by dielectric barrier discharge plasma

In order to further investigate the oxidation of the metals, the top oxide layer thickness was estimated following Strohmeier, assuming separated oxide phases.^[89] Please note that this is just a rough estimation since the actual oxide layer at the surface is inhomogeneous, both in composition and in structure:

$$d = \lambda_o \sin(\theta) \ln \left[\frac{N_m \lambda_m I_o}{N_o \lambda_o I_m} + 1 \right] \quad (38)$$

where d is the oxide layer thickness, λ_m and λ_o are the inelastic mean free paths of the emitted photoelectrons within the metal and oxide layers, θ is the take-off angle with respect to the surface, N_m and N_o are the volume densities of the metal and oxide phases (see **Table 9**) and I_m and I_o are the fitted intensities of the respective metal and oxide photoelectron peaks. The mean free paths were calculated using the Software Quases^[148], which is based on the calculations of Tanuma.^[149]

Table 9 Constants for calculating the oxide layer thickness.^[109]

	λ_m [Å]	λ_o [Å]	θ [°]	N_m [g cm ⁻³]	N_o [g cm ⁻³]
Aluminium	30.85	32.56	30	2.7	3.99
Zinc	9.81	11.38	30	7.14	5.47

The results are presented in **Figure 36**.

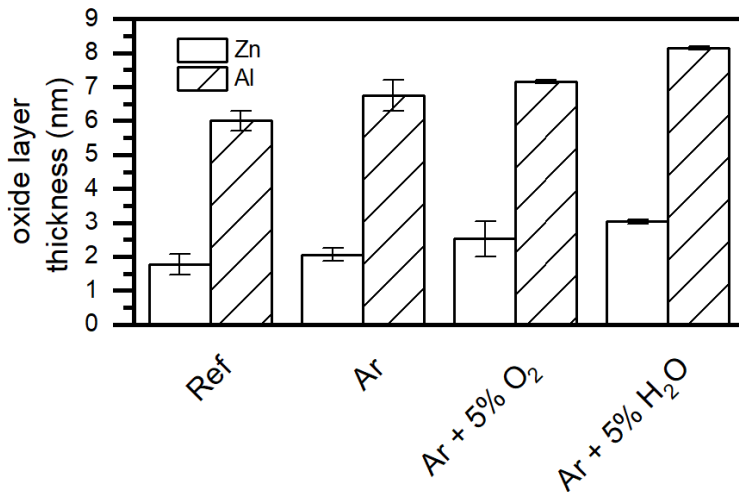


Figure 36: Calculated oxide layer thickness on ZnMgAl based on the evaluated Zn2p and Al2p before and after plasma treatments.^[109]

Ar plasma treatment exhibited a certain increase in the oxide layer thickness for both Zn and Al; the addition of oxygen-containing species enhanced this effect. Thus, as expected, the generation of oxidizing species seems to be the determining factor for increasing the oxide layer thickness. However, why an Ar plasma treatment would induce the oxidation of the surface is not fully understood. In pure Ar plasma, the presence of OH species was determined by OES, and they might be causing the surface oxidation in this case. Adding O₂ to Ar increased the oxide layer thickness slightly, while the addition of H₂O led to a significant enhancement of the oxidizing properties. Thus, water seems to have a higher oxidizing effect than oxygen in this case.

To summarize, XPS confirmed the removal of surface contamination (aliphatic carbon chains) and the conversion of carboxylates to carbonates. Additionally, XPS showed the migration of Zn and Mg towards the surface and an increase in the oxide layer thickness.

4.1 Surface modification of ZnMgAl-coated steel by dielectric barrier discharge plasma

4.1.2.4 TOF-SIMS imaging and depth profiling

After XPS showed that the metal ratios changed at the near-surface sample region, TOF-SIMS was used to investigate the lateral and in-depth redistribution of elements resulting from the plasma treatments.

In ToF-SIMS, secondary ion intensities generally depend both on the specific secondary ion of interest and the matrix.^[97] If matrix effects can be neglected, intensities of a given secondary ion (such as Zn⁺, Mg⁺, or Al⁺ in this case) could be directly compared between different materials. However, the ZnMgAl coating shows an inhomogeneous structure at the micro-and nanoscale, so that matrix effects cannot be excluded in this case. Thus, the intensities can only be compared between the ZnMgAl samples. Moreover, oxygen, e. g. as present in surface oxide layers, is known to increase the signal intensity of metal secondary ions by several orders of magnitude.^[97] These general complications have to be kept in mind when discussing and interpreting the TOF-SIMS data.

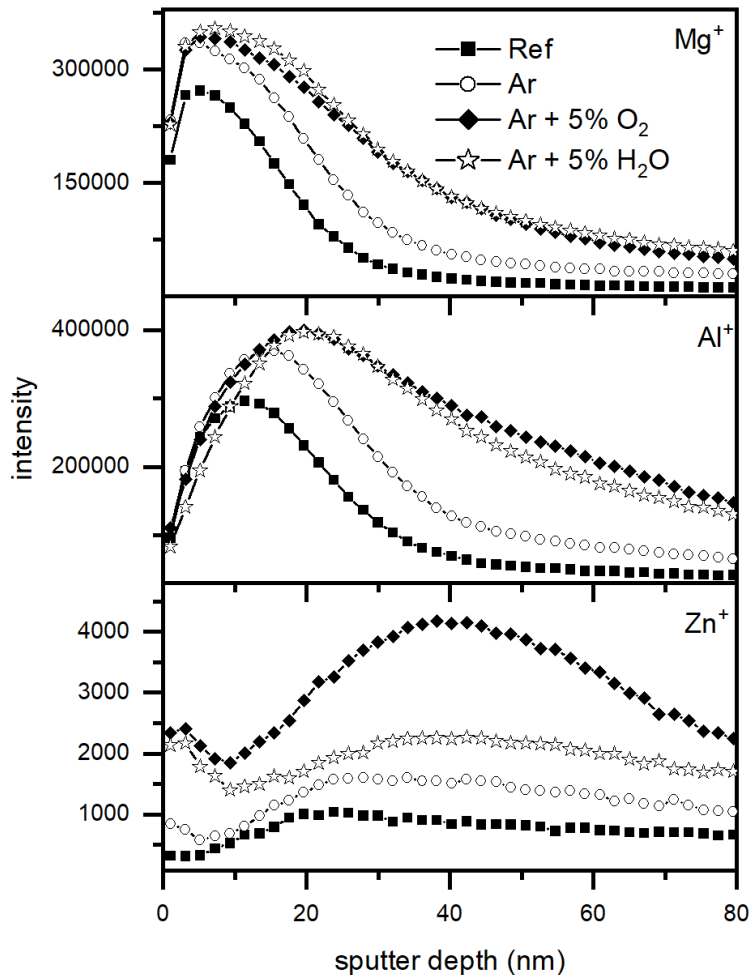


Figure 37: TOF-SIMS depth profiles of the secondary metal ions Mg⁺, Al⁺ and Zn⁺ for untreated samples and samples with plasma treatments using different gas mixtures.^[109]

The depth profiles of the major secondary metal ions, Zn⁺, Mg⁺, and Al⁺, are presented in **Figure 37**. The curves of Mg⁺ and Al⁺ secondary ions showed similar behavior with depth: an initial increase of the signal, followed by a maximum and progressive decrease. This trend is similar to the signals of the corresponding metal oxide cluster signals, i.e., MgO⁺ and AlO⁺. Hence, in a first approximation, it could be said that the profiles show the distribution of the superficial oxide layer. After all plasma treatments, a shift of the intensity maximum towards the bulk was observed, indicating the growth of the oxide layer.

4.1 Surface modification of ZnMgAl-coated steel by dielectric barrier discharge plasma

Interestingly, the Zn^+ secondary ions showed a somewhat different depth profile than Mg^+ and Al^+ . The Zn^+ signal at the surface was low in the untreated sample and increased with increasing depth, reaching a steady-state for depths below 20 nm. This curve is consistent with the reported accumulation of Al and Mg on the surface of ZnMgAl. Thus, Zn was enriched at the outermost surface after all plasma treatments, as already seen by XPS. Note, however, that the Zn^+ signal of the plasma-treated ZnMgAl samples did not reach a steady-state with increasing depth as in the case of the untreated sample: after an initial decrease with depth (around 5 nm), the signal increased again, reaching a maximum between 20 and 60 nm depth before decreasing once more.

The TOF-SIMS analysis of the first 10 nm (**Figure 38**) showed that the top oxide layer, both before and after the plasma treatments, was homogeneous over surface areas of up to 400 μm , independently of the structures underneath and consisted of Al and Mg.

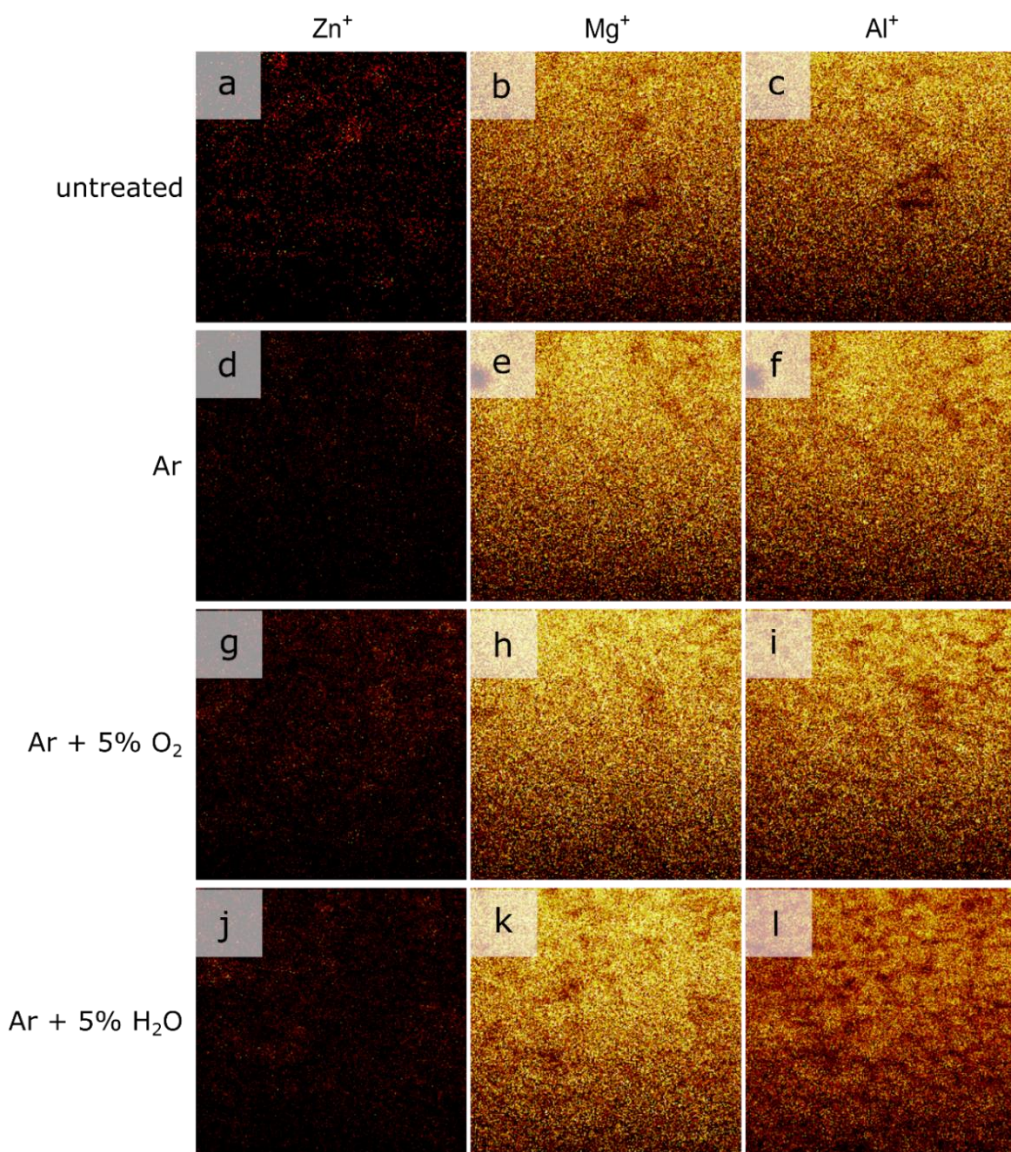


Figure 38: $400 \times 400 \mu m^2$ TOF-SIMS mappings of Zn^+ , Mg^+ , and Al^+ (from left to right) integrated over 10 nm, before and after the plasma treatments.^[109]

Therefore, TOF-SIMS could confirm the growth in the oxide layer thickness seen by XPS and additionally revealed plasma-induced changes in a depth of several nm. The homogeneity of the top oxide layer over large areas is not affected by the plasma.

4.1 Surface modification of ZnMgAl-coated steel by dielectric barrier discharge plasma

4.1.2.5 Kelvin probe studies of average surface potentials after plasma processing

Kelvin Probe measurements were performed in-situ to follow the plasma-induced changes in the surface potential, including changes to the adsorbate layer, metal state, and semiconducting properties. By measuring KP, it is possible to evaluate the Galvani potential, which describes the potential to remove a Fermi-level electron from the surface. The Galvani potential difference ($\Delta\phi_{Ref}^{Me}$) measured by the KP between the underlying metal and the Kelvin probe is determined by the sum of all potential differences of all interfaces according to **Equation 39**:^[108]

$$\Delta\phi_{Ref}^{Me} = \Delta\phi_{ox}^{Me} + \Delta\phi_{ox} + \chi_{ox} + \Delta\Psi_{Ref}^{ox} - \chi_{Ref} \quad (39)$$

where $\Delta\phi_{ox}^{Me}$ is the potential difference between the oxide and the metal. $\Delta\phi_{ox}$ describes the potential drop across the oxide layer and is determined by such factors as the oxide layer's chemical composition, oxide thickness, and conductivity.^{[108],[110],[111]} χ_{ox} is the surface potential of the oxide and is determined by the adsorbed layer on the oxide. Thereby, dipoles formed on the oxide surface play a great role as well as the intrinsic dipole moment of the adsorbed layer.^{[111],[112]} $\Delta\Psi_{Ref}^{ox}$ and χ_{Ref} are the Volta potential and the surface potential of the probe respectively and are constant values.

KP measurements of at least eight samples were averaged for each plasma gas mixture, and the results are shown in **Figure 39**.

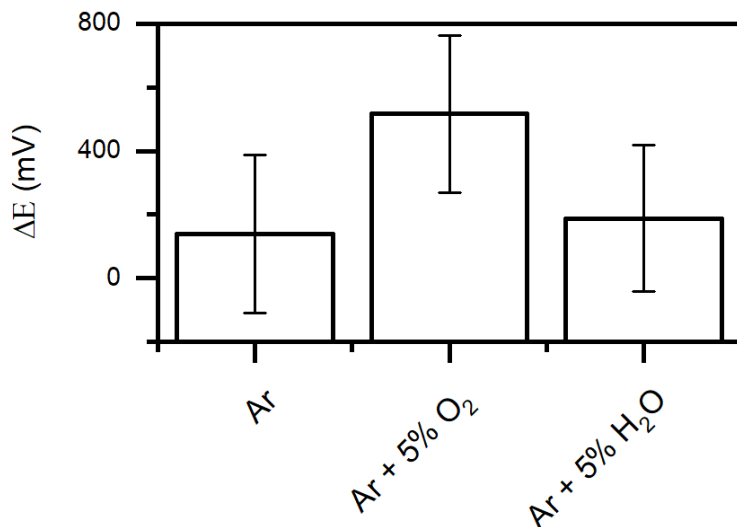


Figure 39: Differences in the surface potential before and after the respective plasma treatment measured in-situ with the KP on ZnMgAl. The error bars are the statistic of at least 8 samples per plasma gas mixture.^[109]

In all cases, a positive shift of the potential was seen after the plasma treatments. According to the IR and XPS characterizations, the chemical changes induced by the plasma treatments can be summarized as follows: (i) removal of adventitious carbon, (ii) conversion of carboxylates to carbonates, (iii) migration of Mg and Zn towards the surface and (iv) increased thickness of the upper oxide layer. The influence of the four effects on the surface potential is discussed in the following.

(i) When adsorbed adventitious carbon and water are removed from the surface, the distribution of surface dipoles changes, with the corresponding effect on the surface potential(χ_{ox}). Taheri et al. investigated the adsorbed layer on Zn-surfaces and showed that adsorption of contamination on the surface shifted the potential to more positive values.^[111] Thus, the removal of surface contaminations should result in a negative shift in the surface potential.

4.1 Surface modification of ZnMgAl-coated steel by dielectric barrier discharge plasma

(ii) Absorbed carboxylates form a strong dipole at the surface and therefore strongly influence the surface potential (χ_{ox}).^{[111],[112]} At the same time, the intrinsic dipole moment of carboxylates attached with an aliphatic tail orientated away from the surface is zero and does not contribute to the overall potential drop in the adsorbate layer.^{[111],[112]} Changes in the structure of the carboxylates lead to a change in the intrinsic dipole moment different than zero and therefore change the overall potential. Consequently, the conversion from carboxylates to carbonates influences the dipole moment at the surface as well as the intrinsic dipole moment of the adsorbate layer.

(iii) The migration of the metals can influence the potential difference between the metal and the oxide ($\Delta\phi_{ox}^{Me}$) when new boundaries are formed. Due to the complex structure of the oxide/metal interface, the influence of the migration cannot be assessed.

(iv) A growth in the oxide layer thickness leads to a positive shift of the potential drop over the oxide layer ($\Delta\phi_{ox}$).^{[108],[110]}

Therefore, the overall positive shift of the potential after the plasma treatments is a combination of the positive shift induced by the oxide layer growth and the changes in the dipole distribution of the adsorbate layer.

4.1.2.6 SKPFM imaging of surface potentials

Ex-situ characterization of the samples by scanning Kelvin probe force microscopy (SKPFM) was performed before and after the plasma treatments to evaluate the surface roughness and the 2D distribution of the surface potential.

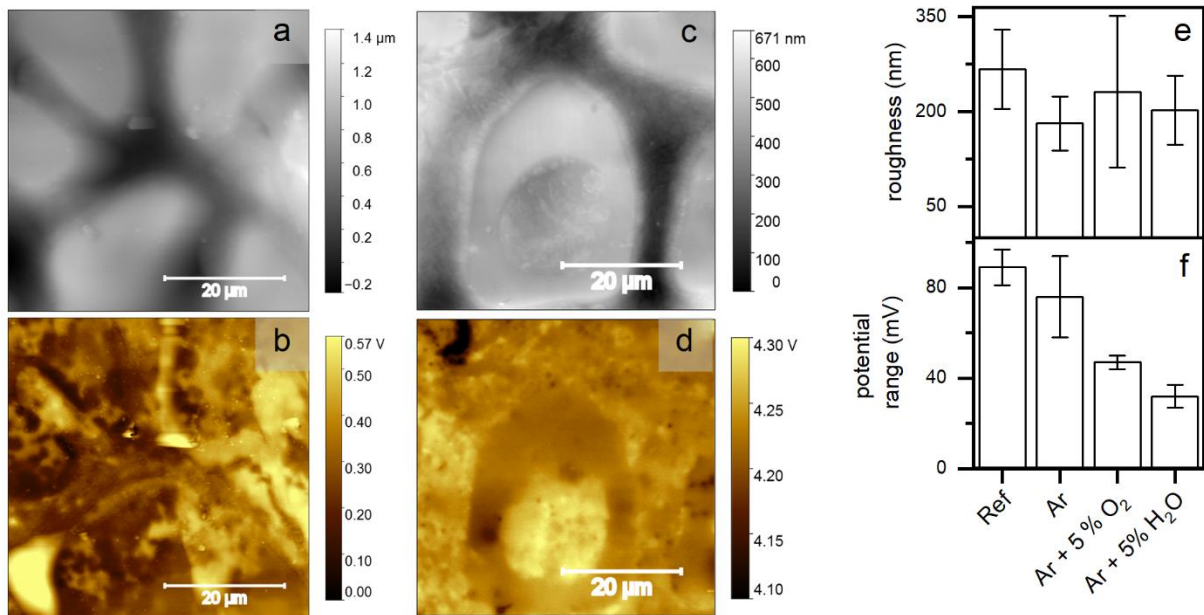


Figure 40 SKPFM mappings of an untreated ZnMgAl alloy (a) topography and b) surface potential) compared to a sample plasma treated with Ar/H₂O (c) topography and d) surface potential). e) Evaluation of the roughness and f) the surface potential range before and after the respective plasma treatment.^[109]

The SKPFM mappings (**Figure 40a-d**) revealed a structure similar to FE-SEM and TOF-SIMS measurements, both in topography and surface potential. **Figure 40a and b** show the situation corresponding to the untreated sample. Previous characterization of such alloys, such as the one done by Lostak et al., showed that the surface potential depends on the local bulk composition for ZnMgAl alloys.^[135] Indeed, given the clear compositional inhomogeneity of the sample, one would expect potential variations corresponding to the individual standard potentials of the separated phases. The mapping presented in **Figure 40b**, however, shows relatively small standard potential variations. This is most

4.1 Surface modification of ZnMgAl-coated steel by dielectric barrier discharge plasma

probably due to the muffling effect of the thin top oxide layer, whose homogeneity over large areas of the sample was determined by the ToF-SIMS measurements presented before. After plasma treatment, the variations in surface potential along the surface area are even smaller. To evaluate the changes, the R_q value for the heightmaps (roughness) and the potential maps (potential range) were calculated (**Figure 40e and f**). All samples exhibited high roughness (300 nm on a 70x70 μm^2 scale), which was not affected by the plasma treatments. However, as already mentioned, the surface potential showed a distinct homogenization after the plasma treatment with Ar/O₂ and Ar/H₂O. The potential homogenization correlates with the increase of the oxide layer thicknesses determined by XPS and TOF-SIMS. With increasing oxide layer thickness, the influence of the bulk material (in-homogeneously distributed) on the surface is reduced, thus leading to a more homogenous surface potential. Additionally, the conversion of carboxylates to carbonates on the surface, with the corresponding redistribution of surface dipoles, might also affect the surface potential.

4.1.2.7 Water contact angle studies

Water contact angles were measured to investigate the change in the wettability of the surface after the plasma treatments. The results are shown in **Figure 41**.

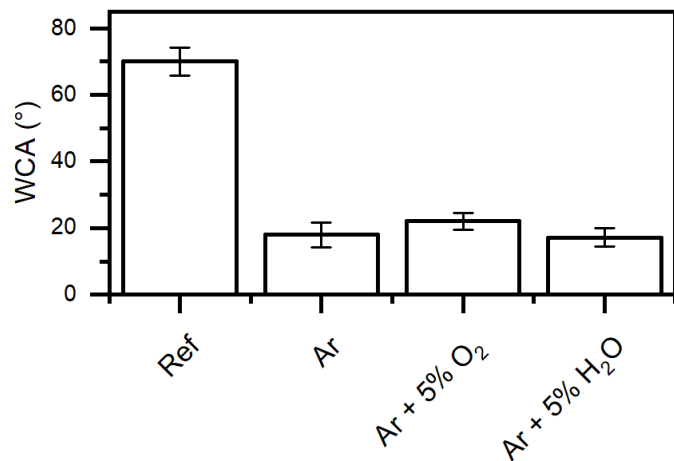


Figure 41 Water contact angle measurements before and after the plasma treatments.^[109]

The untreated surface showed a high contact angle of 70°. This is explained by the presence of the adventitious carboxylate adsorption layer. This leads to an un-polar surface due to the presence of aliphatic carbon chains. As already discussed, one of the main results of the plasma treatments is the removal of these aliphatic chains, which should result in an increase in surface wettability. As expected, the contact angle was reduced to around 20° in all cases after the plasma treatment. The Ar/O₂ plasma, which showed the lowest removal rate of aliphatic carbon, was thus resulting in the highest contact angle.

4.1 Surface modification of ZnMgAl-coated steel by dielectric barrier discharge plasma

4.1.2.8 90°- peel test studies for the analysis of surface adhesive properties

Peel test was used to investigate the influence of the plasma treatments on the adhesion strength for an acrylate adhesive tape and an epoxy amine adhesive. The results are presented in **Figure 42**.

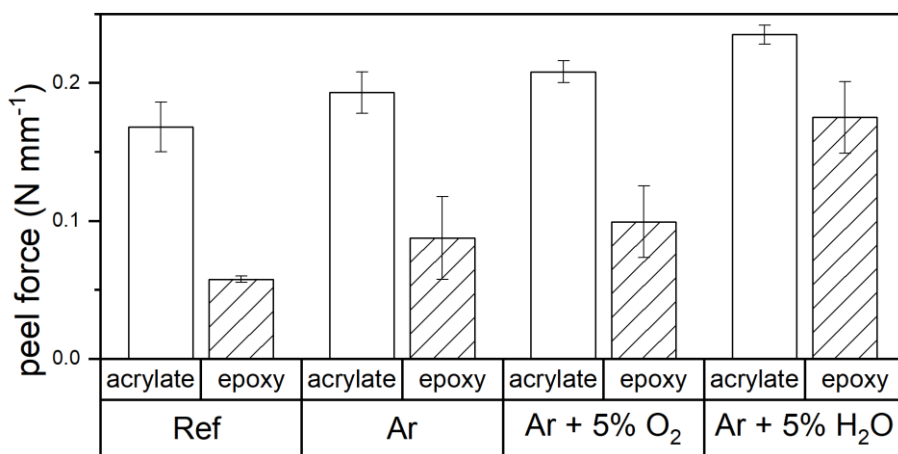


Figure 42 Peel test results before and after the plasma treatment for a) acrylate coated tape and b) epoxy-amine adhesive.^[109]

The peel forces measured for the epoxide amine adhesive on the untreated surface were in the same range as reported in the literature.^{[150],[151]} The acrylate showed a higher peel force than the epoxide amine adhesive. The adsorption of polyacrylic acid molecules to metal oxides such as Al_2O_3 and ZnO has been deeply studied by several authors.^{[132],[152]} We assume that the reason for the increased adhesion forces in the case of acrylate-based adhesive is that carboxylic groups form strong acid-base interactions with the surface metal ions due to bidentate bindings. By comparison, the amine and alcohol functions of the epoxy amine adhesive form interfacial monodentate bonds. All plasma treatments for both adhesives increased the peel force. Plasma treatments with Ar and Ar/O_2 showed only small increases in the peel force, while plasma treatments with $\text{Ar}/\text{H}_2\text{O}$ led to a significant increase for both adhesives. The increase was particularly distinctive in the case of the epoxy-amine adhesive, where the peel force was improved by a factor of 3. This increase in the peel force is in the range of improvements introduced by commonly used adhesion promotion layers such as γ -APS.^[151] As already discussed, the surface of untreated ZnMgAl is made of an oxyhydroxide surface, covered by a layer of adsorbed carboxylates and aliphatic carbon groups. When an adhesive is applied to this surface, the acid-base interaction of the polar groups of the adhesive with the metal surface is hindered by the presence of the aliphatic carbon groups, which are not polar in nature. The plasma treatments etch the aliphatic carbon groups and convert carboxylates to carbonates. The conversion to carbonates (polar) combined with the loss of the aliphatic carbon groups leads to a better interaction of the adhesive with the surface.

Nevertheless, plasma treatments with small carbonate conversion, such as the Ar/O_2 plasma, show a significant increase in adhesion between adhesive and surface as well. That suggests that additional mechanisms might need to be taken into account. While pure Ar plasma mainly created carbonates combined with the etching of aliphatic carbon groups, Ar/O_2 plasma primarily induced an increase in the oxide layer thickness followed by a homogenization of the surface potential. Both processes led to a similar increase in the peel force independent of the adhesive. It is important to note that plasma treatments with $\text{Ar}/\text{H}_2\text{O}$, which induce all the discussed effects to a high degree, showed the highest performance with both adhesives, thus showing the synergistic nature of the plasma-induced changes on the adhesion. How this combination of factors in detail affects the overall adhesive properties of the surface is not clear at present.

4.1 Surface modification of ZnMgAl-coated steel by dielectric barrier discharge plasma

4.1.3 Conclusions

Combining the surface characterization techniques DPM-IRRAS and KP (in-situ) and XPS, TOF-SIMS, and SKPFM (ex-situ), five different plasma-induced surface effects in the DBD plasma treatment of ZnMgAl alloys were identified and are summarized in **Figure 43**.

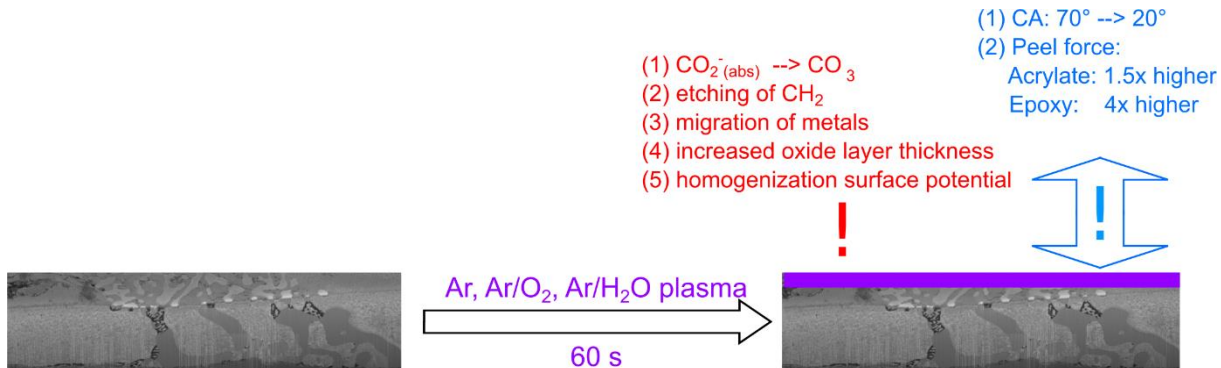


Figure 43: Identified changes on the plasma-treated ZnMgAl surfaces and their most beneficial influence on the adhesion properties.

The plasma-induced changes were: (i) surface conversion of carboxylates to carbonates, (ii) etching of aliphatic carbon groups, (iii) migration of metals, (iv) increased top oxide layer, and (v) homogenization of the surface potential. These changes appeared in greater or lesser degree depending on the gas mixture. Although an improvement of adhesion properties and wettability was observed after all plasma treatments for the chosen adhesive films (see experimental part), there was no clear correlation between a specific surface effect and the improved adhesion behavior. Ar plasma, which primarily produced the etching of aliphatic chains and conversion of carboxylates to carbonates of the surface, showed a similar improvement in adhesion as the Ar/O₂ plasma, where the main effect was the increased oxide layer thickness and homogenization of surface potential. Interestingly, plasma treatment using Ar/H₂O as plasma gas, which induced all discussed effects to a high degree, resulted in the most significant adhesive improvement, suggesting that all effects synergistically contribute to the final improvement. The improved adhesion after removing aliphatic carbon chains and the conversion of carboxylates to carbonates of the surface can be partly explained by the formation of polar groups at the surface that can interact with the polar groups of the adhesive. However, it is not fully understood at present how the combination of all observed factors collectively affects the adhesion.

4.2 Influence of dielectric barrier plasma treatment of ZnMgAl alloy-coated steel on the adsorption of organophosphonic acid monolayers

4.2 Influence of dielectric barrier plasma treatment of ZnMgAl alloy-coated steel on the adsorption of organophosphonic acid monolayers

In chapter 4.1, a thorough study was presented that identified several plasma-induced processes on the ZnMgAl surface and their beneficial influence on adhesion properties, showing increased wettability and adsorption of different adhesives. However, the investigated adhesion properties gave no further information about the surface states after the adhesive application and lateral distributions. Therefore, a more demanding system was investigated in the form of a self-assembled monolayer of ODPA (**Figure 44**). ODPA was chosen due to its simple structure (one anchor group without a further polar functional group) and its well-known adsorption properties (chapter 2.3.1).

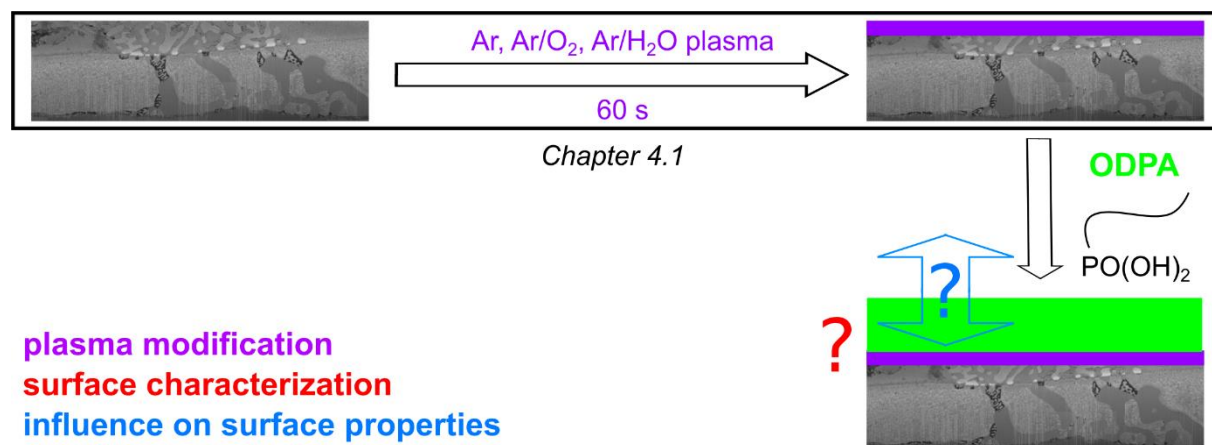


Figure 44: Chapter 4.2 aimed to investigate the adsorption of ODPA monolayers on plasma-treated ZnMgAl alloys using the same plasma gas parameters as in chapter 4.1.

Thus, the samples were prepared exactly the same as in chapter 4.1 and covered with ODPA, investigating the surface state after the ODPA adsorption and the barrier properties of the ODPA-layer as a function of the plasma gas pretreatment. The following chapter is adapted from reference ^[130] with permission of the Journal of Surface and Interface Analysis and can be found at <https://onlinelibrary.wiley.com/doi/10.1002/sia.6782>.

4.2 Influence of dielectric barrier plasma treatment of ZnMgAl alloy-coated steel on the adsorption of organophosphonic acid monolayers

4.2.1 Experimental approach

4.2.1.1 Plasma treatment

Before the measurement, the ignition voltage for the given electrode-sample distance was determined for each gas mixture. Then, the voltage was set 165 V higher than the ignition voltage for each gas mixture, leading to an applied voltage of 2.9 kV for pure Ar, 3.6 kV for Ar/O₂, and 2.6 kV for Ar/H₂O. The duration of the plasma treatment in all cases was 60 s.

4.2.1.2 Octadecyl phosphonic acid adsorption

A 1 mM solution of ODPA in ethanol was used in order to form a self-assembled monolayer on the surface. The samples were immersed in the ODPA-solution for 24h immediately after the plasma treatments, subsequently rinsed with Ethanol, and dried with a stream of Air.

All other modifications and measurements were carried out as described in chapter 3.

4.2.2 Results and Discussion

PM-IRRAS and XPS studies allowed for the characterization of the binding and orientation of adsorbed ODPA. Complementary to this approach, cyclic voltammetry was performed to characterize the barrier properties of the adsorbed monolayers.

4.2.2.1 PM-IRRAS studies

The PM-IRRAS data of the untreated sample and the sample covered in ODPA after different plasma treatments are shown in **Figure 45**.

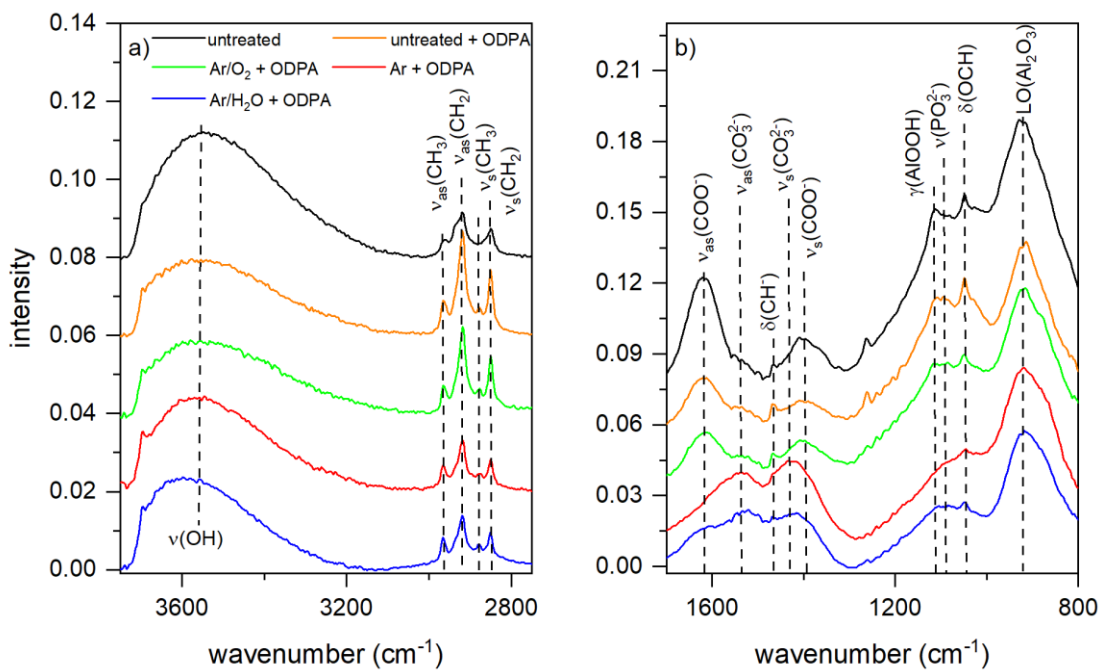


Figure 45: PM-IRRAS data of an untreated ZnMgAl sample and samples coated with ODPA after different plasma treatments
a) spectra in the range between 3750 cm⁻¹ to 2700 cm⁻¹ b) spectra in the range between 1700 cm⁻¹ to 800 cm⁻¹.^[130]

The spectra are shifted along the y-axis for better visibility. The PM-IRRAS data of the original surface show a surface composition consisting of an oxide/hydroxide layer, detecting mainly Al-oxides/oxyhydroxides covered by absorbed carboxylates and aliphatic carbon groups.

4.2 Influence of dielectric barrier plasma treatment of ZnMgAl alloy-coated steel on the adsorption of organophosphonic acid monolayers

The peak positions are summarized in **Table 10**.

Table 10: Band positions found in the PM-IRRAS spectra and their respective assignments.^[130]

Band position (cm ⁻¹)	Band assignment	Reference
940	LO(Al ₂ O ₃)	[39],[153]
1020	δ(OCH)	[16],[138],[140]
1098	ν _s (PO ₃ ²⁻)	[154]
1110	γ(AlOOH)	[39],[153]
1400	ν _s (CO ₂ ⁻)	[142],[143]
1440	ν _s (CO ₃ ²⁻)	[138],[140],[141]
1465	δ(CH ₂)	[153]
1535	ν _{as} (CO ₃ ²⁻)	[138],[140],[141]
1630	ν _{as} (CO ₂ ⁻)	[142],[143]
2850	ν _s (CH ₂)	[21],[155],[156]
2878	ν _s (CH ₃)	[21],[155],[156]
2918	ν _{as} (CH ₂)	[21],[155],[156]
2965	ν _{as} (CH ₃)	[21],[155],[156]
3450	ν(OH), ν(OH ₂)	[39]

The PM-IRRAS data of adsorbed ODPA monolayers show distinctly higher spectral features in the C_xH_y stretching region, which characterize the aliphatic tail of an at least partially ordered monolayer. According to the literature, the peak position can be used to distinguish between a “disordered” and an “ordered” film.^{[155],[157]–[159]} In this regard, well-ordered means an all-trans configuration of the methylene groups. Thereby, a peak position of 2918 cm⁻¹ or lower for the ν_{as}(CH₂) vibration and 2850 cm⁻¹ or lower for the ν_s(CH₂) vibration indicate a well-oriented monolayer. The position for all ODPA coated samples, despite their pre-treatment, was very similar, located around 2918 cm⁻¹ and 2850 cm⁻¹, thus showing for all samples a well-ordered monolayer on the heterogeneous surface independent of the plasma gas mixture. According to the literature, the formed interfacial phosphonate group contributes to the broad peak at about 1150 cm⁻¹.^{[21],[45],[155]} Thus, a strong overlap of the weak phosphonic vibration with the aluminum bands is present and could not be evaluated.

4.2 Influence of dielectric barrier plasma treatment of ZnMgAl alloy-coated steel on the adsorption of organophosphonic acid monolayers

In order to determine whether adsorption has taken place, the peak intensity of the $\nu_{as}(\text{CH}_2)$ vibration at 2918 cm^{-1} was taken as a fingerprint for ODPA adsorption (**Figure 46**).

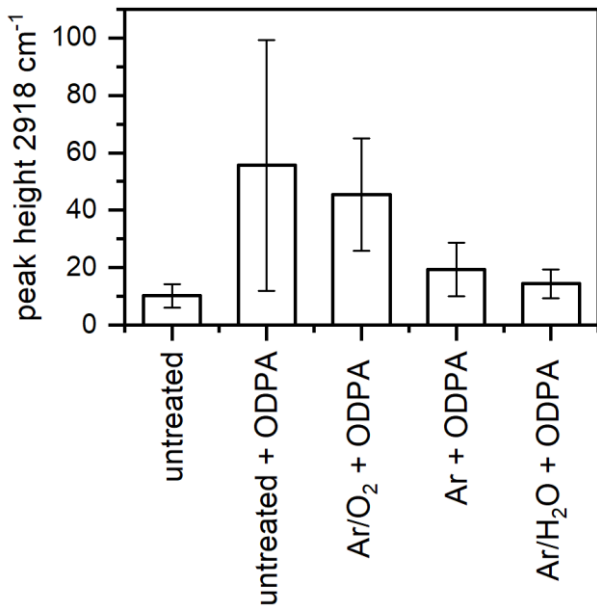


Figure 46: Evaluation of the PM-IRRAS spectra. The peak height of the peak at 2918 cm^{-1} (associated with $-\text{CH}_2-$) was investigated as a marker for aliphatic carbon on the surface. The error bars are a consequence of the measurements carried out on different samples.^[130]

The untreated samples show peaks related to aliphatic carbon due to carboxylates adsorbed on the surface. When ODPA was adsorbed onto the blank surface, the intensity of the CH_2 was strongly increased. In the case of the samples treated with an Ar/O_2 plasma, the ODPA adsorption led to an intensity lower than the ODPA covered untreated surface but still higher than the intensity of the blank surface itself. The adsorption on the samples treated by the Ar plasma and the $\text{Ar}/\text{H}_2\text{O}$ plasma showed an intensity only as high as the untreated surface. The decrease of the intensity for the plasma-treated can be explained by the conversion from carboxylates to carbonates by the parallel etching of the aliphatic carbon of the carboxylates. Additionally, due to the selection rules of PM-IRRAS, the decrease in the peak intensity can hint at a higher ordering of the SAM.

Interestingly, the carboxylate peaks ($\text{R}-\text{CO}_2^-$, at 1400 cm^{-1} and 1630 cm^{-1}) were only slightly decreased after the ODPA adsorption in the case of the untreated surface and the Ar/O_2 plasma-treated sample. Plasma treatments with Ar and $\text{Ar}/\text{H}_2\text{O}$ led to the presence of carbonates (CO_3^{2-} at 1440 cm^{-1} and 1530 cm^{-1}) on the surface instead of carboxylates after the ODPA adsorption. The results indicate that the adsorption of the ODPA occurred on a surface passive film containing metal oxide and metal carbonates, and even metal carboxylates. This demonstrates the stability of the absorbed carboxylates and carbonates on the surface and additionally that the phosphonic acids basically require stable surface metal ion centers for monolayer formation.^[66] Additionally, contact angle studies proved the adsorption based on increased static contact angle: The untreated surface had a contact angle of 75° which was increased by the ODPA adsorption independent of the pre-treatment to 110° . The latter is in good agreement with the literature reported for highly ordered methyl terminated monolayers.^{[63],[155]}

4.2 Influence of dielectric barrier plasma treatment of ZnMgAl alloy-coated steel on the adsorption of organophosphonic acid monolayers

4.2.2.2 XPS analysis of ODPA covered surfaces

To investigate the surface chemical composition, XPS was measured after the ODPA adsorption. The adsorption of ODPA was clearly confirmed by the strong increase of the carbon signal and the appearance of a phosphor signal. The results of the quantification are presented in **Table 11**.

Table 11: Results of the XPS quantification of the ZnMgAl alloys after different treatment steps.^[130]

Substrate treatment	Zn 2p 3/2 (at %)	Mg 1s (at %)	Al 2p (at %)	O 1s (at %)	C 1s (at %)	P 2s (at %)
untreated	0.9 ± 0.3	2.2 ± 0.4	12.3 ± 1.8	41.3 ± 2.8	43.3 ± 2.7	-
untreated +ODPA	0.2 ± 0.1	0.2 ± 0	7.5 ± 1.7	16.4 ± 2	72.5 ± 3.3	3.1 ± 0.4
Ar plasma +ODPA	0.45 ± 0.1	0.3 ± 0	7.2 ± 1.3	20.5 ± 0.8	69.0 ± 1.9	2.5 ± 0.1
Ar/O ₂ plasma +ODPA	0.2 ± 0	0.3 ± 0	9.4 ± 0.4	19.9 ± 0.1	67.7 ± 0.6	2.7 ± 0.2
Ar/H ₂ O plasma +ODPA	0.7 ± 0	0.3 ± 0	8.6 ± 0.3	21 ± 1.1	67 ± 0.7	2.4 ± 0.1

The surface metal ratios normalized to Al of the ZnMgAl coating before and after ODPA adsorption are shown in **Figure 47a**. The adsorption of ODPA led to an increased Al concentration at the interface and the depletion of Mg and Zn. Thereby, the plasma-induced migration of Zn and Mg towards the surface is completely lost, and the Zn and Mg amounts are even lower than before the plasma treatment. The change in interfacial ion concentration depended on the plasma treatment. Plasma treatments with Ar and Ar/H₂O showed a higher amount of Zn for the ODPA coated surface than the untreated sample. In contrast, the Ar/O₂ plasma led to a high decrease in the Zn-concentration, even lower than the Mg-concentration.

4.2 Influence of dielectric barrier plasma treatment of ZnMgAl alloy-coated steel on the adsorption of organophosphonic acid monolayers

The oxide layer thickness was calculated following the procedure published by Strohmeier.^[89]

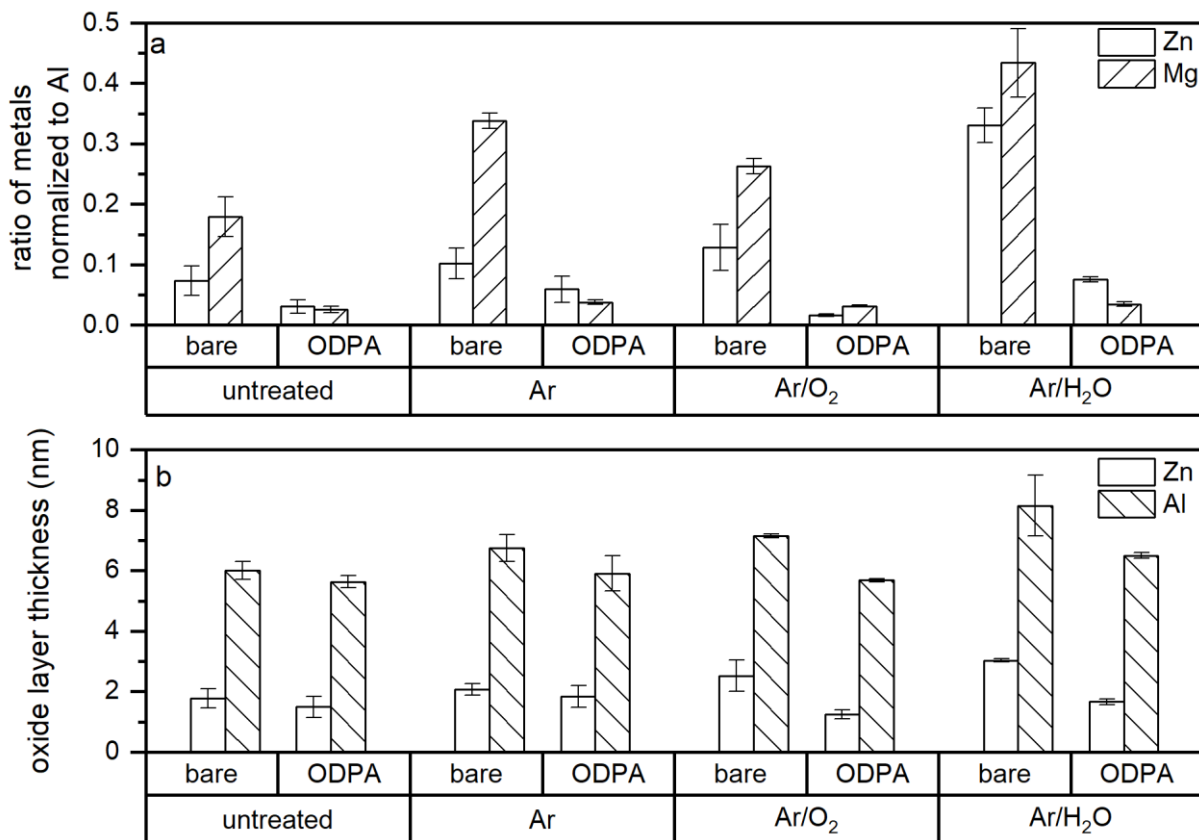


Figure 47: a) ratio of metals normalized to Al based on XPS quantifications and b) oxide layer thickness before and after ODPA adsorption calculated based on XPS.^[130]

Figure 47b shows the estimated thickness of the interfacial oxide layers before and after ODPA adsorption. Due to the presence of an organic monolayer on top of the oxide layer, the calculated oxide layer thicknesses are overestimated in the case of adsorbed ODPA. Therefore, the ODPA adsorption led to a partial etching of the surface passive film build-up during the plasma, explaining the change in the metal ratios: Mg was preferentially dissolved during ODPA adsorption, while the aluminum oxide seemed to be the most stable metal. This behavior can be explained by the low stability of Mg-oxides and carbonates in acidic media.^[160]

4.2 Influence of dielectric barrier plasma treatment of ZnMgAl alloy-coated steel on the adsorption of organophosphonic acid monolayers

4.2.2.3 Blocking properties determined by cyclic voltammetry

Cyclic voltammograms were measured in an aerated borate buffer solution to investigate the barrier properties of the as-prepared ODPA layer. The cathodic electrochemical response was investigated to analyze the defect density and stability of the formed monolayer.^{[161],[162]}

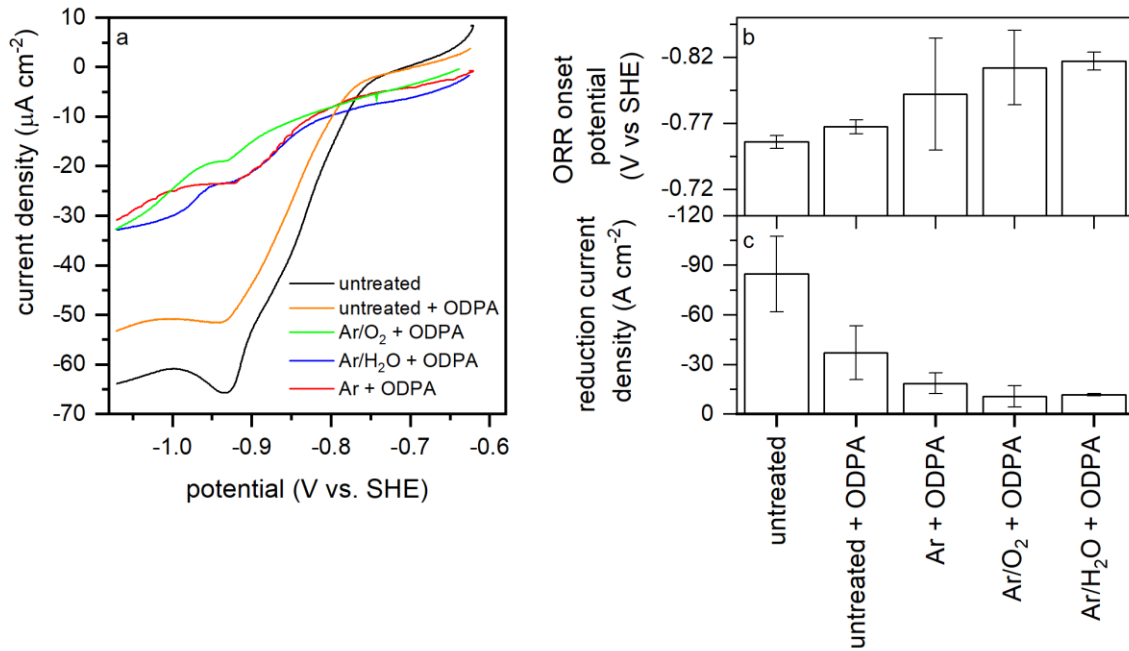


Figure 48: a) 2nd cathodic cyclic voltammograms of an untreated sample and ODPA-coated samples after different pre-treatments b) evaluation of the cathodic onset potential extracted from the cyclic voltammograms. c) evaluation of the peak reduction current density.^[130]

In the potential range assessed, a diffusion-controlled voltammetric peak around -0.95 V (vs. SHE) preceding the hydrogen evolution reaction (HER) has been detected in all the cases, as shown in **Figure 48a**. The latter can be attributed to oxygen and Zn reduction reactions which partially overlap. While the Zn²⁺ electrochemical reduction under similar experimental conditions is characterized by a cathodic peak located around -1.0 V,^[21] the onset potential for the oxygen reduction reaction (ORR) depends on the nature of the substrate.^[161] Both redox processes would be hindered by the presence of a tightly packed monolayer on the metal surface, on the one hand by increasing the overpotentials required for the O₂/Zn²⁺ reduction, and, on the other hand, by decreasing the faradaic currents corresponding to both reduction reactions. Thereby, the inhibition of these redox processes is determined by the defect structure of the ODPA monolayer rather than the macroscopic coverage.^[162] The main focus of our approach lies on assessing the inhibition of the electrochemical response associated with the metal oxide substrate underneath, in this particular case, the electrochemical reduction to metallic Zn, as reported by Pohl et al.^[21] The evaluation of the onset potential is shown in **Figure 48b**. It can be seen that the latter is only a little influenced by the adsorption of the ODPA monolayer on the untreated surface but significantly delayed in the case of the ODPA monolayer adsorbed after the plasma treatments. This indicates a higher ordering and stability of the formed ODPA monolayers onto plasma pre-treated ZnMgAl surfaces. Additionally, the reduction of current density associated with the diffusion-controlled voltammetric peak is displayed in **Figure 48c**. Here, the influence of the ODPA adsorption on the untreated surface is even more evident. Again, the plasma pre-treatments led to a lower current density, indicating an improvement in the barrier properties and a decreased defect density of the ODPA monolayer after the plasma treatments. In total, the evaluation of the cyclic voltammetry showed the decrease of defect density and thus an increased

4.2 Influence of dielectric barrier plasma treatment of ZnMgAl alloy-coated steel on the adsorption of organophosphonic acid monolayers

order in the ODPA monolayer by the delay of the onset potential and the decrease in the reduction current density.

Multiple steps on different time scales determine the formation of a SAM on a surface.^[64] In a simple model, where no other surface processes are present, the initial adsorption starts with random adsorption of molecules at the surface (**Figure 49**). This step is followed by an intermediate density phase where additional molecules adsorb at the surface and can move toward already adsorbed molecules to form islands. The islands grow, until in the end phase, a high-density film is formed. Due to the long immersion time of 24h and the CV results, a high-density film is assumed to be present on all samples, making the defect density responsible for the differences seen in the CV measurements.

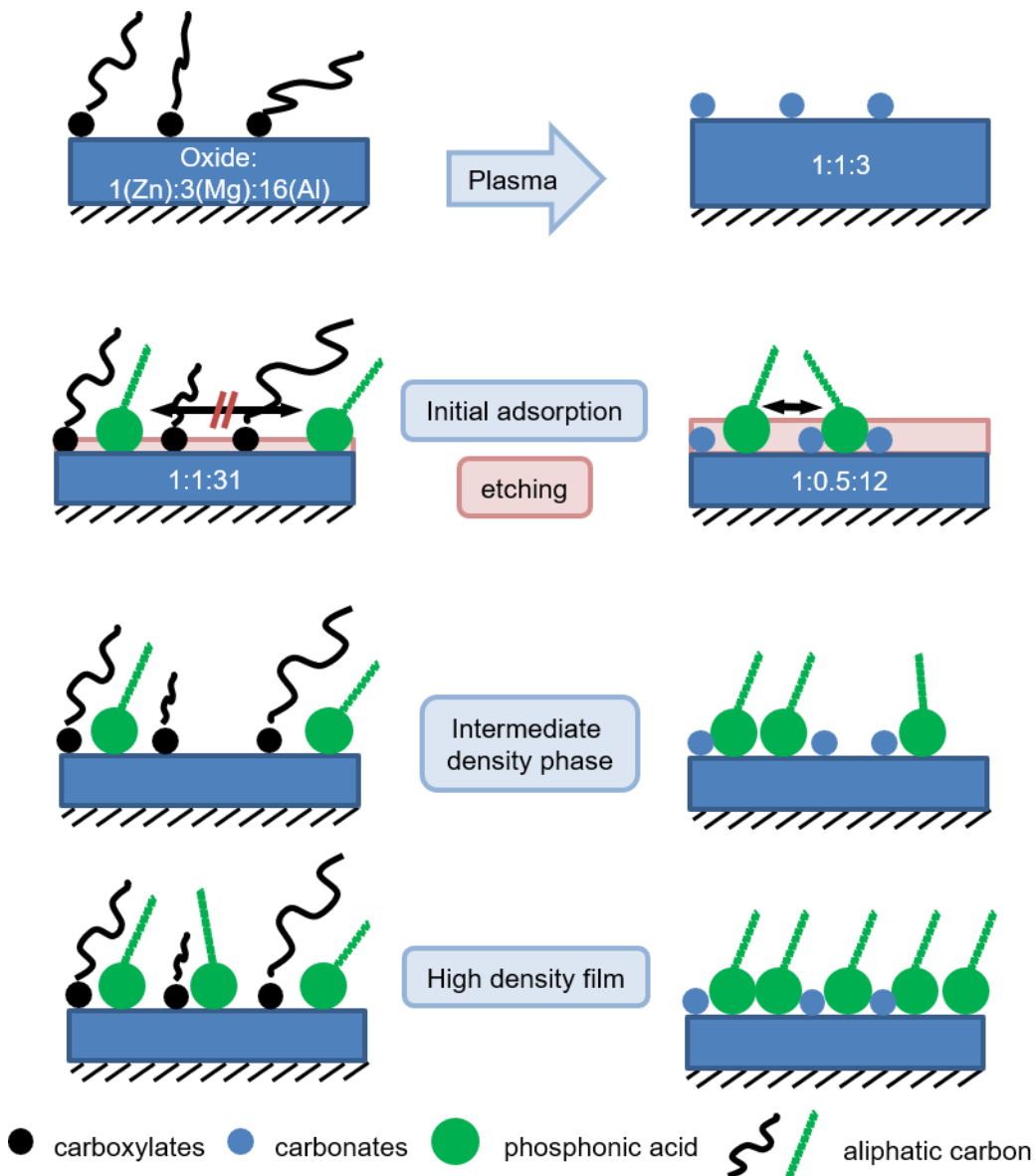


Figure 49: Schematic of the ODPA monolayer formation with and without prior plasma treatment.

Based on the CV results, the pre-treatment with Ar/O₂ and Ar/H₂O led to the highest results. Based on the plasma-induced changes found in chapter 4.1 and the results in chapter 4.2, the effect of the plasma-induced changes on the defect density can be partially explained.

4.2 Influence of dielectric barrier plasma treatment of ZnMgAl alloy-coated steel on the adsorption of organophosphonic acid monolayers

On the untreated surface, the initial adsorption of ODPA and its movement in the intermediate density phase is hindered by the presence of the adventitious absorbed carboxylates. To form a high-density film, the carboxylates must either be replaced by ODPA or incorporated into the high-density film. Due to the uncontrolled aliphatic carbon chain, the incorporation will lead to defects. In comparison, carbonates can act as additional anchor points for the ODPA, neither hindering the initial adsorption nor the movement during the intermediate density phase. In PM-IRRAS, the presence of carboxylates was proven for the untreated surface and Ar/O₂, while carbonates were found in Ar and Ar/H₂O (**Figure 45**). However, Ar/O₂ showed a high density as well in the CV. It has to keep in mind that although Ar/O₂ shows no strong carbonate peak, aliphatic carbon was etched during the plasma. Thus, the aliphatic carbon chain length should be reduced compared to the untreated surface, minimizing the disturbance of the ODPA film.

Additionally, the strong etching of the oxide layer for Ar/O₂ and Ar/H₂O has to be kept in mind. Although the exact nature of the etching cannot be resolved (how can be carboxylates and carbonates be adsorbed on an etched surface?), it is most likely that the etching takes place before or during the initial adsorption. During this process, the formation of a passive layer is possible, which could be beneficial for further film formation.

4.2 Influence of dielectric barrier plasma treatment of ZnMgAl alloy-coated steel on the adsorption of organophosphonic acid monolayers

4.2.3 Conclusions

The surface spectroscopic and electrochemical studies showed that the barrier properties of ODPA monolayers on oxide-covered ZnMgAl-alloy coated steel could be improved by prior atmospheric-pressure plasma treatment (**Figure 50**).

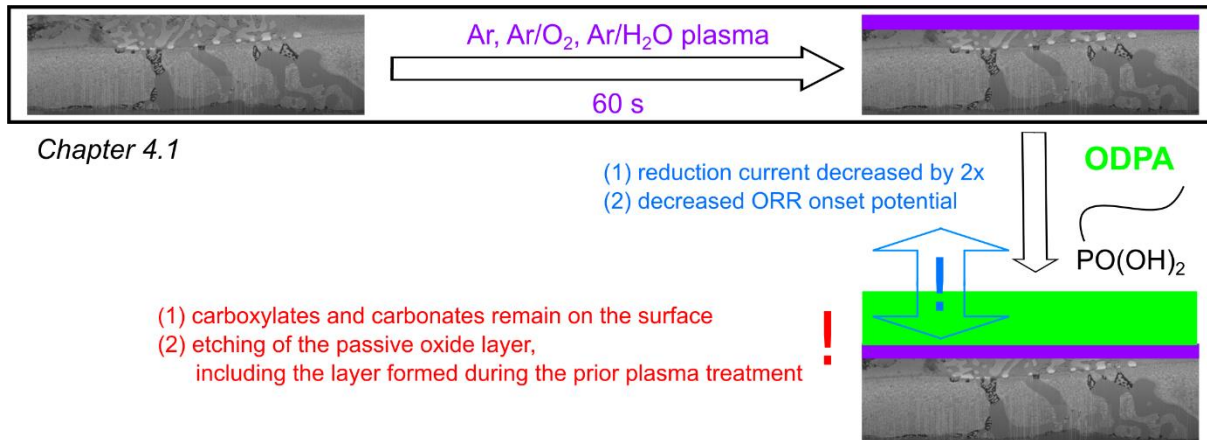


Figure 50: Identified changes on the surface after ODPA adsorption and their influence on the barrier properties of the ODPA film.

The use of different plasma gas mixtures allowed for the correlation of the DBD plasma-induced changes with the adsorption process of ODPA and the structure of these monolayers based on PM-IRRAS and XPS analysis. It was found that metal carboxylates converted to metal carbonates were beneficial for the barrier properties. In parallel to the adsorption process, a partial etching of the passive film was observed. Preferential dissolution of Mg-ions was observed, which indicates that the phosphonic acid groups are mainly bound to Al surface ions. As shown by cyclic voltammetry, all plasma gas mixtures led to improved barrier properties of the ODPA monolayer. However, the oxidative DBD Ar/H₂O and Ar/O₂ plasma pre-treatments showed slight advantages compared to the pure Ar-DBD treatment.

4.3 Reactivity of an argon atmospheric-pressure DBD plasma-activated ZnMgAl alloy with EtOH

4.3 Reactivity of an argon atmospheric-pressure DBD plasma-activated ZnMgAl alloy with EtOH

This chapter introduces the half-side modification of ZnMgAl using Ar as plasma gas and the effect of a post-treatment using EtOH (**Figure 51**). Half-side modifications are a powerful tool to visualize the effect of treatment within one sample, as was shown by Giza et al. when comparing a low-pressure H₂ and O₂ plasma treatment.^[51] Especially for inhomogeneous samples (as was seen for ZnMgAl in chapter 4.1), this method can improve the understanding by highlighting the changes induced due to surface treatments. In chapters 4.1 and 4.2, the plasma treatment using pure Ar showed only slight changes often in the range of the material inhomogeneity. Therefore, this plasma was chosen to produce half-side modified samples.

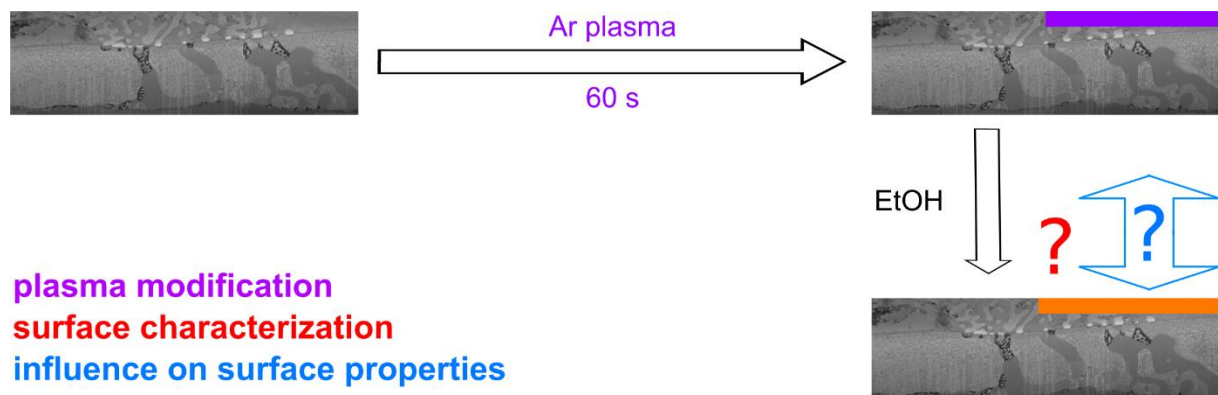


Figure 51: Half-side modification of ZnMgAl in a pure Ar plasma and the effect of a post-treatment using EtOH.

In a second step, the half-side modified sample was rinsed using EtOH directly after the plasma treatment. During prior experiments (e.g., contact angle), changes in the sample behavior were noticed when rinsed with EtOH after the plasma treatment. Additionally, in chapter 4.2, an etching effect was observed in EtOH simultaneously with the adsorption of ODPA. Therefore, the effect of rinsing the sample after the plasma treatment using EtOH was investigated as well on the half-side modified samples.

4.3 Reactivity of an argon atmospheric-pressure DBD plasma-activated ZnMgAl alloy with EtOH

4.3.1 *Experimental approach*

4.3.1.1 *Plasma treatment*

Before the measurement, the ignition voltage for the given electrode-sample distance was determined for each gas mixture. Then, the voltage was set 165 V higher than the ignition voltage for each gas mixture, leading to an applied voltage of 2.9 kV for pure Ar, 3.6 kV for Ar/O₂, and 2.6 kV for Ar/H₂O. The duration of the plasma treatment in all cases was 60 s.

4.3.1.2 *Scanning Kelvin Probe*

Scanning Kelvin Probe line scans were performed at the SKP from Posner using a NiCr tip of approximately 5 mm in normal atmospheric conditions.

4.3.1.3 *90°-peel test under humid conditions*

Peel forces were determined under humid conditions by 90°-peel test measurement for the acrylate adhesive tape (Scotch[®] Magic Tape (3M, Germany)). The application of the adhesive was performed immediately after the respective treatment.

All other modifications and measurements were carried out as described in chapter 3 above.

4.3.2 Results and Discussion

4.3.2.1 Rinsing of the untreated sample with EtOH

First, the effect of rinsing ZnMgAl with EtOH was determined as reference behavior. Therefore, the contact angle and the surface potential were determined after repeatedly rinsing the sample with EtOH. Therefore, two different kinds of experiments were conducted: First, the samples were rinsed with EtOH and subsequently measured by water contact angle. Second, after rinsing with EtOH, a SKP point measurement was performed in the second experiment, and afterward, contact angle measurements using water and DMSO. Thus, the time between washing with EtOH and measuring the contact angles was around 10 minutes longer (time of the SKP measurement) in the case of experiment two. The results are shown in **Figure 52**.

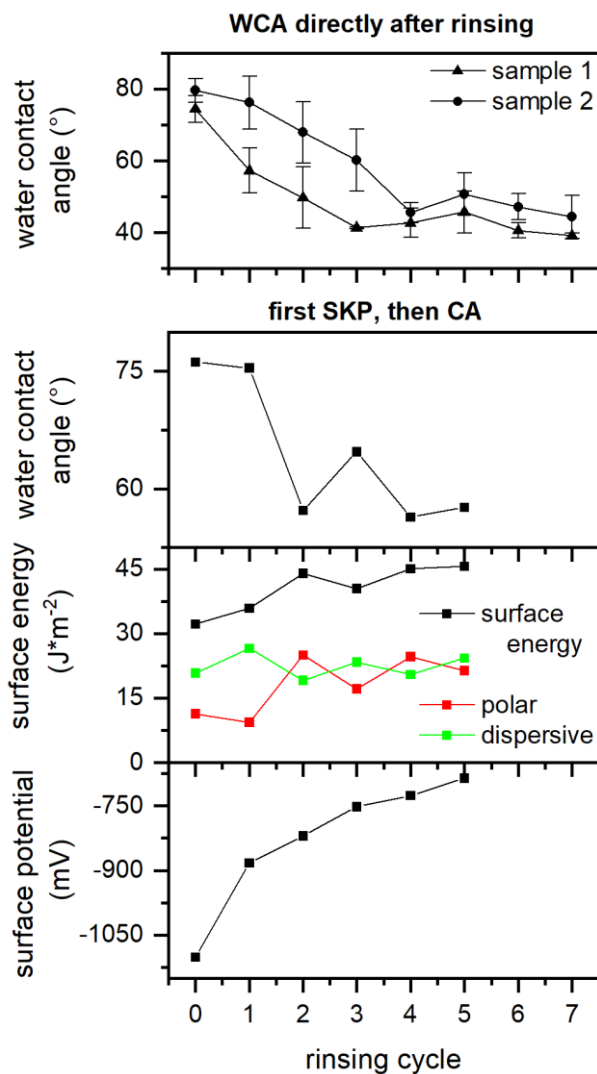


Figure 52: Changes in the surface potential and surface energy after rinsing a solvent cleaned ZnMgAl surface with EtOH. The error bars in the WCA directly after rinsing result from at least three measurements on one sample.

In experiment one, the limitation of cleaning the sample by rinsing with EtOH alone is seen in the contact angle measurements. After 4 cycles of rinsing the samples, the water contact angle measured directly after the rinsing procedure remains around 45°. This is much higher than the contact angle measured in chapter 4.1 after the various plasma treatments (~20°). This demonstrates the efficiency of the plasma treatments compared to pure rinsing. More surprisingly, experiment two reveals that the cleaned surfaces quickly attracted contaminations from the air and regain a higher contact angle in short times. Because

4.3 Reactivity of an argon atmospheric-pressure DBD plasma-activated ZnMgAl alloy with EtOH

SKP was measured first, 10 minutes had passed before measuring water contact angle. However, only contact angles around 55° were reached, showing the fast readsorption of the surface contaminations from the air. When determining the surface energy of the contact angles of water and DMSO, it is seen that the rinsing raised only the polar component while the dispersive component remains steady. The SKP measurements show that already rinsing of the samples had a considerable influence on the surface potential (an increase over 400 mV), revealing the strong impact of surface contaminations on the surface potential.

4.3.2.2 Half-side Ar plasma-treated ZnMgAl

In comparison, the changes after a half-side Ar plasma treatment are shown in **Figure 53**. All measurements were performed as line scans, starting from the untreated (left) to the plasma-treated side (right). After the plasma treatment, first, the surface potential was measured, then the surface energy (water, DMSO), and last the peel force after rinsing the sample with EtOH (acrylate tape).

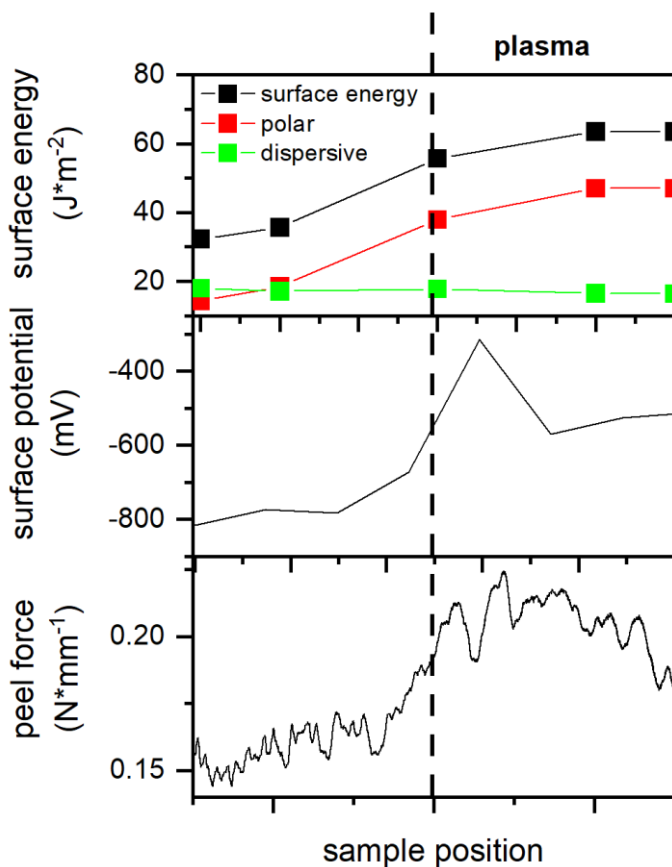


Figure 53: Surface energy, surface potential, and peel force of a half-side plasma treated ZnMgAl sample. Left: not plasma-treated side of the sample, right: plasma-treated side of the sample using Ar as plasma gas.

In all conducted measurements, a difference was seen between the untreated and plasma-treated sides. The surface energy determined from the contact angle measurements (water, DMSO) showed a substantial increase in the total surface energy driven by the polar component while the dispersive component remains steady. Comparing the plasma effect to the rinsing effect evaluated before, the plasma treatment showed a more pronounced increase in the surface energy than the rinsing even after measuring SKP. This hints at the stability of the plasma-induced changes, hindering the readsorption of surface contaminations from the air. The surface potential exhibited an increase in the range of the rinsing, showing that no direct correlation between the surface potential and contact angle exists due to the various influence factors on the surface potential (see chapter 4.1). Following, the increase in the peel-off forces due to the Ar plasma treatment after rinsing with EtOH was observed as well on the half side modified

4.3 Reactivity of an argon atmospheric-pressure DBD plasma-activated ZnMgAl alloy with EtOH

sample. Overall, the results showed that half-side modifications are a versatile method to investigate surface modifications on the inhomogeneous ZnMgAl.

4.3.2.3 Rinsing of the Ar plasma-treated sample with EtOH

Further, the post-treatment of Ar plasma treated ZnMgAl samples using EtOH was evaluated on the half-side modified samples. Therefore, PM-IRRAS before and after each treatment step was performed on the respective sides of one sample (**Figure 54**).

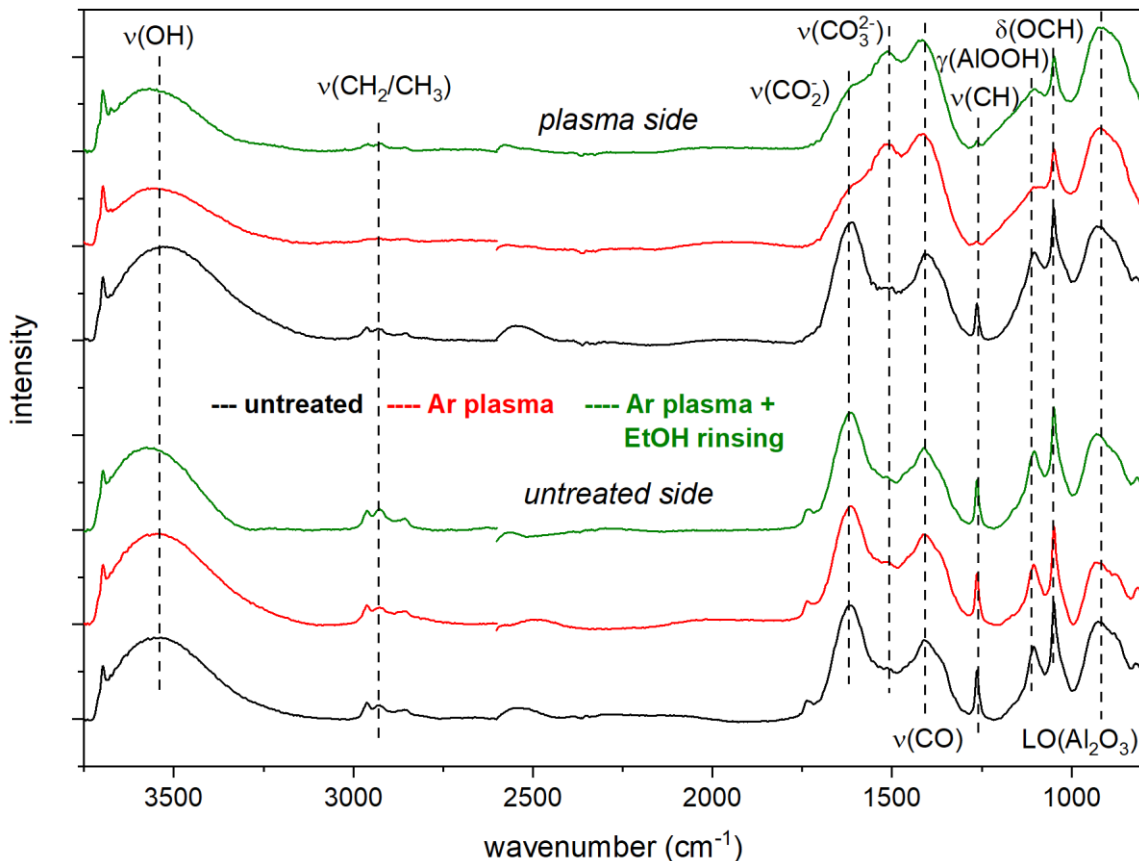


Figure 54: PM-IRRAS of a ZnMgAl sample untreated, after the Ar plasma treatment, and after subsequent rinsing with EtOH.

The untreated side shows no changes after the Ar plasma treatment or after the rinsing with EtOH as expected. On the plasma-treated side, the changes of the Ar plasma treatment seen in chapter 4.1 are confirmed, namely the removal of adventitious carbon and the conversion of carboxylates to carbonates. After the rinsing with EtOH, the carbonates remain on the surface, as already observed after the ODPA adsorption in chapter 4.2. Interestingly, a slight increase in CH_2/CH_3 was observed, which might result from the adsorption of organic contaminations or EtOH.

4.3 Reactivity of an argon atmospheric-pressure DBD plasma-activated ZnMgAl alloy with EtOH

XPS measurements were performed to gain further information on the composition of the surface. The quantification results are presented in **Table 12**.

Table 12: Quantification based on the XPS core-level spectra. The errors are calculated based on the measurement of two samples.

Substrate treatment	Zn 2p 3/2 (at %)	Mg 1s (at %)	Al 2p (at %)	O 1s (at %)	C 1s (at %)	Zn:Mg:Al
Reference (solvent cleaned)	0.9 ± 0.3	2.2 ± 0.4	12.3 ± 1.8	41.3 ± 2.8	43.3 ± 2.7	1 : 2.7 : 16.3
Ar plasma treatment	1.6 ± 0.4	5.3 ± 0.2	15.7 ± 0.7	58.1 ± 1.0	19.3 ± 3.5	1 : 3.5 : 10.6
Ar plasma treatment + rinsing with EtOH	1.2 ± 0.6	2.3 ± 0.2	10.5 ± 2.3	42.2 ± 2.3	43.8 ± 2.2	1 : 1.9 : 8.8

After the rinsing with EtOH, the amount of carbon was increased significantly, similar to the value before the plasma treatment. This observation is in agreement with the PM-IRRAS results (increase in CH_2). Interestingly, a change in the metal ratios similar to chapter 4.2 after the ODPA adsorption was observed. Here, mainly Mg was removed from the surface. To check if the change was again caused by etching, the Zn LMM was investigated (**Figure 55**).

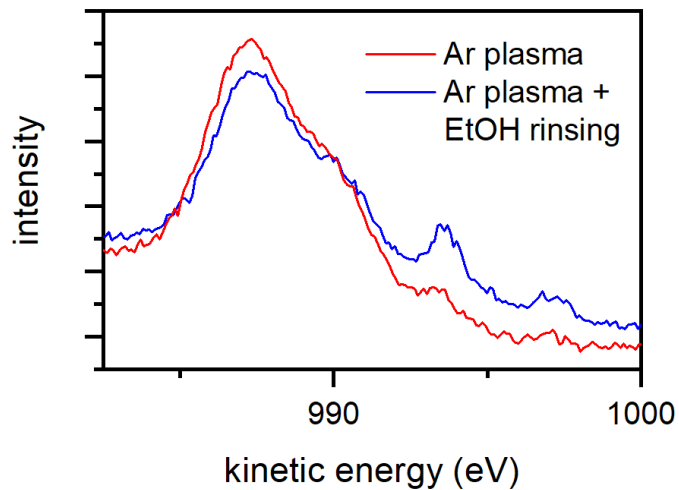


Figure 55: Zn LMM after Ar plasma treatment and after subsequent rinsing with EtOH.

Indeed, the etching was confirmed by a slight increase in the metallic component after the EtOH rinsing. Thus, the etching seen in chapter 4.2 was not only a result of the acid ODPA but is already caused by the EtOH. Two different processes might explain the etching behavior: (i) Either, the plasma-induced changes of Mg were mechanically highly unstable and thus removed by the mechanical impact of the rinsing (ii) or, the plasma-treated surface was highly reactive directly after the plasma treatment, being able to oxidize the EtOH to ethanoic acid. Thus, the ethanolic acid introduced an acid environment on the surface, inducing the etching on the surface and promoting the ethanoic acid's adsorption on the surface.

4.3 Reactivity of an argon atmospheric-pressure DBD plasma-activated ZnMgAl alloy with EtOH

Furthermore, SKP line scans were performed on the half-side modified samples and are displayed in **Figure 56**.

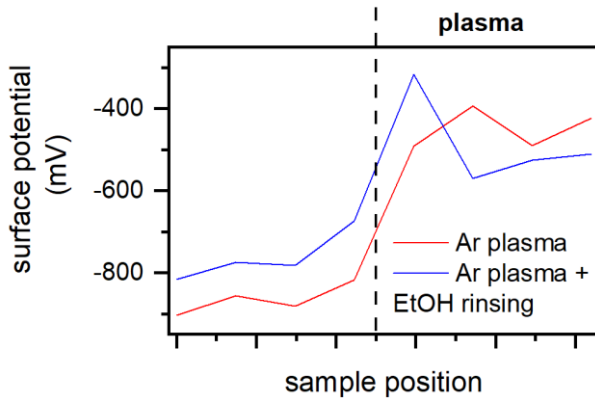


Figure 56: SKP line scans after Ar plasma treatment and after subsequent rinsing with EtOH.

On the untreated side, the increase in the surface potential was similar to the cleaning effect observed after one rinsing cycle. However, on the plasma-treated side, the potential was slightly lower, either due to the decrease in the oxide layer thickness, the adsorption of organic components on the surface, or both.

Last, the peel force with an acrylate tape and the wetting behavior were investigated at the untreated surface, the Ar plasma-treated surface, and after rinsing the Ar plasma-treated surface with EtOH (**Figure 57**).

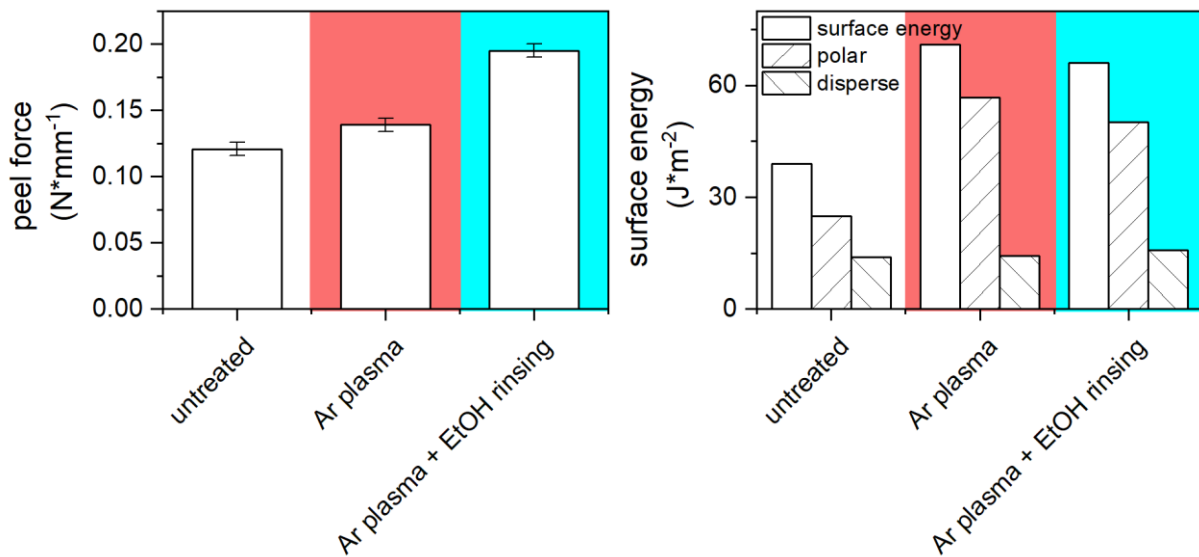


Figure 57: Peel force (left) and surface energy (right) of the untreated sample side, after Ar plasma and after subsequent rinsing using EtOH.

The surface energy decreased after rinsing with EtOH, which can be assigned to the adsorption of organic contaminations observed with PM-IRRAS and XPS. Again, the driving force of the changes in the surface energy was the polar component, while the dispersive part remained unchanged.

Interestingly, the peel force increased significantly after the rinsing with EtOH. Multiple hypotheses could explain this increase: (i) the change in the metal ratios seen in the XPS could allow more favorable binding. (ii) rinsing with EtOH could remove loosely bound plasma products, eliminating a starting point for the failure of the adhesive. (iii) the etching could increase the roughness of the surface, increasing the adhesive/surface area and thus the peel force.

4.3 Reactivity of an argon atmospheric-pressure DBD plasma-activated ZnMgAl alloy with EtOH

4.3.3 Conclusions

The half-side Ar plasma modification could be successfully applied to ZnMgAl, highlighting the changes in the surface potential, the surface energy, and the peel force (**Figure 58**). Furthermore, the effect of subsequently rinsing with Ethanol was investigated. It was found that already the rinsing with EtOH led to increased adsorption of organic components and etching, especially of Mg. The experiments showed that the etching in chapter 4.2 was not only a result of the ODPA but the EtOH as well. While the rinsing with EtOH decreased the surface energy (but still higher than the untreated sample), the peel force was significantly increased. This might either be explained by removing loosely bound plasma products or an increased roughness after the etching. On the one hand, this demonstrated a possible instability of the plasma products after the surface. On the other hand, it introduces a simple method to alter the surface in a beneficial way after the plasma treatment.

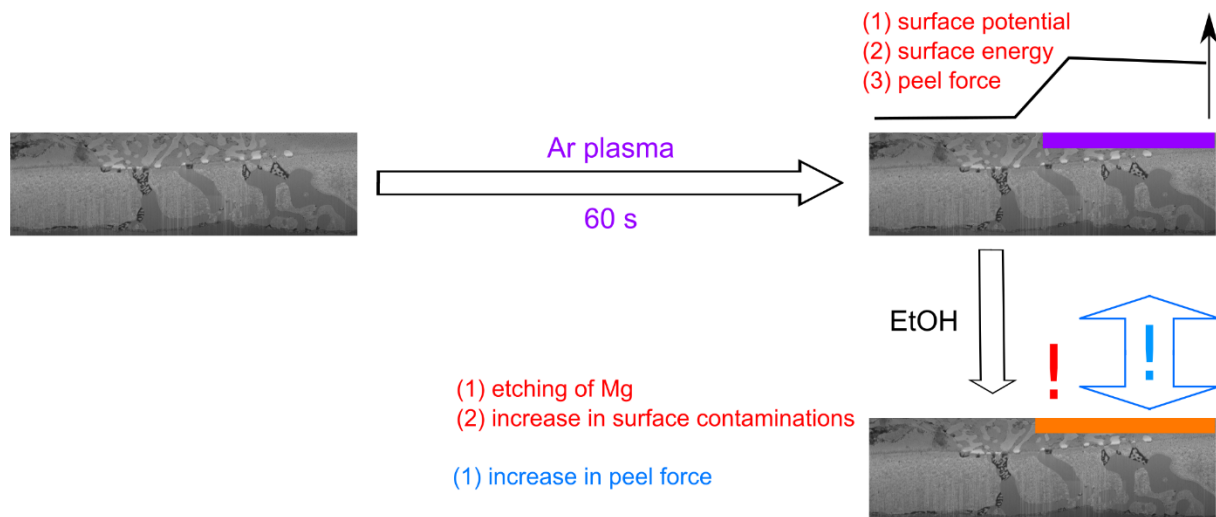


Figure 58: Successfully applied methods to distinguish changes after the Ar plasma treatment on a half-side modified sample and the effects observed after rinsing the half-side modified sample with EtOH.

4.4 Influence of short-time Ar/H₂O atmospheric-pressure DBD plasma treatments on the ZnMgAl surface

4.4 Influence of short-time Ar/H₂O atmospheric-pressure DBD plasma treatments on the ZnMgAl surface

In chapters 4.1 and 4.2, the plasma treatment using Ar/H₂O as plasma gas showed the most promising results in all adsorption-related properties (WCA and peel-off force). However, all experiments before were performed using 60 s plasma treatment times, which is too long for in-line process times (typically 5 s and faster). Therefore, shorter plasma times (5 s, 10 s, and 15 s) were carried out using Ar/H₂O as plasma gas, and the surface state was monitored by DPM-IRRAS, KP, and XPS (**Figure 59**). To evaluate the wetting behavior of the plasma-treated material, the water contact angles were measured. Additionally, the corrosion behavior was investigated by electrochemistry (electrical impedance spectroscopy (EIS) and linear sweep voltammetry (LSV)) here.

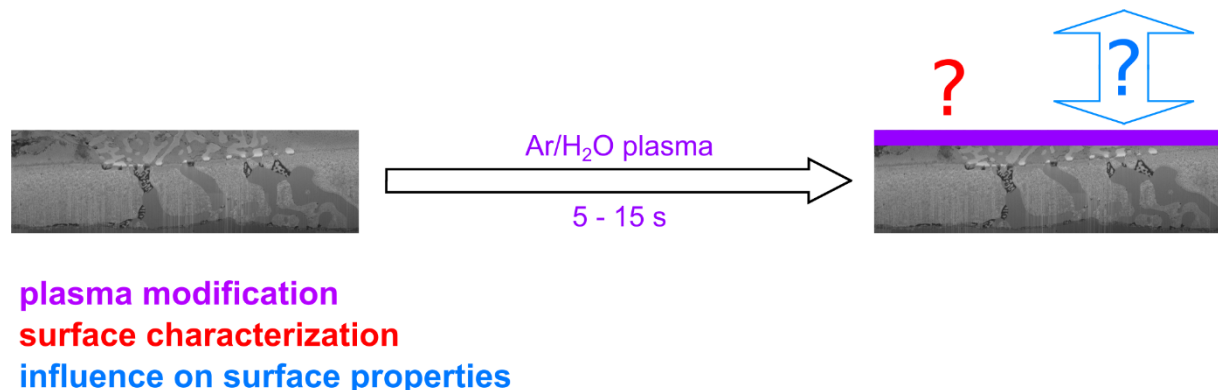


Figure 59: Investigating the time dependence of an Ar/H₂O plasma treatment on ZnMgAl.

4.4 Influence of short-time Ar/H₂O atmospheric-pressure DBD plasma treatments on the ZnMgAl surface

4.4.1 Experimental approach

4.4.1.1 Plasma treatment

Before the measurement, the ignition voltage for the given electrode-sample distance was determined for each gas mixture. Then, the voltage was set 165 V higher than the ignition voltage for each gas mixture, leading to an applied voltage of 2.9 kV for pure Ar, 3.6 kV for Ar/O₂, and 2.6 kV for Ar/H₂O. The duration of the plasma treatment in all cases was 60 s.

All modifications and measurements were carried out as described in previous chapter 3.

4.4.2 Results and Discussion

4.4.2.1 Time dependence of surface modifications

Similar to chapter 4.1, the surface composition was investigated in-situ by DPM-IRRAS and ex-situ by XPS. The DPM-IRRAS spectra after 5 s presented in **Figure 60** already exhibited the same shape as in chapter 4.1 after 60 s plasma treatment, showing mainly the conversion of carboxylates to carbonates. Longer treatment times led only to a slight increase in the carbonate intensity. Thus, the conversion of carboxylates to carbonates mainly takes part within the first 5 s of the plasma treatment, underlining its high capability for fast surface modifications. Interestingly, the peak related to the LO(Al₂O₃) significantly increased after 15 s plasma treatment. These results indicate a stepwise modification of the ZnMgAl.

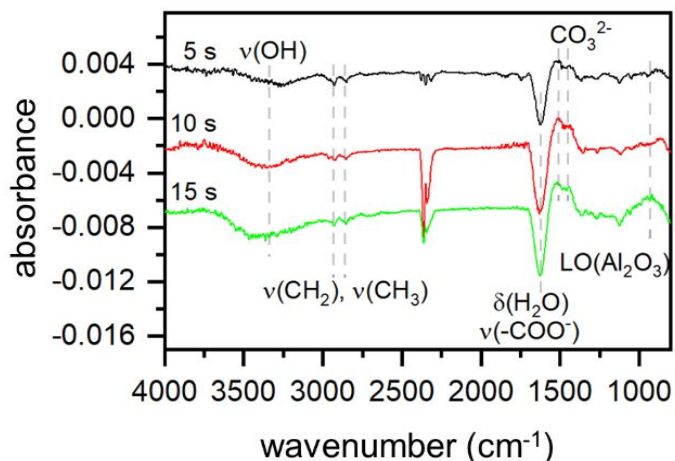


Figure 60: DPM-IRRAS after different Ar/H₂O plasma treatment times.

4.4 Influence of short-time Ar/H₂O atmospheric-pressure DBD plasma treatments on the ZnMgAl surface

For a more detailed analysis, ex-situ XPS was measured. In **Table 13**, the XPS quantification based on core-level spectra is presented.

Table 13: XPS quantification based on the core-level spectra. The errors are the result of different measurements on two samples. The ratio of the metals was normalized to the Zn concentration, where the values in brackets display the highest and lowest ratio determined, taking into account the standard variation of the concentrations.

Plasma duration (s)	C 1s (at %)	O 1s (at %)	Zn 2p 3/2 (at %)	Mg 1s (at %)	Al 2p (at %)	Zn (low) Mg (high) (low) Al (high)
0	39.3 ± 4.5	48.1 ± 6.5	1.1 ± 0.4	1.7 ± 0.4	9.9 ± 2.0	1 (0.9) 1.5 (3.0) (5.3) 9.0 (17)
5	32.2 ± 4.1	49.2 ± 2.2	1.8 ± 0.8	3.6 ± 0.5	13.4 ± 2.2	1 (1.2) 2.0 (4.1) (4.3) 7.6 (15.6)
10	33.5 ± 2.7	48.3 ± 1.4	1.4 ± 0.6	2.9 ± 0.4	14.0 ± 1.5	1 (1.3) 2.0 (4.1) (6.3) 10.0 (19.4)
15	33.4 ± 3.0	48.8 ± 1.7	2.6 ± 0.4	3.3 ± 0.1	12.0 ± 1.6	1 (1.1) 1.2 (1.5) (3.5) 4.6 (6.2)
60 (chapter 4.1)	26.8 ± 1.3	54.7 ± 1.1	3.5 ± 0.3	4.6 ± 0.6	10.6 ± 0.7	1 (1.1) 1.3 (1.6) (2.6) 3.0 (3.5)

The plasma treatment removed carbon from the surface and changed the metal ratios, as already known from chapter 4.1. Interestingly, the metal ratios showed no linear change with time (**Table 13**): After 5 s plasma treatment, Zn and Mg were slightly increased, while after 10 s Al was enriched on the surface with a stable Mg:Zn ratio. After 15 s, the Al content was again decreased by an increase in Zn and Mg. When comparing the results after 15 s to the plasma treatment after 60 s from chapter 4.1, the metal ratios (including their range) are already quite similar. This shows that the migration of metals immediately took place, exhibiting a very fast process, and might be finished within the first 20 s. Furthermore, the carbon concentration immediately decreased after 5 s, but afterward was relatively stable up to 15 s. However, after 60 s plasma treatment, a more considerable amount of carbon was removed. This indicates that some of the carbon (either adventitious carbon species or carbon-related plasma products) might exhibit a certain time-dependent resistance (>15 s) to the plasma treatment.

4.4 Influence of short-time Ar/H₂O atmospheric-pressure DBD plasma treatments on the ZnMgAl surface

As already described in chapter 4.1, the carbonate concentration and the oxide thicknesses of Al and Zn were determined from the respective core-level spectra and are displayed in **Figure 61**.

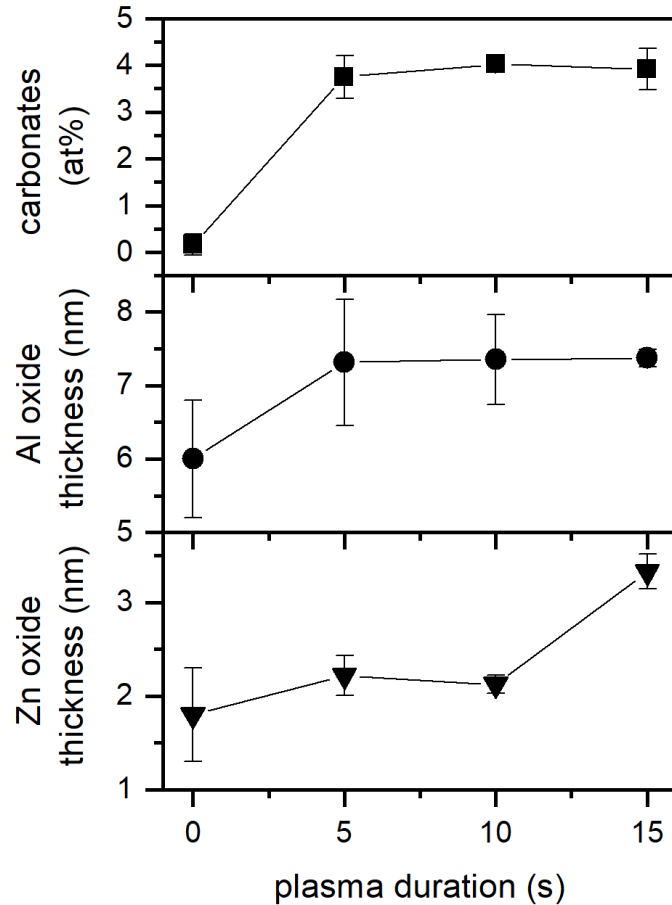


Figure 61: Influence of different plasma treatment times on the amount of carbonates on the ZnMgAl surface Al oxide layer thickness, and Zn oxide layer thickness determined from the respective XPS core-level spectra.

The evolution of carbonates seen in the DPM-IRRAS was confirmed by the XPS quantification, showing an increase after 5 s and afterward a stable concentration. This behavior is also observed for the Al oxide layer thickness. In comparison, the oxide thickness of Zn remains unchanged during the first 10 s plasma treatment but was sharply increased after 15 s. Taken all results into considerations, a step-wise modification of the ZnMgAl surface gets obvious: Within the first 5 s, carboxylates were converted to carbonates, and the Al oxide layer thickness was increased. This was accompanied by the migration of Zn and Mg to the surface. In the following 5 s, Al migrated to the surface. After an additional 5 s, an increase in the Zn oxide layer thickness accompanied by the migration of Zn and Mg to the surface was observed. This evolution might be explained by taking the reason for the metal migration into account: Metal migration is observed in many metal alloys, such as Au/Fe, Au/Ni, and Au/Co systems.^[163] In these examples, the migration is induced by a potential sink created by the oxidation of the respective metal on the surface (Fe, Ni, and Co diffuse through the resistant Au film). Thus, the migration observed after the plasma treatments is likely due to oxidative processes on the surface. In **Figure 61**, after 5 s the oxidation of Al was seen, while Al₂O₃ and the oxidation of Zn were only observed after 15 s. Thus, the oxidation of Al after 5 s is likely linked to the created carbonates. Resulting, the following mechanism is proposed: The plasma led to the conversion of adsorbed carboxylates to metal carbonates (mainly based on Al) on the surface. This conversion created a potential sink, leading to the migration of metals within the first 10 s. Thereby, Mg and Zn migrate more easily through the material than Al, maybe due to the higher number of Zn and Mg-containing phases in the bulk material (Zn, ZnMg₂, ZnMgAl) than that of Al (ZnMgAl). When the

4.4 Influence of short-time Ar/H₂O atmospheric-pressure DBD plasma treatments on the ZnMgAl surface

Al finally migrated to the surface, all carboxylates were already converted, and instead, the respective metal oxides were created, leading to a new potential sink and following migration. When the oxide layer reached a certain thickness, the surface was passivated, and the migration stopped. Taking into account the similar results after 15 s and 60 s, this might already be the case after 20 s.

In-situ KP was measured to determine the change in the surface potential after the plasma treatment. The results are presented in **Figure 62**.

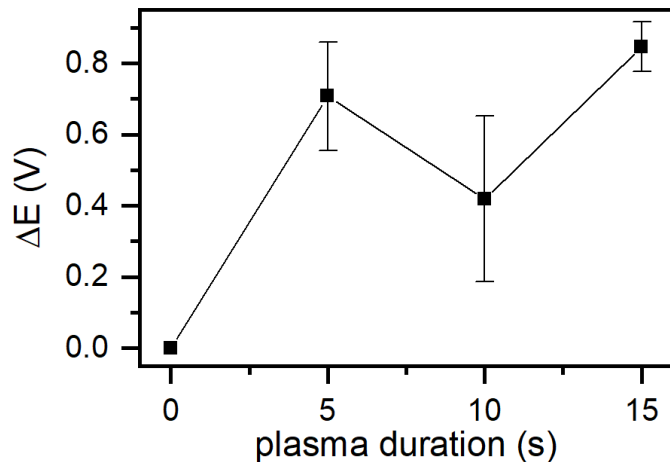


Figure 62: Differences in the surface potential before and after different Ar/H₂O plasma treatment times measured in-situ with the KP on ZnMgAl.

Although no linear trend was observed, a general trend to positive surface potentials compared to the untreated sample is evident. As already described in chapter 4.1, multiple factors influence the surface potential:

- (i) When adsorbed adventitious carbon and water are removed from the surface, the distribution of surface dipoles changes, with the corresponding effect on the surface potential (χ_{ox}). Taheri et al. investigated the adsorbed layer on Zn-surfaces and showed that adsorption of contamination on the surface shifted the potential to more positive values.^[111] Thus, the removal of surface contaminations should result in a negative shift in the surface potential.
- (ii) Absorbed carboxylates form a strong dipole at the surface and therefore strongly influence the surface potential (χ_{ox}).^{[111],[112]} At the same time, the intrinsic dipole moment of carboxylates attached with an aliphatic tail orientated away from the surface is zero and does not contribute to the overall potential drop in the adsorbate layer.^{[111],[112]} Changes in the structure of the carboxylates lead to a change in the intrinsic dipole moment different than zero and therefore change the overall potential. Consequently, the conversion from carboxylates to carbonates influences the dipole moment at the surface as well as the intrinsic dipole moment of the adsorbate layer.
- (iii) The migration of the metals can influence the potential difference between the metal and the oxide ($\Delta\phi_{ox}^{Me}$) when new boundaries are formed. Due to the complex structure of the oxide/metal interface, the influence of the migration cannot be assessed.
- (iv) A growth in the oxide layer thickness leads to a positive shift of the potential drop over the oxide layer ($\Delta\phi_{ox}$).^{[108],[110]}

Considering the step-wise processes identified in DPM-IRRAS and XPS, the initial positive shift can be accounted to the increase in the oxide layer thickness of aluminum and the conversion of carboxylate to

4.4 Influence of short-time Ar/H₂O atmospheric-pressure DBD plasma treatments on the ZnMgAl surface

carbonates. Likewise, the positive shift after 15 s can be assigned to the increased Zn oxide layer thickness. The decrease in the surface potential might be caused by the migration of Al to the surface.

4.4.2.2 Wettability and corrosion properties

The wettability of the surface was accessed by water contact angle measurements and is presented in **Figure 63**.

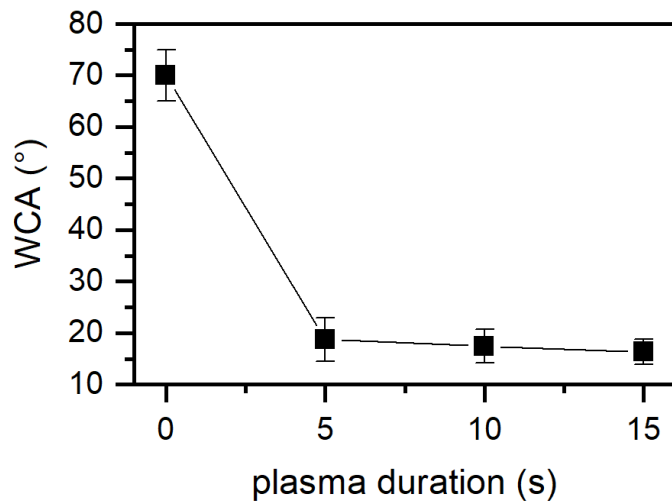


Figure 63: Water contact angle before and after different Ar/H₂O plasma treatment times.

The water contact angle was significantly reduced after the 5 s plasma treatment. Increasing the plasma treatment time did not significantly reduce the water contact angle further. This trend correlates with the evolution of carbonates and shows that the wettability is mainly determined by the adsorbed layer rather than the metal composition of the surface. The contact angle measurements show the high capability of the plasma treatment to achieve high wettability in short treatment times, making it suitable for in-line processes.^[10]

4.4 Influence of short-time Ar/H₂O atmospheric-pressure DBD plasma treatments on the ZnMgAl surface

Last, the corrosion properties of the plasma-treated ZnMgAl surface were determined by LSV and EIS measurements. The respective LSV curves are shown in **Figure 64**.

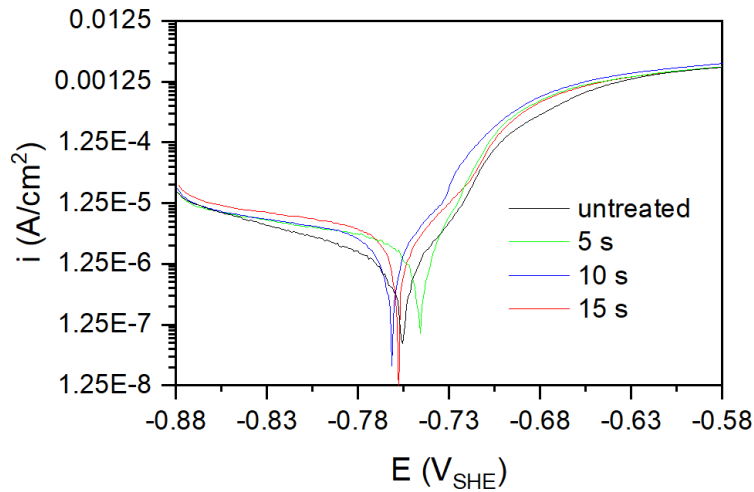


Figure 64: LSV polarization curves of ZnMgAl samples in borate buffer before and after different Ar/H₂O plasma treatment times.

ZnMgAl is known to exhibit superior corrosion behavior compared to Zn and ZnAl alloys.^{[17],[18]} The corrosion current and potential were gained from the LSV measurements by determining the intersection of tangents of the linear area of the LSV plot.

4.4 Influence of short-time Ar/H₂O atmospheric-pressure DBD plasma treatments on the ZnMgAl surface

The maximal impedance was determined from the EIS plot. The results are presented in **Figure 65**.

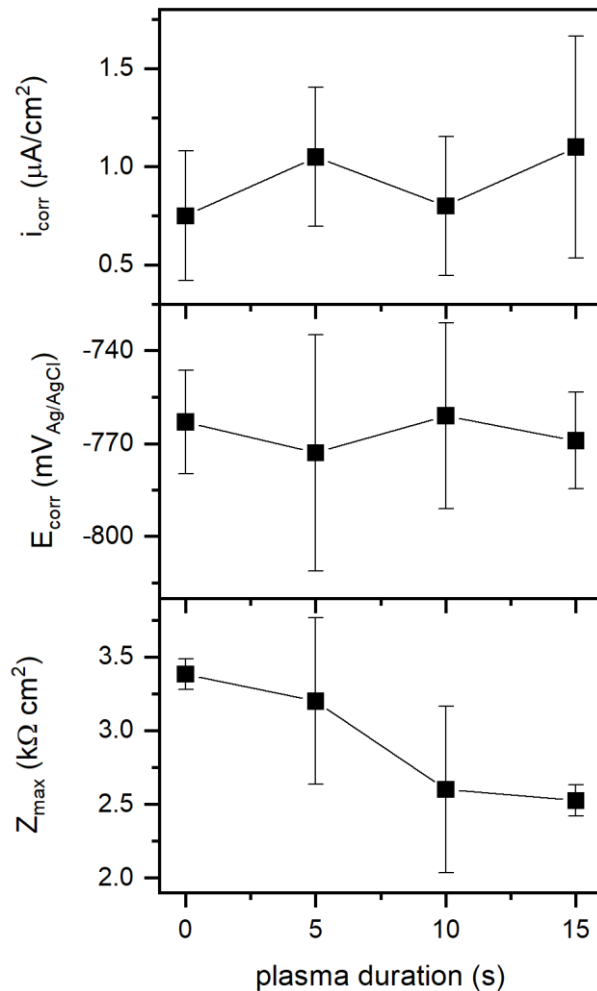


Figure 65: Corrosion current (i_{corr}), corrosion potential (E_{corr}), and maximal impedance dependent (Z_{max}) before and after different Ar/H₂O plasma treatment times.

The plasma treatment had no significant influence on the LSV measurement, showing a stable corrosion current and potential, where the corrosion current is proportional to the corrosion rate.^[164] The decrease in the maximal impedance was explained by the removal of the carboxylates, which formed an additional resistance on the surface due to their aliphatic tail. During the conversion to carbonates, the aliphatic tail was lost, and subsequently, the impedance decreased. It is to note that the increase in the oxide layer did not influence the electrochemical corrosion behavior, most likely due to their low dimension (<10 nm). Although no increase in the corrosion properties was noticed, it has to be kept in mind that ZnMgAl is already a high corrosion resistance material. Therefore, the plasma treatment led to a highly wettable, corrosion-resistant surface.

4.4 Influence of short-time Ar/H₂O atmospheric-pressure DBD plasma treatments on the ZnMgAl surface

4.4.3 Conclusions

The time dependence of the Ar/H₂O plasma treatment of ZnMgAl was investigated for short treatment times (**Figure 66**). It was found that within the first 5 seconds, nearly all carboxylates were converted to carbonates. Additionally, the Al oxide layer grew to its maximum, which might be the result of metal carbonates. This growth was accompanied by the migration of Zn and Mg to the surface. After 10 s, only the migration of Al was detected, while after 15 s, an increase in the Zn oxide layer and the formation of Al₂O₃ were observed. Thereby, Mg and Zn were again migrating to the surface, showing a nonlinear behavior of the migration.

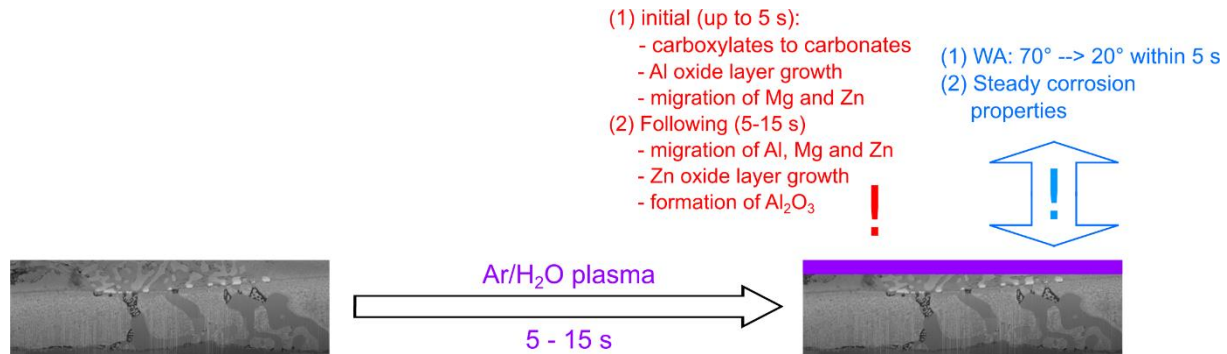


Figure 66: Time dependence observed after different Ar/H₂O plasma treatment times on ZnMgAl and their influence on the wetting and corrosion behavior.

Furthermore, the wetting of the plasma-treated surface and its corrosion properties were investigated by contact angle and electrochemistry. The wetting behavior was seen to be maximally improved after 5 s, relating the wetting behavior to the adsorption layer (carbonates) rather than the composition of the metal surface. The plasma treatment showed no influence on the corrosion properties determined by LSV measurements and a slight decrease in the maximal impedance determined by EIS. Thus, a highly wettable surface with high corrosion resistance was achieved in times suitable for in-line processing.

4.4 Influence of short-time Ar/H₂O atmospheric-pressure DBD plasma treatments on the ZnMgAl surface

4.5 In-situ backside Raman investigation of zinc oxide nanorods in an atmospheric-pressure dielectric barrier discharge plasma

As was seen in the chapters before, even thoroughly ex-situ characterization methods are insufficient to resolve exact mechanisms at the plasma/surface interface. Therefore, in-situ and real-time methods are of high interest in the field of plasma surface modifications. Because the necessary plasma geometry (the small gap between both electrodes of 1 or 2 mm) and disturbances by the plasma (e.g., UV radiation) hamper the monitoring of surfaces in direct contact with the plasma (as is present in chapter 4.1 till 4.4), new and innovative setups had to be developed. In the following, one setup is called “backside setup”. A considerable advantage of the developed setup is its excellent combination potential with different characterization methods (e.g., Raman, DRIFTS).

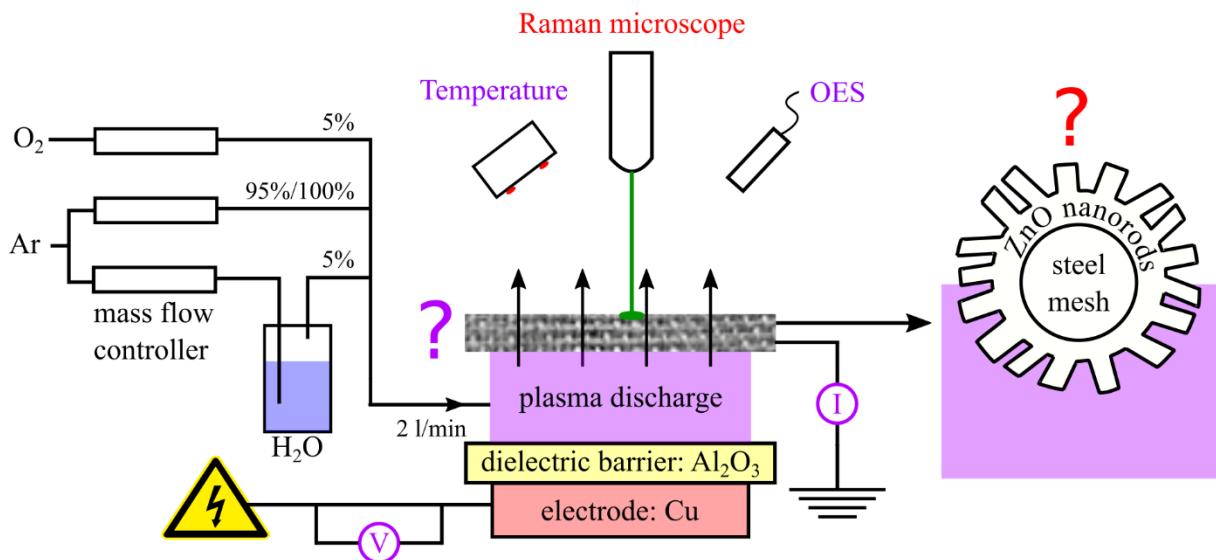


Figure 67: Plasma characterization and in-situ monitoring of the indirect plasma interactions with ZnO nanorods using the backside setup combined with Raman measurements.

The idea of the backside setup is the following: The plasma is ignited between the conventional high voltage side and a porous substrate as a ground electrode (Figure 67). The porous electrode allows the plasma effluent to penetrate and, on its way, modify the membrane's surface. Thus, the setup geometry limits the plasma/surface interaction to the plasma effluent, allowing to determine the impact of long-living plasma-produced species on the surface. Thereby, additional effects of the plasma such as radiation and electrons, including synergistic effects, are neglected. Furthermore, the results gained by the backside setup are of great interest for plasma jets and similar devices, which are based on the plasma effluent rather than the direct contact with the plasma. It was recently shown that results gained in one plasma setup can be transferred to another plasma setup: At a more fundamental study, Budde et al. followed the decomposition of poly(propylene) using in-situ FTIR regarding the synergistic effects of Ar-ions and UV radiation.^[23] They found that the combination of UV radiation and Ar-ions led to a higher graphitization probability and proposed a decomposition model. Recently, this model was validated in an inductively coupled plasma setup by ellipsometry.^[24] Thus, separating different plasma-related effects can lead to a deeper understanding of the overall plasma process and afterward be transferred to different and more complex plasma systems.

Although the plasma-induced surface modifications are the motivation of the carried-out work, the characterization of the plasma properties is of high relevance: On the one hand, the plasma properties determine the plasma/surface interaction. Without knowing the plasma properties, the observed plasma-induced changes cannot be adequately explained. On the other hand, the plasma properties have to be

4.5 In-situ backside Raman investigation of zinc oxide nanorods in an atmospheric-pressure dielectric barrier discharge plasma

known to transfer the results to different setups and conditions. Therefore, the setup was characterized regarding the mesh temperature, its average dissipated power per half cycle, and its reactive species by OES (**Figure 67**).

The results gained by the plasma characterization are then correlated to the indirect plasma treatment of ZnO nanorods investigated in the backside setup using Raman spectroscopy (**Figure 67**). Raman spectroscopy is a powerful tool for investigating inorganic oxides, which are interesting materials for various applications such as electronics, sensors, and energy conversion.^{[25],[165],[166]} In-situ Raman spectroscopy can monitor the surface state during the plasma treatment, leading to a deeper understanding of the surface/plasma interactions. ZnO is a material of broad interest as a stable, low toxic semi-conductor.^[25] In particular, the synthesis of diverse ZnO nanostructures has attracted significant attention due to their tunability in shape and properties, enabling application in nanodevices, e.g., as field-effect transistor^[62] or adhesion-promoting particles in hybrid films^[167]. In nanostructures, crystallinity is of great importance, determining the material's growth direction and overall properties. Plasma treatments have been shown to be able to improve the electrical properties of ZnO thin films^[43], the adhesive properties of ZnO nanowires^[44], and even the corrosion properties of ZnO nanorods^[45]. It is understood that defects are introduced by the plasma, which in turn changes the semiconducting properties of the film.^{[43],[46]} Therefore, if defect type and density can be modified, the functional properties can be tuned to the respective application. As was seen in chapter 4.1 and chapter 4.2, the plasma gas composition was seen to play a central role in determining the nature of the plasma/surface interaction.

Thus, the indirect plasma treatment of ZnO nanorods was investigated as a function of the plasma gas composition by Raman spectroscopy in the novel backside plasma setup. Thereby, the results gained in-situ are compared to XPS results and Raman measurements after one month of storage. The Raman-related part of this chapter is adopted from reference ^[131] with permission of the Journal of Raman spectroscopy and can be found at <https://analyticalsciencejournals.onlinelibrary.wiley.com/doi/10.1002/jrs.6123>.

4.5.1 Experimental approach

4.5.1.1 Plasma treatment

The high voltage was produced by a G2000 high voltage generator (Redline, Germany) and was set to 5.3 kV for all plasma gas mixtures using a frequency of 35 kHz.

All other modifications and measurements were carried out as described in chapter 3.

4.5 In-situ backside Raman investigation of zinc oxide nanorods in an atmospheric-pressure dielectric barrier discharge plasma

4.5.2 Results and Discussion

The successful deposition was confirmed by FE-SEM images, as seen in **Figure 68**, showing a typical nanorod structure with a width of $150 \text{ nm} \pm 50 \text{ nm}$. In addition, FE-SEM cross-sectional analysis revealed a complete coverage of the steel surface and an average nanorod length of $657.5 \text{ nm} \pm 108 \text{ nm}$.

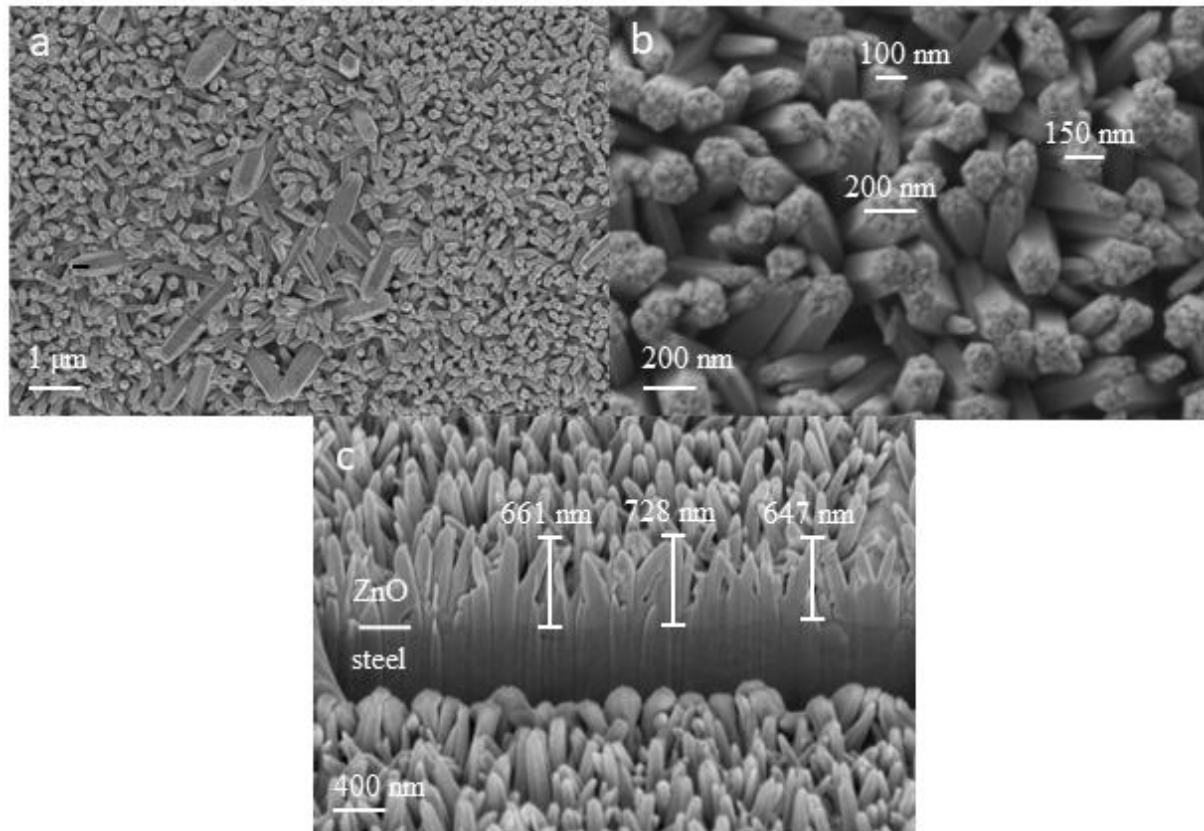


Figure 68: a) FE-SEM image of the ZnO-NR coated steel mesh at a magnification of 10 000x. b) FE-SEM image of the ZnO-NR coated steel mesh at a magnification of 50 000x. The width of some nanorods is marked. c) SEM cross-section of the ZnO-NR coated mesh showing three different nanorod lengths.^[131]

4.5 In-situ backside Raman investigation of zinc oxide nanorods in an atmospheric-pressure dielectric barrier discharge plasma

4.5.2.1 Characterization of the plasma

The temperature of the mesh measured in-situ using an infrared thermometer is displayed in **Figure 69**. The plasma was ignited at 0 s and was running for 600 s. The measurement started 600 s before the measurement and was continued for another 600 s after the plasma was turned off.

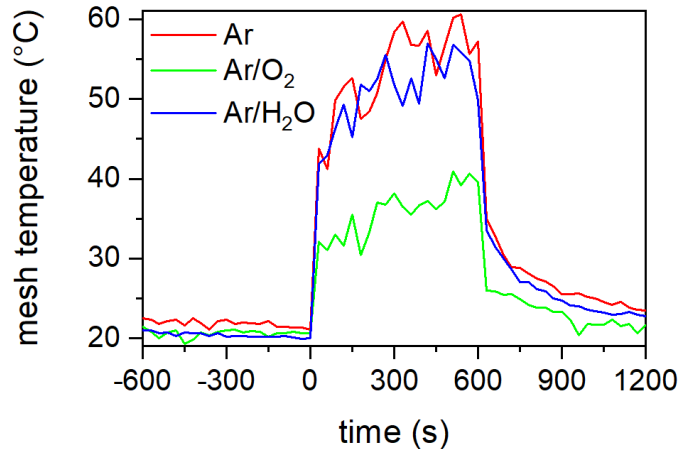


Figure 69: In-situ measurement of the temperature at the ZnO-coated mesh for the respective plasma gas mixture.

It is seen that all plasmas led to an increase in the mesh temperature, whereby the addition of Ar/O₂ reduced the temperature increase. When the plasma was turned on, the temperature immediately showed a strong temperature increase. During the plasma treatment, the temperature slowly increased further. After the plasma is turned off, the temperature immediately dropped and subsequently slowly decreased towards room temperature. This could be due to the good thermal conductivity of the steel mesh, allowing an immediate contact cooling by the remaining setup. However, it could also be a result of intrusions created by plasma radiation. Nonetheless, the bare hand could also feel a significant increase when touching the plasma setup after the plasma. The temperature growth at the end of the plasma and directly after that are presented in **Table 14**. For other DBD setups, temperature increases measured ex-situ range from 25 °C (measured at a metal electrode after 300 s)^[168] to 94 °C (measured at the dielectric barrier after 2700 s).^[169] Thus, the temperature measured here is in good agreement with the literature.

4.5 In-situ backside Raman investigation of zinc oxide nanorods in an atmospheric-pressure dielectric barrier discharge plasma

The plasma voltage and current were monitored to determine the average dissipated power per full cycle and are displayed in **Figure 70**.

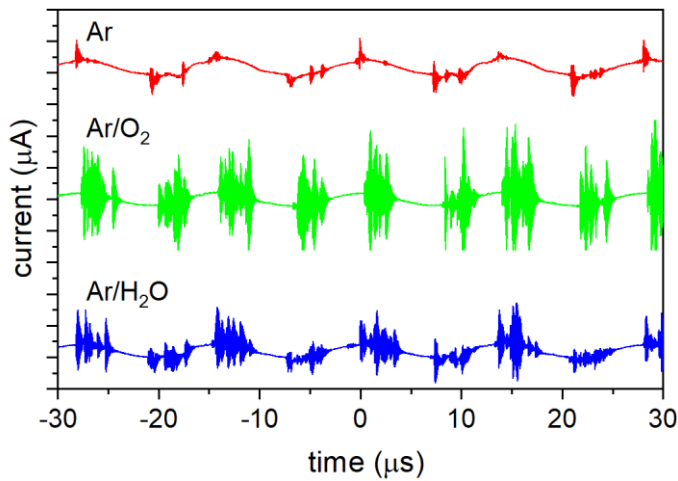


Figure 70: Time-resolved current signal as response to an applied voltage of 5.3 kV for each plasma gas mixture.

The addition of water and oxygen led to an increased number of plasma filaments, which was already reported in the literature for Ar/H₂O.^[170] An increased number of filaments can prove beneficial for a more homogenous treatment of substrates. The respective Lissajous figures were determined by integrating the current over time and plot the obtained charge against the voltage. The area disclosed by the Lissajous figures was multiplied by the plasma frequency to obtain the average dissipated power in a complete discharge cycle of the plasma (**Equation 5**).^[76] The results are presented in **Figure 71** and **Table 14**. The addition of water did not influence the active power, while the addition of oxygen significantly reduced the dissipated power in the plasma.

Furthermore, the dissipated power was compared with and without the ZnO-NR coating. No difference was observed in the current signal regarding the ZnO-NR coating. This was confirmed by calculated averaged dissipated power (shown in **Figure 71**), showing no significant change either. This behavior was expected as the change in the dielectric constant caused by the nanometer-thick ZnO-NR film is very small (600 nm) compared to the high thickness of the dielectric barrier (3 cm).

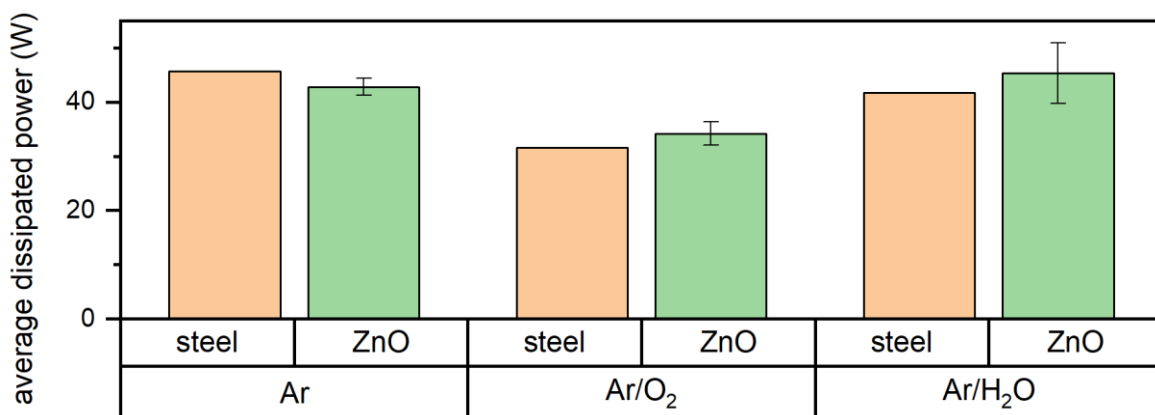


Figure 71: Influence of the ZnO mesh coating on the average dissipated power in a complete discharge cycle with respect to the plasma gas mixture.

4.5 In-situ backside Raman investigation of zinc oxide nanorods in an atmospheric-pressure dielectric barrier discharge plasma

In **Table 14**, a correlation between the dissipated power and the temperature rise was seen, where the higher the dissipated power was, the higher the temperature rose.

Table 14: Dissipated power and temperature increase of the respective plasma gas mixture.

	Ar	Ar/O ₂	Ar/H ₂ O
Dissipated power (W)	42 ± 3	33 ± 2	41 ± 3
Temperature increase in-situ (°C)	36 ± 5	15 ± 2	32 ± 5
Temperature increase ex-situ (°C)	12 ± 2	8 ± 2	12 ± 2

Furthermore, OES was performed. While Ar and Ar/H₂O plasmas showed strong optical signals, the Ar/O₂ plasmas exhibit very low optical emission (similar to chapter 4.1), which was attributed to the quenching of the transitions by the oxygen^[171] and water^[137]. However, by choosing a high integration time, the Ar/O₂ discharge emission could be measured in higher intensity (**Figure 72**).

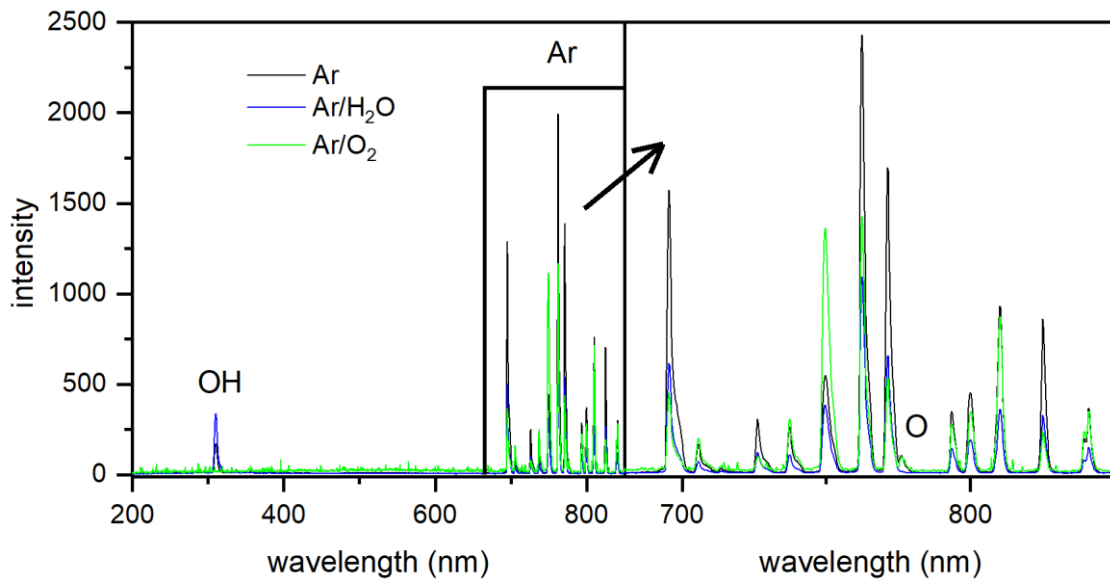


Figure 72: In-situ OES measured in the backside setup through the zinc oxide coated mesh.

All-optical plasmas emission consisted mainly of already known Ar transitions (680 nm – 900 nm)^[137]. Additionally, one peak associated with OH (310 nm)^{[137],[172]} and one to oxygen (775 nm)^[137] was found: Both peaks are present in pure Ar plasmas, while in Ar/H₂O plasmas, the OH peak was increased and the O peak diminished. Contrary, in Ar/O₂ plasmas, the OH peak was suppressed. It is known that OH can react with O, forming atomic H and O₂.^[173] Thus, by increasing one of the components, the other was reduced respectively.

4.5 In-situ backside Raman investigation of zinc oxide nanorods in an atmospheric-pressure dielectric barrier discharge plasma

4.5.2.2 Real-time in-situ backside Raman spectroscopy of ZnO coated mesh

After the characterization of the plasma, the plasma treatment of the ZnO nanorods was monitored in-situ by Raman spectroscopy. The following chapter is adapted from reference [131] with permission of the Journal of Raman spectroscopy and can be found at <https://analyticalsciencejournals.onlinelibrary.wiley.com/doi/10.1002/jrs.6123>

In **Figure 73a**, the normalized spectra (to E_2^{high} at 437 cm^{-1}) collected in-situ before, during, and after the plasma treatment using Ar/H₂O as plasma gas are displayed as a contour map. The black areas indicate low intensity, whereas bright green areas illustrate high intensities of the respective Raman spectra. The x-axis shows the time in seconds, where the plasma was switched on at 0 s and off after 600 s. **Figure 73b** presents the evolution of the intensity of selected peaks determined from the contour plot. **Figure 73c** displays the averaged spectra over 600 s before, during, and after the plasma, respectively.

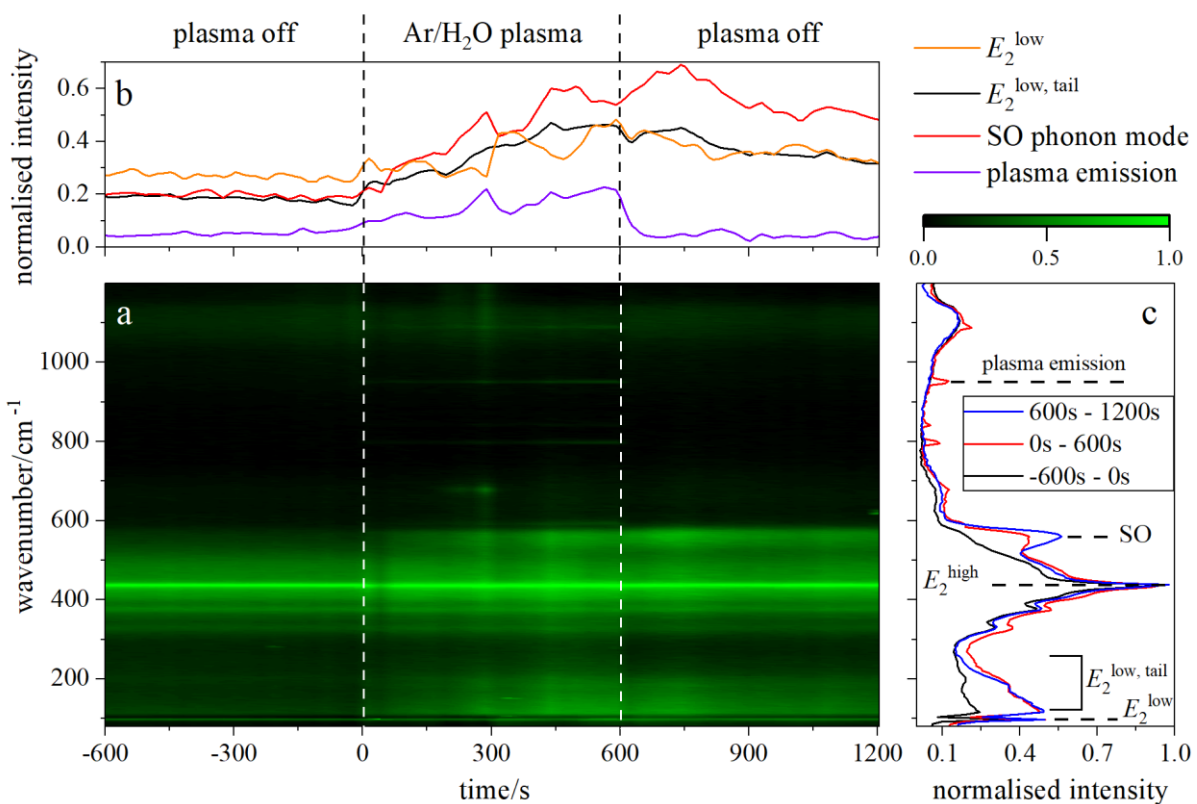


Figure 73: In-situ contour profile of the normalized (to E_2^{high} at 437 cm^{-1}) Raman spectra during the Ar/H₂O plasma treatment. Spectra were recorded continuously 600 s before, during, and after the plasma treatment, where the plasma treatment started at 0 s. a) Time-resolved contour map of the Raman spectra. b) Time-resolved peak evolution of chosen peak intensities. c) Normalized, averaged spectra over the entire time before, during, and after the plasma. [131]

The Raman spectra of the untreated ZnO-NR (-600 s to 0 s, **Figure 73c**) exhibited characteristic peaks for the ZnO wurtzite structure. The spectra were fitted using Gaussian functions to obtain the respective peak contributions (**Figure 74**). While the Raman peaks associated with the crystal lattice of ZnO are well established, peaks related to defects are quite diverse and often controversial. For instance, Khachadarian et al. showed the high diversity of different defect modes by calculating the phonon density of states for isolated Zn and O vacancies and interstitial Zn using DFT studies, where a large number of related phonon branches around 300 cm^{-1} and between 450 cm^{-1} and 520 cm^{-1} were found. [174]

4.5 In-situ backside Raman investigation of zinc oxide nanorods in an atmospheric-pressure dielectric barrier discharge plasma

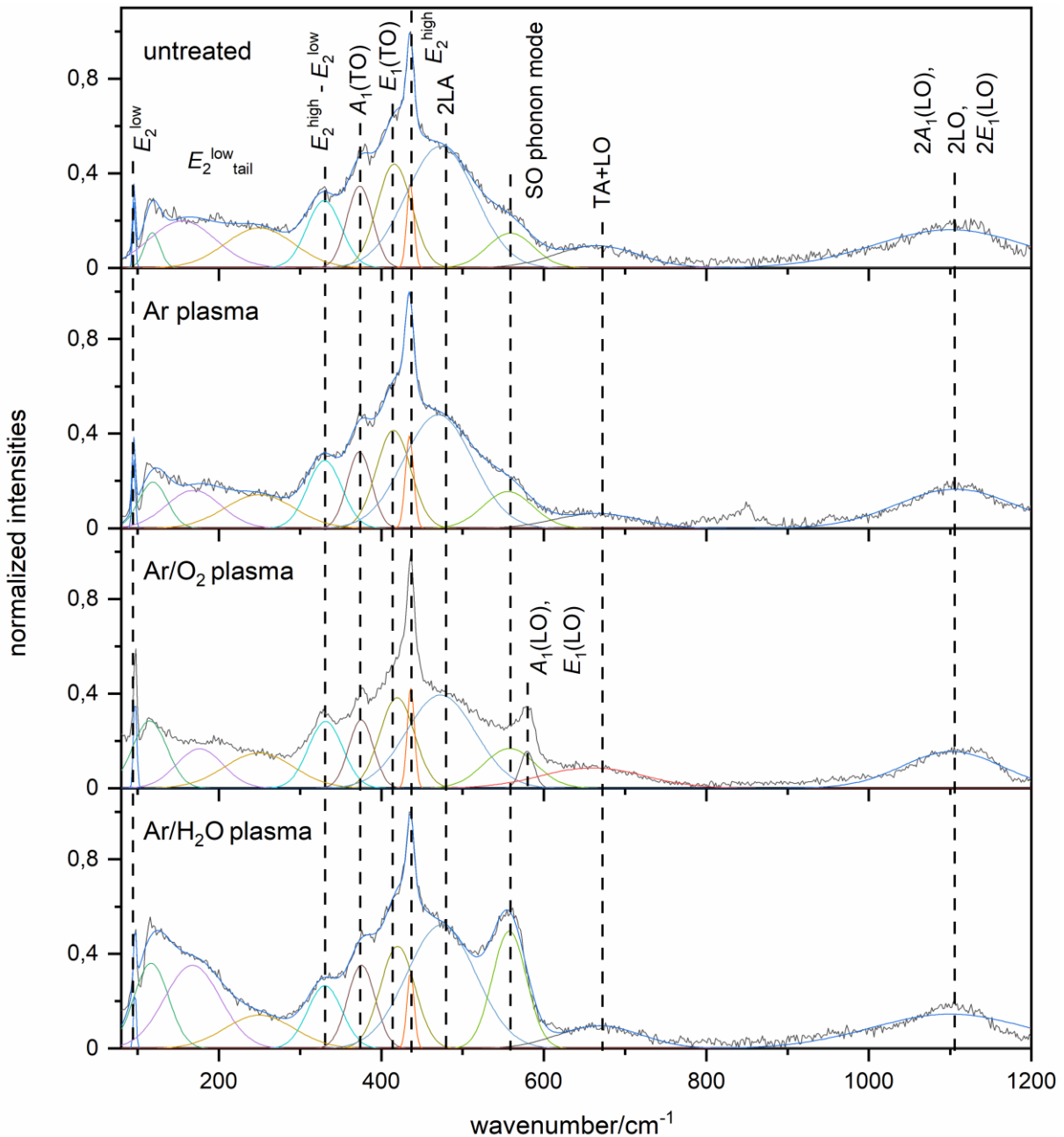


Figure 74: Fitting of the Raman spectra before and after the respective plasma treatments using Gaussian functions.^[131]

The changes induced by the plasma treatments identified in the fitting results are in very good agreement with the evaluation of the peak intensities performed in **Figure 73**, **Figure 78**, and **Figure 79**: After the Ar plasma, no change related to the plasma was seen. However, after the Ar/O₂ plasma treatment, a new peak appeared at 580 cm⁻¹ (A₁(LO) and E₁(LO)), while after the Ar/H₂O plasma treatment, the peak at 555 cm⁻¹ (SO phonon mode) increased. This increase was accompanied by the increase of the peaks at 117 cm⁻¹, 165 cm⁻¹, and 250 cm⁻¹ (E₂^{low, tail}). All other peaks were unaffected by the plasma treatments. Thus, the evaluation of the intensities performed in **Figure 73**, **Figure 78**, and **Figure 79** is directly related to the evolution of the respective peaks.

4.5 In-situ backside Raman investigation of zinc oxide nanorods in an atmospheric-pressure dielectric barrier discharge plasma

Table 15: Fitting results of the Raman spectra using Gaussian functions. xc represents the position, A the area, and w the half-width of the respective peak.^[131]

		Untreated	Ar plasma	Ar/O ₂ plasma	Ar/H ₂ O plasma
Peak 1 E_2^{low}	xc / cm ⁻¹	96,8	96,7	97,0	96,7
	A	1,2	1,4	1,9	1,0
	w / cm ⁻¹	3,9	4,5	4,5	3,8
Peak 2 $E_2^{\text{low, tail}}$	xc / cm ⁻¹	118,1	119,0	115,0	116,8
	A	3,6	8,5	15,1	19,2
	w / cm ⁻¹	22,5	41,0	50,0	50,0
Peak 3 $E_2^{\text{low, tail}}$	xc / cm ⁻¹	165,0	168,9	166,5	167,6
	A	20,5	13,5	12,0	30,3
	w / cm ⁻¹	96,8	79,2	67,4	81,0
Peak 4 $E_2^{\text{low, tail}}$	xc / cm ⁻¹	250,0	250,0	249,6	250,0
	A	18,0	15,1	15,9	15,0
	w / cm ⁻¹	100,0	100,0	100,0	100,0
Peak 5 $E_2^{\text{high}} - E_2^{\text{low}}$	xc / cm ⁻¹	329,6	330,2	331,3	330,4
	A	15,1	15,2	15,0	14,1
	w / cm ⁻¹	50,0	50,0	49,9	50,0
Peak 6 $A_1(\text{TO})$	xc / cm ⁻¹	373,4	373,0	375,0	375,5
	A	13,6	12,1	10,9	15,0
	w / cm ⁻¹	37,0	35,1	35,6	40,0
Peak 7 $E_1(\text{TO})$	xc / cm ⁻¹	416,0	415,0	419,3	420,0
	A	23,4	22,0	20,4	23,0
	w / cm ⁻¹	50,0	50,0	50,0	50,0
Peak 8 E_2^{high}	xc / cm ⁻¹	435,6	434,6	436,2	435,9
	A	4,0	5,0	4,7	3,6
	w / cm ⁻¹	10,3	12,0	10,4	10,7
Peak 9 2LA, phonon branches, Zn _i	xc / cm ⁻¹	473,0	470,0	473,0	473,9
	A	54,8	51,0	41,9	55,5
	w / cm ⁻¹	100,0	100,0	100,0	100,0
Peak 10 SO phonon mode	xc / cm ⁻¹	559,0	555,9	557,9	557,5
	A	10,6	11,9	13,5	26,0
	w / cm ⁻¹	67,2	72,1	75,5	49,2
Peak 11 $A_1(\text{LO})$ and $E_1(\text{LO})$	xc / cm ⁻¹	579,5	579,5	579,5	579,5
	A	0,0	0,0	3,3	0,0
	w / cm ⁻¹	0,0	0,0	20,0	0,0
Peak 12 TA+LO	xc / cm ⁻¹	665,3	665,3	660,0	668,7
	A	12,1	8,0	13,8	12,3
	w / cm ⁻¹	120,0	120,0	150,1	120,0
	A	37,7	30,1	23,6	35,3
	w / cm ⁻¹	219,4	171,2	142,8	227,9

Based on the fitting results, the ratio of $2E_1(\text{LO})/E_1(\text{LO})$ (or Peak11/Peak13, or $580 \text{ cm}^{-1}/1100 \text{ cm}^{-1}$) was calculated to estimate the disorder present in the material. Only after the Ar/O₂ plasma treatment an $E_1(\text{LO})$ peak was found, and the determined ratio was 7.2. Mondal et al. obtained for nitrogen implanted

4.5 In-situ backside Raman investigation of zinc oxide nanorods in an atmospheric-pressure dielectric barrier discharge plasma

polycrystalline ZnO ratios in the range between 3 to 0.^[175] Since the disorder is reduced with an increasing ratio, we conclude that the Ar/O₂ plasma treatment introduced only minor disorders.

The results of the fits are presented in **Tabel 15** and are summarized in **Table 16**. Interestingly, the surface optical (SO) phonon mode (located at 555 cm⁻¹) related to defects such as disorderly arranged areas and grain boundaries was observed in the spectra.^{[175],[176]} Additionally, the positions of the E_2^{low} and E_2^{high} are redshifted and broadened (**Table 15**), indicating a defect-rich structure of the deposited zinc oxide nanorods.^[177]

Table 16: Peak positions and their respective assignment found in the Raman spectra before and after the respective plasma treatments.^[131]

Wavenumber	Assignment ^{[176]–[180]}	Appear in
97 cm ⁻¹	E_2^{low}	all
132 cm ⁻¹ – 300 cm ⁻¹ (117 cm ⁻¹ , 165 cm ⁻¹ , 250 cm ⁻¹)	$E_2^{\text{low, tail}}$	all
203 cm ⁻¹	$2E_2^{\text{low}}$	all
330 cm ⁻¹	$E_2^{\text{high}} - E_2^{\text{low}}$	all
376 cm ⁻¹	$A_1(\text{TO})$	all
415 cm ⁻¹	$E_1(\text{TO})$	all
437 cm ⁻¹	E_2^{high}	all
485	2LA	all
555 cm ⁻¹	SO phonon mode ^[176]	all
580 cm ⁻¹	$A_1(\text{LO})$ and $E_1(\text{LO})$ ^{[181]–[183]}	Ar/O ₂ plasma
670 cm ⁻¹	TA+LO	all
594, 797, 848, 951, and 1092 cm ⁻¹	plasma emissions	Ar/H ₂ O plasma
1100 cm ⁻¹	$2A_1(\text{LO})$, 2LO, 2 $E_1(\text{LO})$	all

During the plasma treatment using Ar/H₂O, new narrow peaks appeared at 594 cm⁻¹, 797 cm⁻¹, 848 cm⁻¹, 951 cm⁻¹, and 1092 cm⁻¹ immediately after the plasma was turned on: The five narrow peaks displayed a high intensity during an additional measurement (not shown here) in which the power of the Raman laser was reduced to zero while focusing on a gap of the net. Therefore, these peaks are assigned to plasma emissions which were gathered as stray light of the plasma emission. This is in agreement with the temporal development of the peaks (displayed in detail in **Figure 73b** for the peak centered at 950 cm⁻¹), which immediately disappeared as soon as the plasma was turned off.

Besides, an increase in the E_2^{low} peak (at 97 cm⁻¹), the E_2^{low} asymmetric tail (132 cm⁻¹ to 300 cm⁻¹) and at 555 cm⁻¹ (SO phonon vibration mode) was seen: The E_2^{low} vibration is dominated by the Zn atoms (in comparison to the E_2^{high} (437 cm⁻¹), which is dominated by the oxygen atoms of the ZnO lattice), while the E_2^{low} asymmetric tail and the SO phonon mode are associated to lattice stress or displacement.^{[175]–[178]} In the case of the SO phonon mode, Zeng et al. assigned its appearance to the loss of the long-range periodicity (and thus the symmetry) at the surface, which they confirmed by HRTEM measurements.^{[176],[184]} Thus, additional TEM measurements were conducted before and after the Ar/H₂O plasma treatment by Julius Bürger (work group of Prof. Dr. Lindner, University of Paderborn).

4.5 In-situ backside Raman investigation of zinc oxide nanorods in an atmospheric-pressure dielectric barrier discharge plasma

The resulting TEM bright-field images of two different nanorods before and after the Ar/H₂O plasma treatment are shown in **Figure 75**.

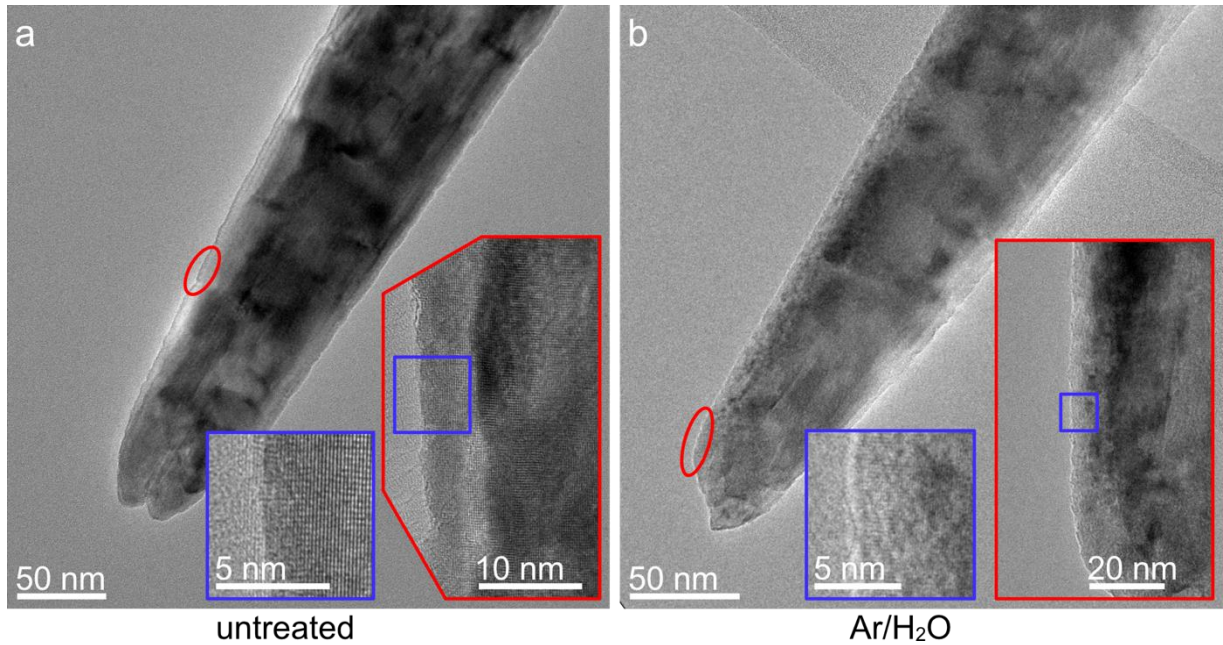


Figure 75: TEM bright-field images of a ZnO-nanorod a) before and b) after the Ar/H₂O plasma treatments. The insets show magnified images of the corresponding areas marked by a red circle or a blue-framed rectangle.^[131]

Both rods are completely crystalline up to the surface. While the edges of both the untreated (inset in **Figure 75a**) and the Ar/H₂O plasma treated (inset in **Figure 75b**) showed a similar roughness in projection, the roughening by the plasma treatment was evident on the surface of the plasma-treated ZnO-NR, leading to a mottled appearance in the thinnest parts of the rod (inset in **Figure 75b**).

The roughening of the surface was even more visible in the EFTEM thickness maps shown in **Figure 76**.

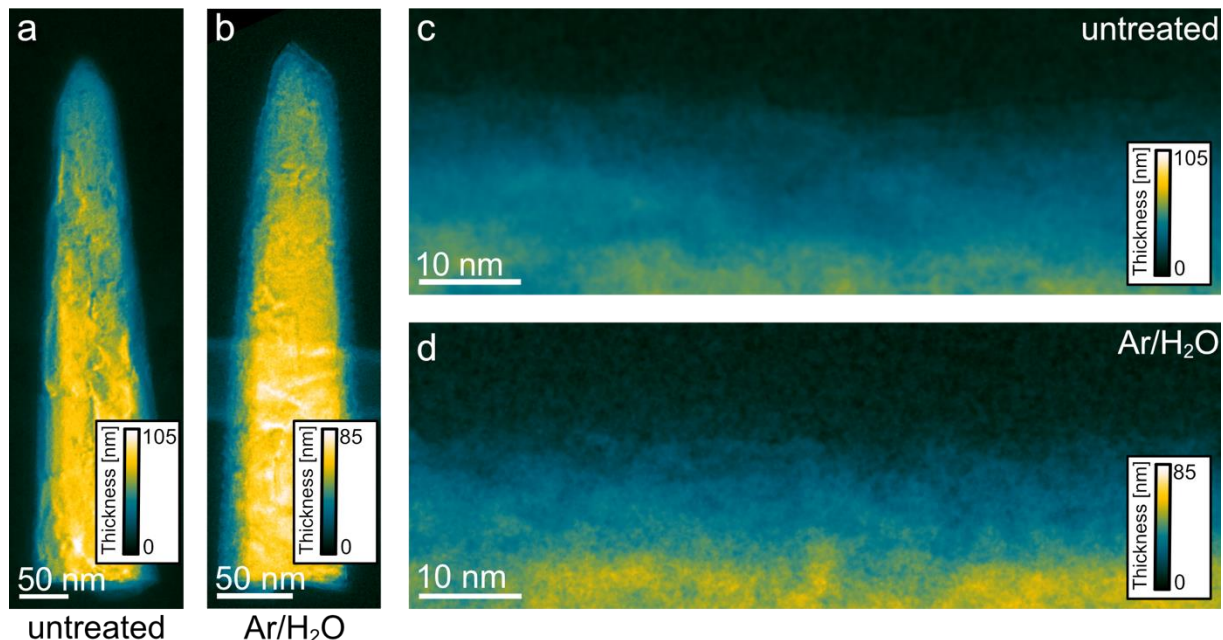


Figure 76: EFTEM thickness mapping of a ZnO-nanorod a) before and b) after the Ar/H₂O plasma treatment. Magnified images of the EFTEM thickness at the edges of the same c) untreated and d) plasma-treated ZnO-rods.^[131]

4.5 In-situ backside Raman investigation of zinc oxide nanorods in an atmospheric-pressure dielectric barrier discharge plasma

On a macroscopic scale, the untreated ZnO-NR exhibited a smooth surface (**Figure 76a**). In comparison to this, the Ar/H₂O plasma-treated specimen showed a cystic surface, which was particularly observable on the edges of the ZnO-NR (**Figure 76b**). For comparison, the edges of an untreated and an Ar/H₂O plasma-treated ZnO-NR are displayed in **Figure 76c** and **Figure 76d**, respectively. While the untreated ZnO-NR had a sharp edge and exhibited a smooth surface, the edge of the Ar/H₂O plasma-treated ZnO-NR was nearly impossible to determine. This is due to the surface roughening by the plasma leading to a strongly varying projected thickness.

To monitor the presence of crystal structure modifications on the surface of ZnO-NRs by the Ar/H₂O plasma, HRTEM images shown in **Figure 76** were captured. The crystal structure was determined by subsequently calculating the fast Fourier transformation (FFT) of several regions of interest.

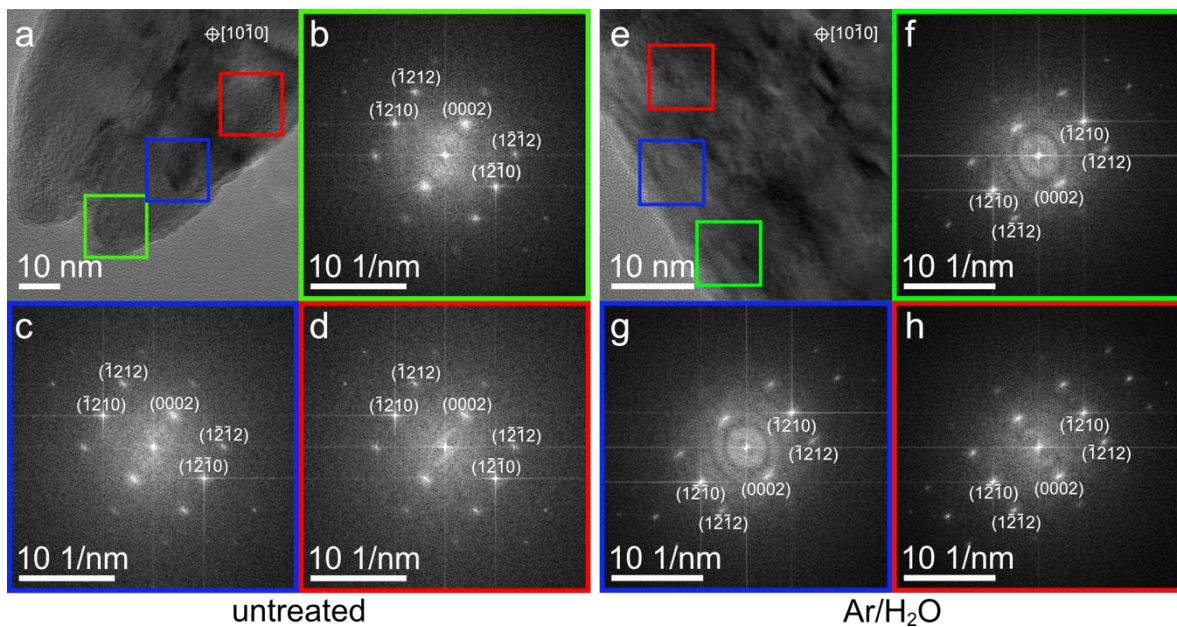


Figure 77: a) HRTEM image of an untreated ZnO-nanorod imaged in $[10\bar{1}0]$ zone axis orientation and the corresponding FFTs of the three red, blue, and green marked regions of interest in b), c), and d). e) HRTEM image of an Ar/H₂O plasma-treated ZnO-NR. The FFTs in f), g), and h) do not reveal the presence of different crystallographic phases.^[131]

No significant changes in the crystal structure, as well as orientation, were observed. The untreated ZnO-NR exhibited a $[10\bar{1}0]$ zone axis orientation (**Figure 77a**) deduced from the FFT patterns in **Figure 77b-d**. Besides, all FFTs only showed one crystallographic phase. The same behavior was observed in the case of an Ar/H₂O plasma-treated ZnO-NR (**Figure 77e**), also imaged in $[10\bar{1}0]$ zone axis orientation. Again, the FFTs in **Figure 77f-h** exhibited only one crystallographic phase. Thus, the SO phonon mode was most likely be linked to the surface roughening by the Ar/H₂O plasma rather than changes in the crystal lattice. Thus, the TEM results showing that this roughening most likely caused the symmetry loss at the surface and gave rise to the SO phonon mode.

This process induced stress in the lattice due to the creation of interfacial defects in agreement with the results of Mondal et al.^[175] SO phonon mode, E_2^{low} , and the E_2^{low} asymmetric tail were continuously and simultaneously increased over the complete 600 s plasma treatment, showing their direct correlation. After the plasma was turned off, these changes slowly decreased.

4.5 In-situ backside Raman investigation of zinc oxide nanorods in an atmospheric-pressure dielectric barrier discharge plasma

The in-situ measurement of the plasma treatment using Ar/O₂ is displayed in **Figure 78**.

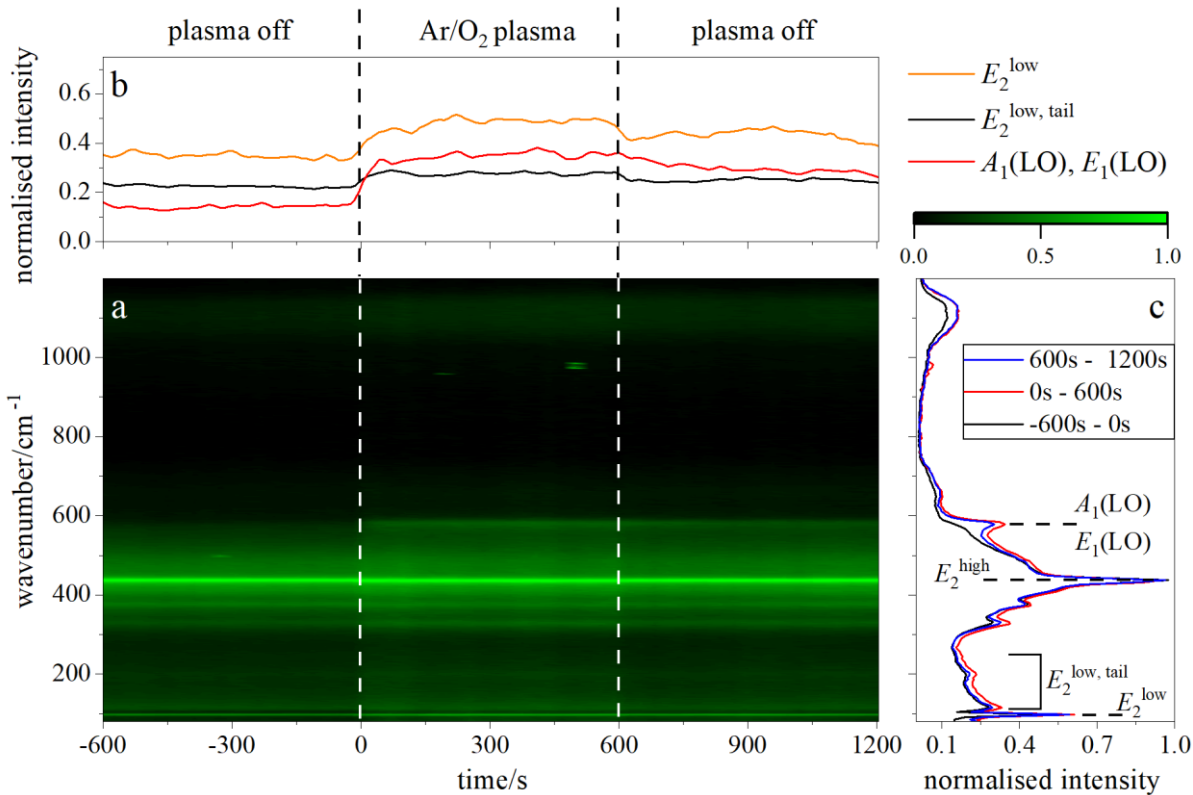


Figure 78: In-situ contour profile of the normalized (to E_2^{high} at 437 cm^{-1}) Raman spectra during the Ar/O₂ plasma treatment. Spectra were recorded continuously 600 s before, during, and after the plasma treatment, where the plasma treatment started at 0 s. a) Time-resolved contour map of the Raman spectra. b) Time-resolved peak evolution of chosen peak intensities. c) Normalized, averaged spectra over the entire time before, during, and after the plasma.^[131]

Here, a new peak located at 580 cm^{-1} rapidly rose during the plasma “on” time. This peak position is associated with the closely located $A_1(\text{LO})$ and $E_1(\text{LO})$ modes.^{[181]–[183]} Thereby, the $E_1(\text{LO})$ is very sensitive to oxygen-related defects, such as V_O .^{[175],[181]} The new peak was accompanied by a simultaneous rise in the E_2^{low} (97 cm^{-1}) and slightly the E_2^{low} asymmetric tail (132 cm^{-1} – 300 cm^{-1}) as already seen during the Ar/H₂O plasma. It has to be noted that although oxygen-related defects are created, the interaction of the plasma effluent is based on the Zn atoms (E_2^{low}) rather than the O atoms (E_2^{high}). The fast rise within the first 100 s plasma treatment was followed by a steady behavior during the rest of the plasma treatment. Afterward, the asymmetric tail immediately dropped, while the $A_1(\text{LO})/E_1(\text{LO})$ peak and the E_2^{low} slowly decreased. Thus, the minor lattice stress is caused by the plasma effluent and not by the created defects. This supports an assignment of the peak at 580 cm^{-1} as oxygen vacancy because, contrary to interfacial defects, oxygen vacancies lead to a relaxation of the surrounding lattice.^[185]

4.5 In-situ backside Raman investigation of zinc oxide nanorods in an atmospheric-pressure dielectric barrier discharge plasma

In comparison, the in-situ measurement using pure Ar (Figure 79) showed no defect formation during the plasma treatment. Only the signal corresponding to E_2^{low} increased slightly during the plasma “on” time and relaxed immediately when the plasma was turned off.

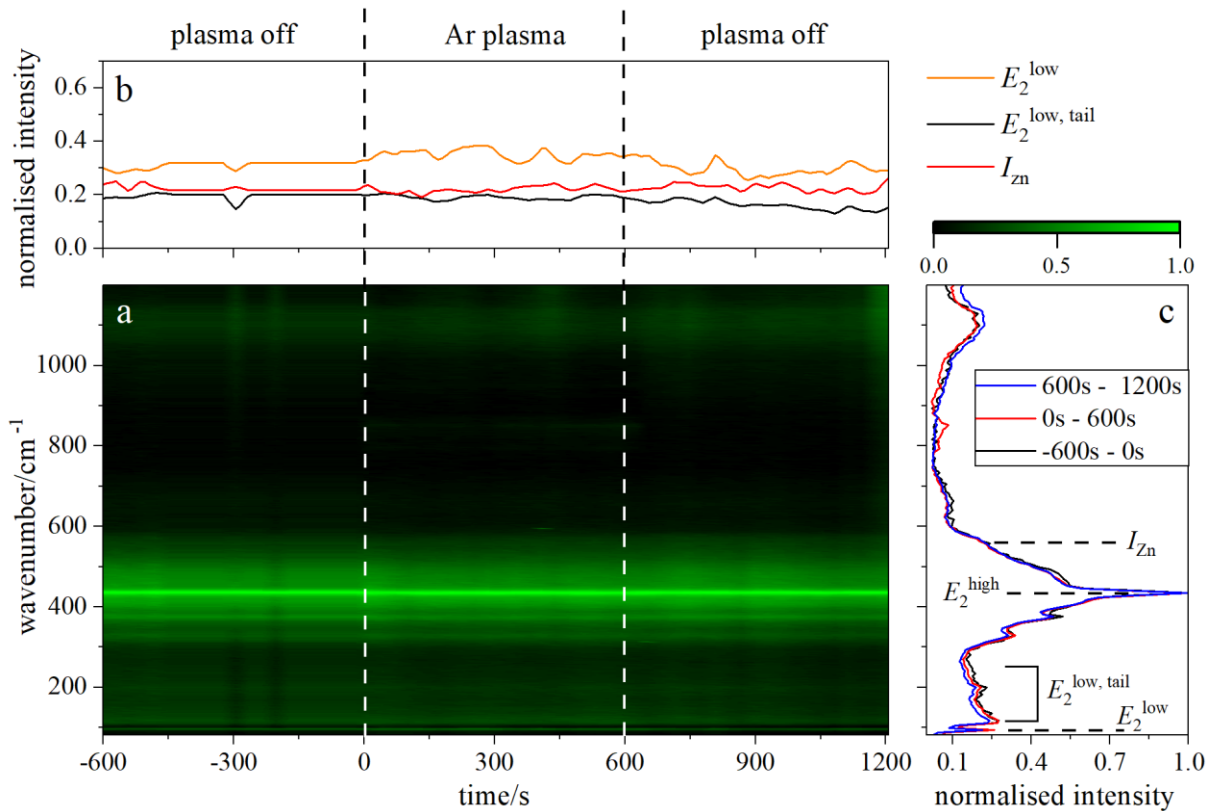


Figure 79: In-situ contour profile of the normalized (to E_2^{high} at 437 cm^{-1}) Raman spectra during the Ar plasma treatment. Spectra were recorded continuously 600 s before, during, and after the plasma treatment, where the plasma treatment started at 0 s. a) Time-resolved contour map of the Raman spectra. b) Time-resolved peak evolution of chosen peak intensities. c) Normalized, averaged spectra over the entire time before, during, and after the plasma.^[131]

This shows that the indirect plasma/surface interaction is mainly determined by the reactive species and their amount rather than the dissipated power or the substrate temperature (same for Ar and Ar/H₂O), at least in the given limitations (limited determining reactive species, relatively low temperature). Taking all results into account, we conclude that all plasma gas mixtures produced a measurable interaction with the zinc sub-lattice (visible by the increased E_2^{low}), but only the addition of oxygen-containing components (O₂ or H₂O) led to the formation of defects. It has to be kept in mind that due to the backside geometry, only the plasma effluent (long-time stable reactive species) could interact with the ZnO-NRs. Pure atmospheric-pressure Ar plasma effluents are known to contain various metastable excited Ar species.^[186] Both Ar/H₂O and Ar/O₂ plasmas contain additional oxidizing species in the plasma effluent, but these species are different in both cases: While Ar/H₂O plasma discharges are known to mainly produce reactive OH radicals and H₂O₂^[170], Ar/O₂ plasma discharges generate activated O and O₃^[46].

4.5 In-situ backside Raman investigation of zinc oxide nanorods in an atmospheric-pressure dielectric barrier discharge plasma

4.5.2.3 XPS analysis of the plasma-treated ZnO nanorods

To further investigate the defect formation and the elemental composition of the ZnO nanorods, X-ray photoelectron spectroscopy was performed in an ESCA+ facility (Oxford Instruments, Taunusstein, Germany). The base pressure was $< 2.0 \times 10^{-10}$ mbar, and a monochromatic Al K α radiation (1486.7 eV) without neutralization was used. The take-off angle was 30° with respect to the surface. The spectra were calibrated to adventitious carbon (C 1s signal at 284.6 eV). While survey spectra were recorded using a pass energy of 100 eV and a step size of 0.2 eV, core-level spectra were recorded at a pass energy of 20 eV and a step size of at least 0.1 eV. When necessary, the core level spectra were mathematically decomposed into different components using a product of Gaussian (70%) and Lorentzian (30%) profiles.

Thereby, the survey spectra only exhibit characteristic peaks of Zn, O, and C on the sample (**Figure 80**), confirming the successful deposition of pure ZnO nanorods.

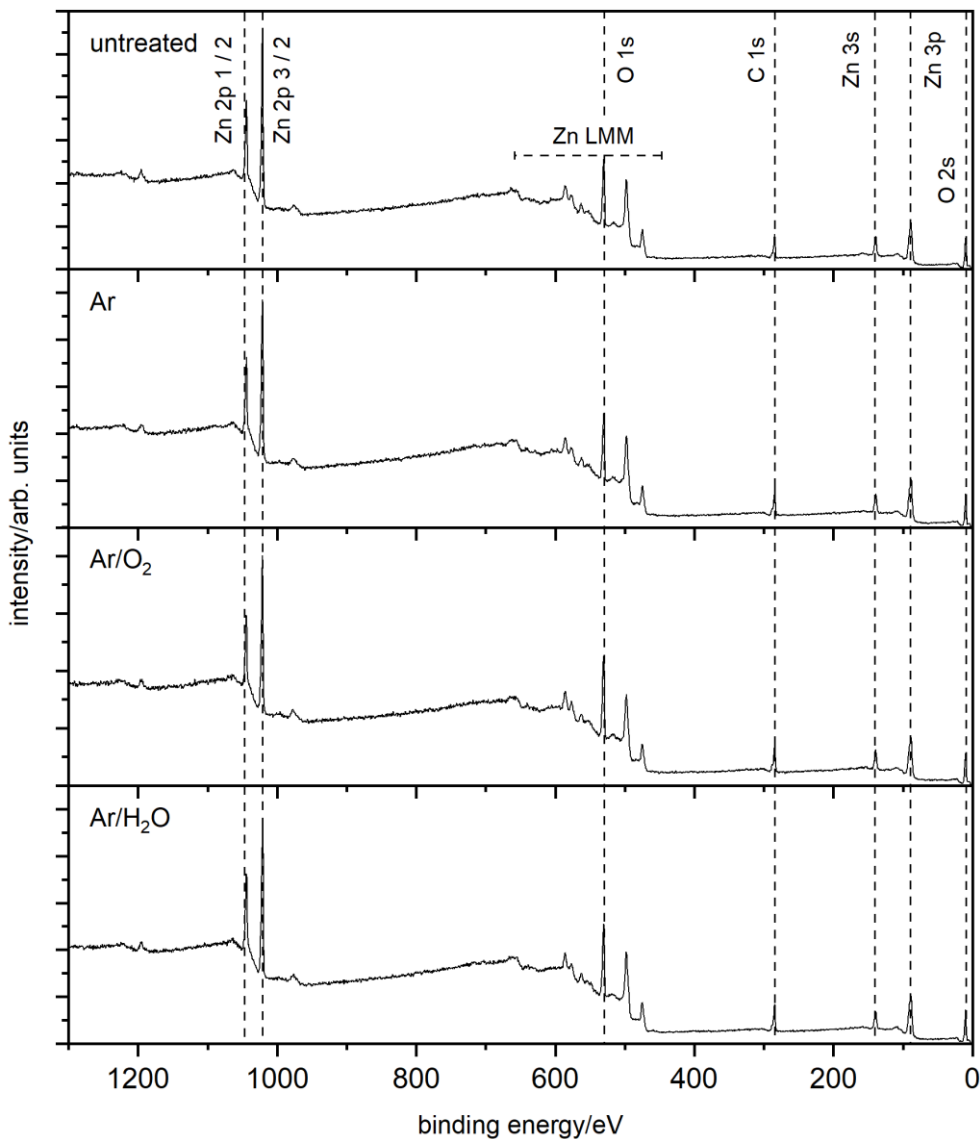


Figure 80: Survey measurement before and after the respective plasma treatment.^[131]

4.5 In-situ backside Raman investigation of zinc oxide nanorods in an atmospheric-pressure dielectric barrier discharge plasma

Based on the core-level spectra, XPS quantification was performed. The results are presented in **Table 17**.

Table 17: Results of XPS quantifications based on the core-level spectra before and after the respective plasma treatment.^[131]

	C 1s / at%	O1s / at%	Zn 2p 3/2 / at%	O/Zn
untreated	35.1	36.8	28.1	1,31
Ar	36.5	36.3	27.2	1,33
Ar/O₂	34.7	38.9	26.5	1,45
Ar/H₂O	37.2	39.4	23.4	1,7

No plasma treatment led to permanent removal of adventitious surface absorbates, as seen in the amount of carbon. However, small changes were seen in the O 1s and Zn 2p 3/2. To neglect the effect of the carbon concentration, the ratio O/Zn was determined. It is seen that the ratio increased slightly after the Ar/O₂ plasma treatment and even more after the Ar/H₂O plasma treatment.

4.5 In-situ backside Raman investigation of zinc oxide nanorods in an atmospheric-pressure dielectric barrier discharge plasma

To further analyze the plasma-induced changes, the core-level spectra were evaluated. The C 1s core-level spectra before and after the respective plasma treatment are shown in **Figure 81**.

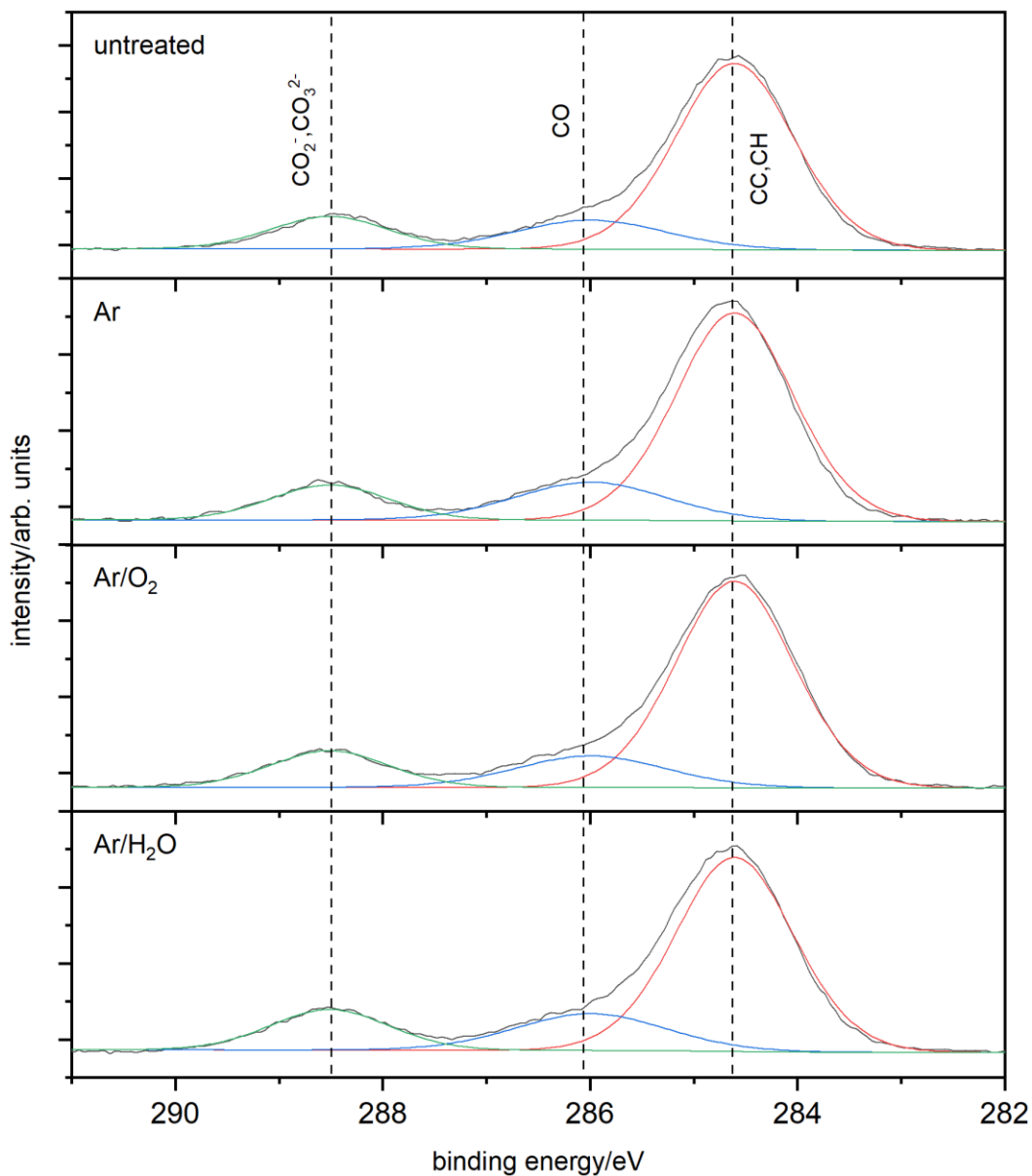


Figure 81: C 1s core-level spectra before and after the respective plasma treatment.^[131]

The spectra resemble typical spectra of adventitious carbon. To further analyze the spectra, three peaks were fitted related to CC/CH (284.6 eV), CO (286.1 eV), and $\text{CO}_2^-/\text{CO}_3^{2-}$ (288.5 eV).^[109]

4.5 In-situ backside Raman investigation of zinc oxide nanorods in an atmospheric-pressure dielectric barrier discharge plasma

The results are presented in **Table 18**.

Table 18: Results of fitting the C 1s core-level spectra before and after the respective plasma treatment.^[131]

	CC, CH / %	CO / %	CO ₂ /CO ₃ ²⁻ / %
untreated	72.6	14.6	12.8
Ar	72.2	15.7	12.1
Ar/O₂	68.7	16.7	14.4
Ar/H₂O	72.7	14.3	13.0

The quantification of the fitting of the C 1s showed that only the Ar/O₂ plasma treatment led to slight oxidation of the adventitious surface adsorbates, while Ar and Ar/H₂O plasma treatments induced no changes at all. This oxidation of the adventitious absorbed carbon could explain the increased O/Zn ratio after the Ar/O₂ plasma treatment.

4.5 In-situ backside Raman investigation of zinc oxide nanorods in an atmospheric-pressure dielectric barrier discharge plasma

Moreover, the O 1s core-level spectra were evaluated as well (Figure 82).

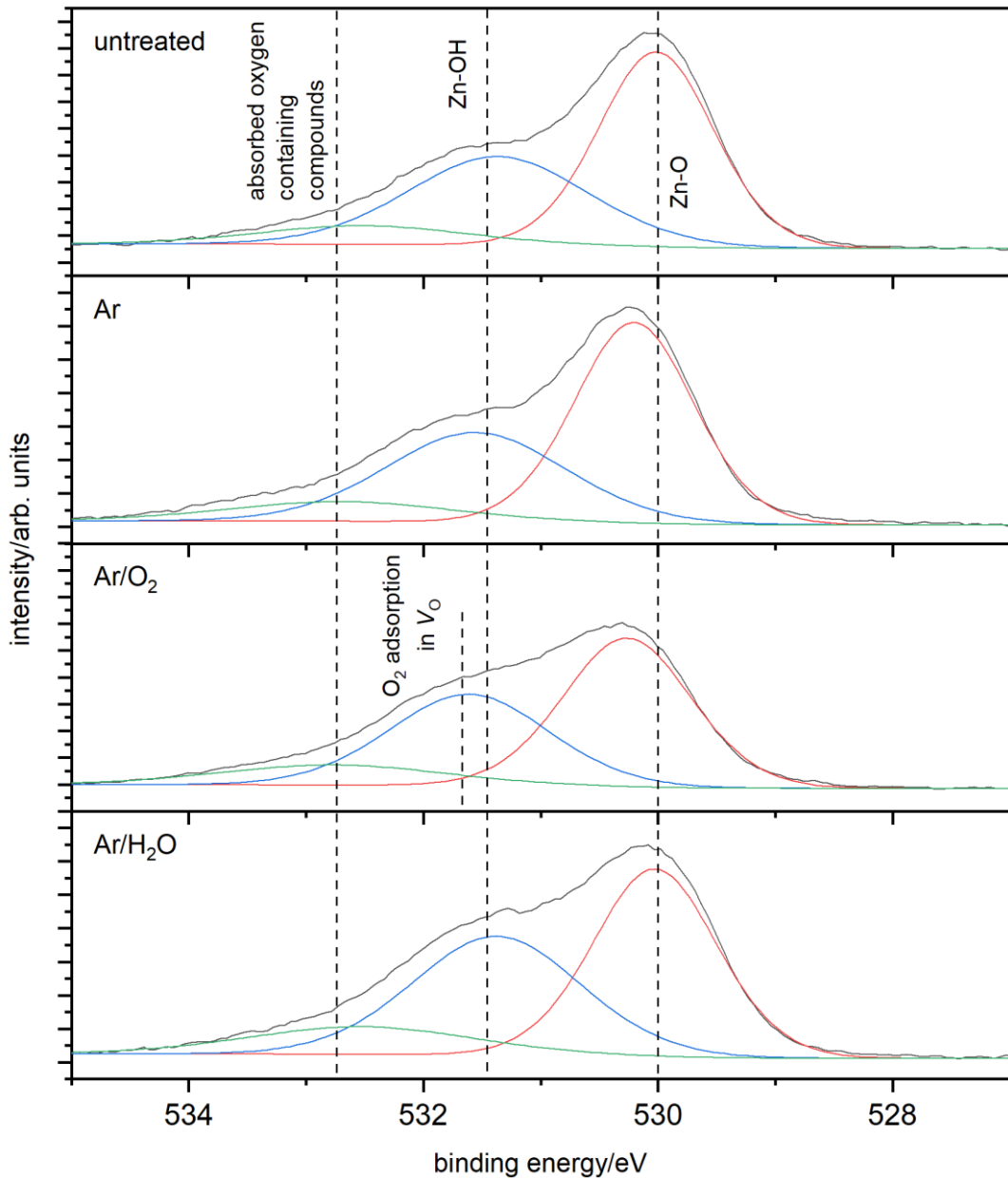


Figure 82: O 1s core-level spectra before and after the respective plasma treatment.^[131]

In the spectra, three major contributions can be separated: The peak at 530 eV is related to the oxygen in ZnO, the peak at 531.5 eV can be either related to Zn-OH^[70] or loosely adsorbed oxygen in oxygen vacancies (V_O),^[43] and the peak at 532.4 eV is related to oxygen-containing species adsorbed on the surface such as CO_2^- or water. As shown in the spectra, the second peak position at 531.5 eV was shifted to higher binding energies after the Ar/O₂ plasma treatment. Taking the two different assignments and the Raman results into account, the shift could result from oxygen vacancies created during the Ar/O₂ plasma.

4.5 In-situ backside Raman investigation of zinc oxide nanorods in an atmospheric-pressure dielectric barrier discharge plasma

Last, the Zn 2p 3/2 core-level spectra and the Zn LMM spectra were investigated before and after the respective plasma treatment (**Figure 83**).

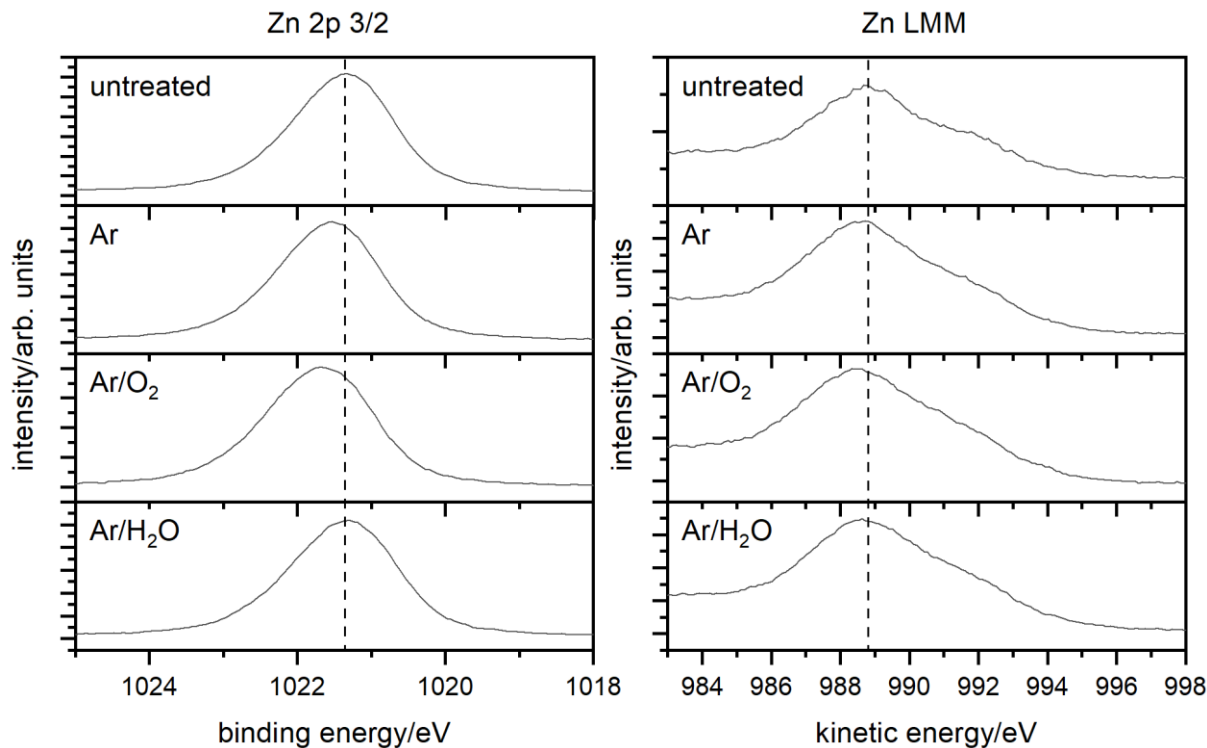


Figure 83: Zn 2p 3/2 core-level spectra and Zn LMM Auger spectra before and after the respective plasma treatment.^[131]

All samples exhibit very similar features. The most pronounced effect was small shifts of the Zn 2p 3/2 and the Zn LMM. The modified auger parameter was determined to evaluate the effect further and rule out possible charging effects (**Table 19**).

Table 19: Modified auger parameter for Zn before and after the respective plasma treatment.^[131]

Modified Auger parameter / eV	
untreated	2010,1
Ar	2010,1
Ar/O₂	2010,2
Ar/H₂O	2010,0

It is seen that the modified Auger parameter is very similar for all samples and is in good agreement with values stated in the literature for ZnO.^[187]

4.5 In-situ backside Raman investigation of zinc oxide nanorods in an atmospheric-pressure dielectric barrier discharge plasma

4.5.2.4 Raman spectroscopy at an expanded timescale

In order to determine the long-term stability of the plasma-induced defects, the results gathered in-situ were compared to ex-situ Raman measurements performed directly after the plasma treatment and after one-month storage in vacuo. The time dependence of the peak ratios (including the in-situ results presented beforehand) is shown in **Figure 84**. The error bars are based on at least three samples measured at multiple spots (except for the in-situ measurements) on the same mesh.

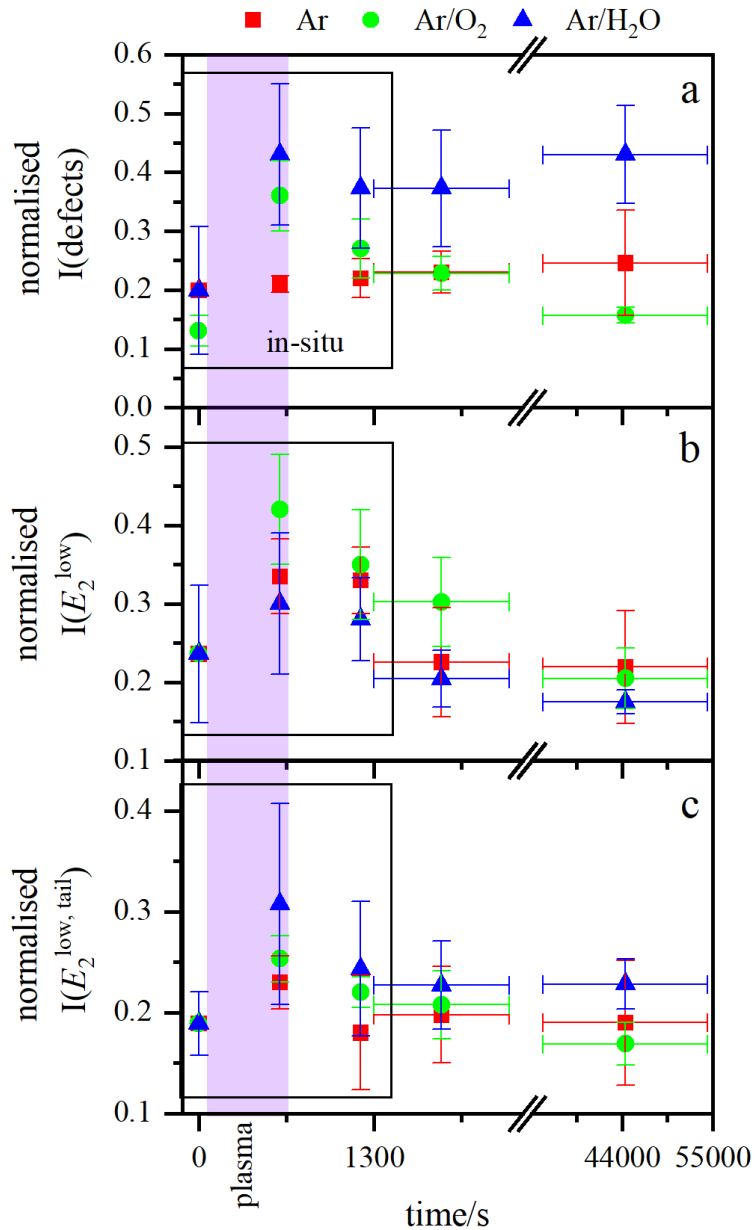


Figure 84: Comparison of in-situ (the value at the end of the plasma treatment and the end of the in-situ measurements were taken and are indicated by a black frame) and ex-situ measurements after the plasma for different plasma-induced changes in the ZnO-NR. The plasma duration is indicated by a violet band. The peak ratios (all normalized to E_2^{high} at 437 cm^{-1}) are shown for: a) defect peak (located at 555 cm^{-1} for Ar and Ar/H₂O and 580 cm^{-1} for Ar/O₂), b) Zn lattice vibration correlated to the E_1^{low} at 97 cm^{-1} and c) the lattice stress associated to the E_1^{low} asymmetric tail from 132 cm^{-1} - 300 cm^{-1} .^[131]

Figure 84 illustrates the difference of the measurements in-situ compared to measurements after the plasma: already 600 s after the plasma has been switched off (corresponding to t=1200 s in **Figure 84**), a decrease in nearly all peak ratios is visible. Especially the stress induced by the plasma and the increase in the E_1^{low} due to the pure Ar plasma treatment is only detectable during and shortly after the plasma

4.5 In-situ backside Raman investigation of zinc oxide nanorods in an atmospheric-pressure dielectric barrier discharge plasma

treatment. This emphasizes the benefit of in-situ measurements and their contribution to the knowledge of plasma effluent/surface interfaces.

Different behaviors were seen depending on both the plasma gas mixture and the investigated normalized intensities:

For the Ar/O₂ plasma-treated ZnO-NR, all plasma-induced changes immediately started to relax after the plasma was switched off (compare with **Figure 78**). Within the 600 s, after the plasma is switched off (in-situ), the stress and defects were seen to relax quite fast. No permanent change induced by the plasma could be detected on the treated surfaces after one month.

In comparison, the plasma treatment using Ar/H₂O led to highly stable defects even after one month. The lattice stress measured ex-situ stayed at a higher level compared to the untreated sample, although not as high as seen during the plasma. Thus, both the defects themselves and the plasma effluent/surface interaction caused stress in the material.

Pure Ar plasma showed no plasma-effluent-induced changes except for the already discussed increase in the E_2^{low} during the plasma treatment during the in-situ measurements. Despite this, a small increase in the E_2^{low} asymmetric tail and the SO phonon mode was visible in the ex-situ measurements. These are attributed to not homogeneously distributed residual humidity.^[109]

4.5.3 Conclusions

First, the backside setup was characterized regarding the temperature of the mesh, the activated species measured by optical emission spectroscopy, and the dissipated power per half cycle determined by electrical characterization. The results are displayed in **Figure 85**.

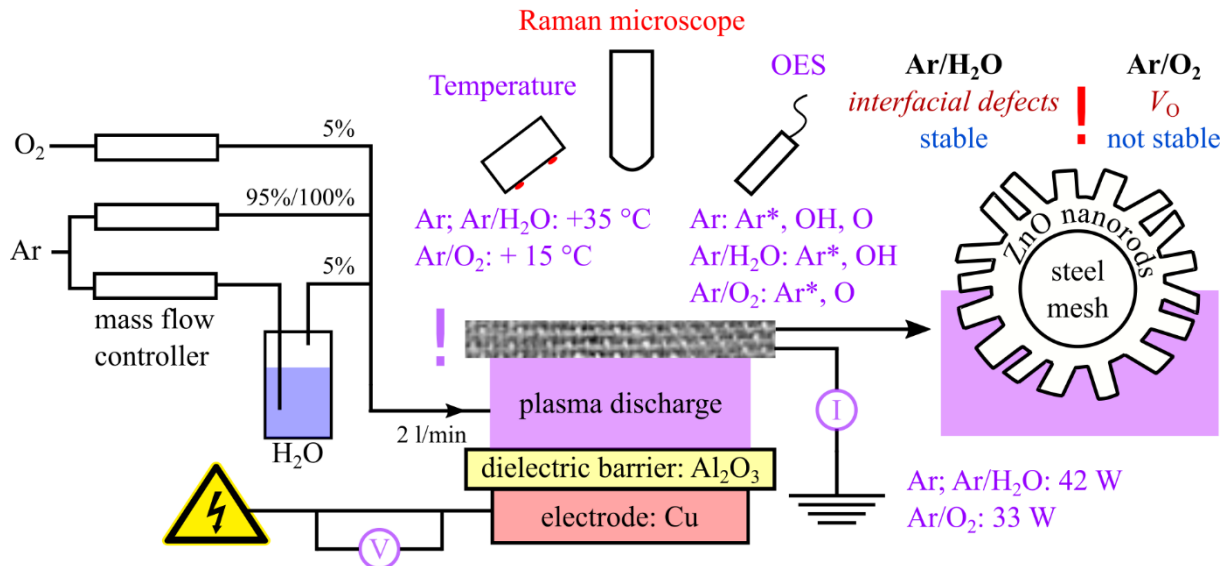


Figure 85: Results of the characterization of the plasma setup and defects determined in-situ by Raman spectroscopy induced by the remote plasma treatment dependent on the plasma gas mixture.

The temperature rise was determined to be 35 °C in Ar and Ar/H₂O plasma treatments, while the Ar/O₂ plasma only increased the temperature by 14 °C. This was related to the dissipated power per half cycle, which was higher in the case of Ar and Ar/H₂O plasmas (42 W) compared to Ar/O₂ plasmas (33 W). The optical emission spectroscopy revealed that the excited Ar species were very similar for all investigated gas mixtures, but the reactive oxygen species differed: While for Ar/O₂ plasma, only transitions related to O were found, Ar/H₂O plasma showed only OH related transmissions. The pure Ar plasma showed both reactive oxygen species. Although the characterization of the plasma is far from complete, it gave a first impression of the plasma properties.

By using the backside in-situ Raman spectroscopy, the plasma effluent-induced changes on zinc oxide nanorods were studied. In particular, the modification of the ZnO-NR surface-near region as a function of different plasma gas mixtures was evaluated: The plasma treatment using pure Ar led to minor interactions with the Zn sub-lattice, while Ar/O₂ and Ar/H₂O plasma treatments introduced defects in the ZnO-NR surface near region (**Figure 85**). Furthermore, Ar/H₂O plasma treatments steadily increased the SO phonon mode throughout the complete plasma treatment, most likely caused by an increased surface roughness as seen in HR-TEM. On the contrary, Ar/O₂ led to a rapid increase in oxygen-related defect density (e.g. VO), mainly during the initial phase of the plasma treatment (**Figure 85**). Overall, the presented in-situ study demonstrated that oxygen-related reactive species must be present in the plasma effluent in order to introduce defects via interactions with the Zn sub-lattice, determining the defect structure rather than the dissipated power or (low) temperature of the substrate.

Ex-situ measurements showed that the plasma-induced oxygen defects using Ar/O₂ were not stable, while Ar/H₂O plasma treatments formed long-time stable interfacial defects in the zinc oxide nanorods. These results have a strong impact on the understanding of oxidative plasma processes.

4.5 In-situ backside Raman investigation of zinc oxide nanorods in an atmospheric-pressure dielectric barrier discharge plasma

4.6 In-situ backside XANES investigation of zinc oxide nanorods in an atmospheric-pressure DBD plasma

4.6 *In-situ backside XANES investigation of zinc oxide nanorods in an atmospheric-pressure DBD plasma*

The results gained in chapter 4.5 by Raman spectroscopy were insufficient to fully understand the respective mechanism behind the seen ZnO NR modifications: It remains unclear how the plasma interacted explicitly with the Zn (seen in the increased E_2^{low}), how oxygen vacancies were formed in an Ar/O₂ plasma, and, most of all, what modifications resulted in the increased surface optical photon mode seen for the Ar/H₂O plasma treatment. Therefore, an additional measurement method was needed for detailed analysis.

XANES measurements provide information about the coordination environment of a chosen element, including atomic geometrical distortions as well as the unoccupied band structure. Thus, it is a perfect addition to the Raman investigation performed in chapter 4.5. However, the conditions on the beamline regarding space and measurement method required a new measurement approach displayed in **Figure 86**.

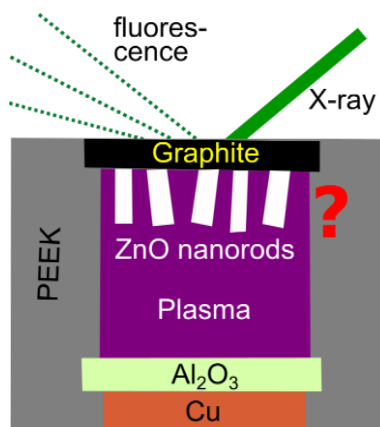


Figure 86: Experimental approach for investigating the plasma treatment of ZnO nanorods *in-situ* by XANES.

The porous electrode was substituted by a graphite foil, which is almost transparent for X-rays at 8-10 keV, thus for the incident beam and the resulting fluorescence. The electrical conductivity of the graphite allowed the application of the same coating process used for the steel mesh. Thereby, the ZnO nanorods should protect the graphite, shielding it from the influence of the plasma. Moreover, in this approach, direct contact of the ZnO nanorods with the plasma was studied, contrary to the indirect plasma treatment investigations described in chapter 4.5.

4.6 In-situ backside XANES investigation of zinc oxide nanorods in an atmospheric-pressure DBD plasma

4.6.1 Experimental approach

The plasma was ignited at a voltage of 10 kV and 12 kV. These high ignition voltages are a result of the increased plasma gap (2 mm). Because after 10 minutes plasma treatment (used in chapter 4.5) no significant change in the XANES spectra was observed, the in-situ measurement was extended. Unfortunately, during the Ar measurement at 12 kV and over 1 h treatment time, the cell broke down, likely caused by the increased temperature inside the plasma cell. Post-evaluation of the cell revealed that the adhesive (UHU 300 plus) entered the plasma gap due to liquefaction at elevated temperatures. The UHU 300 plus is stable up to 100 °C, showing that significantly elevated temperature had to be present during the 1 h plasma treatment at 12 kV. Due to the lack of a cooling system for the plasma setup, this temperature rise is not against expectation. Unfortunately, due to an unexpected breakdown of the second cell, not all experiments could be carried out during the given measurement time at PETRA III. Therefore, in-situ Ar/O₂ measurements are missing completely as well as the Ar/H₂O measurement at 12 kV.

All other modifications and measurements were carried out as described in chapter 3.

4.6.2 Results and Discussion

The successful deposition of the graphite foil with ZnO nanorods was confirmed by FE-SEM images shown in **Figure 87**.

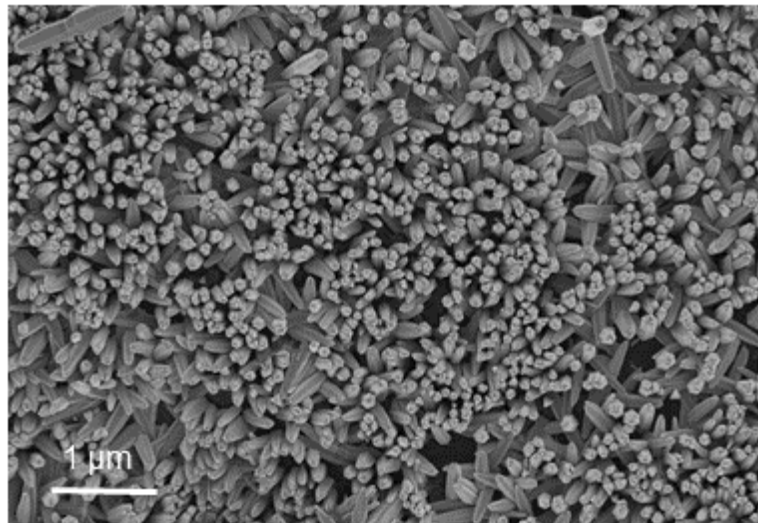


Figure 87: FE-SEM image of ZnO nanorods on graphite foil.

The ZnO nanorods homogenously cover the foil, showing a nanorod size comparable to the coating of the mesh seen in chapter 4.5. Due to the high density of the ZnO nanorods, the graphite foil should be mostly shielded from the plasma, suppressing unwanted side reactions.

4.6 In-situ backside XANES investigation of zinc oxide nanorods in an atmospheric-pressure DBD plasma

Typical XANES and EXAFS spectra of the ZnO NR (Zn K-edge) are presented in **Figure 88**.

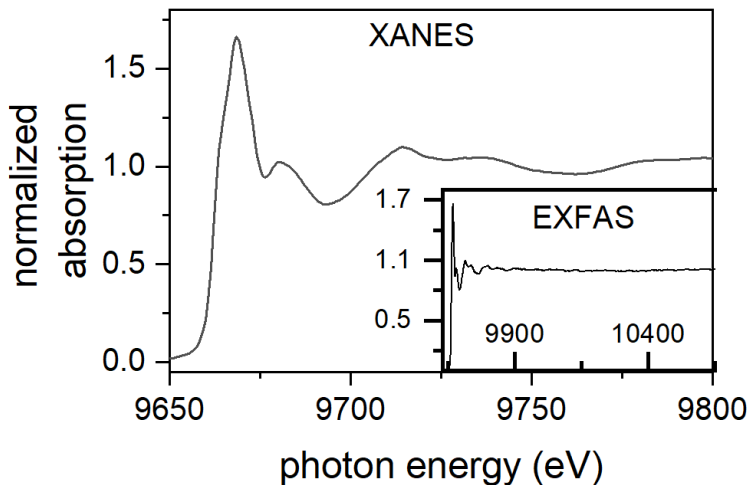


Figure 88: Zn K-edge XANES and EXAFS spectra of untreated ZnO nanorods electrochemically deposited on graphite foil.

The obtained spectra looked similar to spectra reported in the literature for ZnO nanorods^{[188],[189]}, concerning the measurement angle^[189] (in our case 45 °) and the polarization^[188] (in our case default linear polarization in plane of the storage ring).

In **Figure 89**, the evolution of the normalized absorption of the in-situ XANES absorption edge maximum (at 9670 eV) for the different plasma gases and voltages is displayed.

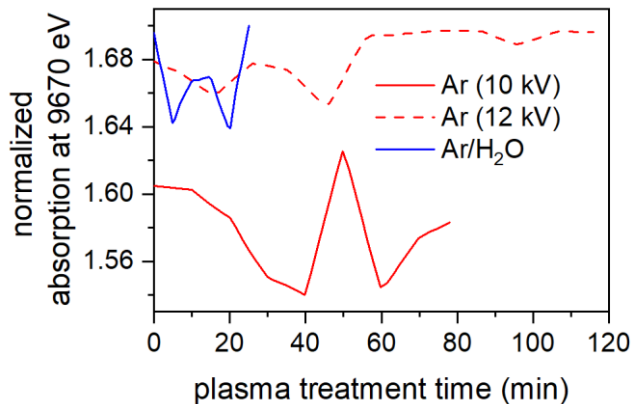


Figure 89: Evolution of the normalized absorption of the in-situ XANES spectra at 9670 eV for different plasma gases and voltages.

The amplitude of the absorption edge should be sensitive to changes in the oxidation state of the ZnO and, in limits, its coordination.^[190] However, no clear trend was observed during the plasma treatment regardless of the voltage or plasma gas. Because the evaluation of the XANES spectrum is not limited to the amplitude of the absorption edge, in the following, the contour maps of the XANES spectra for the different plasma treatments will be presented. To increase the visibility of the changes, the absorption edge maximum is not further considered in the display range.

4.6 In-situ backside XANES investigation of zinc oxide nanorods in an atmospheric-pressure DBD plasma

The in-situ XANES measurement of the Ar plasma treatment is presented in **Figure 90**. Although the time between two XANES measurements was roughly 1 min, only every 10th spectra were normalized by Michal Nowakowski (workgroup of Prof. Dr. Bauer, University of Paderborn) due to the slow and subtle changes over the whole dataset. Therefore, the contour plots display only one spectrum each 10 min.

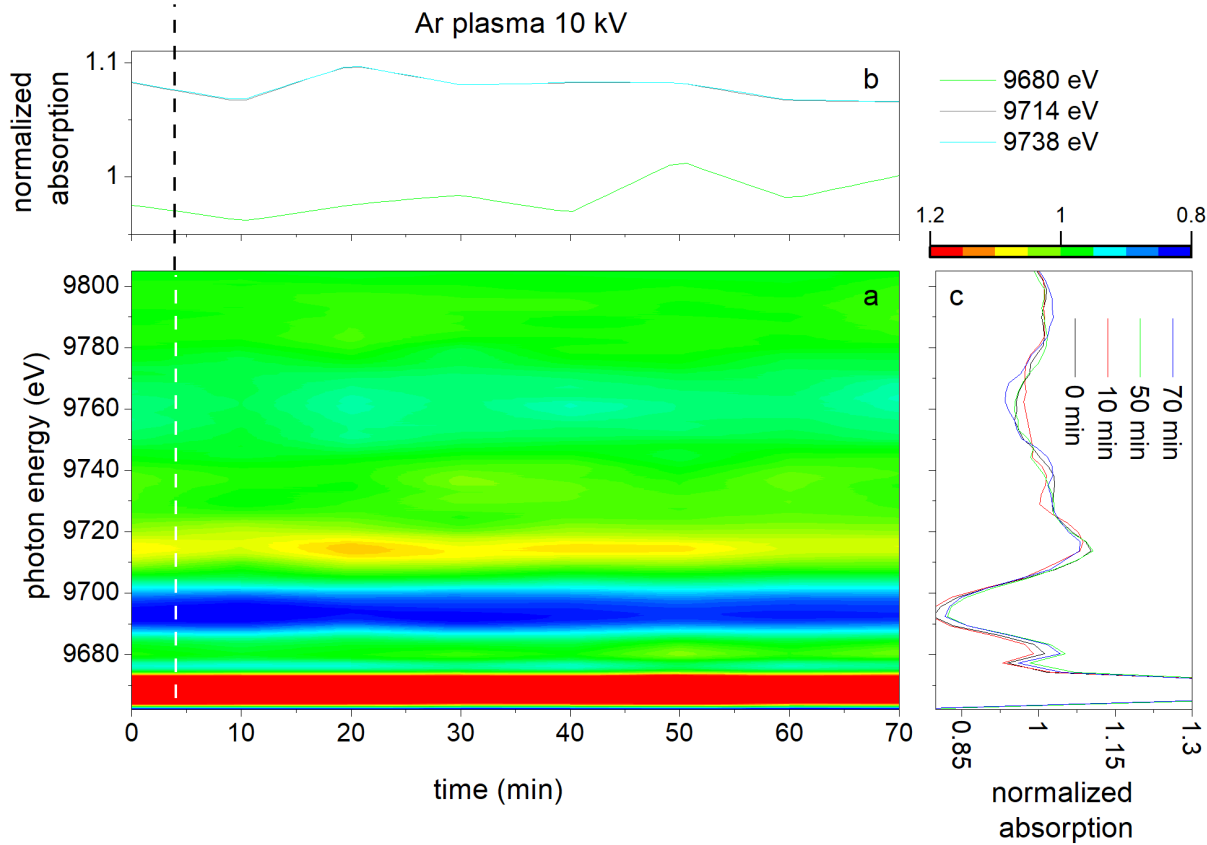


Figure 90: a) Contour map of the in-situ XANES investigation of the Ar plasma treatment at 10 kV, the range adjusted to the region below the absorption edge. b) Line profile for chosen photon energies and c) XANES spectra for the respective time.

In **Figure 90**, no trend during the plasma was seen. The fluctuations observed were assigned to the measurement uncertainty, giving an error in the normalized absorption of approximately ± 0.02 . In chapter 4.5, an increase in the E_2^{low} was seen during the Ar plasma. However, no similar response was found in the XANES spectra. It is not straightforward to compare both approaches because they differ in the plasma gap (resulting in a different voltage) and direct and indirect plasma treatment of ZnO. However, the direct plasma treatment studied by the XANES measurements should lead to a more pronounced interaction of ZnO with the plasma than for indirect plasma treatments. Likewise, an increased voltage should lead to a higher amount of reactive species in the plasma and therefore increase the plasma/surface interactions. Thus, stronger interactions are expected, but no significant changes were observed.

4.6 In-situ backside XANES investigation of zinc oxide nanorods in an atmospheric-pressure DBD plasma

A similar result is achieved when evaluating the in-situ XANES measurement of the Ar/H₂O plasma treatment of the ZnO nanorods (**Figure 91**).

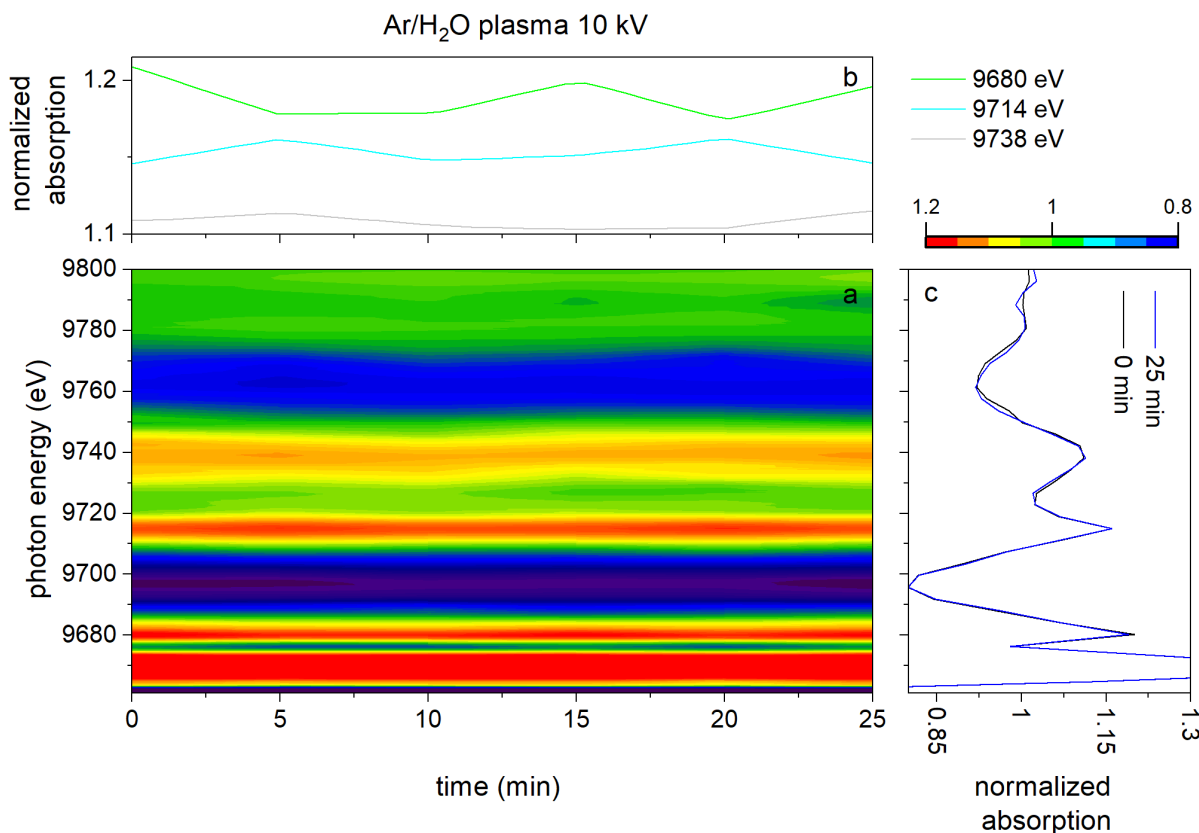


Figure 91: a) Contour map of the in-situ XANES investigation of the Ar/H₂O plasma treatment, the range adjusted to the region below the absorption edge. b) Line profile for chosen photon energies and c) XANES spectra for the respective time.

No pronounced effect or trend was observed during the 25 minutes Ar/H₂O plasma treatment either, although in Raman a pronounced and steady increase in the surface optical mode during the 10 minutes plasma treatment was observed. The increase in the surface optical mode should be related to changes in the grain boundaries or intrinsic zinc. Both changes should be evident in the XANES measurements by changes in the amplitude in the absorption edge, changes in the edge jump, and changes in the interference positions.^[190] Different explanations are possible for the missing response: again, a different cell is used, changing important plasma parameters (reactive species, synergistic effects, voltage, plasma gas). Consequently, the properties of the plasma might have changed in such a way that ZnO nanorods were not modified. Secondly, and most likely, the used approach to measure the fluorescence through the backside of the ZnO nanorods led to a signal dominated by the bulk properties of the ZnO rather than the surface. Sipr et al. found by modeling that the intensity of XANES spectra is more related to the bulk than to the surface.^[191] Additionally, fluorescence is known to be more bulk sensitive than XANES measured directly in transmission.^[79] Thus, the chosen in-situ setup is most likely not surface-sensitive enough to monitor the surface modifications induced by the plasma treatment.

4.6 In-situ backside XANES investigation of zinc oxide nanorods in an atmospheric-pressure DBD plasma

To rule out that the plasma was not sufficient to modify the ZnO nanorods, the Ar plasma treatment was repeated using a higher voltage (12 kV) and a longer treatment time (2 h) (**Figure 92**).

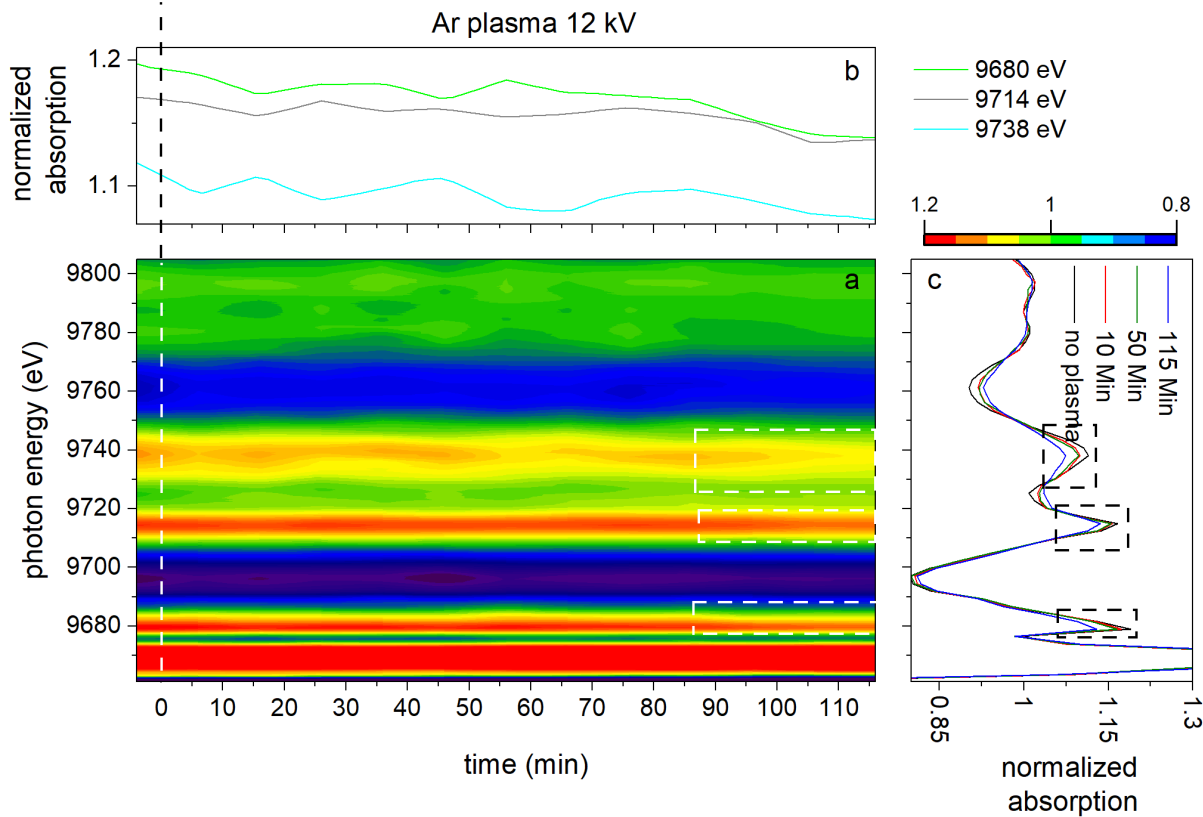


Figure 92: a) Contour map of the in-situ XANES investigation of the Ar plasma treatment at 12 kV, the range adjusted to the region below the absorption edge. b) Line profile for chosen photon energies and c) XANES spectra for the respective time.

At higher voltages, minor changes following a trend were seen in the XANES spectra, showing the amplitude of the interferences at photon energies higher than the adsorption edge to converge with time, first slightly within the error determined in **Figure 90**, but after 90 minutes in a more pronounced way. However, the change after long treatment times is more likely due to the increased temperature in combination with the plasma rather than the influence of the plasma itself. As was already described in the experimental part, the plasma cell broke due to the melting of the adhesive, indicating a temperature above 100 °C at the end of the plasma treatment. However, if the changes were (i) an effect of temperature alone, (ii) a result of adhesive entering the plasma gap, or (iii) a synergetic effect of temperature and plasma to initiate the modification of the surface or modification of the ZnO bulk by the synergetic effect cannot be answered. To completely understand the changes seen in the XANES spectra, detailed fitting by using ab-initio calculations would have to be performed. Because the origin of the changes seen in **Figure 92** is unclear, no such time-consuming post-treatment was performed. However, it demonstrates that certain changes in ZnO nanorods can be monitored in-situ by XANES using fluorescence.

4.6 In-situ backside XANES investigation of zinc oxide nanorods in an atmospheric-pressure DBD plasma

4.6.3 Conclusions

In-situ XANES was applied to monitor the changes induced by the atmospheric-pressure plasma treatment of ZnO nanorods. No significant changes were detected during the Ar and Ar/H₂O plasma treatment using 10 kV, while the Ar plasma treatment at 12 kV showed a response in the XANES spectra after prolonged treatment times. However, if these changes resulted from the temperature alone or synergetic effects of the plasma and the temperature was not obvious. However, XANES in fluorescence mode performed from the backside might not be surface-sensitive enough to monitor the plasma-induced changes on the ZnO nanorods.

4.6 In-situ backside XANES investigation of zinc oxide nanorods in an atmospheric-pressure DBD plasma

4.7 In-situ backside DRIFTS investigation of functional groups in an atmospheric-pressure DBD plasma

4.7 In-situ backside DRIFTS investigation of functional groups in an atmospheric-pressure DBD plasma

In plasma treatments of organic components (polymers, medicine), multiple functional groups are in contact with the plasma and show different reactions based on the surface and the plasma parameters, exacerbating the identification of reaction pathways and optimizations. To determine the interactions between the plasma gas effluent and one specified functional group, the backside method was applied by investigating a self-assembled monolayer (SAM) as a “reporter molecule” using DRIFTS (**Figure 93**). Due to the spontaneous unidirectional orientation of the adsorbing molecules, only one specific functional group (determined by the chosen SAM molecule) is in contact with the plasma effluent. This approach was verified using octadecyl phosphonic acid (ODPA) as SAM on top of ZnO-nanorods (coated the same way as in chapter 4.5) to ensure complete adsorption. ODPA consists of a phosphonic acid group responsible for the adsorption on the surface and an aliphatic tail built up of 17 CH_2 groups and ending in a CH_3 group. The etching of aliphatic carbon in a direct DBD plasma was already observed in chapter 4.1.

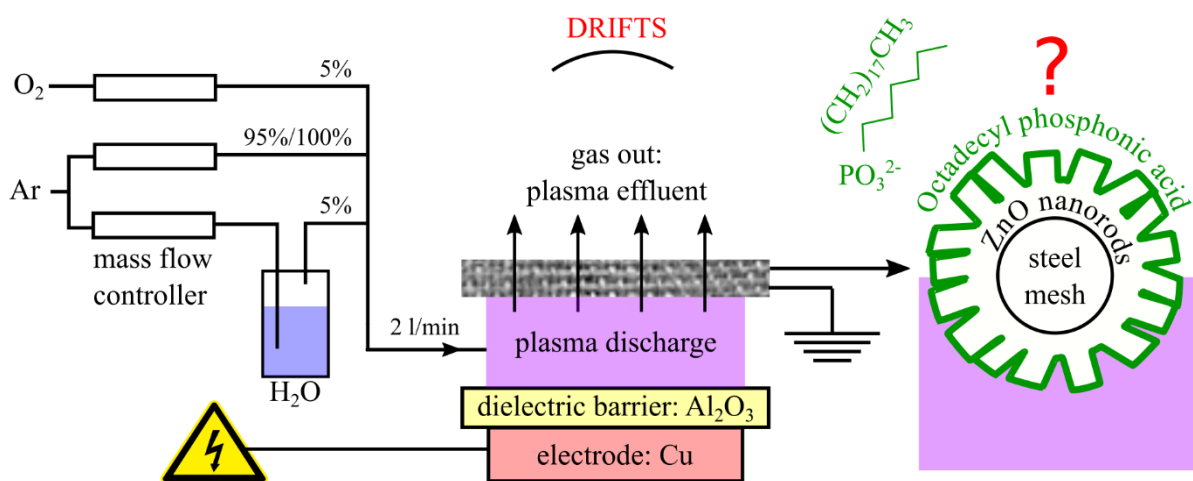


Figure 93: In-situ monitoring of the indirect plasma/ODPA interaction using the backside setup combined with DRIFTS measurements.

4.7.1 Experimental approach

4.7.1.1 Plasma treatment

The high voltage was produced by a G2000 high voltage generator (Redline, Germany) and was set to 5.3 kV for all plasma gas mixtures using a frequency of 35 kHz.

4.7.1.2 Octadecyl phosphonic acid (ODPA) adsorption

A 1 mM solution of ODPA in THF was used in order to form a self-assembled monolayer on the ZnO coated mesh. The samples were immersed in the ODPA-solution for 2 h, subsequently rinsed with THF, and dried with a stream of air. Afterward, the mesh was stored in an exsiccator for at least overnight.

All other modifications and measurements were carried out as described in chapter 3.

4.7.2 Results and Discussion

FE-SEM images of the meshes were taken before and after the immersion in ODPA to ensure that no etching effects were visible as were detected on ZnMgAl in chapter 4.2 (**Figure 94**).

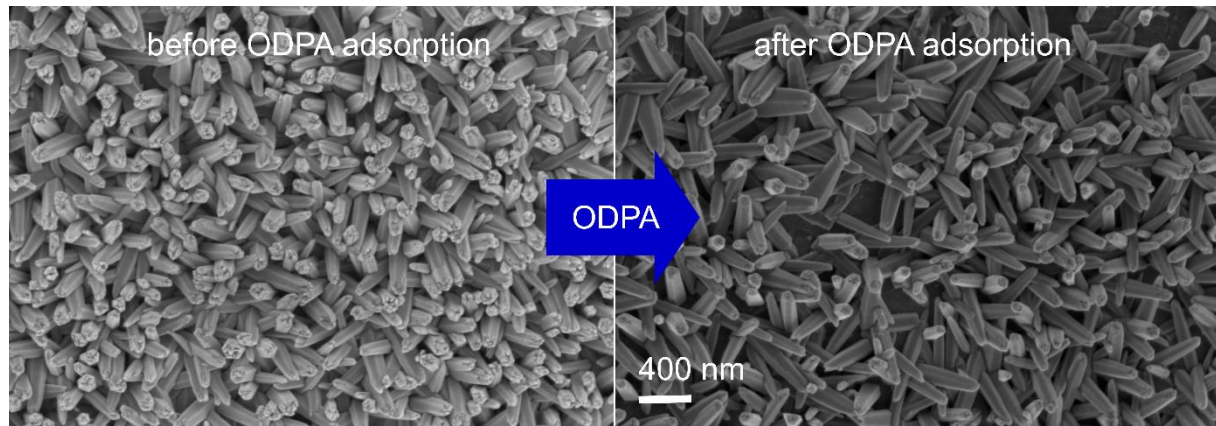


Figure 94: FE-SEM images before and after the ODPA adsorption on the ZnO coated steel mesh.

The FE-SEM images showed no change in the morphology of the ZnO nanorods after the ODPA adsorption, confirming the stability of the ZnO nanorods in the ODPA solution. This was not the case for immersions in 12-aminododecyl phosphonic acid (data not shown here), where the nanorods were highly etched. Thus, ZnO nanorods may not be suitable for all kinds of self-assembled monolayers. Instead, the usage of thiol-gold chemistry for adsorption experiments on gold-coated meshes could offer a good alternative.

4.7.2.1 In-situ DRIFTS evaluation of the gas phase

In the backside plasma setup, the plasma-activated gas is directed through the ODPA/ZnO/steel mesh sample, where the backside is monitored in-situ and real-time by DRIFTS (**Figure 93**). Thus, DRIFTS not only detects the sample surface but the plasma effluent as well. This includes, for example, atmospheric CO₂. Often, the signal coming from the gas phase was much stronger than the signal from the surface. Thus, two contour maps will be presented for each measurement: first, the range of contour map intensity was adjusted to the most notable changes coming from the gas phase. Later the same contour map intensity was adjusted to the changes ascribed to the surface. The in-situ measurements were performed in the same way as in chapter 4.5 for the in-situ Raman measurements: After the respective gas flow was adjusted, DRIFTS was measured for 10 minutes without any plasma to determine the baseline. Then, the plasma was turned on for 10 minutes while continuing the DRIFTS measurements, detecting the plasma-induced changes. The measurement was continued further for 10 minutes after the plasma was turned off to monitor reversible changes on the surface and gas. In **Figure 95**, the in-situ DRIFTS measurement of the ODPA coated mesh using Ar/O₂ is presented as contour plot the same way as the Raman measurements in chapter 4.5. In **Figure 95a**, the absorption spectra collected in-situ before, during, and after the plasma treatment using Ar/O₂ as plasma gas are displayed as contour map. The black areas indicate low intensity, whereas bright green areas illustrate high intensities of the respective absorption spectra. The x-axis shows the time in seconds, where the plasma was switched on at 0 s and off after 600 s. **Figure 95b** presents the evolution of the absorbance of selected peaks determined from the contour

4.7 In-situ backside DRIFTS investigation of functional groups in an atmospheric-pressure DBD plasma

plot. **Figure 95c** displays the averaged spectra over 600 s before, during, and after the plasma, respectively.

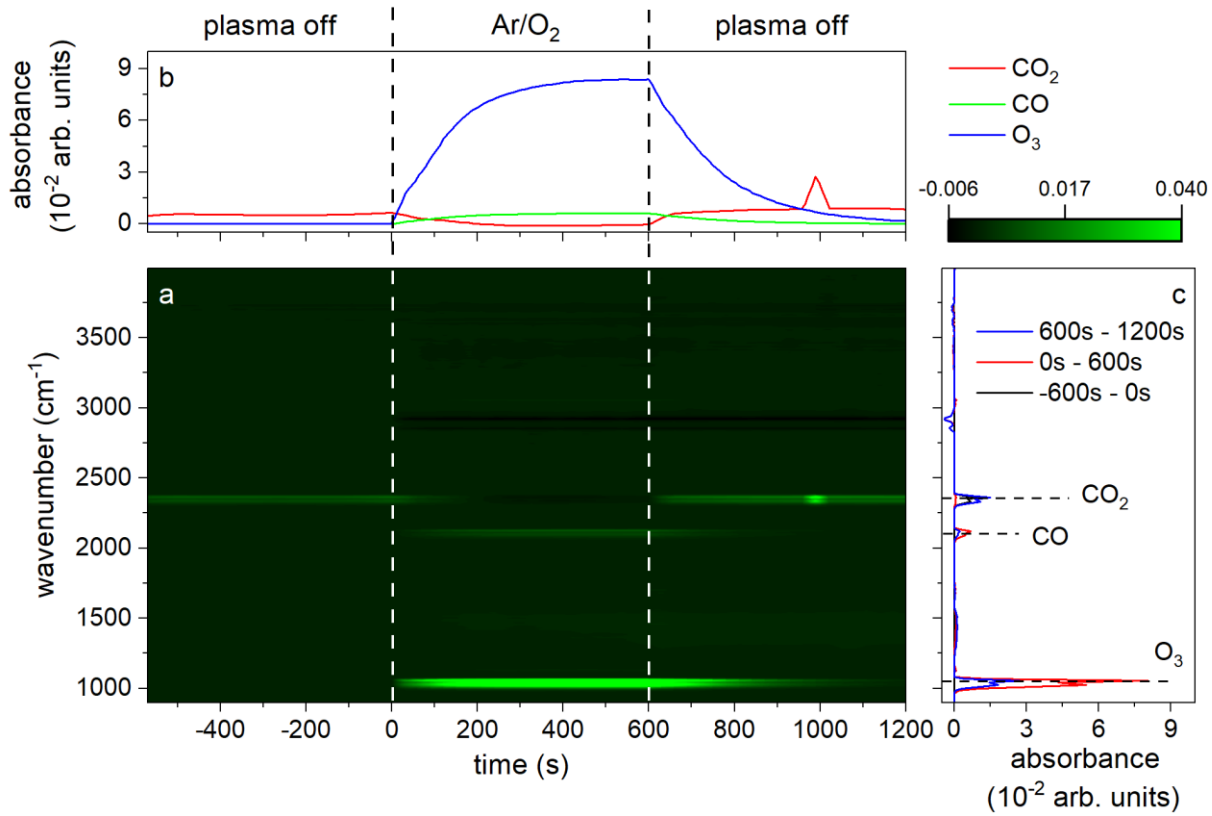


Figure 95: a) Contour map of the in-situ DRIFTS investigation of the Ar/O_2 plasma treatment range adjusted to the gas phase, b) line profile for detected gas phase components, and c) averaged DRIFTS spectra over the respective time.

In **Figure 95**, the influence of the plasma is clearly seen: When the plasma was turned on (0 s), peaks at 1050 cm^{-1} and 2050 cm^{-1} evolved, while peaks at 2450 cm^{-1} , 2950 cm^{-1} , and 3400 cm^{-1} decreased. Thereby, the peak at 1050 cm^{-1} is assigned to ozone^{[192]–[194]}, the peak at 2050 cm^{-1} to CO ^{[195]–[198]}, and 2450 cm^{-1} to CO_2 ^{[197],[199]}, all being in the gas phase. As stated before, the backside setup allows the monitoring of the surface and the gas phase (containing now stable species of the plasma effluent). The contour map adjusted to the surface will be presented and discussed separately in more detail later in this chapter.

The capability of DBDs to create ozone when containing oxygen is already known^{[46],[168],[200]}, as well as its capability of decomposing CO_2 forming CO .^{[11],[201],[202]} Thereby, the rotational energy of CO_2 is excited in the plasma, giving rise to its decomposition with other reactive species.^{[11],[57]} In **Figure 95b**, a correlation of the CO and the CO_2 signal is seen: the CO_2 decreased in the same way as CO increased, making the decomposition of CO_2 to CO in the Ar/O_2 plasma likely. However, the decomposition reported in the literature was conducted in mixtures containing a high amount of CO_2 . Here, the CO_2 is present in an Ar/O_2 gas mixture (both gases are Linde 6.0 (high purity)), showing that only a low amount of CO_2 could be present in the gas phase. Thus, the decomposition seems to be working even with low concentrations of CO_2 . In addition to CO , O_3 increased steadily during the plasma. This can be attributed to the fact that the plasma cell was open to the DRIFTS cell, allowing the plasma effluent to distribute into the DRIFTS cell and thus constantly enriching the signal. When the plasma was turned off (600 s), a slow decrease of CO and O_3 was seen, while CO_2 quickly gained a similar level than before the plasma. As the plasma cell was continuously flushed with the respective gas mixture (even when the plasma was turned off), this accumulation can explain both the origin of the CO_2 (from the gas mixture) and the enrichment of ozone

4.7 In-situ backside DRIFTS investigation of functional groups in an atmospheric-pressure DBD plasma

during the plasma. Interestingly, the ozone was relatively stable in the DRIFTS cell, being present in at least small quantities even after 10 minutes after the plasma was turned off.

Contrary, in the real-time pure Ar and Ar/H₂O DRIFTS measurements, only CO₂ was detected. Interestingly, in both measurements, a decrease in the CO₂ was found without a corresponding CO peak. The evolution of the CO₂ for the respective plasma treatments is compared in **Figure 96**.

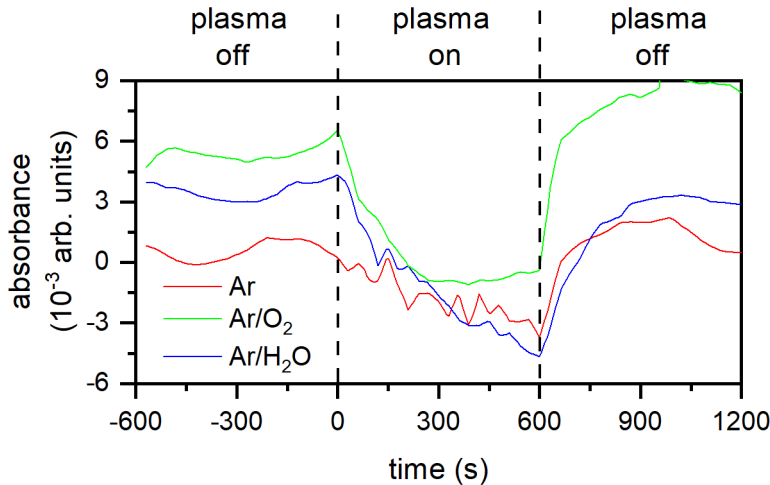


Figure 96: Evolution of the CO₂ peak absorbance during the respective plasma gas treatment.

While the CO₂ amount stabilized during the Ar/O₂ plasma treatment after 250 s, Ar and Ar/H₂O showed a steady decrease during the plasma treatment. Combined with the missing of a CO peak, a different mechanism had to be present during the Ar and Ar/H₂O plasma reducing the CO₂ amount in the gas phase.

4.7 In-situ backside DRIFTS investigation of functional groups in an atmospheric-pressure DBD plasma

4.7.2.2 XPS characterization of the ODPA adsorption and the plasma treatments

XPS of the ZnO coated steel mesh was measured before and after the ODPA adsorption and the respective plasma treatments thereafter. **Figure 97** shows the respective survey spectra.

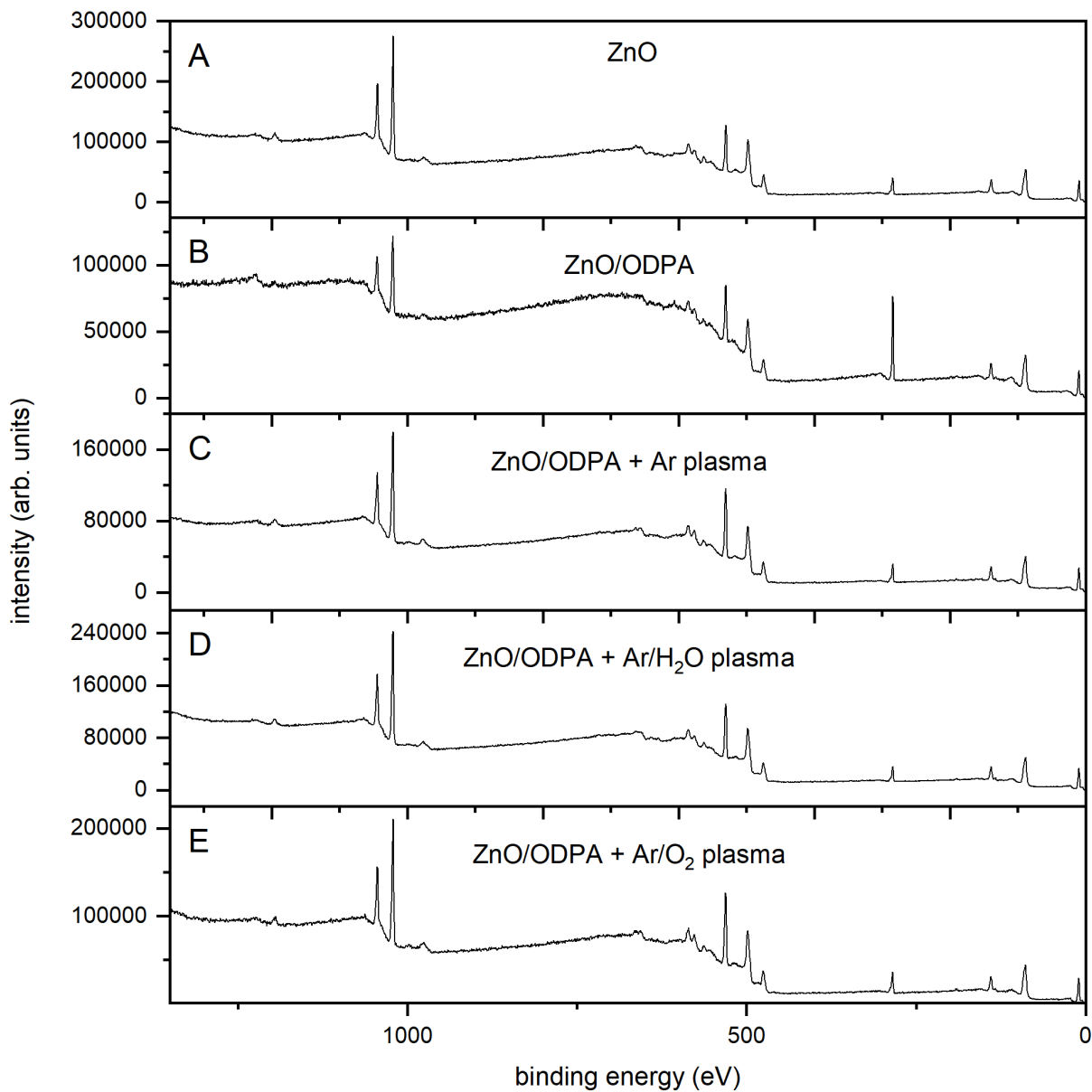


Figure 97: Survey spectra of A) steel mesh coated with ZnO nanorods, B) immersed for 2 h in 1 mM ODPA solution, and C, D, E) after the respective plasma treatment.

The survey spectra of the ZnO-coated steel mesh only showed the presence of Zn, O, and C, confirming the complete covering of the steel mesh. The successful adsorption of ODPA was confirmed by the presence of phosphor and a strong increase in the carbon, as already described in chapter 4.2. After the plasma treatments, no additional elements were found, so that all plasma products seen in the DRIFTS measurements have to be consisting of C and O.

4.7 In-situ backside DRIFTS investigation of functional groups in an atmospheric-pressure DBD plasma

The quantification based on the respective core-level spectra is presented in **Table 20**.

Table 20: XPS quantification of the pure ZnO nanorods, after the immersion in 1 mM ODPA, and thereafter performed plasma treatments based on the core-level spectra. Additionally, some ratios are presented calculated from the respective at%.

	C (at%)	O (at%)	Zn (at%)	P (at%)	O/Zn	C/P
ZnO	33.8	38.5	27.7	--	1.4	--
ZnO/ODPA	66.9	21.8	9.4	1.9	2.3	35.2
ZnO/ODPA Ar plasma	29.0	43.4	24.5	3.0	1.8	9.7
ZnO/ODPA Ar/O₂ plasma	31.3	43.0	23.0	2.7	1.9	11.6
ZnO/ODPA Ar/H₂O plasma	27.6	42.6	26.6	3.2	1.6	8.6

In **Table 20**, additional ratios based on the respective quantification results are presented as well. The O/Zn ratio gives an impression of the amount of oxygen on the surface. In a perfect ZnO bulk crystal, the O/Zn ratio is 1. This value naturally increases on the surface due to stabilization by hydroxide groups. Additionally, oxygen coming from the adventitious carbon layer increase the ratio as well. The C/P ratio indicates how much carbon is present on the surface compared to the ODPA molecule. In the ODPA molecule, the C/P ratio is 18 due to the given chain length. By comparing this expectation to the experimental ratio after the ODPA immersion (35.2), many carbon contaminations had to be still present on the surface after the ODPA adsorption. All plasma gas mixtures led to very similar quantification results, reducing the carbon even lower than for the untreated ZnO. The removal of carbon in the plasma was also observed on ZnMgAl (chapter 4.1). Most interestingly, P was still found on the surface after all plasma treatments. The observed increase in the atomic percentage is solely due to the simultaneous drop in the carbon concentration. The presence of the P after the plasma treatment can be explained either by the strong binding on the ZnO surface, or it was protected by plasma-stable C-related plasma products formed during the decomposition, such as COOH terminating an aliphatic carbon chain. That oxygen-containing products were formed during the plasma can be expected due to the increase in the total amount of O on the surface supported by the increase in the O/Zn ratio with respect to untreated ZnO.

4.7 In-situ backside DRIFTS investigation of functional groups in an atmospheric-pressure DBD plasma

In chapter 4.1, carbonates were identified as the primary plasma product. Thus, the C 1s peak was evaluated as well (**Figure 98**). As it is difficult to distinguish between CO_2^- and CO_3^{2-} on Zn, the broad peak at 288,5 eV was assigned to both components.

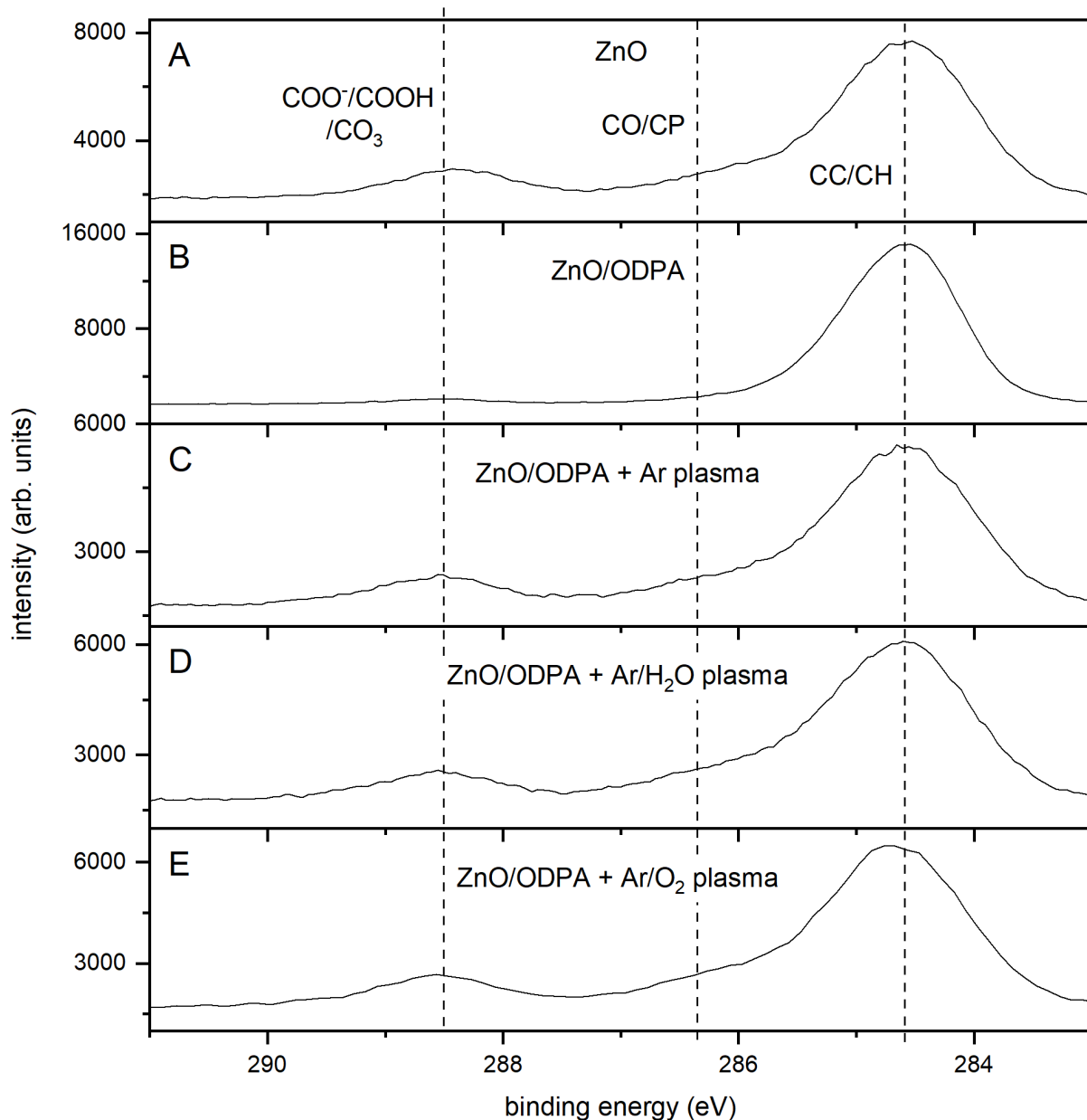


Figure 98: C 1s high-resolution spectra at different treatment steps: A) untreated ZnO-NR, B) ODPA coated ZnO-NR, C) ODPA coated ZnO-NR after Ar plasma treatment, D) ODPA coated ZnO-NR after Ar/O₂ plasma treatment, and E) ODPA coated ZnO-NR after Ar/H₂O plasma treatment.

The increase in the CC/CH functionality after the ODPA adsorption is clearly seen in **Figure 98b**. Unfortunately, still signs of $-\text{CO}-$ and CO_2/CO_3 were found, indicating a not complete coverage of the ODPA as already indicated by the C/P ratio.

4.7 In-situ backside DRIFTS investigation of functional groups in an atmospheric-pressure DBD plasma

After the plasma treatments (**Figure 98 c-e**), all C 1s spectra look alike and very similar to the pure ZnO. Thus, a fitting of the C 1s was performed. The resulting percentage was multiplied with the amount of carbon gained by the quantification (**Table 20**) to obtain the atomic concentration of the respective carbon species on the surface. The results are presented in **Table 21**.

Table 21: Quantification of the C 1s of the pure ZnO nanorods, after the immersion in 1 mM ODPA, and thereafter performed plasma treatments.

	CC/CH (at%)	-CO-/CP (at%)	CO ₂ ⁻ /CO ₃ (at%)
ZnO	25.0	4.4	4.4
ZnO/ODPA	60.5	4.5	1.9
ZnO/ODPA Ar plasma	21.5	3.9	3.6
ZnO/ODPA Ar/O₂ plasma	22.5	4.7	4.1
ZnO/ODPA Ar/H₂O plasma	19.8	4.3	3.5

Again, the adsorption of ODPA is clearly visible by the strong increase in the CC/CH peak. Still, CO₂⁻/CO₃ was found on the surface but in a lower amount than on the untreated sample. Thus, despite the remaining carbon, nearly complete coverage is assumed. After the plasma treatments, the amount of CC/CH was clearly decreased, and CO₂⁻/CO₃ was increased. The -CO-/CP peak nearly remained constant. Since the P remained unchanged on the surface, as was seen by the quantification results, CO₂⁻/CO₃ should be the main reaction product during the CH₂ decomposition. However, since the spectra before and after the plasma treatment look so much alike, desorption of plasma products in the high vacuum of the XPS chamber or adsorption of contaminations from the air (especially at the unpolar sidewalls of the ZnO NR) after the plasma treatment cannot be ruled out.

4.7 In-situ backside DRIFTS investigation of functional groups in an atmospheric-pressure DBD plasma

4.7.2.3 In-situ DRIFTS evaluation of the surface

To get a better impression of the changes on the surface, the contour maps were adjusted to the absorbances of the signals assigned to the surface. The contour map of the in-situ DRIFTS measurement during the indirect Ar plasma treatment is shown in **Figure 99**.

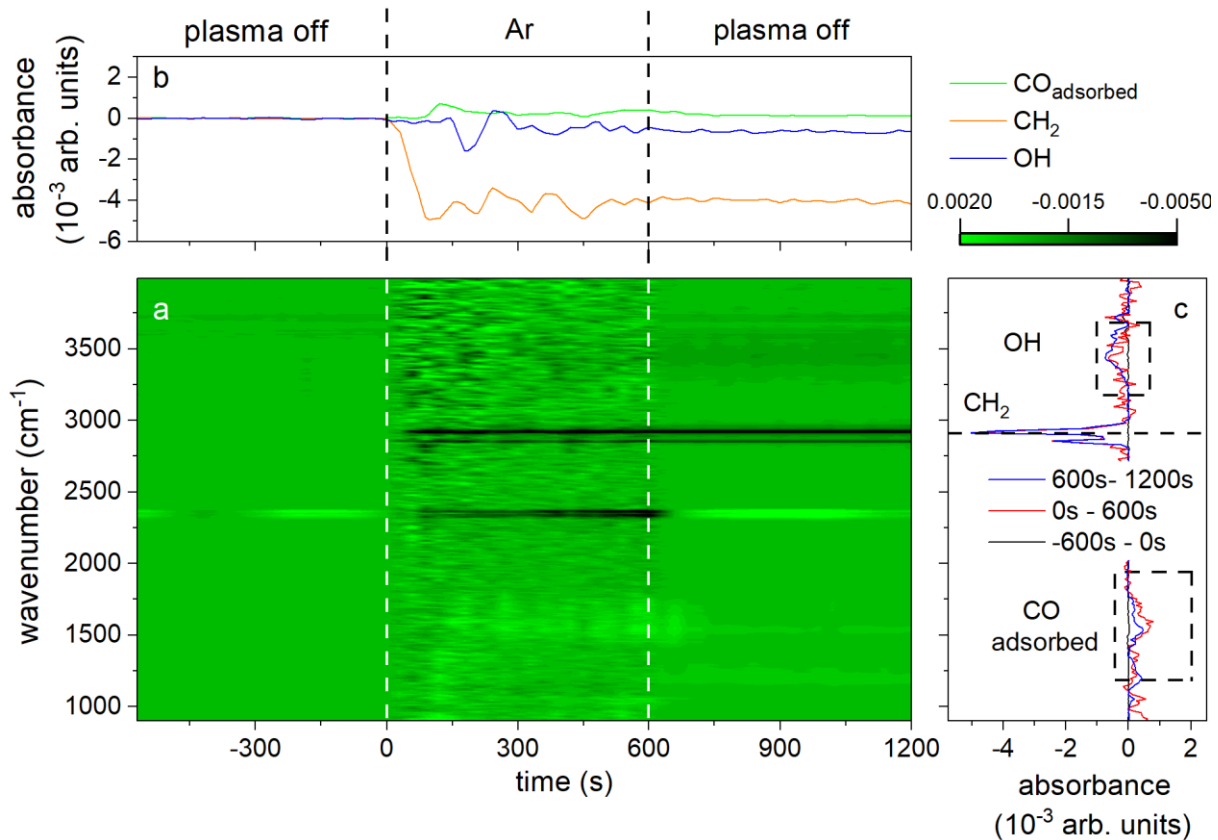


Figure 99: a) Contour map of the in-situ DRIFTS investigation of the Ar plasma treatment range adjusted to the surface, b) line profile for detected surface changes, and c) averaged DRIFTS spectra over the respective time.

Again, the influence of the plasma is clearly seen: When the plasma was turned on (0 s), peaks in the fingerprint region rose while peaks at 2950 cm^{-1} and 3400 cm^{-1} decreased. The peaks in the fingerprint are likely some kind of CO components, the peaks at 2920 cm^{-1} and 2960 cm^{-1} were assigned to CH_2 [70],[203], and the peak at 3400 cm^{-1} to adsorbed OH on the surface^[187]. This is in agreement with the XPS results, which showed the decomposition of CH_2 and an increase in $\text{CO}_2^-/\text{CO}_3$. Because multiple CO-related peaks can be found in the fingerprint region, this region will be evaluated in detail later in this chapter. The CH_2 is quickly removed within the first 90 s, showing the high impact of the plasma effluent on organic contaminations. However, within the first 30 s, only minor changes were seen, while in the succeeding 60 s (30 s – 90 s), a strong impact was observed. Here, it has to be kept in mind that the spectra are an accumulation of the total 30 s measurement time. Thus, the decomposition might begin before 30 s, but was masked by the accumulation. Interestingly, the fingerprint region just changed after the decomposition of CH_2 . Thus the plasma products forming on the surface are not a product of the CH_2 decomposition but of a subsequent process later in the plasma. After the plasma was turned off, a decrease in the CO_x region was seen, while the CH_2 and OH remained steady.

4.7 In-situ backside DRIFTS investigation of functional groups in an atmospheric-pressure DBD plasma

In **Figure 100**, the contour map of the in-situ DRIFTS measurement during the indirect Ar/O₂ plasma treatment is shown.

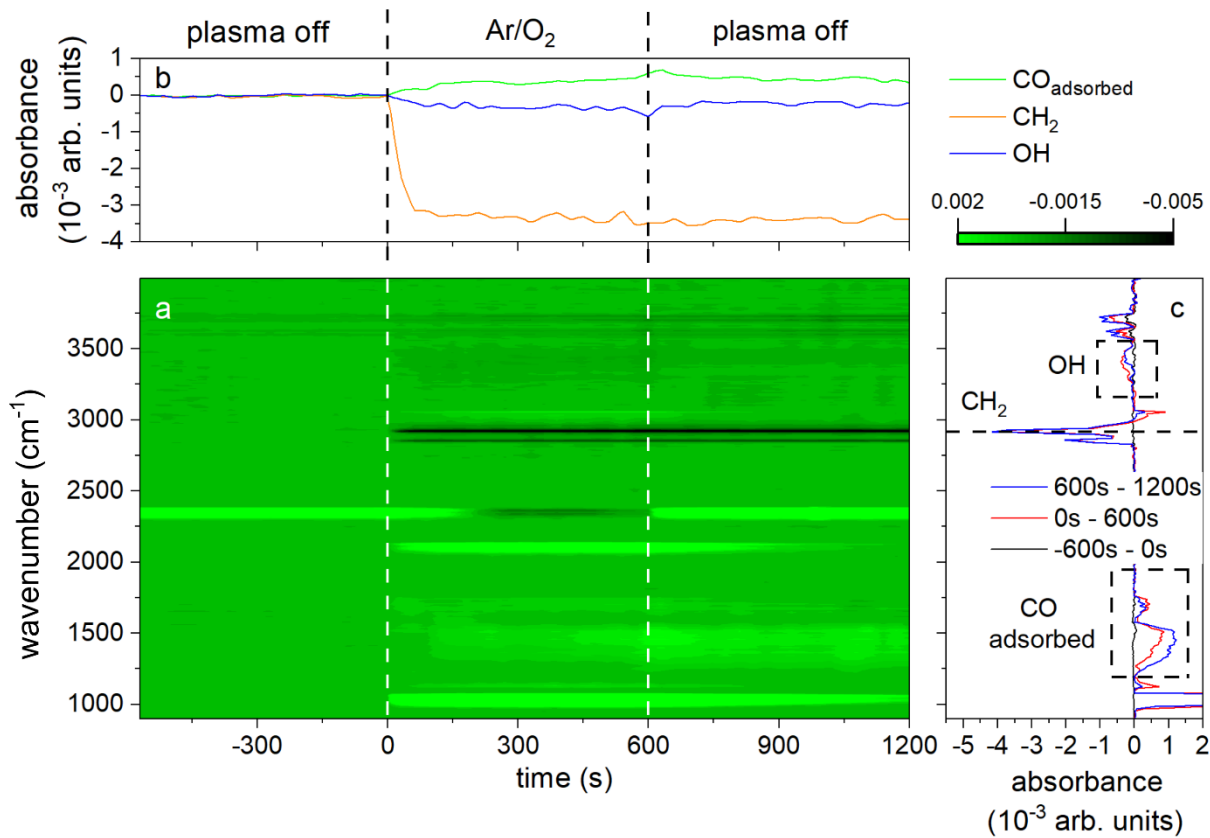


Figure 100: a) Contour map of the in-situ DRIFTS investigation of the Ar/O₂ plasma treatment range adjusted to the surface, b) line profile for detected surface changes, and c) averaged DRIFTS spectra over the respective time.

In addition to the peaks assigned to the gas phase (discussed before), peaks similar to those observed during the Ar plasma treatment were found for the indirect Ar/O₂ plasma treatment: CH₂ and OH were removed, while CO-related products formed on the surface. The CH₂ decomposition was even faster than for pure Ar, showing no delay and being completed after 60 s. Again, due to the accumulation of the spectra, the decomposition might be even faster. Interestingly, CO-related products were formed already during the decomposition of CH₂. This is either a result of the accumulation of multiple spectra (if the decomposition was finished before 30 s, the accumulated spectra captured both the end of the decomposition and the start of the CO_x accumulation), or a different CH₂ decomposition pathway was present. Additionally, signals of carbon trioxide were found at 1070 cm^{-1} , 2045 cm^{-1} (overlap with CO), and 3090 cm^{-1} .^[204] Carbon trioxide is known to form in plasmas in the presence of O₃ and CO₂ or O₂ and CO.^[204] If carbon trioxide is present in the gas phase or adsorbed on the surface cannot be distinguished.

4.7 In-situ backside DRIFTS investigation of functional groups in an atmospheric-pressure DBD plasma

Figure 101 presents the contour map of the in-situ DRIFTS measurement during the indirect Ar/H₂O plasma treatment.

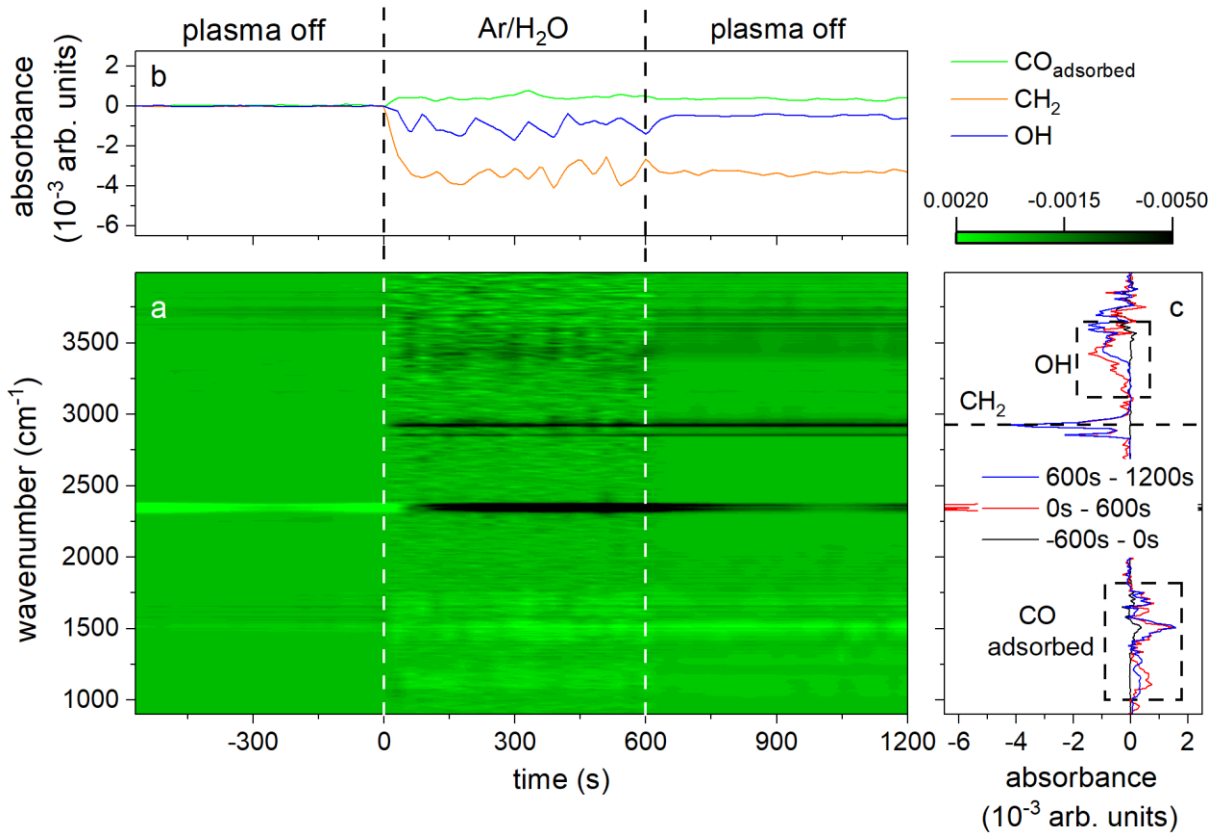


Figure 101: a) Contour map of the in-situ DRIFTS investigation of the Ar/H₂O plasma treatment range adjusted to the surface, b) line profile for detected surface changes, and c) averaged DRIFTS spectra over the respective time.

Again, the same surface-related peaks were found in the Ar/H₂O plasma, showing a similar trend as during the Ar/O₂ plasma treatment: the decomposition of CH_2 was as fast as using Ar/O₂, accompanied by a similar simultaneously accumulation of CO-related products on the surface.

In **Figure 102**, the evolution of the CH_2 peak for the respective plasma gas mixtures is compared.

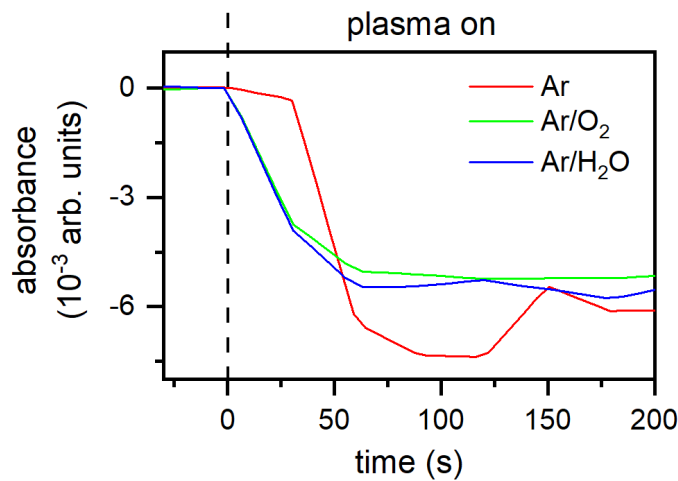


Figure 102: Evolution of the peak related to CH_2 during the respective plasma gas treatment.

4.7 In-situ backside DRIFTS investigation of functional groups in an atmospheric-pressure DBD plasma

As is clearly visible, the indirect Ar plasma treatment showed a delayed CH_2 decomposition, whereas the addition of oxygen-containing molecules to the plasma gas mixture led to an increased response time. Thereby, no difference in the decomposition of CH_2 was evident between the indirect Ar/O_2 and $\text{Ar}/\text{H}_2\text{O}$ plasma treatment.

4.7.2.4 In-situ DRIFTS evaluation of the CO_x region

To identify the peaks and related species in the CO_x region, in-situ spectra during and after the plasma are shown in **Figure 103**.

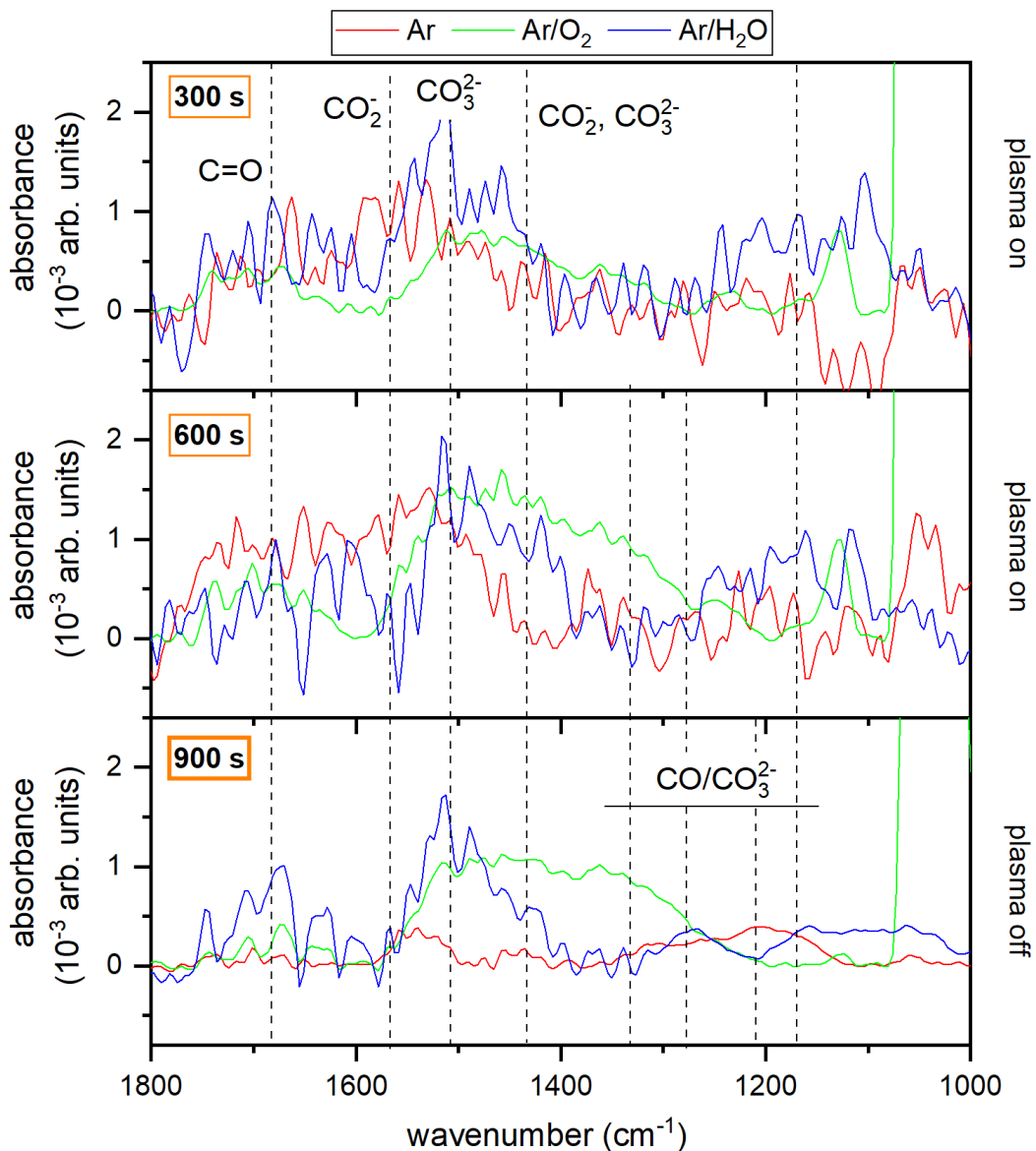


Figure 103: In-situ DRIFTS spectra of the CO_x region for different times after the plasma was turned on (at 0 s). Peaks are marked by a line, and the respective assignment is given.

Unfortunately, spectra collected during the Ar and $\text{Ar}/\text{H}_2\text{O}$ “plasma on” phase exhibited additional noise, probably due to the higher increase in temperature, vibration of the mesh, or additional emission from the plasma. Therefore, the resolution of the peaks is not sufficient for precise assignments. XPS predicted carboxylates, carboxylic acids, and carbonates as the main products formed during the plasma. As already discussed in chapter 4.1, the respective peaks of carbonates depend on the binding mode of the carbonates. Additionally, other CO-related peaks such as ether and ester are located in the same region,

4.7 In-situ backside DRIFTS investigation of functional groups in an atmospheric-pressure DBD plasma

making a precise assignment difficult. However, some peaks are outstanding: The peak at 1700 cm^{-1} can be assigned to the C=O vibration of a carboxylic acid or a carboxylate, while the peak around 1500 cm^{-1} can be assigned to one CO vibration of the carbonates. Other modes related to carbonates are located at lower wavenumbers, depending on the binding mechanism (detailed described in chapter 4.1) (monodentate, bridging, etc.). A similar adsorption of CO-related species during atmospheric-pressure plasmas was also found in the case of Ni surfaces^[12] and Cu-containing surfaces^[15]. However, in these studies, gas-phase reactions of highly-concentrated methane were investigated, increasing the number of reaction products in the gas phase and making adsorption of CO species created in the plasma much more likely.

After 300 s plasma treatment, Ar and Ar/H₂O spectra look very similar, showing some carboxylic acids and carbonates. On the contrary, Ar/O₂ showed the same amount of carboxylic acid but a lower carbonate amount with a different peak shape. After 600 s plasma treatment (last measurement during the plasma), the carbonate peaks of Ar and Ar/O₂ increased, while the Ar/H₂O plasma-treated surface look pretty similar. After 900 s (plasma was turned off at 600 s), only Ar/H₂O still showed a peak related to a carboxylic acid. The carbonate peak observed during the indirect Ar/O₂ and Ar/H₂O plasma treatment peaks remained in the same intensity. In contrast, all peaks observed during the indirect pure Ar plasma treatment were significantly decreased. However, while after the indirect Ar/O₂ plasma treatment all peaks stayed quite similar, the peak position changed after the indirect Ar and Ar/H₂O plasma treatment, indicating a change in the binding mode of carbonates.

4.7 In-situ backside DRIFTS investigation of functional groups in an atmospheric-pressure DBD plasma

The contour maps were adjusted to the CO_x region for further insight both in absorbance, wavenumber, and time. The adjusted contour map of the in-situ DRIFTS measurement during the indirect Ar plasma treatment is shown in **Figure 104**.

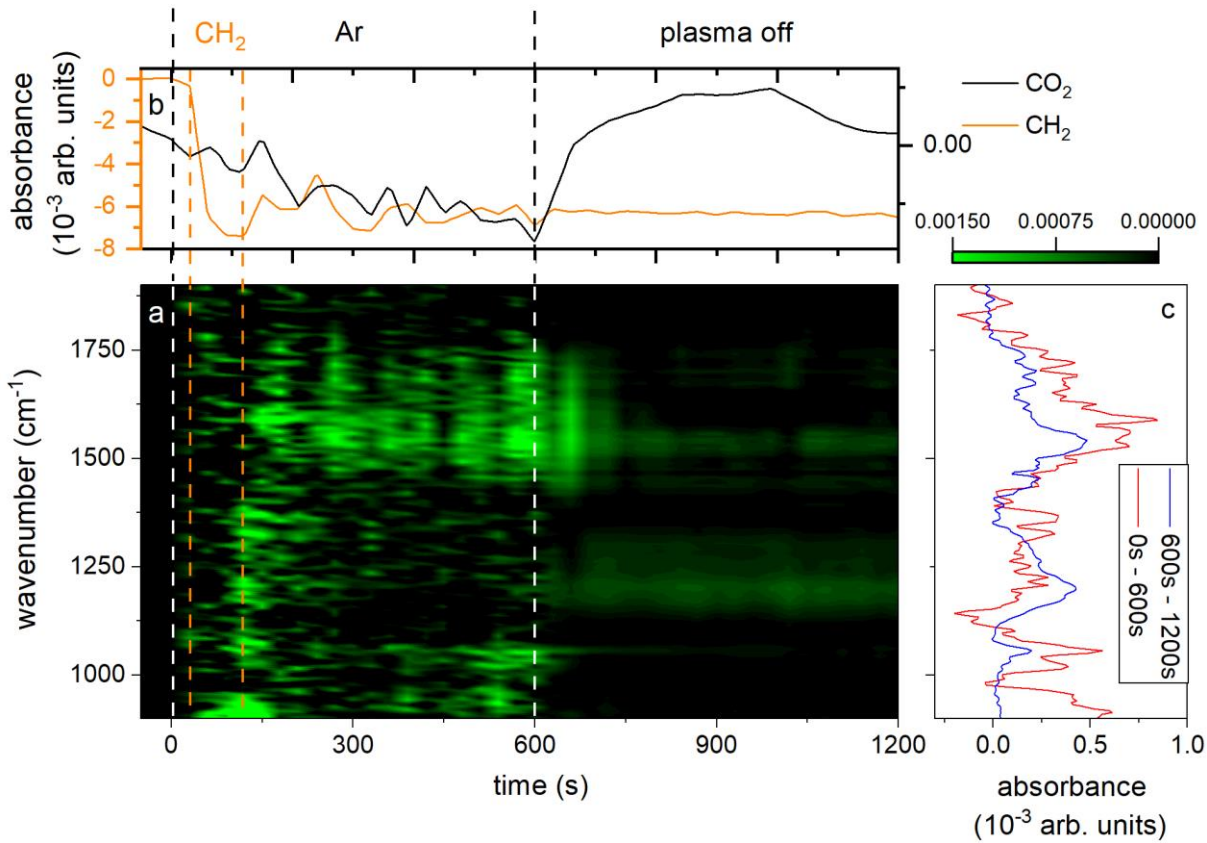


Figure 104: a) Contour map of the in-situ DRIFTS investigation of the Ar plasma treatment range adjusted to the CO range, b) line profile of CH₂ and CO₂ (out of range in this contour map) for comparison, and c) averaged DRIFTS spectra over the respective time. The time of the decomposition of CH₂ is marked with dashed orange lines.

In **Figure 104**, a clear correlation between the decomposition of CH₂ and the location of peaks in the CO_x region was present:

1. Within the first 30 s of the indirect Ar plasma treatment, no change is seen neither in the CH₂ nor in the CO_x region.
2. During the decomposition of CH₂, a peak arised at 920 cm⁻¹. This peak was assigned to vinyl groups (R-CH=CH₂). The vinyl was present during the decomposition and thereafter vanished. Thus, the decomposition of the CH₂ chain by an indirect Ar plasma is driven by the subtraction of an H by the reactive species in the effluent, forming a vinyl group in an intermediate state which dissipates, probably by an additional interaction with reactive species.
3. When the decomposition of CH₂ is finished after 120 s, CO-related peaks appear at 1100 cm⁻¹, 1220 cm⁻¹, and 1320 cm⁻¹. These peaks most likely belong to ethers and esters rather than carbonates/carboxylates, where additional peaks would have to be present at higher wavenumbers.
4. After 150 s, the CO-related peaks are replaced by a single peak at 1540 cm⁻¹, which is assigned to carbonates, and an unsteady appearance at 1700 cm⁻¹ related to carboxylic acids. These peaks steadily increased throughout the indirect Ar plasma treatment. Interestingly, the increase in these peaks was accompanied by a decrease in the CO₂ in the gas phase. Because no other source for the carbonate growth is available during the indirect Ar plasma treatment, the adsorption of the carbon dioxide on the surface forming carbonates is the only reasonable explanation. As already stated for the decomposition in an Ar/O₂ plasma, the CO₂ is excited in a DBD plasma, making it more likely to adsorb and react after that.

4.7 In-situ backside DRIFTS investigation of functional groups in an atmospheric-pressure DBD plasma

5. Instantaneously after the plasma, an additional peak at 1200 cm^{-1} was present, which might result from the change in the binding mode of the carbonates. Usually, at least two peaks are present for all carbonate binding modes, one around 1550 cm^{-1} and one at lower wavenumbers. That only one peak could be detected during the indirect plasma treatment might result from an excited state of the carbonate. After the plasma, the excitation of the carbonates ended, allowing a conventional carbonate binding to the surface (peak around 1300 cm^{-1}).

6. However, after the plasma, most adsorbed carbonates were not stable and desorbed from the surface.

The contour map of the in-situ DRIFTS measurement during the indirect Ar/O₂ plasma treatment is shown in **Figure 105**.

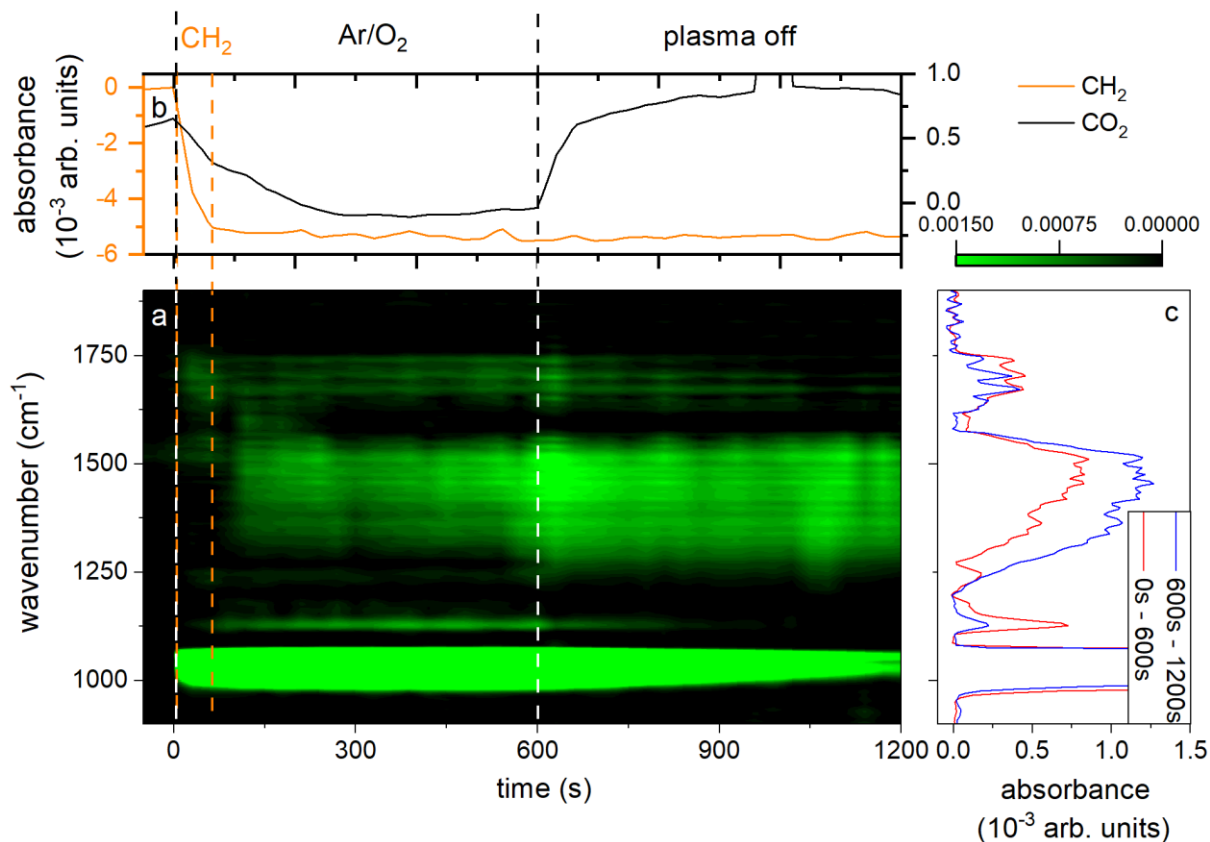


Figure 105: a) Contour map of the in-situ DRIFTS investigation of the Ar/O₂ plasma treatment range adjusted to the CO range, b) line profile of CH_2 and CO_2 (out of range in this contour map) for comparison, and c) averaged DRIFTS spectra over the respective time. The time of the decomposition of CH_2 is marked with dashed orange lines.

Similar to the indirect Ar plasma treatment, the signals in the CO_x region are different during and after the CH_2 decomposition. But instead of showing signs of vinyl groups, carboxylic acids are formed at 1700 cm^{-1} during the decomposition of CH_2 . Most likely, this was the result of a changed decomposition pathway due to different reactive species in the plasma effluent. However, it is possible that due to the shortened CH_2 decomposition time, intermediate states such as vinyl groups did not exhibit a sufficient signal and were not detected. When the decomposition of CH_2 was finished, carbonates were formed steadily throughout the plasma (More slowly after an initial rapid growth). This development is, again, in agreement with the evolution of CO_2 , indicating a correlation. However, during the Ar/O₂ plasma treatment, CO was formed as well, allowing CO and CO_2 surface interactions. Indeed, the carbonate peak shape was quite different than during the indirect Ar plasma treatment, showing a rather broad peak from 1500 cm^{-1} to 1300 cm^{-1} , indicating a conventional binding of the carbonates rather than an excited state (see chapter 4.1). This assumption is supported by the peak shape seen after the plasma, showing the same peak shape and a

4.7 In-situ backside DRIFTS investigation of functional groups in an atmospheric-pressure DBD plasma

stable absorbance. While carboxylic acids were present during the entire plasma treatment (1700 cm^{-1}), their intensities slowly decreased after the plasma. Thus, the formation of carbonates during the Ar/O₂ plasma treatment might be linked to the presence of carboxylic acids, eventually as an intermediate step in the CO₂ adsorption.

The contour map of the in-situ DRIFTS measurement during the indirect Ar/H₂O plasma treatment is shown in **Figure 106**.

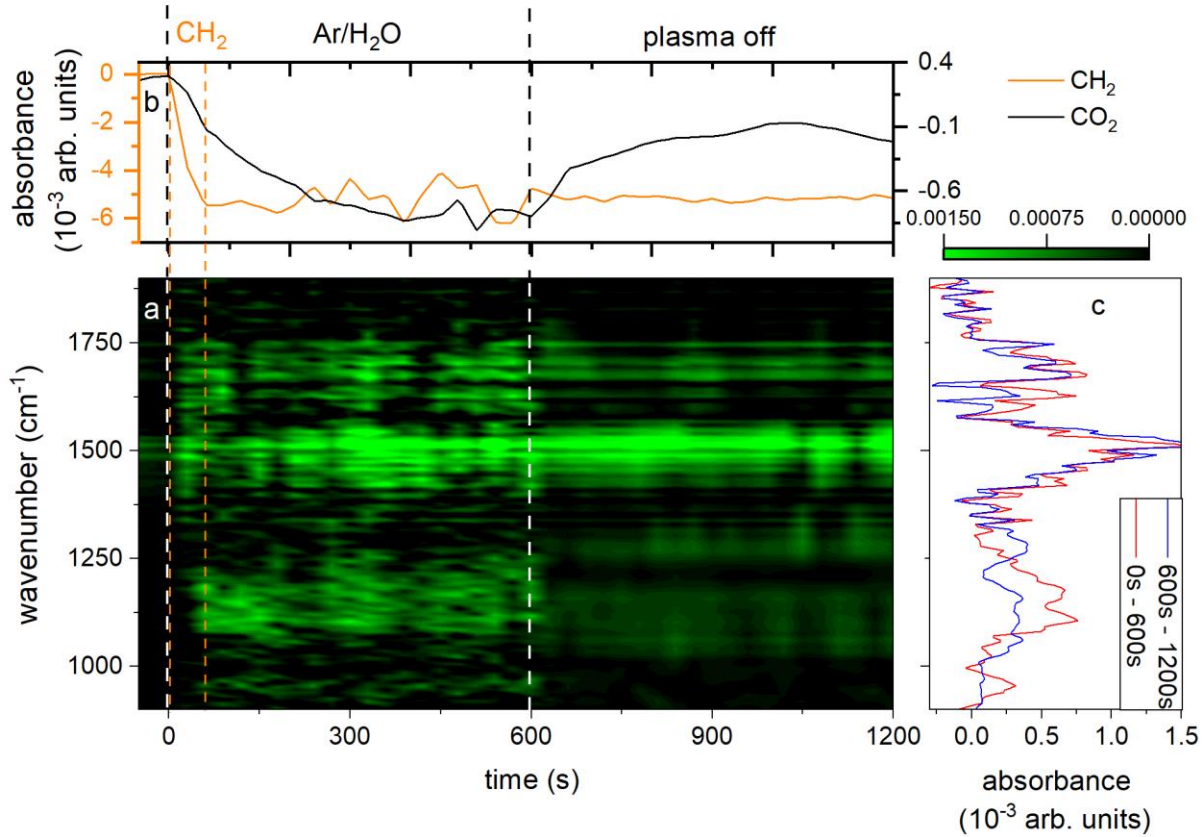


Figure 106: a) Contour map of the in-situ DRIFT investigation of the Ar/H₂O plasma treatment range adjusted to the CO range, b) line profile of CH_2 and CO_2 (out of range in this contour map) for comparison, and c) averaged DRIFT spectra over the respective time. The time of the decomposition of CH_2 is marked with dashed orange lines.

Here, again, carboxylic acids were present during the decomposition of CH_2 . However, an additional signal related to carbonates was already observed at 1500 cm^{-1} . Thus, the Ar/H₂O plasma showed (again) a different decomposition pathway than the indirect Ar and Ar/O₂ plasma treatments. After the decomposition of CH_2 was completed, a peak around 1150 cm^{-1} immediately appeared. The peak was assigned to another binding mode of the carbonates, different from the binding modes observed during the Ar and Ar/O₂ plasma. Both signals increased over time, again in agreement with the decrease in the gas phase absorbance of CO_2 . As for the indirect Ar/O₂ plasma treatment, carboxylic acids (1700 cm^{-1}) were present during the indirect Ar/H₂O plasma treatment. After the plasma was turned off, the signal at 1150 cm^{-1} splitted up in two peaks located at 1130 cm^{-1} and 1280 cm^{-1} , indicating another change in the binding mode of the carbonates. The carbonates and carboxylic acids exhibited a stable absorbance after the plasma.

4.7 In-situ backside DRIFTS investigation of functional groups in an atmospheric-pressure DBD plasma

In **Figure 107**, the different reaction pathways identified in the contour maps are presented.

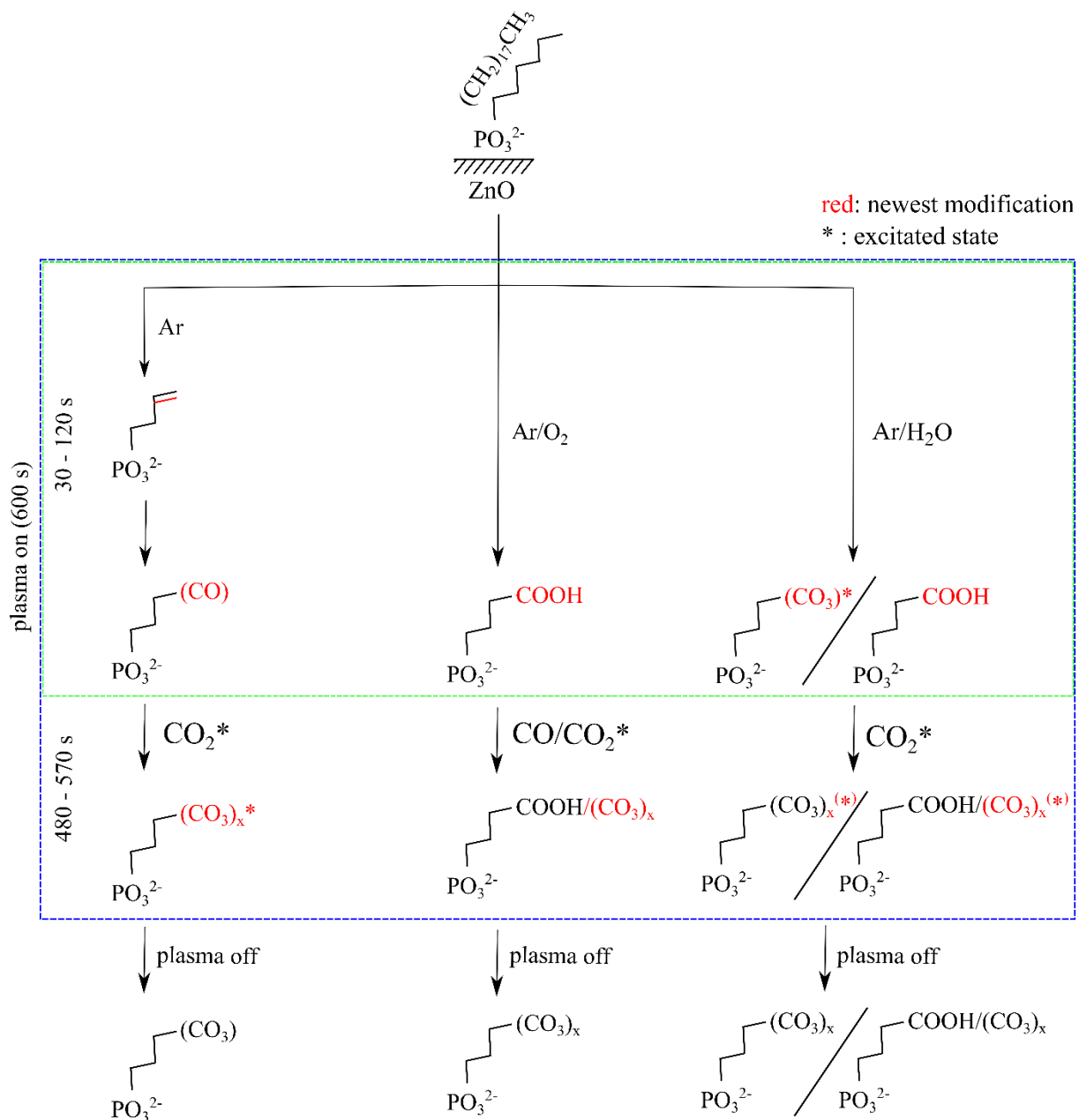


Figure 107: Pathway of the ODPA degradation and CO_2 adsorption dependent on the used plasma gas mixture during and after the indirect plasma treatment. The displayed chain length of the ODPA is only symbolic and can vary between the different plasma gas mixtures and steps.

The decomposition of CH_2 was very fast and completed within 120 s indirect plasma treatment. Thereby, the decomposition mechanism and the resulting functional groups were dependent on the plasma gas: While the indirect Ar plasma treatment led to different CO-related groups on the surface via a decomposition including vinyl groups, the indirect Ar/O_2 plasma treatment showed the presence of carboxylic acids during the decomposition. The indirect $\text{Ar}/\text{H}_2\text{O}$ plasma treatment showed, additionally to the carboxylic acids, already the presence of carbonates. Thus, as expected, the addition of oxidizing species led to highly oxidized functional groups on the surface already during the decomposition. If these functional groups are intermediate states during the decomposition or the “final” functional group that ended the CH_2 decomposition could not be distinguished. When the decomposition finished, all plasma gas composition led to the adsorption of excited CO_2 on the surface, forming carbonates in distinct different

4.7 In-situ backside DRIFTS investigation of functional groups in an atmospheric-pressure DBD plasma

binding modes. Thereby, only the carbonates formed during the indirect Ar plasma treatment were unstable after the plasma treatment.

The results show the high reactivity of the long-living reactive species, decomposing the CH₂ functional groups within at least 120 s. Furthermore, the high impact of the plasma gas mixture on the plasma-surface interaction was confirmed, showing that the plasma gas strongly determined the reaction pathway even if only the effluent is considered. Thereby, the reactivity of the plasma gas effluent was increased when adding oxidizing species to the plasma gas.

Interestingly, when comparing the DRIFTS spectra after the plasma treatment with the spectra found after the plasma treatment of ZnMgAl, the spectra after the indirect Ar/O₂ and Ar/H₂O plasma treatments were very similar to their respective gas composition on ZnMgAl (**Figure 33**). This similarity allows us to transfer the pathways identified in the backside setup to the ZnMgAl surface. Thus, two different pathways led to the formation of carbonates on ZnMgAl. (i) While the Ar plasma showed no stable carbonates in this study, the largest amount of carbonates was found after the Ar plasma treatment on ZnMgAl. Thus, either synergetic processes in the direct plasma treatment (electrons, radiation, etc.) are required, or the carboxylates natively present on the ZnMgAl surface enabled the formation of stable carbonates in the Ar plasma. (ii) Contrary, the carbonates formed on the surface during the Ar/O₂ and Ar/H₂O plasma treatments were mainly based on the CO₂ in the gas phase rather than a direct conversion of carboxylates on the surface. Thereby, the long-living reactive species of each plasma gas determined the interaction. Comparing the times required to form carbonates on the surface, surfaces in direct contact with the plasma seemed to require less time for the surface modifications (60 s). This speed-up can be either a result of the short distance between the plasma and the surface or is a result of synergetic effects within the plasma, accelerating (but not altering) the adsorption of carbonates.

Thus, the results gained in real-time by the backside setup on an indirect plasma-treated surface can be transferred to other setups and surfaces, confirming the approach of separating different plasma influences on model systems and still being able to transfer the results to surfaces and reactions of interest.

4.7.3 Conclusions

Using the backside setup in combination with DRIFTS, the decomposition by indirect plasma treatments of octadecyl phosphonic acid could be monitored in real-time (**Figure 108**).

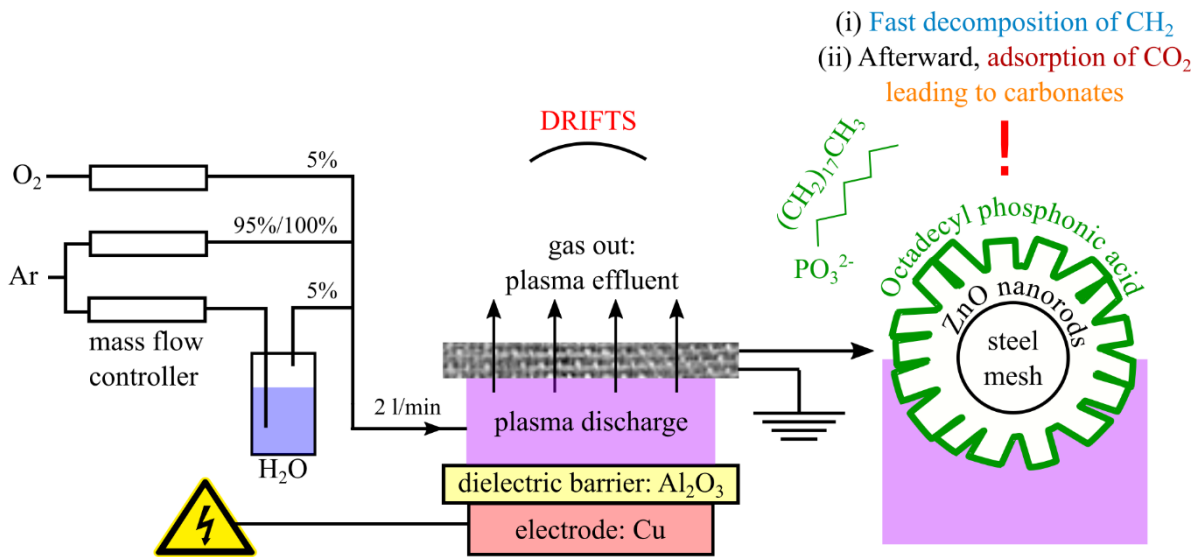


Figure 108: Changes identified on the ODPA surface by DRIFTS spectroscopy in real-time.

In the DRIFTS spectra, a fast decomposition of CH_2 was detected, which enabled the adsorption of excited CO_2 , which formed carbonates on the surface. Thereby, both the surface and the plasma effluent were measured, allowing the correlation between the gas phase and the surface. In so doing, different reaction pathways were identified depending on the plasma gas mixture. First, the addition of oxidizing species to the plasma change and accelerated the decomposition of the CH_2 group, forming highly oxidized functional groups on the surface. Second, after the CH_2 decomposition was completed, all surfaces adsorbed excited CO_2 from the gas phase, forming carbonates. Thereby, the carbonates formed in the indirect Ar plasma treatment desorbed after the plasma, while carbonates formed during the indirect Ar/O_2 and $\text{Ar}/\text{H}_2\text{O}$ plasma treatments remained on the surface. Finally, using the same different plasma gas mixtures as before, correlations between the results gained in real-time on the indirect plasma-treated surfaces could be transferred to the results gained after the direct plasma treatment of ZnMgAl in chapter 4.1. This approach emphasizes the need for in-situ measurements as the functional groups measured after the surface treatment give no direct insight into the reaction pathway. Thus, the backside setup in combination with DRIFTS and a self-assembled monolayer provides a powerful tool for investigating the modification of functional groups in an atmospheric-pressure DBD plasma.

4.7 In-situ backside DRIFTS investigation of functional groups in an atmospheric-pressure DBD plasma

5. Overall conclusions and outlook

The scientific goals for the atmospheric-pressure plasma treatment of ZnMgAl were defined in the introduction as:

1. Mimic the beneficial effects on the adhesive properties of ZnMgAl after the low-pressure plasma treatment seen before.
2. Identifying the plasma-induced changes on the ZnMgAl surface.
3. Link the changes in the surface to the surface properties.
4. Examine the plasma treatment for its in-line capability.

These questions could be successfully addressed using three different plasma gas compositions (Ar, Ar + 5% O₂, Ar + 5% H₂O) in the stationary plasma chamber. The results can be concluded as follows:

Mimic the beneficial effects on the adhesive properties of ZnMgAl after the low-pressure plasma treatment seen before.

The effect of the plasma treatment on the adhesion properties of the ZnMgAl alloy was investigated using contact angle measurements, different model adhesives, and an ODPA self-assembled monolayer. An improvement of the adhesion properties and wettability (reduced water contact angle, increased peel-off forces of two adhesives, and increased barrier properties of an octadodecyl phosphonic acid self-assembled monolayer (ODPA-SAM)) was observed after all plasma treatments, showing the most significant improvement after the Ar/H₂O plasma treatment for all processes. Additionally, the adhesive properties of the ZnMgAl surface after an Ar plasma treatment could be significantly increased by a post-treatment using ethanol.

Identifying the plasma-induced changes on the ZnMgAl surface

On ZnMgAl, a combination of the surface characterization techniques DPM-IRRAS and KP (in-situ), as well as XPS, TOF-SIMS, and SKPFM (ex-situ) allowed the identification of five plasma-induced surface changes after the DBD plasma treatments: (i) surface conversion of carboxylates to carbonates, (ii) etching of aliphatic carbon groups, (iii) migration of metals, (iv) increased oxide layer thickness, and (v) homogenization of the surface potential. These changes appeared in greater or lesser degree depending on the used gas mixture. Moreover, half-side plasma modifications were conducted using pure Ar as plasma gas. This approach showed superior comparability to the untreated state on the inhomogeneous ZnMgAl surface. An etch process of plasma products was observed during the adsorption of ODPA and the rinsing with ethanol. This hints at a low stability of some plasma-induced changes in ethanol.

Link the changes in the surface to the surface properties

When investigating the time dependence of the Ar/H₂O plasma treatment, a clear correlation between the increased wettability and the conversion of carboxylates to carbonates was seen. Contrary, there was no clear correlation between one specific plasma-induced change in the surface and the improved adhesion of two adhesives and ODPA. On the one hand, Ar plasma (mainly exhibiting etching of aliphatic chains and conversion of carboxylates to carbonates of the surface) showed a similar improvement in adhesion of adhesives as the Ar/O₂ plasma (increased oxide layer thickness and homogenization of surface potential). On the other hand, Ar/O₂ plasma treatments led to higher barrier properties of the ODPA monolayer than the pure Ar-DBD treatment. Interestingly, the plasma treatments using Ar/H₂O, which induced all discussed effects to a high degree, resulted in all cases in the most significant adhesive improvement. This suggests that all effects contribute synergistically to the final improvement in the adhesion properties.

Examine the plasma treatment for its in-line capability

To further investigate the potential use of DBD plasmas in in-line processes, the time dependence of the Ar/H₂O plasma treatment of ZnMgAl was investigated for short treatment times. It was found that within the first 5 seconds nearly all carboxylates were converted to carbonates and the Al oxide layer grew to its maximum. Both effects might be linked to a preferred carbonate formation on Al. The following migration of Al, Mg, and Zn over time exhibited a nonlinear behavior, showing the complex correlations within the ternary alloy. However, the plasma treatment showed no significant influence on the corrosion properties of the ZnMgAl alloy. Thus, a plasma treatment using Ar/H₂O of only 5 s leads to a highly wettable surface with high natural corrosion resistance in times suitable for in-line treatments.

To gain further knowledge of the processes on the plasma/surface interactions, further scientific goals were defined:

1. Develop a plasma setup that enables the in-situ and real-time characterization of surfaces in indirect contact with the plasma.
2. Examine the setup capabilities on ZnO nanorods by revealing plasma-induced changes on the surface in-situ and in real-time.
3. Extent the material range examinable by the new setup to organic functional groups.
4. Correlate the gained results of the new in-situ setup to the results gained on ZnMgAl.

Develop a plasma setup that enables the in-situ and real-time characterization of surfaces in indirect contact with the plasma

Because the necessary plasma geometry (the small gap between both electrodes of 1 or 2 mm) and disturbances by the plasma (e.g., UV radiation) hamper the monitoring of surfaces in direct contact with the plasma, a backside setup was developed. It enables the in-situ and real-time characterization of the surface in indirect contact with the plasma. Therefore, a steel mesh was coated with the material of interest (ZnO nanorods and ODPA) and served as a grounded plasma electrode. The changes induced by the plasma effluent penetrating the mesh were monitored in-situ and in real-time using Raman (ZnO nanorods) and DRIFTS (ODPA) on the backside of the mesh.

Examine the setup capabilities on ZnO nanorods by revealing plasma-induced changes on the surface in-situ and in real-time.

It could be shown that the backside Raman spectroscopic analysis allowed the detailed study of plasma effluent-induced changes on zinc oxide nanorods in-situ and in real-time. It showed that the plasma treatment using pure Ar only led to minor interactions with the Zn sub-lattice. In contrast, Ar/O₂ and Ar/H₂O plasma treatments introduced defects in the ZnO-nanorods surface near region. Ar/H₂O plasma treatments induced a steady increase in interfacial defects such as grain boundaries by roughening the surface of the nanorods. Contrary, Ar/O₂ plasma treatments rapidly increased the oxygen-related defect density (e.g., V_O) mainly during the initial phase of the plasma treatment. Thereby, the presented in-situ studies demonstrated that oxygen-related reactive species must be present in the plasma effluent in order to introduce defects via interactions with the Zn sub-lattice. Furthermore, ex-situ Raman measurements showed that the plasma-induced oxygen defects (Ar/O₂ plasma) were not stable, while Ar/H₂O plasma treatments formed long-time stable interfacial defects at the ZnO nanorod surface. Complementary studies using XANES measurements didn't show significant changes of the ZnO nanorods during plasma, likely being not surface-sensitive enough in the given setup geometry.

Extent the material range examinable by the new setup to organic functional groups

A single functional group could be defined in the plasma-surface interaction by applying a self-assembled monolayer on the mesh surface. Using the backside setup in combination with DRIFTS, the decomposition of an ODPA SAM was investigated in real-time. Thereby, both the surface and the plasma effluent were measured, allowing the correlation of changes in the gas phase to changes on the surface. In the DRIFTS spectra, a fast decomposition of CH₂ was detected, where afterward the adsorption of excited CO₂ led to the formation of excited carbonates on the surface. Thereby, different reaction pathways were identified, depending on the plasma gas mixture: Here, the addition of oxidizing species to the plasma accelerated the decomposition of the CH₂ group and formed highly oxidized functional groups on the surface. After the decomposition, all functionalized surfaces adsorbed excited CO₂ from the gas phase forming excited carbonates. After the plasma treatment, the carbonates formed in the indirect Ar plasma treatment desorbed after the plasma, while carbonates formed during the indirect Ar/O₂ and Ar/H₂O plasma treatments were stabilized on the surface.

Correlate the gained results of the new in-situ setup to the results gained on ZnMgAl

Using the same different plasma gas mixtures as before, correlations between the results gained in real-time on the indirect plasma-treated surfaces could be transferred to the results gained after the direct plasma treatment of ZnMgAl.

The study of ZnO nanorods confirmed the need for oxygen-containing species in the plasma gas composition to alter the metal surface strongly. Thereby, Ar/H₂O showed a completely different behavior than Ar/O₂, indicating different pathways for the increased oxide layer thickness on ZnMgAl. However, the high complexity of the amorphous, ternary ZnMgAl-alloy compared to the highly crystalline ZnO nanorods has to be noted, making direct transfer of the results difficult.

While investigating the ODPA self-assembled monolayer, the formation of carbonates on ZnMgAl could be understood further: The carbonates formed on ZnMgAl in the Ar/O₂ and Ar/H₂O plasma are most likely not a direct result of the conversion of carboxylates to carbonates, but results from the adsorption of excited carbon dioxide on the plasma cleaned surface. Contrary, the Ar plasma treatment, which showed no long-time stable carbonates in the backside setup but the highest amount of carbonates on ZnMgAl, directly converts carboxylates to carbonates. Thereby, some intermediate products of the decomposition of ODPA in an indirect plasma could be identified, showing the power of the novel backside setup to resolve reaction pathways and, at the same time, emphasizes that surface modifications measured only after the surface treatment (chapter 4.1 – 4.4) solely give direct insight into the reaction pathway.

Overall, the atmospheric-pressure plasma treatment of ZnMgAl, presenting an industrially relevant process, could be successfully understood and optimized towards increased adsorption properties by in-situ measurements and thorough ex-situ characterization. Furthermore, the plasma-induced changes observed on the complex alloy surface could be linked to results gained by a novel in-situ setup investigating the fundamental plasma/surface interactions, bridging the gap between fundamental and applied research. Thereby, the developed in-situ setup showed to be adaptable to different materials and characterization techniques.

6. Outlook

The results of the Ar + 5% H₂O plasma treatment on ZnMgAl already exhibited a satisfying increase in the adhesive properties of the surface. However, no optimization of the plasma parameters was performed, making the beneficial effects presented in this thesis a starting point for further improvements. The most promising plasma parameters to consider are the water concentration in the gas phase and the voltage. In addition, a thorough characterization of the plasma can benefit the experiments, revealing critical reactive species in the plasma and their time-dependence. Here, the application of mass spectroscopy can provide detailed information in combination with optical electron spectroscopy and the electrical characterization of the plasma discharges.

When other surface properties besides adhesion are of interest (e.g., corrosion properties, mechanical properties), this thesis showed the massive influence of the plasma gas mixture on the resulting surface properties. Here, the addition of nitrogen or small organic molecules (e.g., ethanol) to Ar as carrier gas can heavily change the behavior of the plasma. Furthermore, the carrier gas can be changed from argon to nitrogen or air, showing the high diversity of the plasma gas composition.

When considering the application of the presented plasma treatment in an in-line process, further aspects have to be examined. First, the substrate moves in an in-line process and, in doing so, possibly changes the interaction between the plasma and the substrate. Here, the stationary plasma chamber can be easily used to simulate the movement of the substrate during the plasma treatment. Secondly, the plasma's stability is essential, as was seen during the in-situ XANES experiments. Thus, a different plasma electrode layout is needed for a long-time stable plasma source which includes the cooling of the electrode. Last, the duration of the adhesion promotion during storage is of interest. Suppose the stability of the modified surface shows to be not long-lasting. In that case, a subsequent post-treatment might be of interest, for instance, the easy-to-use rinsing of the treated surface with EtOH or a well-defined deposition of a SAM.

When solving all these open questions, a highly efficient, versatile, and environmentally friendly surface treatment is ready to use in the industrial in-line processing of ZnMgAl steel.

The developed backside setup has shown to be a powerful tool for investigating modifications of metal oxides and functional groups in an atmospheric-pressure DBD plasma in-situ and in real-time, being adaptable to many materials (which are applicable on a mesh or other porous materials) and characterization methods. Accordingly, it can be used to investigate various systems of interest with respect to their application.

One example is the plasma treatment of metal oxides to tailor the properties of electrical devices. Small electrical devices are the enabler of digitalization, smart applications, and regulation of renewable energies, all demanding metal oxides which exhibit well-defined properties. Thus, the root cause of changes in the work function and the bandgap, as well as their correlation to plasma parameters, are of concern. As the backside plasma approach gives insight into the surface/plasma interactions and thereby reveals the defect formations and their stability, the back side setup allows a targeted parameter study. In this context, in-situ measurements using the Kelvin probe and UV-VIS spectroscopy would greatly complement the existing measurement methods. The setup to use the Kelvin probe was already prepared, but the experiments could not be completed due to complications during the "plasma on" phase as the plasma changes the distance between the mesh and KP tip.

Another potential field of application is the plasma catalysis. The conversion of carbon dioxide to usable resources by plasma catalysis in a DBD plasma was recently demonstrated and could help to reduce the

amount of carbon dioxide in the atmosphere, minimizing global warming. However, selecting a highly effective catalyst and optimizing the respective plasma parameters are of high relevance in a potential application. As was seen during the decomposition of ODPA, the backside setup, in combination with DRIFT measurements, is capable of monitoring the amount and state of the carbon dioxide both in the gas phase and on the surface during the plasma treatment. This information, combined with the monitoring of the surface by Raman spectroscopy, can further refine the understanding of the interplay between the surface and the plasma gas, accelerating the research.

In the last example, the applications of SAMs can be used to simulate the behavior of organic functional groups in a plasma. This insight can be used either for the plasma treatments of polymers, or lays the foundation of a more profound understanding in the treatment of complex biological molecules and, even more complex, plasma medicine. Here, often a deeper understanding of the highly complex interaction of the plasma with the various organic molecules is missing. The advantages of SAMs are their high purity and their structural diversity, where a SAM can be formed containing only one functional group (as ODPA) or contain complete biological molecules. This diversity enables nearly infinite possibilities for different experimental approaches using the real-time information gained by the backside setup. Furthermore, besides monitoring different plasma parameters on a specific function, the functional group can be varied for one plasma parameter set to compare their stability, reaction mechanisms, and plasma products. This insight would allow a rough prediction of the behavior of complex molecules in a plasma based on their functional groups. However, the interaction of different functional groups could cause a possible drawback of this prediction. To address these effects, the structure of a SAM can either be adapted to contain multiple functional groups, directly contain biological molecules, or co-adsorbed multiple SAMs on one surface. By comparing their response to the responses of the respective one-functional SAMs, interactions and dependencies can be revealed and the knowledge transferred to complex situations. By this approach, a prediction model for the behavior of biological molecules in a plasma could be obtained.

7. References

- 1 R. Brandenburg, *Dielectric barrier discharges: progress on plasma sources and on the understanding of regimes and single filaments*, Plasma Sources Sci. Technol., 2017, **26**, 53001.
- 2 L. Bárdos and H. Baránková, *Cold atmospheric plasma: Sources, processes, and applications*, Thin Solid Films, 2010, **518**, 6705–6713.
- 3 C. Tendero, C. Tixier, P. Tristant, J. Desmaison and P. Leprince, *Atmospheric pressure plasmas: A review*, Spectrochimica Acta Part B: Atomic Spectroscopy, 2006, **61**, 2–30.
- 4 H. Yasuda, *Plasma for Modification of Polymers*, Journal of Macromolecular Science: Part A - Chemistry, 1976, **10**, 383–420.
- 5 M. Xi, Y.-L. Li, S. Shang, D.-H. Li, Y.-X. Yin and X.-Y. Dai, *Surface modification of aramid fiber by air DBD plasma at atmospheric pressure with continuous on-line processing*, Surface and Coatings Technology, 2008, **202**, 6029–6033.
- 6 S. B. Lee and Y.-K. Kim, *Adhesion Improvement of Polyimide/Metal Interface by He/O₂/NF₃ Atmospheric Pressure Plasma*, Plasma Processes and Polymers, 2009, **6**, S525-S529.
- 7 M. Shekargoftar, J. Kelar, R. Krumpolec, J. Jurmanova and T. Homola, *A Comparison of the Effects of Ambient Air Plasma Generated by Volume and by Coplanar DBDs on the Surfaces of PP/Al/PET Laminated Foil*, IEEE Trans. Plasma Sci., 2018, **46**, 3653–3661.
- 8 Y. Yoshikawa, T. Hara and P. Abraha, *Surface Treatment of Tool Steel in Controlled Plasma Nitriding Environment*, Tribology Online, 2008, **3**, 348–351.
- 9 E. Panousis, F. Clément, J.-F. Loiseau, N. Spyrou, B. Held, J. Larrieu, E. Lecoq and C. Guimon, *Titanium alloy surface treatment using an atmospheric plasma jet in nitrogen pulsed discharge conditions*, Surface and Coatings Technology, 2007, **201**, 7292–7302.
- 10 M. Černák, L. Černáková, I. Hudec, D. Kováčik and A. Zahoranová, *Diffuse Coplanar Surface Barrier Discharge and its applications for in-line processing of low-added-value materials*, The European Physical Journal - Applied Physics, 2009, **47**, 22806.
- 11 P. A. Christensen, Ali, Abd Halim Bin Md, Z. T. A. W. Mashhadani and P. A. Martin, *A Direct Fourier Transform Infrared Spectroscopic Comparison of the Plasma- and Thermally-Driven Reaction of CO₂ at Macor*, Plasma Chemistry and Plasma Processing, 2018, **38**, 293–310.
- 12 A. J. Knoll, S. Zhang, M. Lai, P. Luan and G. S. Oehrlein, *Infrared studies of gas phase and surface processes of the enhancement of catalytic methane decomposition by low temperature plasma*, J. Phys. D: Appl. Phys., 2019, **52**, 225201.
- 13 A. Rodrigues, J.-M. Tatibouët and E. Fourré, *Operando DRIFT Spectroscopy Characterization of Intermediate Species on Catalysts Surface in VOC Removal from Air by Non-thermal Plasma Assisted Catalysis*, Plasma Chemistry and Plasma Processing, 2016, **36**, 901–915.
- 14 N. Turan, P. M. Barboun, P. K. Nayak, J. C. Hicks and D. B. Go, *Development of a small-scale helical surface dielectric barrier discharge for characterizing plasma–surface interfaces*, J. Phys. D: Appl. Phys., 2020, **53**, 275201.
- 15 S. Xu, S. Chansai, C. Stere, B. Inceesungvorn, A. Goguet, K. Wangkawong, S. F. R. Taylor, N. Al-Janabi, C. Hardacre, P. A. Martin and X. Fan, *Sustaining metal–organic frameworks for water–gas shift catalysis by non-thermal plasma*, Nat Catal, 2019, **2**, 142–148.

16 E. Diler, B. Rouvellou, S. Rioual, B. Lescop, G. Nguyen Vien and D. Thierry, *Characterization of corrosion products of Zn and Zn–Mg–Al coated steel in a marine atmosphere*, Corrosion Science, 2014, **87**, 111–117.

17 M. Salgueiro Azevedo, C. Allély, K. Ogle and P. Volovitch, *Corrosion mechanisms of Zn(Mg,Al) coated steel: 2. The effect of Mg and Al alloying on the formation and properties of corrosion products in different electrolytes*, Corrosion Science, 2015, **90**, 482–490.

18 T. Prosek, J. Hagström, D. Persson, N. Fuertes, F. Lindberg, O. Chocholatý, C. Taxén, J. Šerák and D. Thierry, *Effect of the microstructure of Zn–Al and Zn–Al–Mg model alloys on corrosion stability*, Corrosion Science, 2016, **110**, 71–81.

19 T. Prosek, A. Nazarov, A. Le Gac and D. Thierry, *Coil-coated Zn–Mg and Zn–Al–Mg: Effect of climatic parameters on the corrosion at cut edges*, Progress in Organic Coatings, 2015, **83**, 26–35.

20 K. Pohl, O. Ozcan, M. Voigt and G. Grundmeier, *Adhesion and corrosive delamination of epoxy films on chemically etched ZnMgAl-alloy coatings*, Materials and Corrosion, 2016, **67**, 1020–1026.

21 K. Pohl, J. Otte, P. Thissen, M. Giza, M. Maxisch, B. Schuhmacher and G. Grundmeier, *Adsorption and stability of self-assembled organophosphonic acid monolayers on plasma modified Zn–Mg–Al alloy surfaces*, Surface and Coatings Technology, 2013, **218**, 99–107.

22 B. W. Çetinkaya, F. Junge, G. Müller, F. Haakmann, K. Schierbaum and M. Giza, *Impact of alkaline and acid treatment on the surface chemistry of a hot-dip galvanized Zn–Al–Mg coating*, Journal of Materials Research and Technology, 2020, **9**, 16445–16458.

23 M. Budde, C. Corbella, S. Große-Kreul, T. de los Arcos, G. Grundmeier and A. von Keudell, *Decoupling of ion- and photon-activation mechanisms in polymer surfaces exposed to low-temperature plasmas*, Plasma Process Polym, 2018, **15**, 1700230.

24 C. Corbella, A. Pranda, S. Portal, T. de los Arcos, G. Grundmeier, G. S. Oehrlein and A. von Keudell, *Validation of etching model of polypropylene layers exposed to argon plasmas*, Plasma Processes and Polymers, 2019, **16**, 1900019.

25 A. Kolodziejczak-Radzimska and T. Jasionowski, *Zinc Oxide-From Synthesis to Application: A Review*, Materials (Basel, Switzerland), 2014, **7**, 2833–2881.

26 G.-C. Yi, C. Wang and W. I. Park, *ZnO nanorods: synthesis, characterization and applications*, Semicond. Sci. Technol., 2005, **20**, S22–S34.

27 M. Skompska and K. Zarębska, *Electrodeposition of ZnO Nanorod Arrays on Transparent Conducting Substrates—a Review*, Electrochimica Acta, 2014, **127**, 467–488.

28 B. K. Kim, K. S. Kim, C. E. Park and C. M. Ryu, *Improvement of wettability and reduction of aging effect by plasma treatment of low-density polyethylene with argon and oxygen mixtures*, Journal of Adhesion Science and Technology, 2002, **16**, 509–521.

29 G. Fridman, A. D. Brooks, M. Balasubramanian, A. Fridman, A. Gutsol, V. N. Vasilets, H. Ayan and G. Friedman, *Comparison of Direct and Indirect Effects of Non-Thermal Atmospheric-Pressure Plasma on Bacteria*, Plasma Processes and Polymers, 2007, **4**, 370–375.

30 M.J. Kirkpatrick, B. Dodet, E. Odic, *Atmospheric Pressure Humid Argon DBD Plasma for the Application of Sterilization - Measurement and Simulation of Hydrogen, Oxygen, and Hydrogen Peroxide Formation*, International Journal of Plasma Environmental Science and Technology, 2017, **5**, 96–101.

31 Z. Ke, Z. Yu and Q. Huang, *Assessment of Damage of Glutathione by Glow Discharge Plasma at the Gas-Solution Interface through Raman Spectroscopy*, *Plasma Process Polym.*, 2013, **10**, 181–188.

32 F. Kogelheide, K. Kartaschew, M. Strack, S. Baldus, N. Metzler-Nolte, M. Havenith, P. Awakowicz, K. Stapelmann and J.-W. Lackmann, *FTIR spectroscopy of cysteine as a ready-to-use method for the investigation of plasma-induced chemical modifications of macromolecules*, *J. Phys. D: Appl. Phys.*, 2016, **49**, 84004.

33 P. Lu, P. J. Cullen and K. Ostrikov, in *Cold Plasma in Food and Agriculture*, ed. N. N. Misra, O. Schlüter and P. J. Cullen, Elsevier Reference Monographs, s.l., 1st edn., 2016, pp. 83–116.

34 J. S. TOWNSEND, *The Conductivity produced in Gases by the Motion of Negatively-charged Ions*, *Nature*, 1900, **62**, 340–341.

35 E. C. Neyts, *Plasma-Surface Interactions in Plasma Catalysis*, *Plasma Chem Plasma Process*, 2016, **36**, 185–212.

36 A. Bogaerts, R. Aerts, R. Snoeckx, W. Somers, W. van Gaens, M. Yusupov and E. Neyts, *Modeling of plasma and plasma-surface interactions for medical, environmental and nano applications*, *J. Phys.: Conf. Ser.*, 2012, **399**, 12011.

37 T. E. Sheridan and J. Goree, *Collisional plasma sheath model*, *Physics of Fluids B: Plasma Physics*, 1991, **3**, 2796–2804.

38 C. Z. Liu, J. Q. Wu, L. Q. Ren, J. Tong, J. Q. Li, N. Cui, N. Brown and B. J. Meenan, *Comparative study on the effect of RF and DBD plasma treatment on PTFE surface modification*, *Materials Chemistry and Physics*, 2004, **85**, 340–346.

39 I. Giner, M. Maxisch, C. Kunze and G. Grundmeier, *Combined in situ PM-IRRAS/QCM studies of water adsorption on plasma modified aluminum oxide/aluminum substrates*, *Applied Surface Science*, 2013, **283**, 145–153.

40 N. Saleema and D. Gallant, *Atmospheric pressure plasma oxidation of AA6061-T6 aluminum alloy surface for strong and durable adhesive bonding applications*, *Applied Surface Science*, 2013, **282**, 98–104.

41 M. A. Castillo Acero and L. C. López, *Effect of plasma treatment in Aluminum and composites bonding joints: Shear load tests results*, *Procedia Manufacturing*, 2017, **13**, 183–189.

42 D. F. Williams, E. J. Kellar, D. A. Jesson and J. F. Watts, *Surface analysis of 316 stainless steel treated with cold atmospheric plasma*, *Applied Surface Science*, 2017, **403**, 240–247.

43 S. Lee, S. Bang, J. Park, S. Park, W. Jeong and H. Jeon, *The effect of oxygen remote plasma treatment on ZnO TFTs fabricated by atomic layer deposition*, *phys. stat. sol. (a)*, 2010, **207**, 1845–1849.

44 X. Q. Meng, D. X. Zhao, J. Y. Zhang, D. Z. Shen, Y. M. Lu, L. Dong, Z. Y. Xiao, Y. C. Liu and X. W. Fan, *Wettability conversion on ZnO nanowire arrays surface modified by oxygen plasma treatment and annealing*, *Chemical Physics Letters*, 2005, **413**, 450–453.

45 O. Ozcan, K. Pohl, P. Keil and G. Grundmeier, *Effect of hydrogen and oxygen plasma treatments on the electrical and electrochemical properties of zinc oxide nanorod films on zinc substrates*, *Electrochemistry Communications*, 2011, **13**, 837–839.

46 J. S. Meena, M.-C. Chu, Y.-C. Chang, H.-C. You, R. Singh, P.-T. Liu, H.-P. D. Shieh, F.-C. Chang and F.-H. Ko, *Effect of oxygen plasma on the surface states of ZnO films used to produce thin-film transistors on soft plastic sheets*, *J. Mater. Chem. C*, 2013, **1**, 6613.

47 S. Jiang, Z. Ren, S. Gong, S. Yin, Y. Yu, X. Li, G. Xu, G. Shen and G. Han, *Tunable photoluminescence properties of well-aligned ZnO nanorod array by oxygen plasma post-treatment*, Applied Surface Science, 2014, **289**, 252–256.

48 C. F. Windisch, G. J. Exarhos, C. Yao and L.-Q. Wang, *Raman study of the influence of hydrogen on defects in ZnO*, Journal of Applied Physics, 2007, **101**, 123711.

49 J.-H. Bang, H.-S. Uhm, W. Kim and J.-S. Park, *Effects of additive gases and plasma post-treatment on electrical properties and optical transmittance of ZnO thin films*, Thin Solid Films, 2010, **519**, 1568–1572.

50 S. Daria, S. Sindu, H. Mathias, H. Luka, M. Janik, D. Jannes, K. Zaho, F. Bodo, K. Holger and A. Rainer, *Surface modification of highly porous 3D networks via atmospheric plasma treatment*, Contributions to Plasma Physics, 2018, **58**, 384–393.

51 M. Giza and G. Grundmeier, *Combination of FTIR Reflection Absorption Spectroscopy and Work Function Measurements for In Situ Studies of Plasma Modified Passive Films on MgZn2*, Plasma Process. Polym., 2011, **8**, 607–616.

52 J. Duchoslav, M. Kehrer, T. Truglas, H. Groiß, M. Nadlinger, L. Hader-Kregl, C. K. Riener, M. Arndt, K. H. Stellnberger, G. Luckeneder, G. Angeli, T. Stehrer and D. Stifter, *The effect of plasma treatment on the surface chemistry and structure of ZnMgAl coatings*, Applied Surface Science, 2020, **504**, 144457.

53 G. Grundmeier and M. Stratmann, *Influence of oxygen and argon plasma treatments on the chemical structure and redox state of oxide covered iron*, Applied Surface Science, 1999, **141**, 43–56.

54 G. Grundmeier, M. Brettmann and P. Thiemann, *In situ spectroscopic and corrosion studies of ultra-thin gradient plasma polymer layers on zinc*, Applied Surface Science, 2003, **217**, 223–232.

55 B. Anthony, *In situ cleaning of silicon substrate surfaces by remote plasma-excited hydrogen*, J. Vac. Sci. Technol. B, 1989, **7**, 621.

56 E. C. Neyts, K. K. Ostrikov, M. K. Sunkara and A. Bogaerts, *Plasma Catalysis: Synergistic Effects at the Nanoscale*, Chemical Reviews, 2015, **115**, 13408–13446.

57 C. Stewig, S. Schüttler, T. Urbanietz, M. Böke and A. von Keudell, *Excitation and dissociation of CO 2 heavily diluted in noble gas atmospheric pressure plasma*, J. Phys. D: Appl. Phys., 2020, **53**, 125205.

58 M.-S. Oh, S.-H. Kim, J.-S. Kim, J.-W. Lee, J.-H. Shon and Y.-S. Jin, *Surface and cut-edge corrosion behavior of Zn-Mg-Al alloy-coated steel sheets as a function of the alloy coating microstructure*, Met. Mater. Int., 2016, **22**, 26–33.

59 M. Arndt, J. Duchoslav, H. Itani, G. Hesser, C. K. Riener, G. Angeli, K. Preis, D. Stifter and K. Hingerl, *Nanoscale analysis of surface oxides on ZnMgAl hot-dip-coated steel sheets*, Analytical and bioanalytical chemistry, 2012, **403**, 651–661.

60 P. Volovitch, T. N. Vu, C. Allély, A. Abdel Aal and K. Ogle, *Understanding corrosion via corrosion product characterization: II. Role of alloying elements in improving the corrosion resistance of Zn-Al-Mg coatings on steel*, Corrosion Science, 2011, **53**, 2437–2445.

61 J. Duchoslav, M. Arndt, R. Steinberger, T. Keppert, G. Luckeneder, K. H. Stellnberger, J. Hagler, C. K. Riener, G. Angeli and D. Stifter, *Nanoscopic view on the initial stages of corrosion of hot dip galvanized Zn–Mg–Al coatings*, Corrosion Science, 2014, **83**, 327–334.

62 Z. L. Wang, *Zinc oxide nanostructures: growth, properties and applications*, J. Phys.: Condens. Matter, 2004, **16**, R829-R858.

63 E. Hoque, J. A. DeRose, G. Kulik, P. Hoffmann, H. J. Mathieu and B. Bhushan, *Alkylphosphonate modified aluminum oxide surfaces*, The journal of physical chemistry. B, 2006, **110**, 10855–10861.

64 D. K. Schwartz, *Mechanisms and kinetics of self-assembled monolayer formation*, Annual review of physical chemistry, 2001, **52**, 107–137.

65 A. Bulusu, S. A. Paniagua, B. A. MacLeod, A. K. Sigdel, J. J. Berry, D. C. Olson, S. R. Marder and S. Graham, *Efficient modification of metal oxide surfaces with phosphonic acids by spray coating*, Langmuir : the ACS journal of surfaces and colloids, 2013, **29**, 3935–3942.

66 S. Szillies, P. Thissen, D. Tabatabai, F. Feil, W. Fürbeth, N. Fink and G. Grundmeier, *Formation and stability of organic acid monolayers on magnesium alloy AZ31: The role of alkyl chain length and head group chemistry*, Applied Surface Science, 2013, **283**, 339–347.

67 S. P. Pujari, L. Scheres, A. T. M. Marcelis and H. Zuilhof, *Covalent surface modification of oxide surfaces*, Angewandte Chemie (International ed. in English), 2014, **53**, 6322–6356.

68 A. P. Hinckley and A. J. Muscat, *Detecting and Removing Defects in Organosilane Self-Assembled Monolayers*, Langmuir, 2020, **36**, 2563–2573.

69 A. N. Parikh, D. L. Allara, I. B. Azouz and F. Rondelez, *An Intrinsic Relationship between Molecular Structure in Self-Assembled n-Alkylsiloxane Monolayers and Deposition Temperature*, J. Phys. Chem., 1994, **98**, 7577–7590.

70 P. J. Hotchkiss, M. Malicki, A. J. Giordano, N. R. Armstrong and S. R. Marder, *Characterization of phosphonic acid binding to zinc oxide*, J. Mater. Chem., 2011, **21**, 3107.

71 M. Dubey, T. Weidner, L. J. Gamble and D. G. Castner, *Structure and order of phosphonic acid-based self-assembled monolayers on Si(100)*, Langmuir : the ACS journal of surfaces and colloids, 2010, **26**, 14747–14754.

72 C. Vericat, M. E. Vela and R. C. Salvarezza, *Self-assembled monolayers of alkanethiols on Au(111): surface structures, defects and dynamics*, Physical chemistry chemical physics : PCCP, 2005, **7**, 3258–3268.

73 T. Belmonte, C. Noël, T. Gries, J. Martin and G. Henrion, *Theoretical background of optical emission spectroscopy for analysis of atmospheric pressure plasmas*, Plasma Sources Sci. Technol., 2015, **24**, 64003.

74 X.-M. Zhu and Y.-K. Pu, *Optical emission spectroscopy in low-temperature plasmas containing argon and nitrogen: determination of the electron temperature and density by the line-ratio method*, J. Phys. D: Appl. Phys., 2010, **43**, 403001.

75 U. N. Pal, A. K. Sharma, J. S. Soni, S. Kr, H. Khatun, M. Kumar, B. L. Meena, M. S. Tyagi, B.-J. Lee, M. Iberler, J. Jacoby and K. Frank, *Electrical modelling approach for discharge analysis of a coaxial DBD tube filled with argon*, J. Phys. D: Appl. Phys., 2009, **42**, 45213.

76 F. Peeters and T. Butterworth, *Electrical Diagnostics of Dielectric Barrier Discharges*, IntechOpen, 2018.

77 H. Hug, *Instrumentelle Analytik. Theorie und Praxis*, Verlag Europa-Lehrmittel, Haan-Gruiten, 3rd edn., 2015.

78 W. G. Fateley, N. T. McDevitt and F. F. Bentley, *Infrared and Raman Selection Rules for Lattice Vibrations: The Correlation Method*, Applied Spectroscopy, 1971, **25**, 155–173.

79 *Handbook of spectroscopy*, Wiley-VCH, Weinheim, Cambridge, 2003.

80 B. A. Lengyel, *A Michelson-Type Interferometer for Microwave Measurements*, Proc. IRE, 1949, **37**, 1242–1244.

81 G. Grundmeier, A. von Keudell and T. de los Arcos, *Fundamentals and Applications of Reflection FTIR Spectroscopy for the Analysis of Plasma Processes at Materials Interfaces*, Plasma Process. Polym., 2015, **12**, 926–940.

82 Y. J. Chabal, *Surface infrared spectroscopy*, Surface Science Reports, 1988, **8**, 211–357.

83 T. Buffeteau, B. Desbat and J. M. Turlet, *Polarization Modulation FT-IR Spectroscopy of Surfaces and Ultra-Thin Films: Experimental Procedure and Quantitative Analysis*, Applied Spectroscopy, 1991, **45**, 380–389.

84 L. Dixit, D. L. Gerrard and H. J. Bowley, *Laser Raman Spectra of Transition Metal Oxides and Catalysts*, Applied Spectroscopy Reviews, 1986, **22**, 189–249.

85 A. K. Yadav and P. Singh, *A review of the structures of oxide glasses by Raman spectroscopy*, RSC Adv., 2015, **5**, 67583–67609.

86 R. A. Meyers, ed., *Encyclopedia of analytical chemistry. Applications, theory and instrumentation*, Wiley, Chichester, 2000.

87 N. H. Turner, *X-Ray Photoelectron and Auger Electron Spectroscopy*, Encyclopedia of Analytical Chemistry, 2006.

88 P. Steiner, H. Hchst and S. Hfner, *XPS investigation of simple metals*, Z Physik B, 1978, **30**, 129–143.

89 B. R. Strohmeier, *An ESCA method for determining the oxide thickness on aluminum alloys*, Surf. Interface Anal., 1990, **15**, 51–56.

90 G. S. Henderson, F. M. F. de Groot and B. J. A. Moulton, *X-ray Absorption Near-Edge Structure (XANES) Spectroscopy*, Reviews in Mineralogy and Geochemistry, 2014, **78**, 75–138.

91 J. J. Rehr and A. L. Ankudinov, *Progress in the theory and interpretation of XANES*, Coordination Chemistry Reviews, 2005, **249**, 131–140.

92 A. Benninghoven, *Surface analysis by Secondary Ion Mass Spectrometry (SIMS)*, Surface Science, 1994, **299-300**, 246–260.

93 H. W. Werner, *The use of secondary ion mass spectrometry in surface analysis*, Surface Science, 1975, **47**, 301–323.

94 K. L. Busch, B. H. Hsu, Y. X. Xie and R. G. Cooks, *Matrix effects in secondary ion mass spectrometry*, Anal. Chem., 1983, **55**, 1157–1160.

95 F. Zanderigo, S. Ferrari, G. Queirolo, C. Pello and M. Borgini, *Quantitative TOF-SIMS analysis of metal contamination on silicon wafers*, Materials Science and Engineering: B, 2000, **73**, 173–177.

96 V. R. Deline, W. Katz, C. A. Evans and P. Williams, *Mechanism of the SIMS matrix effect*, Appl. Phys. Lett., 1978, **33**, 832–835.

97 I. F. Urazgil'din, *Secondary ion emission from metal surfaces*, Nuclear Instruments and Methods in Physics Research Section B: Beam Interactions with Materials and Atoms, 1993, **78**, 271–277.

98 C. H. Hamann and W. Vielstich, *Elektrochemie*, Wiley-VCH-Verlag GmbH & Co. KGaA, Weinheim, 4th edn., 2005.

99 M. I. Montenegro, M. A. Queirós and J. L. Daschbach, *Microelectrodes: Theory and Applications*, 1991, **197**.

100 M. Ciobanu, J. P. Wilburn, M. L. Krim and D. E. Cliffel, *Handbook of Electrochemistry*, Elsevier, 2007.

101 C. G. Zoski, *Handbook of electrochemistry*, Elsevier, Amsterdam, 2007.

102 E. McCafferty, *Introduction to corrosion science*, Springer, New York, NY, 2010.

103 D. Yan, M. Z. Bazant, P. M. Biesheuvel, M. C. Pugh and F. P. Dawson, *Theory of linear sweep voltammetry with diffuse charge: Unsupported electrolytes, thin films, and leaky membranes*, *Physical review. E*, 2017, **95**, 33303.

104 D. D. Macdonald, *Review of mechanistic analysis by electrochemical impedance spectroscopy*, *Electrochimica Acta*, 1990, **35**, 1509–1525.

105 B.-Y. Chang and S.-M. Park, *Electrochemical impedance spectroscopy*, *Annual review of analytical chemistry* (Palo Alto, Calif.), 2010, **3**, 207–229.

106 A. Tahara and T. Kodama, *Potential distribution measurement in galvanic corrosion of Zn/Fe couple by means of Kelvin probe*, *Corrosion Science*, 2000, **42**, 655–673.

107 I. D. Baikie, E. Venderbosch, J. A. Meyer and P. J. Z. Estrup, *Analysis of stray capacitance in the Kelvin method*, *Review of Scientific Instruments*, 1991, **62**, 725–735.

108 E. Juzeliūnas, A. Sudavičius, K. Jüttner and W. Fürbeth, *Study of initial stages of Al–Mg alloy corrosion in water, chloride and Cu(II) environment by a scanning Kelvin probe and XPS*, *Electrochemistry Communications*, 2003, **5**, 154–158.

109 Steffen Knust, Andreas Kuhlmann, T. de los Arcos and Guido Grundmeier, *Surface modification of ZnMgAl-coated steel by dielectric-barrier discharge plasma*, *RSC Advances*, 2019, **9**, 35077–35088.

110 G. Bäck, A. Nazarov and D. Thierry, *Localized Corrosion of Heat-Treated and Welded Stainless Steel Studied Using a Scanning Kelvin Probe*, *CORROSION*, 2005, **61**, 951–960.

111 P. Taheri, K. Pohl, G. Grundmeier, J. R. Flores, F. Hannour, J. H. W. de Wit, J. M. C. Mol and H. Terryn, *Effects of Surface Treatment and Carboxylic Acid and Anhydride Molecular Dipole Moments on the Volta Potential Values of Zinc Surfaces*, *J. Phys. Chem. C*, 2013, **117**, 1712–1721.

112 J. Wielant, R. Posner, G. Grundmeier and H. Terryn, *Interface Dipoles Observed after Adsorption of Model Compounds on Iron Oxide Films: Effect of Organic Functionality and Oxide Surface Chemistry*, *J. Phys. Chem. C*, 2008, **112**, 12951–12957.

113 H. O. Jacobs, H. F. Knapp and A. Stemmer, *Practical aspects of Kelvin probe force microscopy*, *Rev. Sci. Instrum.*, 1999, **70**, 1756–1760.

114 W. Melitz, J. Shen, A. C. Kummel and S. Lee, *Kelvin probe force microscopy and its application*, *Surface Science Reports*, 2011, **66**, 1–27.

115 W. Zhou and Z. L. Wang, *Scanning microscopy for nanotechnology. Techniques and applications*, Springer, New York, NY, 2007.

116 K. D. Vernon-Parry, *Scanning electron microscopy: an introduction*, *III-Vs Review*, 2000, **13**, 40–44.

117 D. B. Williams and C. B. Carter, *Transmission Electron Microscopy*, Springer, Boston, 1996.

118 S. Utsunomiya and R. C. Ewing, *Application of high-angle annular dark field scanning transmission electron microscopy, scanning transmission electron microscopy-energy dispersive X-ray spectrometry, and energy-filtered transmission electron microscopy to the characterization of nanoparticles in the environment*, *Environmental science & technology*, 2003, **37**, 786–791.

119 M. Hayashida and M. Malac, *Practical electron tomography guide: Recent progress and future opportunities*, Micron (Oxford, England : 1993), 2016, **91**, 49–74.

120 M. R. Libera and R. F. Egerton, *Advances in the Transmission Electron Microscopy of Polymers*, *Polymer Reviews*, 2010, **50**, 321–339.

121 R. Egerton, *Electron energy-loss spectroscopy in the electron microscope*, Springer, New York, NY, 3rd edn., 2011.

122 K. Iakoubovskii, K. Mitsuishi, Y. Nakayama and K. Furuya, *Thickness measurements with electron energy loss spectroscopy*, Microscopy research and technique, 2008, **71**, 626–631.

123 J.-G. Kim, S. J. Yoo, C.-Y. Kim and H.-T. Jou, *Circular Fast Fourier Transform Application: A Useful Script for Fast Fourier Transform Data Analysis of High-resolution Transmission Electron Microscopy Image*, Applied Microscopy, 2014, **44**, 138–143.

124 H.-J. Butt and M. Kappl, *Surface and interfacial forces*, Wiley-VCH, Weinheim, 2010.

125 T. T. Chau, W. J. Bruckard, P. T. L. Koh and A. V. Nguyen, *A review of factors that affect contact angle and implications for flotation practice*, Advances in Colloid and Interface Science, 2009, **150**, 106–115.

126 D. P. Subedi, *Contact Angle Measurement for The Surface Characterization of Solids*, Himalayan Physics, 2011, **2**, 1–4.

127 D. K. Owens and R. C. Wendt, *Estimation of the surface free energy of polymers*, J. Appl. Polym. Sci., 1969, **13**, 1741–1747.

128 P. A. Steinmann and H. E. Hintermann, *A review of the mechanical tests for assessment of thin-film adhesion*, Journal of Vacuum Science & Technology A: Vacuum, Surfaces, and Films, 1989, **7**, 2267–2272.

129 K.-H. Tsai and K.-S. Kim, *Stick-slip in the thin film peel test—I. the 90° peel test*, International Journal of Solids and Structures, 1993, **30**, 1789–1806.

130 S. Knust, A. Kuhlmann, A. G. Orive, T. Arcos and G. Grundmeier, *Influence of dielectric barrier plasma treatment of ZnMgAl alloy-coated steel on the adsorption of organophosphonic acid monolayers*, Surf Interface Anal, 2020.

131 S. Knust, L. Ruhm, A. Kuhlmann, D. Meinderink, J. Bürger, J. K. N. Lindner, M. T. Arcos de Pedro and G. Grundmeier, *In situ backside Raman spectroscopy of zinc oxide nanorods in an atmospheric-pressure dielectric barrier discharge plasma*, J. Raman Spectrosc., 2021.

132 D. Meinderink, A. G. Orive, S. Ewertowski, I. Giner and G. Grundmeier, *Dependance of Poly(acrylic acid) Interfacial Adhesion on the Nanostructure of Electrodeposited ZnO Films*, ACS Appl. Nano Mater., 2019, **2**, 831–843.

133 G. Grundmeier, E. Matheisen and M. Stratmann, *Formation and stability of ultrathin organosilane polymers on iron*, Journal of Adhesion Science and Technology, 1996, **10**, 573–588.

134 R. F. Egerton, *Electron Energy-Loss Spectroscopy in the Electron Microscope*, Springer Science+Business Media LLC, Boston, MA, 3rd edn., 2011.

135 T. Lostak, A. Maljusch, B. Klink, S. Krebs, M. Kimpel, J. Flock, S. Schulz and W. Schuhmann, *Zr-based conversion layer on Zn-Al-Mg alloy coated steel sheets: insights into the formation mechanism*, Electrochimica Acta, 2014, **137**, 65–74.

136 N. LeBozec, D. Thierry, M. Rohwerder, D. Persson, G. Luckeneder and L. Luxem, *Effect of carbon dioxide on the atmospheric corrosion of Zn–Mg–Al coated steel*, Corrosion Science, 2013, **74**, 379–386.

137 A. Sarani, A. Y. Nikiforov and C. Leys, *Atmospheric pressure plasma jet in Ar and Ar/H₂O mixtures: Optical emission spectroscopy and temperature measurements*, Physics of Plasmas, 2010, **17**, 63504.

138 T. Prosek, A. Nazarov, U. Bexell, D. Thierry and J. Serak, *Corrosion mechanism of model zinc–magnesium alloys in atmospheric conditions*, Corrosion Science, 2008, **50**, 2216–2231.

139 G. N. Vayssilov, M. Mihaylov, P. St. Petkov, K. I. Hadjiivanov and K. M. Neyman, *Reassignment of the Vibrational Spectra of Carbonates, Formates, and Related Surface*

Species on Ceria: A Combined Density Functional and Infrared Spectroscopy Investigation, J. Phys. Chem. C, 2011, **115**, 23435–23454.

140 A. Strålin and T. Hjertberg, *FTIR Study on interfacial interactions between hydrated aluminium and polar groups in ethylene copolymers*, Surf. Interface Anal., 1993, **20**, 337–340.

141 C. Weilach, C. Spiel, K. Föttinger and G. Rupprechter, *Carbonate formation on Al₂O₃ thin film model catalyst supports*, Surface Science, 2011, **605**, 1503–1509.

142 C. Fotea, J. Callaway and M. R. Alexander, *Characterisation of the surface chemistry of magnesium exposed to the ambient atmosphere*, Surf. Interface Anal., 2006, **38**, 1363–1371.

143 G. Busca and V. Lorenzelli, *Infrared spectroscopic identification of species arising from reactive adsorption of carbon oxides on metal oxide surfaces*, Materials Chemistry, 1982, **7**, 89–126.

144 M. Giza, P. Thissen and G. Grundmeier, *Adsorption kinetics of organophosphonic acids on plasma-modified oxide-covered aluminum surfaces*, Langmuir, 2008, **24**, 8688–8694.

145 M. R. Alexander, G. Beamson, C. J. Blomfield, G. Leggett and T. M. Duc, *Interaction of carboxylic acids with the oxyhydroxide surface of aluminium: poly(acrylic acid), acetic acid and propionic acid on pseudoboehmite*, Journal of Electron Spectroscopy and Related Phenomena, 2001, **121**, 19–32.

146 C. D. Wagner and P. Biloen, *X-ray excited Auger and photoelectron spectra of partially oxidized magnesium surfaces: The observation of abnormal chemical shifts*, Surface Science, 1973, **35**, 82–95.

147 M. R. Alexander, G. E. Thompson, X. Zhou, G. Beamson and N. Fairley, *Quantification of oxide film thickness at the surface of aluminium using XPS*, Surf. Interface Anal., 2002, **34**, 485–489.

148 Sven Tougaard, Quases. *IMFP calculation by TPP2M formula*, Quases-Tougaard Inc., 2000-2016.

149 S. Tanuma, C. J. Powell and D. R. Penn, *Calculations of electron inelastic mean free paths (IMFPs). IV. Evaluation of calculated IMFPs and of the predictive IMFP formula TPP-2 for electron energies between 50 and 2000 eV*, Surf. Interface Anal., 1993, **20**, 77–89.

150 K. A. Yasakau, I. Giner, C. Vree, O. Ozcan, R. Grothe, A. Oliveira, G. Grundmeier, M. Ferreira and M. L. Zheludkevich, *Influence of stripping and cooling atmospheres on surface properties and corrosion of zinc galvanizing coatings*, Applied Surface Science, 2016, **389**, 144–156.

151 R. Grothe, M. Wiesing, I. Giner, D. Meinderink and G. Grundmeier, *Scanning Kelvin probe blister studies of the delamination of epoxy films on organosilane modified ZnMgAl alloy coated steel*, Materials and Corrosion, 2017, **68**, 1314–1320.

152 S. Pletincx, L. Trotochaud, L.-L. Fockaert, J. M. C. Mol, A. R. Head, O. Karslıoğlu, H. Bluhm, H. Terryn and T. Hauffman, *In Situ Characterization of the Initial Effect of Water on Molecular Interactions at the Interface of Organic/Inorganic Hybrid Systems*, srep, **7**, 45123.

153 P. Brüesch, R. Kötz, H. Neff and L. Pietronero, *Vibrational properties of Al₂O₃ films on gold, aluminum, and silicon*, Phys. Rev. B, 1984, **29**, 4691.

154 P. Thissen, M. Valtiner and G. Grundmeier, *Stability of phosphonic acid self-assembled monolayers on amorphous and single-crystalline aluminum oxide surfaces in*

aqueous solution, *Langmuir : the ACS journal of surfaces and colloids*, 2010, **26**, 156–164.

155 P. Thissen, J. Wielant, M. Köyer, S. Toews and G. Grundmeier, *Formation and stability of organophosphonic acid monolayers on ZnAl alloy coatings*, *Surface and Coatings Technology*, 2010, **204**, 3578–3584.

156 O. Ozcan, K. Pohl, B. Ozkaya and G. Grundmeier, *Molecular Studies of Adhesion and De-Adhesion on ZnO Nanorod Film-Covered Metals*, *The Journal of Adhesion*, 2013, **89**, 128–139.

157 W. Gao, L. Dickinson, C. Grozinger, F. G. Morin and L. Reven, *Self-Assembled Monolayers of Alkylphosphonic Acids on Metal Oxides*, *Langmuir*, 1996, **12**, 6429–6435.

158 M. S. Lim, K. Feng, X. Chen, N. Wu, A. Raman, J. Nightingale, E. S. Gawalt, D. Korakakis, L. A. Hornak and A. T. Timperman, *Adsorption and desorption of stearic acid self-assembled monolayers on aluminum oxide*, *Langmuir*, 2007, **23**, 2444–2452.

159 M. L. Schilling, H. E. Katz, S. M. Stein, S. F. Shane, W. L. Wilson, S. B. Ungashe, G. N. Taylor, T. M. Putvinski, C. E. D. Chidsey and S. Buratto, *Structural studies of zirconium alkylphosphonate monolayers and multilayer assemblies*, *Langmuir*, 1993, **9**, 2156–2160.

160 H. Medhashree and A. N. Shetty, *Electrochemical investigation on the effects of sulfate ion concentration, temperature and medium pH on the corrosion behavior of Mg–Al–Zn–Mn alloy in aqueous ethylene glycol*, *Journal of Magnesium and Alloys*, 2017, **5**, 64–73.

161 M. I. Muglali, A. Bashir and M. Rohwerder, *A study on oxygen reduction inhibition at pyridine-terminated self assembled monolayer modified Au(111) electrodes*, *physica status solidi (a)*, 2010, **207**, 793–800.

162 E. R. Vago, K. de Weldige, M. Rohwerder and M. Stratmann, *Electroreduction of oxygen on octadecylmercaptan self-assembled monolayers*, *Fresenius' Journal of Analytical Chemistry*, 1995, **353**, 316–319.

163 W. E. Swartz, J. H. Linn, J. M. Ammons and M. G. Kovac, *A x-ray photoelectron spectroscopy study of the diffusion of iron, nickel and cobalt through gold films*, *Thin Solid Films*, 1984, **114**, 349–356.

164 H. S. Kim, Y. N. Jo, W. J. Lee, K. J. Kim and C. W. Lee, *Coating on Zinc Surface to Improve the Electrochemical Behavior of Zinc Anodes for Zinc-Air Fuel Cells*, *Electroanalysis*, 2015, **27**, 517–523.

165 M. M. Arifat, B. Dinan, S. A. Akbar and Haseeb, A. S. M. A., *Gas sensors based on one dimensional nanostructured metal-oxides: a review*, *Sensors (Basel, Switzerland)*, 2012, **12**, 7207–7258.

166 R. S. Kate, S. A. Khalate and R. J. Deokate, *Overview of nanostructured metal oxides and pure nickel oxide (NiO) electrodes for supercapacitors: A review*, *Journal of Alloys and Compounds*, 2018, **734**, 89–111.

167 D. Meinderink, K. J. Nolkemper, J. Bürger, A. G. Orive, J. K. Lindner and G. Grundmeier, *Spray coating of poly(acrylic acid)/ZnO tetrapod adhesion promoting nanocomposite films for polymer laminates*, *Surface and Coatings Technology*, 2019, **375**, 112–122.

168 J. Jeon, T. G. Klaempfl, J. L. Zimmermann, G. E. Morfill and T. Shimizu, *Sporicidal properties from surface micro-discharge plasma under different plasma conditions at different humidities*, *New J. Phys.*, 2014, **16**, 103007.

169 Q. Sun, B. Yu and C. Liu, *Characterization of ZnO Nanotube Fabricated by the Plasma Decomposition of Zn(OH)2 Via Dielectric Barrier Discharge*, Plasma Chem Plasma Process, 2012, **32**, 201–209.

170 Y. Du, G. Nayak, G. Oinuma, Z. Peng and P. J. Bruggeman, *Effect of water vapor on plasma morphology, OH and H2O2 production in He and Ar atmospheric pressure dielectric barrier discharges*, J. Phys. D: Appl. Phys., 2017, **50**, 145201.

171 S. Rauf and M. J. Kushner, *Argon metastable densities in radio frequency Ar, Ar/O2 and Ar/CF4 electrical discharges*, Journal of Applied Physics, 1997, **82**, 2805–2813.

172 Y. J. Hong, C. J. Nam, K. B. Song, G. S. Cho, H. S. Uhm, D. I. Choi and E. H. Choi, *Measurement of hydroxyl radical density generated from the atmospheric pressure bioplasma jet*, J. Inst., 2012, **7**, C03046-C03046.

173 N. C. ROY, M. R. TALUKDER and A. N. CHOWDHURY, *OH and O radicals production in atmospheric pressure air/Ar/H2O gliding arc discharge plasma jet*, Plasma Sci. Technol., 2017, **19**, 125402.

174 S. Khachadorian, R. Gillen, S. Choi, C. Ton-That, A. Kliem, J. Maultzsch, M. R. Phillips and A. Hoffmann, *Effects of annealing on optical and structural properties of zinc oxide nanocrystals*, Phys. Status Solidi B, 2015, **252**, 2620–2625.

175 A. Mondal, S. Pal, A. Sarkar, T. S. Bhattacharya, S. Pal, A. Singha, S. K. Ray, P. Kumar, D. Kanjilal and D. Jana, *Raman investigation of N-implanted ZnO: Defects, disorder and recovery*, Journal of Raman Spectroscopy.

176 H. Zeng, X. Ning and X. Li, *An insight into defect relaxation in metastable ZnO reflected by a unique luminescence and Raman evolutions*, Phys. Chem. Chem. Phys., 2015, **17**, 19637–19642.

177 M. Šćepanović, M. Grujić-Brojčin, K. Vojisavljević, S. Bernik and T. Srećković, *Raman study of structural disorder in ZnO nanopowders*, J. Raman Spectrosc., 2010, **41**, 914–921.

178 V. Russo, M. Ghidelli, P. Gondoni, C. S. Casari and A. L. Bassi, *Multi-wavelength Raman scattering of nanostructured Al-doped zinc oxide*, Journal of Applied Physics, 2014, **115**, 73508.

179 H. Fukushima, H. Uchida, H. Funakuba, T. Katoda and K. Nishida, *Evaluation of oxygen vacancies in ZnO single crystals and powders by micro-Raman spectroscopy*, J. Ceram. Soc. Japan, 2017, **125**, 445–448.

180 S. S. Gaikwad, A. C. Gandhi, S. D. Pandit, J. Pant, T.-S. Chan, C.-L. Cheng, Y.-R. Ma and S. Y. Wu, *Oxygen induced strained ZnO nanoparticles: an investigation of Raman scattering and visible photoluminescence*, J. Mater. Chem. C, 2014, **2**, 7264–7274.

181 S. Pal, N. Gogurla, A. Das, S. S. Singha, P. Kumar, D. Kanjilal, A. Singha, S. Chattopadhyay, D. Jana and A. Sarkar, *Clustered vacancies in ZnO: chemical aspects and consequences on physical properties*, J. Phys. D: Appl. Phys., 2018, **51**, 105107.

182 Y. Y. Tay, T. T. Tan, M. H. Liang, F. Boey and S. Li, *Nature of quasi-LO phonon in ZnO*, Applied Physics Letters, 2008, **93**, 111903.

183 E. Alarcón-Lladó, R. Cuscó, L. Artús, J. Jiménez, B. Wang and M. Callahan, *Raman scattering of quasimodes in ZnO*, J. Phys.: Condens. Matter, 2008, **20**, 445211.

184 H. Zeng, W. Cai, B. Cao, J. Hu, Y. Li and P. Liu, *Surface optical phonon Raman scattering in Zn/ZnO core-shell structured nanoparticles*, Appl. Phys. Lett., 2006, **88**, 181905.

185 A. Janotti and C. G. van de Walle, *New insights into the role of native point defects in ZnO*, Journal of Crystal Growth, 2006, **287**, 58–65.

186 G.-D. Wei, C.-S. Ren, M.-Y. Qian and Q.-Y. Nie, *Optical and Electrical Diagnostics of Cold Ar Atmospheric Pressure Plasma Jet Generated With a Simple DBD Configuration*, IEEE Trans. Plasma Sci., 2011, **39**, 1842–1848.

187 J. Winiarski, W. Tylus, K. Winiarska, I. Szczygiel and B. Szczygiel, *XPS and FT-IR Characterization of Selected Synthetic Corrosion Products of Zinc Expected in Neutral Environment Containing Chloride Ions*, Journal of Spectroscopy, 2018, **2018**, 1–14.

188 R. Bhardwaj, A. Bharti, J. P. Singh, K. H. Chae, N. Goyal and S. Gautam, *Structural and electronic investigation of ZnO nanostructures synthesized under different environments*, Heliyon, 2018, **4**, e00594.

189 J. W. Chiou, J. C. Jan, H. M. Tsai, C. W. Bao, W. F. Pong, M.-H. Tsai, I.-H. Hong, R. Klauser, J. F. Lee, J. J. Wu and S. C. Liu, *Electronic structure of ZnO nanorods studied by angle-dependent x-ray absorption spectroscopy and scanning photoelectron microscopy*, Appl. Phys. Lett., 2004, **84**, 3462–3464.

190 A. Kuzmin, S. Larcheri and F. Rocca, *Zn K-edge XANES in nanocrystalline ZnO*, J. Phys.: Conf. Ser., **93**, 12045.

191 O. Šípr and F. Rocca, *Zn K edge and O K edge x-ray absorption spectra of ZnO surfaces: implications for nanorods*, Journal of physics. Condensed matter : an Institute of Physics journal, 2011, **23**, 315501.

192 P. Brosset, R. Dahoo, B. Gauthier-Roy, L. Abouaf-Marguin and A. Lakhlii, *Analysis of IR absorption spectrum of O₃ in inert matrices: spectroscopic evidence for two trapping sites*, Chemical Physics, 1993, **172**, 315–324.

193 B.-Y. Chang, C.-Y. Kung, C. Kittrell, C.-W. Hsiao, B. R. Johnson, S. G. Glogover and J. L. Kinsey, *High-accuracy measurement of vibrational Raman bands of ozone at 266 and 270 nm excitations*, The Journal of Chemical Physics, 1998, **101**, 1914.

194 J. F. da Silveira Petrucci, P. R. Fortes, V. Kokoric, A. Wilk, I. M. Raimundo, A. A. Cardoso and B. Mizaikoff, *Real-time monitoring of ozone in air using substrate-integrated hollow waveguide mid-infrared sensors*, Scientific reports, 2013, **3**, 3174.

195 S. Bailey, G. F. Froment, J. W. Snoeck and K. C. Waugh, *A DRIFTS study of the morphology and surface adsorbate composition of an operating methanol synthesis catalyst*, Catalysis Letters, 1995, **30**, 99–111.

196 W. Krasser, A. Fadini and A. J. Renouprez, *The Raman spectrum of carbon monoxide chemisorbed on silica-supported nickel*, Journal of Catalysis, 1980, **62**, 94–98.

197 M. S. Moss, K. Yanallah, R. W. K. Allen and F. Pontiga, *An investigation of CO₂ splitting using nanosecond pulsed corona discharge: effect of argon addition on CO₂ conversion and energy efficiency*, Plasma Sources Sci. Technol., 2017, **26**, 35009.

198 R. G. Urso, C. Scirè, G. A. Baratta, G. Compagnini and M. E. Palumbo, *Combined infrared and Raman study of solid CO*, A&A, 2016, **594**, A80.

199 S. Jiang, K. Klingan, C. Pasquini and H. Dau, *New aspects of operando Raman spectroscopy applied to electrochemical CO₂ reduction on Cu foams*, The Journal of Chemical Physics, 2018, **150**, 41718.

200 M. Polak, J. Winter, U. Schnabel, J. Ehlbeck and K.-D. Weltmann, *Innovative Plasma Generation in Flexible Biopsy Channels for Inner-Tube Decontamination and Medical Applications*, Plasma Processes and Polymers, 2012, **9**, 67–76.

201 P. A. Christensen, Ali, Abd Halim Bin Md, Z. T. A. W. Mashhadani, M. A. Carroll and P. A. Martin, *The Production of Ketene and C₅O₂ from CO₂, N₂ and CH₄ in a Non-thermal Plasma Catalysed by Earth-Abundant Elements: An In-Situ FTIR Study*, Plasma Chemistry and Plasma Processing, 2018, **38**, 461–484.

202 A. Ozkan, T. Dufour, T. Silva, N. Britun, R. Snyders, A. Bogaerts and F. Reniers, *The influence of power and frequency on the filamentary behavior of a flowing DBD—application to the splitting of CO₂*, *Plasma Sources Sci. Technol.*, 2016, **25**, 25013.

203 R. Lushtinetz, G. Seifert, E. Jaehne and H.-J. P. Adler, *Infrared Spectra of Alkylphosphonic Acid Bound to Aluminium Surfaces*, *Macromol. Symp.*, 2007, **254**, 248–253.

204 N. G. Moll, D. R. Clutter and W. E. Thompson, *Carbon Trioxide: Its Production, Infrared Spectrum, and Structure Studied in a Matrix of Solid CO₂*, *The Journal of Chemical Physics*, 1966, **45**, 4469–4481.

Glossary

AFM	Atomic Force Microscopy
Ar/H ₂ O	gas composition of Ar + 5 % H ₂ O
Ar/O ₂	gas composition of Ar + 5 % O ₂
CA	contact angle
CV	cyclic voltammetry
DBD	dielectric barrier discharge
DMSO	dimethylsulfoxide
DPM-IRRAS	discrete polarization modulated IRRAS
DRIFTS	diffuse reflectance infrared Fourier transformed spectroscopy
EDX	Energy-Dispersive X-ray
EIS	electron impedance spectroscopy
EtOH	ethanol
EXAFS	X-ray absorption fine structure spectroscopy
FTIR	fourier transformed infrared
IR	infrared
IRRAS	infrared reflection absorption spectroscopy
KP	Kelvin Probe
LSV	linear sweep voltammetry
ODPA	octadecyl phosphonic acid
OES	optical emission spectroscopy
PEEK	Polyether ether ketone
PM-IRRAS	polarization modulated IRRAS
SAM	self-assembled monolayer
SEM	Scanning Electron Microscopy
SHE	standard hydrogen electrode
SKP	Scanning Kelvin Probe
SKPFM	Scanning Kelvin Probe Force Microscopy
TEM	Transmission Electron Microscopy
THF	tetrahydrofuran
TOF-SIMS	time-of-flight secondary ion mass spectroscopy
XANES	X-ray absorption near-edge structure
XAS	X-ray absorption spectroscopy
XPS	X-ray photon spectroscopy
ZnO	zinc oxide
ZnO-NR	zinc oxide nanorods

List of publications

- [1] S. Knust, A. Kuhlmann, T. de los Arcos and G. Grundmeier, *RSC Advances*, 2019, **9**, 35077–35088
- [2] S. Knust, A. Kuhlmann, A. G. Orive, T. Arcos and G. Grundmeier, *Surf Interface Anal*, 2020.
- [3] S. Knust, L. Ruhm, A. Kuhlmann, D. Meinderink, J. Bürger, J. K. N. Lindner, M. T. Arcos de Pedro and G. Grundmeier, *J. Raman Spectrosc.*, 2021
- [4] R. Grothe, S. Knust, D. Meinderink, M. Voigt, A. G. Orive and G. Grundmeier, *Surf. Coat. Tech.*, 2020
- [5] Y. Yang, M. Yu, F. Böke, Q. Qin, R. Hübner, S. Knust, S. Schwiderek, G. Grundmeier, H. Fischer and A. Keller, *Appl. Surf. Sci.*, 2021
- [6] Y. Yang, S. Knust, S. Schwiderek, Q. Qin, Q. Yun, G. Grundmeier and A. Keller, *nanomaterials*, 2021
- [7] J. A. G. D., A. G. Orive, C. Weinberger, S. Schwiderek, S. Knust, M. Tiemann, G. Grundmeier, A. Keller and R. J. C. Amado, *J. Biomed. Mat. Res.*, 2021
- [8] S. Knust, M. Wahle, H.-S. Kitzerow, *J. Phys. Chem. B*, 2017, **121**, 19, 5110-5115

Acknowledgments

In the end, I would like to thank all who made this thesis possible and an enjoyable time.

First, I thank Prof. Grundmeier for introducing me to the interesting field of plasmas and their applications. Although it was not always bright times, you showed always faith in me and offered your constant guiding. Thereby, you had a friendly ear and always gave your professional opinion on the subject in professional discussions. I am also thankful for the possibility to attend international conferences and workshops, expanding my horizons.

Furthermore, I would like to thank Teresa for her no lesser guidance, especially, but not limited to, all plasma-related topics. I will miss our talks and discussion, changing from German to English and back, constantly tossing in Spanish words. Your expertise and friendly mood enlighten the workgroup and are a source of constant joy. Don't let the work get you, get the work. ☺

Without my SHKs Andreas and Lukas, my work would be far from complete. Andreas, although you had to spend hours on the plasma setup and especially the Kelvin Probe, I think in the end we controlled her and not the other way round, so we surely succeeded. You were always clever, reliable, curious, and independent, which made you incredibly helpful. Similarly, Lukas experienced the moods of the backside setup, but in the end, it gave us what we wanted. You are clever, reliable, curious, and independent as well, and without both of you, it would have been a much more challenging and less fun time.

I also would like to thank the whole workgroup, which exhibited at any time a friendly and cooperative atmosphere. You made working an enjoyable time, even if the whole set of measurement methods resisted and were close to being thrown out of the window (by the whole workgroup). Special thanks go to Dennis and Sabrina, who didn't hesitate to jump in my work as my hand was not functional (and all the other times ☺). One last piece of advice: You work too much, go home! ;)

I want to thank Dennis, Andreas, Lukas, Julius, and Theresa for their proofreading of this thesis.

I thank Prof. Dr. Lindner, PD. Dr. Egold and Prof. Dr. bremser for participating in the examination board of this work.

Last I would like to thank my family, for their patience and their love.